Using Digital Hydraulics in Secondary Control of Motor Drive

Sondre Nordås

Using Digital Hydraulics in Secondary Control of Motor Drive

Doctoral Dissertation for the Degree *Philosophiae Doctor (PhD)* at
the Faculty of Engineering and Science, Specialisation in Mechatronics

University of Agder
Faculty of Engineering and Science
2020

Doctoral Dissertation at the University of Agder 265
ISSN: 1504-9272
ISBN: 978-82-7117-966-3

©Sondre Nordås, 2020

Printed by Wittusen & Jensen
Oslo

Preface

The research presented in this thesis has received funding from the Norwegian Research Council, SFI Offshore Mechatronics, project number 237896. The research has been carried out in the period between March 2016 and September 2019 at the University of Agder, Department of Engineering Sciences. Professor Torben Ole Andersen from Aalborg University has been the main supervisor and Associate Professor Morten Kjeld Ebbesen has been the co-supervisor.

Acknowledgments

I want to thank my main supervisor Professor Torben Ole Andersen for his guidance throughout the project. I also want to thank my co-supervisor Associate Professor Morten Kjeld Ebbesen for his great help with writing papers and always taking the time to answer all kind of questions.

I also want to thank all members in the SFI work package 1 reference group for valuable information regarding offshore applications. My gratitude also goes to Associate Professor Michael Møller Bech and Assistant Engineer Jan Christiansen at Aalborg University for their help with the experimental test. Jan Christiansen and his team did an excellent job when they manufactured the valve block and assembled the prototype. Michael Møller Bech was essential in designing valve drives and the implementation of the control strategy of the modified digital displacement cylinder. I also want to thank Rune Risholt at MHWirth for designing the valve block for the prototype.

My gratitude also goes to my mentor Andreas Klausen for always taking the time to answer my questions. I am also grateful for all the great fellow Ph.D. candidates that I have learned to know in the time of this project. A special thanks to Daniel Hagen for all the academic and non-academic discussions.

Finally, I want to thank my family for their patience and acceptance for prioritizing the Ph.D. work higher than almost everything. They have always been there for me.

Sondre Nordås,
University of Agder, September, 2019

Summary

Due to the increased focus on pollution and global warming, there is a demand for energy efficient systems. This also applies to the offshore oil and gas industry. Normally used hydraulic systems tend to suffer from low energy efficiency, especially when operating with part loads. In the last decades, a new pump and motor technology has experienced increased interest due to the potential of high energy efficiency in a wide range of operation conditions. This new technology is called digital displacement machine technology. Nowadays, there is a desire from the offshore oil and gas industry to use this digital displacement machine technology to design highly efficient hydraulic winch drive systems.

The main objectives of the work presented in this thesis are to design a controller for a digital displacement winch drive system and evaluate its control performance. The design of a controller is one part of the work needed to realizing a winch drive system with digital displacement machines. A winch with a lifting capacity of 20000 kg and a drum capacity of 3600 m of wire rope is used as a case study.

Digital displacement machines have strict requirements for the on/off valves used to control each cylinder chamber. It is important to activate the valves at optimal times to ensure operation with high energy efficiency and low pressure and flow peaks. Only a small mistiming of the valves will affect the performance of the digital displacement machine significantly. One of the first contributions presented in this thesis is a method for defining how early or late the valves can be timed without reducing the energy efficiency significantly.

The control of digital displacement machines is complicated and non-conventional. Each cylinder can be controlled individually and multiple displacement strategies can be used to achieve the same displacement. Each displacement strategy has its dynamic response characteristics and energy efficiency characteristics. The dynamic response characteristics of the drive system are highly relevant when designing control systems. Therefore, in addition to the conventional classical controller, also a suitable displacement strategy must be designed. Designing controllers for digital displacement machines are therefore more complex than designing controllers for conventional hydraulic machines.

One of the main focuses of this project has been to analyze the transient and steady-

state response characteristics of different displacement strategies. In all, three displacement strategies are examined: full stroke displacement strategy, partial stroke displacement strategy and sequential partial stroke displacement strategy. Also, during this work, a new version of the partial stroke displacement strategy has been developed and included in the dynamic response analysis.

The dynamic response analysis is a simulation study, where the simulation model is experimentally validated. The experimental work is conducted on a prototype of a single cylinder digital displacement machine. The prototype consists of a five cylinder radial piston motor where one cylinder is modified to operate with the digital displacement technology. The rest of the cylinders are not changed and not used. In addition to validating the simulation model, the prototype is used to test all of the analyzed displacement strategies in low speed operation.

The results from the dynamic response analysis are used to select the displacement strategy that is most suited for use in a winch drive system. Then, controllers for the digital displacement winch drive system are developed. The main focus in the control design phase is not to design a new type of controller but to examine already developed controllers and fit them to a winch system driven by digital displacement machines. In the end, the simulation results of the designed controllers are shown and the results are discussed. The simulation results show that digital displacement machines can be used in winch drive systems and achieve both high motion control performance and wire tension control performance.

Publications

The following six articles have been published or submitted for publication in conference proceedings and journals.

Paper A S. Nordås, M. K. Ebbesen, and T. O. Andersen. The Potential of a Digital Hydraulic Winch Drive System. In *The Proc. of The Ninth Workshop on Digital Fluid Power*, Aalborg, Denmark, 2017.

Paper B S. Nordås, M. K. Ebbesen, and T. O. Andersen. Feasibility Study of a Digital Hydraulic Winch Drive System. In *The Proc. of The Ninth Workshop on Digital Fluid Power*, Aalborg, Denmark, 2017.

Paper C S. Nordås, M. K. Ebbesen, and T. O. Andersen. Analysis of Requirements for Valve Accuracy and Repeatability in High Efficient Digital Displacement Motors. In *The Proc. of the BATH/ASME 2018 Symposium on Fluid Power and Motion Control*, Bath, United Kingdom, 2018.

Paper D S. Nordås, M. M. Beck, M. K. Ebbesen, and T. O. Andersen. Dynamic Response of a Digital Displacement Motor Operating with Various Displacement Strategies. *Energies*, 2019, 12.9.

Paper E S. Nordås, M. K. Ebbesen, and T. O. Andersen. Definition of Performance Requirements and Test Cases for Offshore/Subsea Winch Drive Systems with Digital Hydraulic Motors. In *The Proc. of the BATH/ASME 2019 Symposium on Fluid Power and Motion Control*, Sarasota, Florida, 2019.

Paper F S. Nordås, M. K. Ebbesen, and T. O. Andersen. Control of a Digital Displacement Winch Drive System. Submitted to *Modeling, Identification and Control*, December 5, 2019

Contents

Abbreviations

AC	Adaptive controller
AIP	Artemis Intelligent Power Ltd.
AHC	Active heave compensation
BC	Base controller
BDC	Bottom dead center
CT	Constant tension
CWD	Conventional winch drive system
DDM	Digital displacement motor
DDP	Digital displacement pump
DHPMS	Digital hydraulic power managment system
FDWD	Full digital displacement winch drive system
FSDS	Full stroke displacement strategy
HPU	Hydraulic power unit
HPV	High pressure valve
LCM	Linz Center of Mechatronics
LPV	Low pressure valve
LQG	Linear quadratic gaussian
LQR	Linear quadratic regulator
MCA	Moving coil actuator
MHI	Mitsubishi Heavy Industries
MMA	Moving magnet actuator
MRU	Motion reference unit
PHC	Passive heave compensation
PSDS	Partial stroke displacement strategy
ROV	Remotely operated underwater vehicle
SMDC	Sliding mode disturbance controller
SPSDS	Sequential partial stroke displacement strategy
SWL	Safe working load
TDC	Top dead center

Chapter 1

Introduction

The main objectives of the work presented in this thesis are to design a control system for a secondary controlled high torque low speed digital displacement motor and evaluate its control performance. The need for such a control system origins in the potential of using digital displacement machines in offshore winch drive systems in, for example, a subsea crane. This chapter gives a short introduction to current hydraulic winch drive systems, followed by a presentation of a new alternative: the secondary controlled digital displacement winch drive system. This leads to a presentation of the digital displacement machine. At the end of this chapter, the research objectives and the main contributions are presented in addition to the reading guidelines.

1.1 Offshore Winch Systems and Their Drive System

Big offshore winches are typically found on subsea cranes on floating vessels. They are normally used for deployment, recovery and relocation of equipment on the seabed. Floating vessels tend to move up and down due to waves. This vertical motion is often called "heave motion". This heave motion makes subsea lifting operations challenging, especially in rough weather conditions.

Winches used in subsea lifting operations have a safe working load (SWL) from a few tonnes up to 900 tonnes and can operate in water depths beyond 3000 m. The winch is normally a single drum type. The drum is large and designed to accommodate a long wire rope arranged in several overlapping layers. The winch drum is normally actuated by one or more high speed hydraulic motors with gearboxes. The driving torque is transfered to the winch drum through a pinion and gear ring mounted on the drum. Figure 1.1 shows an example of a subsea crane with an offshore winch actuated by 12 hydraulic motors.

The winch is normally controlled by a human operator that operates a joystick. In harsh weather conditions where the vessel has a significant heave motion, additional

Figure 1.1: Subsea crane equiped with a hydraulic winch system [1].

control systems may ease the operation and increase the weather window of operation. The weather window is a set of weather conditions, for example wind speed and wave hight that must not be exceeded during the lift. Examples of additional control systems are active heave compensation and constant tension system.

An active heave compensation (AHC) system is a control system used to decouple the vertical vessel motion from the payload motion. This means that the winch operator can use the joystick to control the payload motion relative to a fixed surface, which makes it easier to, for example, land a payload on a fixed installation or the seabed. The AHC system normally utilizes a motion reference unit (MRU) to measure the unwanted vessel motion and actively controls the winch to counteract the influence on the payload motion.

The constant tension (CT) system is a control system used to keep the wire tension at a given pre-set value regardless of the vessel motion. A load cell is typically used to measure the wire tension. If the measured value deviates from the pre-set value, the winch will pull in or pay out wire rope to maintain the pre-set value. The CT system is typically used during lift-off and lift-down on the sea bed.

To conduct lifting operations with high quality, the winch drive system must be able to operate in all four quadrants and provide high motion and torque control. Normally, only two quadrant operation are needed. Quadrant 1 during hoisting and quadrant 3 during lowering. However, in special cases as for example in AHC mode or operations with an empty hook, all four quadrants may be used. High motion control is needed in the operator mode and the AHC mode. High torque controll is needed in the CT mode. The hydraulic system is normally an open loop or closed loop circuit. The open loop circuit is used in small winches typically below 20-50 tonnes and the closed circuit system is normally used in large winches.

1.1.1 Open Loop Hydraulic Circuit

In an open loop hydraulic circuit, the fluid from the pump is regulated by a directional control valve before it reaches the motor, performs work and returns to the tank via the directional control valve. Figure 1.2 shows a simplified hydraulic diagram of a general open loop circuit driving a winch. The benefits of the open loop circuit are simple design, low

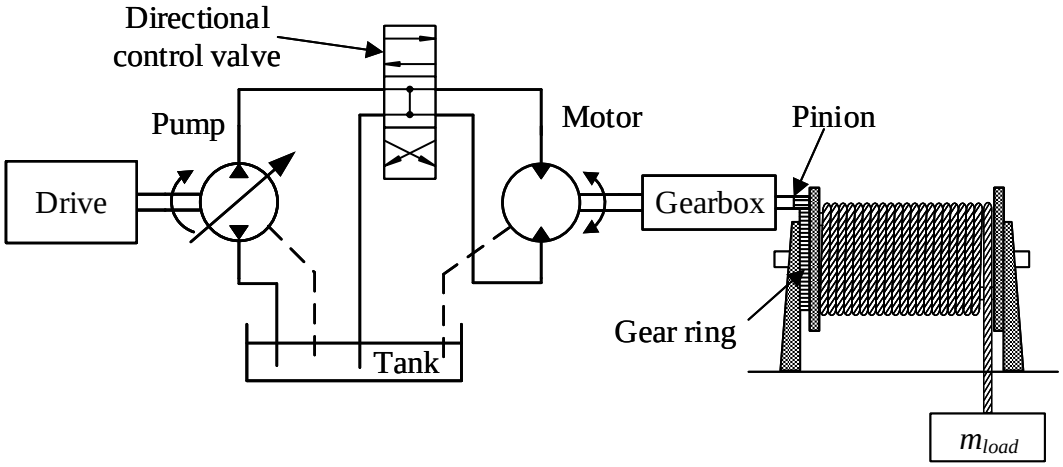

Figure 1.2: Schematic illustration of open loop winch drive system.

cost and that one hydraulic power unit (HPU) can supply multiple actuators. The main disadvantage is low energy efficiency. In some applications, the average energy efficiency of open loop systems may be as low as 10-35 % [2]. However, efficiencies as low as these occur normally only when operating at low loads. The least energy efficient system utilizes a fixed displacement pump operating at constant speed and thereby delivers a constant flow. The directional control valve regulates the flow that is delivered to the motor. The unused flow is routed back to tank resulting in significant energy losses. This type of system may be acceptable for systems that are only operated for short periods of time, and where simplicity, low initial cost and ease of maintenance are more important than high energy efficiency.

In larger systems or systems that are running over a long period of time, a variable displacement pump may be used to improve the energy efficiency. A variable displacement pump will only deliver fluid when necessary and thereby reduce the amount of unused fluid that is routed back to the tank. The energy losses in such a system are mainly caused by throttling flow in the directional control valve and losses in the pump and motor. It is not unreasonable to achieve an energy efficiency between 50 % and 80 % in such a system [3].

Another drawback of the closed loop system is that it is not suited for regenerating energy during, for example, heave compensation or lowering of the payload.

1.1.2 Closed Loop Hydraulic Circuit

In the closed loop hydraulic circuit, the directional control valve is removed and the motor is directly connected to a variable displacement pump, as shown in Figure 1.3. In order to

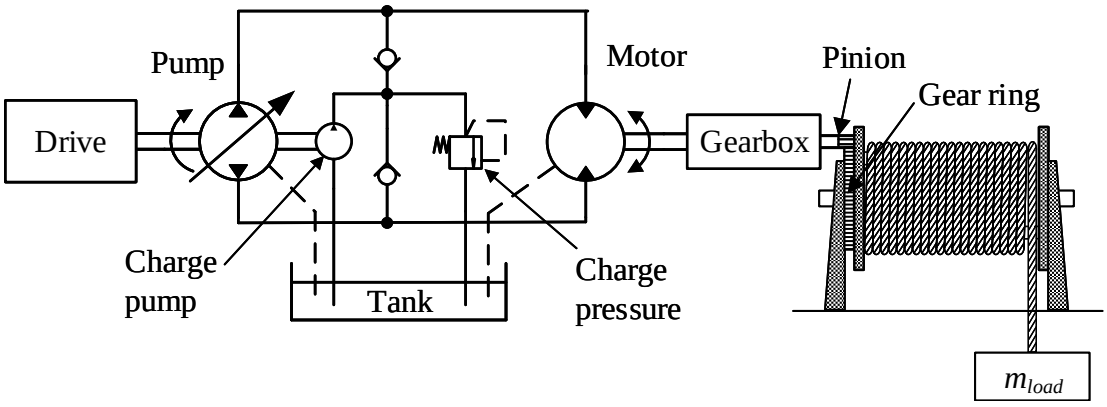

Figure 1.3: Schematic illustration of closed loop winch drive system.

account for leakage in the pump and motor, and to ensure that the pressure lines maintain a minimum pressure, the circuit has a charge pump that supplies cooled and filtered fluid to the pressure lines.

The closed loop system provides high motion tracking performance. The motor speed is linearly controlled by the pump outlet instead of the nonlinear response found in most of the proportional control valves. Energy efficiency of 80 % may be realized [4].

Compared to open loop systems, closed loop systems have increased costs since more expensive components are used and a dedicated pump is needed for each actuator to operate independently and at high energy efficiency. Closed loop systems are also considered to be more difficult to diagnose and repair [5].

1.2 Secondary Controlled Digital Displacement Winch Drive System

An alternative to the commonly used winch drive systems with open loop and closed loop circuits and conventional hydraulic pumps and motors, is a secondary controlled hydraulic system with digital displacement machines. An illustration of such a system is shown in Figure 1.4. The stepped arrow on the pump and motor symbol indicates that it is a digital displacement machine. The alternative system consists of a prime mover, accumulator and a secondary unit capable of operating in both motor mode and pump mode with positive and negative direction of rotation. Unlike conventional winch drive systems that utilize high speed motors and gearboxes, the alternative system consists of a low speed motor directly connected to the gear ring on the winch drum without any

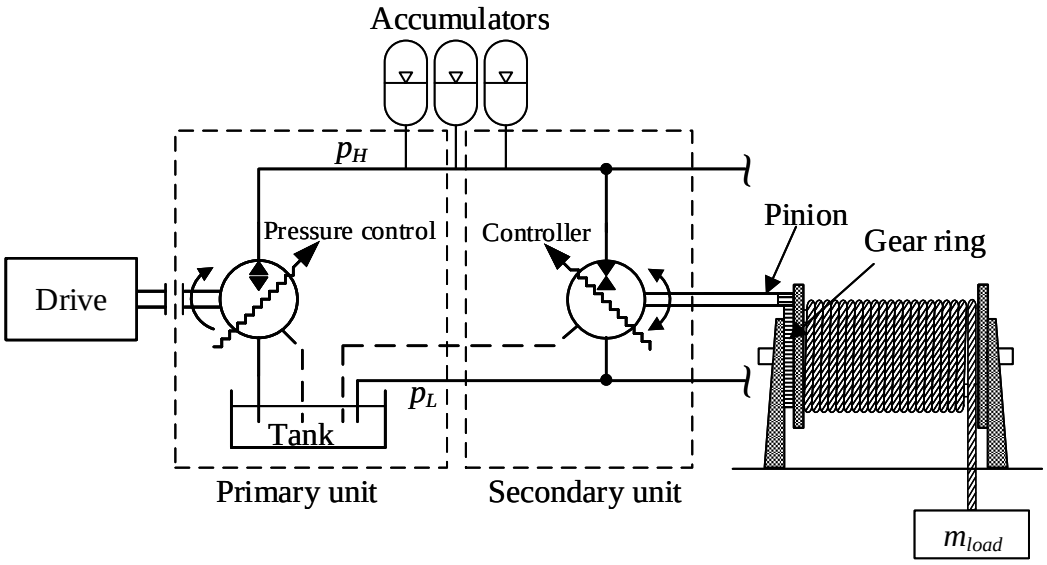

Figure 1.4: Schematic illustration of secondary controlled digital displacement winch drive system.

gearbox. The prime mover, or pump, has a pressure controller and its main task is to keep the high pressure level, p_H, on a minimum level. The secondary unit, or hydraulic motor, is directly connected to the high- and low pressure line, without the use of any throttling valves. The output torque is controlled by controlling the displacement of the secondary unit. The purpose of the accumulators is to store energy whenever the secondary unit operates in pump mode. The stored energy can later be reused when the secondary unit operates in motor mode. One primary unit and one accumulator bank can supply several secondary control units that operate with varying loads.

This thesis is limited to development of a control system for the secondary controlled digital displacement motor. It is therefore not in the scope of this thesis to design a pressure controller for the primary unit nor design a suitable accumulator bank. For simplicity reasons, it is assumed that the primary unit, together with the accumulator bank, can keep the high pressure level at a nearly constant level. The secondary controlled winch drive system can then be simplified as illustrated in Figure 1.5, where it is assumed that the digital displacement motor is connected to a constant high and low pressure source.

This winch drive system is further in this thesis referred to as the digital displacement winch drive system.

1.2.1 Motivation

The main motivation of using the digital displacement winch drive system is to increase the energy efficiency. The conventional closed loop circuit is considered to be the most

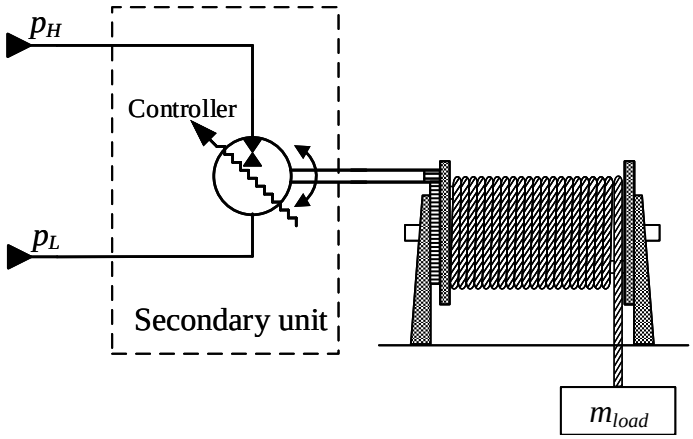

Figure 1.5: Schematic illustration of the simplified secondary controlled digital displacement winch drive system.

energy efficient of the existing systems. The main losses come from the pump, motor and gearbox. Conventional hydraulic pumps and motors are known to suffer from low energy efficiency, especially at partial displacement while digital displacement machines are known to have a potential for high energy efficiency even at partial displacement. In addition, it is reasonable to assume that the digital displacement winch drive system can provide reduced losses, cost and mass of hydraulic winch drive systems [6].

Secondary controlled hydraulic systems combine the benefits of both the open and closed circuit system by providing high energy efficiency, high motion control and the capability to use the same primary unit to supply several secondary units. In addition, the secondary controlled system is suitable for use in energy recovery systems. Energy recovery systems can, for example, be used during lowering of payloads. The energy can be recovered by storing the energy in accumulator banks and reuse the energy at a later point in time, reuse the energy continuously by other hydraulic actuators or in case of an electric prime mover, the energy can be fed back to the electric grid by using the primary unit as a motor and the electric drive as a generator.

Increasing the energy efficiency and removing the gearbox have several benefits. By increasing the energy efficiency, less power is consumed which makes the operation more cost effective. In addition, less heat is generated in the hydraulic system which may result in downsizing of the cooling system. Since less power is used, the HPU may also be downsized. The gearbox is costly and requires maintenance. In case of gearbox failure, the gearbox needs to be replaced, which is time consuming and requires lifting equipment.

Lately, due to increased focus on pollution and global warming, there has been a trend of replacing hydraulically actuated offshore applications by more environmentally friendly electric actuated applications. Electric systems are known to be energy efficient and easy to control. On the other hand, they are also known to be expensive, big in size and heavy. The energy efficiency of digital displacement motors is comparable to electric motors with

frequency converters in addition to be lighter and smaller in size [6]. In Figure 1.6 the size of a high torque low speed digital displacement motor is compared to the size of an electrical motor and gearbox. Both drive systems have almost the same power rating. The

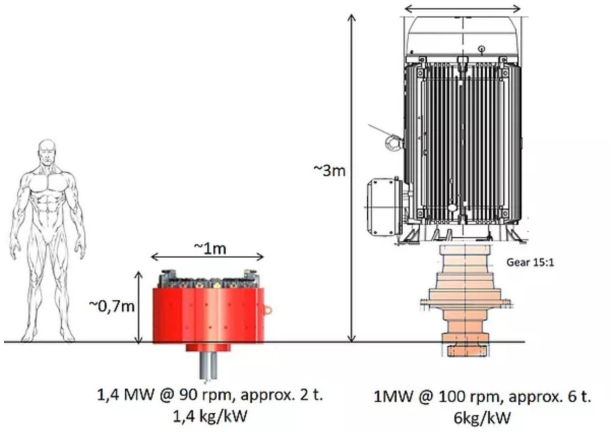

Figure 1.6: High torque low speed digital displacement motor vs high speed electrical motor with gearbox [6].

digital displacement machine has a mass to power ratio of 1.4 kg/kW while it is 6 kg/kW for the electrical solution. Hence, the digital displacement machine requires less space and is lighter compared to the electrical solution. This is an important characteristic when considering applications that shall operate offshore where space is limited and mass should be minimized.

The disadvantages of the digital displacement winch drive system are that the technology is relatively new, the control is complicated and non-conventional and the valve requirements are strict. The valves should have high flow capacity, low response time, high durability, low power consumption, be cheap and easy to replace.

The main motivations for using a digital displacement winch drive system are summarized in the following bullet points:

- Increase energy efficiency in winch systems.
- Reduce system and operation costs by removing the gearbox and downsizing the cooling system and the HPU.
- Reduce space requirements and mass of the application.

1.2.2 Control Design Considerations

Digital displacement motors deviate from traditional piston motors in the way the hydraulic fluid is diverted in and out of the cylinder chambers. Each cylinder chamber is connected to two fast switching on/off valves which divert the hydraulic fluid to and from the low or high pressure line. The displacement ratio can be changed by changing the activation sequence of the on/off valves. Also, the same displacement ratio can be achieved

by using different valve activation sequences. A valve activation sequence is further in this thesis referred to as a displacement strategy.

Each displacement strategy has its own dynamic response characteristics and energy efficiency characteristics. Therefore, when designing controllers for digital displacement machines, it is not enough to design a classic controller for the desired displacement. Also, a suitable displacement strategy needs to be designed or selected from previously designed displacement strategies. In addition, different displacement strategies have different requirements for the on/off valves used in the digital displacement motor. Therefore, the valve properties are also important to consider when designing the controller.

A general control structure for a digital displacement motor is illustrated in Figure 1.7. First, the input signal is transformed into a desired displacement ratio of the digital

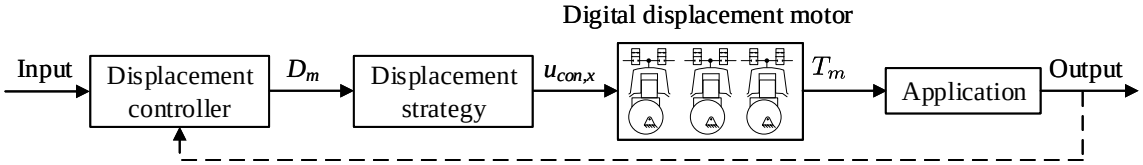

Figure 1.7: General schematic illustration of a digital displacement motor controller.

displacement motor, D_m, by a displacement controller. The displacement controller is a classic controller that can be of any type, with or without feedback signals, like for example an open loop proportional controller or a closed loop PID controller. The desired displacement ratio is then transformed into valve activation signals, $u_{con,x}$, by a displacement strategy. After that, the on/off valves activate and deactivate the cylinder chambers in order to achieve the desired displacement ratio. The activated chambers creates an output torque, which finally drives the application.

When designing a controller for a digital displacement motor, it is important to have knowledge about its working principle, different displacement strategies, the properties of the on/off valves used in the digital displacement motor and also classic control design.

The next section, Section 1.3, will therefore start by describing the working principle of the digital displacement machine and continue with the advantages and disadvantages related to the digital displacement machine technology. Then, the state of the art of different displacement strategies, valves for digital displacement machines, and control of digital displacement machines are presented and it is pointed out where knowledge is missing. The section ends by summarizing the development trends of digital displacement machines. The research objectives presented in Section 1.4 are based on the missing knowledge revealed in the state of the art.

1.3 Digital Displacement Machine

Digital displacement machines deviate from traditional piston machines in the way the cylinders are connected to high and low pressure. In, for example, a conventional radial piston machine, the cylinders are connected to high and low pressure in conjunction with the shaft position through a rotary valve, as shown to the left in Figure 1.8. The displacement is changed by changing the eccentricity of the cam disk. During one shaft revolution, all cylinders are pressurized resulting in almost constant leakage, friction and compressibility losses independent of the displacement. The machine efficiency will therefore be significant reduced when operating at low displacements.

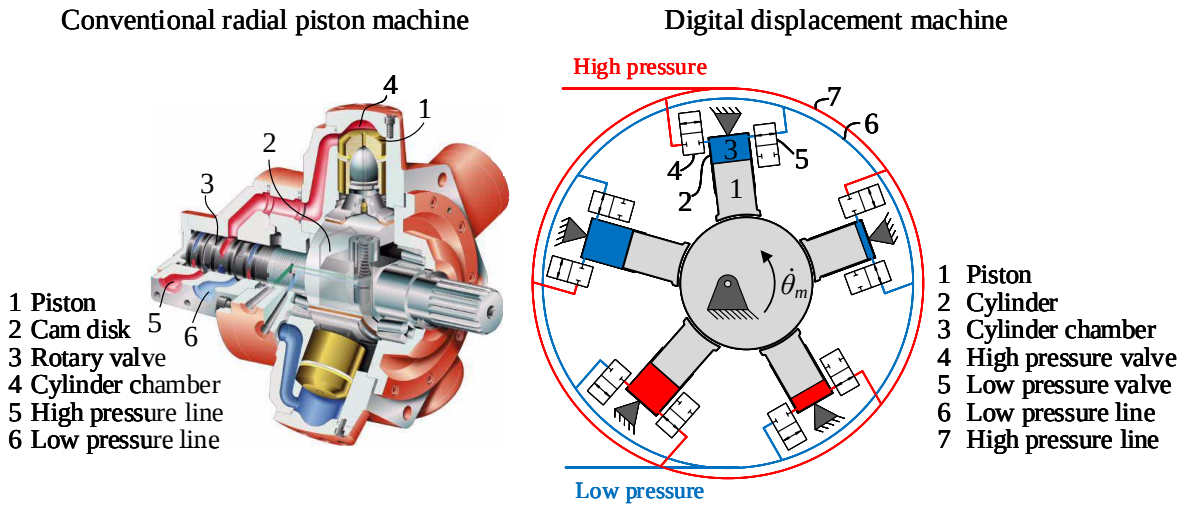

Figure 1.8: Illustration of a conventional radial piston machine [7] (left) and a radial piston type digital displacement machine (right).

In a digital displacement machine each cylinder is connected to two fast switching on/off valves as shown to the right in Figure 1.8. The high pressure valve is connecting the high pressure manifold to the cylinder chamber and the low pressure valve is connecting the cylinder chamber to the low pressure manifold. By controlling the on/off valves, each cylinder can be controlled individually, which makes this unit very flexible and suited for new system designs. The displacement is changed by only pressurizing cylinders when necessary, resulting in leakage and friction losses that scale with the displacement providing high energy efficiency even at partial displacement.

The digital displacement machine is not limited to a radial cylinder configuration, but the radial configuration provides several advantages. The radial configuration with pistons facing outwards leaves enough space for mounting two on/off valves to each cylinder. The machine displacement can easily be increased by adding several motor modules/cylinder banks, side-by-side along the same shaft. A more detailed description of the digital displacement technology can be found in [8, 9, 10].

1.3.1 Advantages and Disadvantages

There are several advantages and disadvantages of digital displacement machines compared to conventional hydraulic machines. The main advantages and disadvantages mentioned in the literature [11, 12, 13] are:

Advantages:

- Higher energy efficiency at partial displacement, since each cylinder chamber is only pressurized when necessary. Unpressurized cylinder chambers have typically losses less than one percent of an active one at high pressure [14].
- Superb scalability due to the modular structure. In case of a radial motor configuration, several motor modules can be added side-by-side along the same shaft.
- Fast response (at high shaft speed) since the displacement can be changed from zero to full in half a shaft revolution.
- Require less cooling due to higher energy efficiency. Hence, the cooling systems can be downsized.
- Completely new solutions like machines with several independent outlets, also called digital hydraulic power management systems, are possible due to individual cylinder control.
- The capability of full four quadrant operation and high energy efficiency makes the digital displacement machine suitable for use in secondary control systems and energy recovery systems. The energy can be recovered to hydraulic accumulators, other actuators or back to the prime mover.
- Reliable load holding since the on/off valves are leak free.

Disadvantages:

- Pulsation in machine output, especially when operating at partial displacements.
- Complicated and non-conventional control. Instead of, for example, changing the angle of the swash plat in an axial swash plate machine, each on/off valve needs to be controlled individually.
- High valve requirements. The on/off valves should have low cost, compact design, high durability, be easy to replace, low electric power consumption, zero leakage, low switching time and high flow capacity.
- Noise due to switching between active and inactive cylinder chambers.

The high energy efficiency is the key feature of digital displacement machines. The high energy efficiency is achieved due to the low losses of de-pressurized cylinders, only switching the valves at low pressure difference and low flow rates and having zero leakage valves. Figure 1.9 maps the energy efficiency from a variable displacement bent axis pump and a digital displacement pump at full and 20 % displacement. The upper plots show the energy efficiency maps for the variable bent axis pump and the bottom plots show

the energy efficiency maps for the digital displacement pump. The bent axis pump has

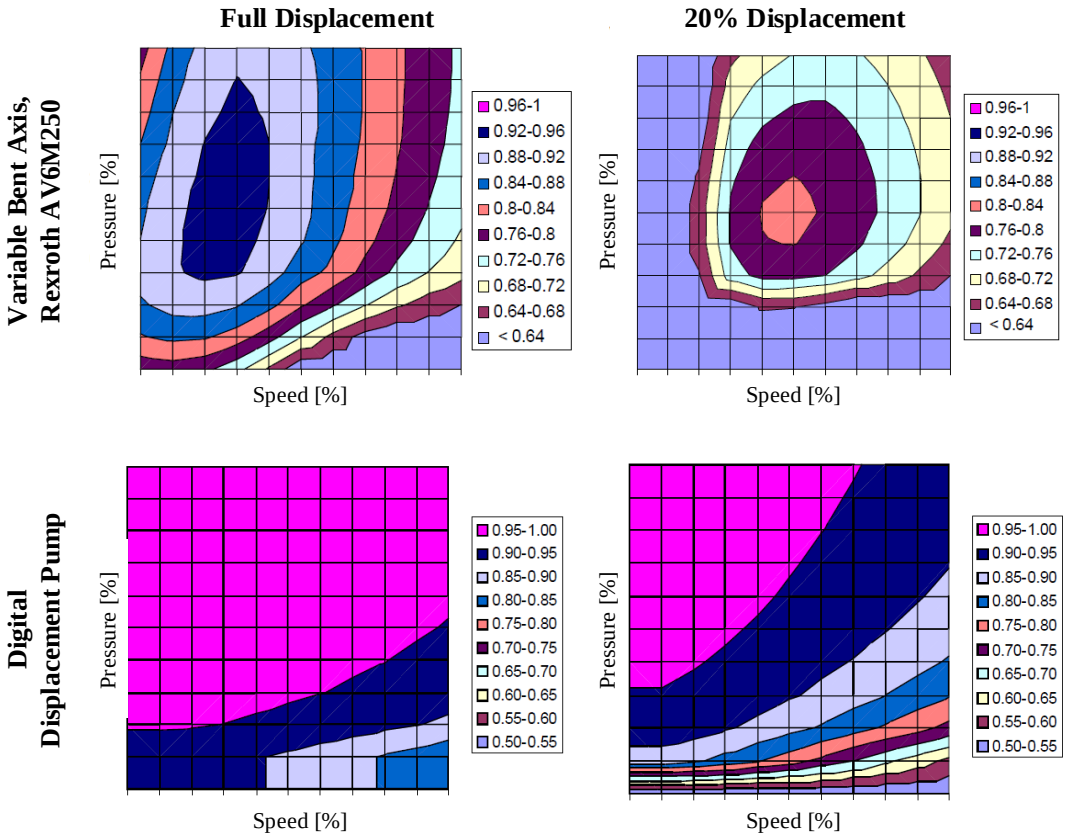

Figure 1.9: Efficiency map of a typical bent axis machine (top) and a digital displacement machine (bottom) at full displacement (left) and 20 % displacement (right) [15].

a peak efficiency of 93 % at full displacement and can keep the efficiency above 80 % in a relatively large operation area (speed and pressure). The peak efficiency is reduced to 81 % at 20 % displacement and the efficiency is only kept above 80 % in a very small operation area. For the digital displacement pump, the peak efficiency is 97 % at full displacement and only reduced to 96 % at partial displacement. The energy efficiency is kept above 80 % for a very large operation area, even at 20 % displacement. This example clearly shows the improvement on energy efficiency in digital displacement pumps.

1.3.2 Variable Displacement Control

In general, each cylinder chamber can either be connected to the high pressure manifold or the low pressure manifold. A chamber that is connected to high pressure is called an active cylinder and a chamber connected to low pressure is called a deactivated or inactive cylinder. The cylinder acts as a motor if the chamber is active in the downstroke piston motion and as a pump if the chamber is active in the upstroke piston motion.

By systematically activating and deactivating the cylinder chambers, the digital displacement machine can operate as a motor or pump at variable displacements. This

systematic activation and deactivation strategy is referred to as a displacement strategy. Examples of displacement strategies mentioned in the literature are full stroke and partial stroke displacement strategy [16], sequential partial stroke displacement strategy [17] and creep mode [18]. Two other displacement strategies are full stroke and partial stroke flow limiting [16]. These displacement strategies are very similar to the full stroke and partial stroke displacement strategy but introduce cavitation in the cylinder chambers. Cavitation should normally be avoided in hydraulic systems. The full stroke and partial stroke flow limiting strategy should therefore be further investigated to see if cavitation in the cylinder chambers will damage the hydraulic fluid or the digital displacement machine some how. The full stroke and partial stroke flow limiting strategy are therefore not considered in this project.

Different displacement strategies have different energy efficiency characteristics, dynamic response characteristics and control challenges. One of the simplest displacement strategies are the full stroke displacement strategy. Further down in this section, only a short description of the full stroke displacement strategy is given. A detailed description of full stroke, partial stroke and sequential partial stroke can be found in section 2.2 or in [16, 19, 20, 21]. A detailed description of creep mode can be found in [18]. At the end of this section, the energy characteristics and the dynamic response characteristics for all displacement strategies are presented.

Full Stroke Displacement Strategy

In the full stroke displacement strategy, the cylinder chambers are activated and deactivated on a stroke-by-stroke basis, meaning that a cylinder is either activated or deactivated for an entire piston stroke. This is illustrated for a single cylinder, cylinder i, in Figure 1.10. Plot 1 shows the piston position, $x_{cyl,i}$, Plot 2 shows the opening ratio of the high

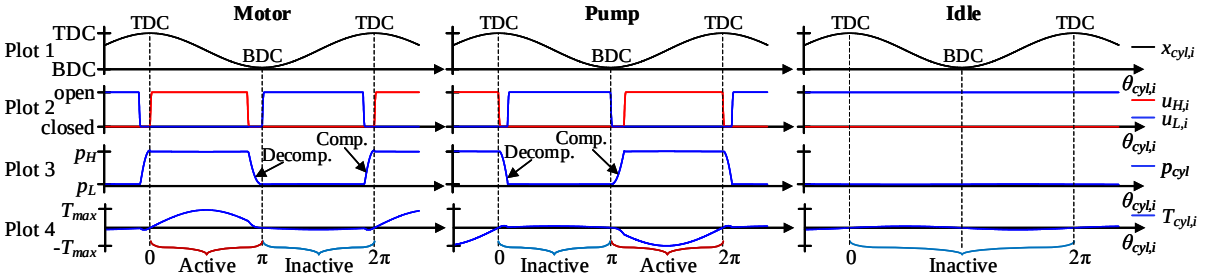

Figure 1.10: Schematics of the valve activation sequence for the full stroke displacement strategy. The left plot shows motor operation, the middle plot shows pump operation and the right plot shows idle operation.

pressure valve, $u_{H,i}$, and the low pressure valve, $u_{L,i}$, Plot 3 shows the chamber pressure, $p_{cyl,i}$, and Plot 4 shows the cylinder torque contribution, $T_{cyl,i}$. Note that TDC and BDC are abbreviations for top dead center and bottom dead center respectively. In the left

plot, the cylinder chamber is active in the downstroke piston motion giving a high positive output torque and deactivated in the upstroke piston motion giving a low negative output torque. Hence, the cylinder acts as a motor. In the middle plot, the chamber is active in the upstroke piston motion giving a high negative output torque and deactivated in the downstroke piston motion giving a small positive output torque. Hence, the cylinder chamber pumps fluid out to the high pressure source and operates as a pump. In the right plot, the cylinder chamber is deactivated for the entire shaft revolution. This operation is referred to as idle mode. In idle mode, the cylinder chamber pumps and receives low pressure fluid to and from the low pressure source, resulting in a minimum of friction losses, leakage losses and compressibility losses. Note that for motor and pump operations, the valves are timed to only switch when the chamber fluid is fully compressed or decompressed such that the pressure difference across the valve is small during the valve switching. This results in a minimum of flow throttling losses and flow and pressure peaks during the valve switchings. The displacement can be changed by idling one or more cylinders. For example, motor operation with 50 % displacement can be achieved by motoring and idling every other cylinder.

Energy efficiency characteristics

Operation with different displacement strategies results in different energy efficiency of the digital displacement machine. The energy efficiency for full stroke and partial stroke displacement strategy have earlier been investigated in the literature [19, 22, 21, 23], but there are still missing energy efficiency analysis for the sequential partial stroke displacement strategy and creep mode. Experimental results show that the energy efficiency at 20 % displacement is 70 % for full stroke displacement strategy, but only 45 % for partial stroke displacement strategy. In order to achieve higher energy efficiency, the on/off valves need to be faster and have lower electric power consumption [19]. At full displacement, the energy efficiency is approximately 90 % for both the full and partial stroke displacement strategies. The sequential partial stroke displacement strategy and creep mode are based on switching the valves more often than full and partial stroke, in addition to allow switching when the pressure difference across the on/off valves is high. The sequential partial stroke displacement strategy and creep mode are therefore considered to have lower energy efficiency compared to full and partial stroke displacement strategy.

In the literature, there are experimental results of digital displacement machines operating with full stroke displacement strategy and partial stroke displacement strategy [16, 19, 23]. There are still missing experimental results for sequential partial stroke displacement strategy and creep mode.

Dynamic response characteristics

Different displacement strategies give different dynamic response characteristics. The transient and steady-state response for digital displacement motors have been investigated in a limited number of papers. In [22], the authors investigate the steady-state flow ripples for a digital displacement machine operating at two different displacement ratios and with two different displacement strategies, full and partial stroke displacement strategy respectively. The results show that when operating at displacements greater than 50 %, the full stroke displacement strategy has the lowest flow ripples, but when operating at displacements down to 20 %, the partial stroke displacement strategy has the lowest flow ripples.

In [24], the authors investigate the transient and steady-state response for full and partial stroke displacement strategy when operating at different speeds and with different number of cylinders. The results show that the transient response is highly affected by the shaft speed for both displacement strategies. The transient response of partial stroke displacement strategy is also affected by the magnitude of the displacement step. The steady-state response is affected by the number of cylinders in the machine.

There is still missing a more in-depth analysis of the dynamic response characteristics of digital displacement machines that considers all displacement strategies.

1.3.3 Valves for Digital Displacement Machines

This section presents important details regarding valves used in digital displacement machines. First, important features of the valves are discussed and then prototype and commercially available valves suitable for use in digital displacement machines are presented.

Valve Functionalities

The on/off valves are the key components in digital displacement machines. In order to achieve high energy efficiency, it is important to use valves with suitable functionalities. Important features are low switching time, high flow capacity and accurate timing. On/off valves can typically be divided into two types: passively and actively activated valves. Passively activated valves are typically poppet valves that are being passively opened and closed by pressure forces. For example, a passively activated high pressure valve can only be opened when the cylinder pressure is higher than the high pressure level and thereby forces the poppet valve to open. This operation is illustrated to the left in Figure 1.11. The valve actuator is only capable of keeping the valve open against flow forces such that flow can run from the high pressure source and into the cylinder chamber. In order for the valve to close, the valve actuator must be turned off and the cylinder pressure must be lower than the high pressure level. The main advantages of passively actuated valves are

that they can only be switched when the pressure drop across them is small which results in a minimum of valve throttling losses, and that the actuators can be small since they only need to keep the valves open against flow forces. The disadvantages are that this valve type can not self-start in motor mode [25] nor be used for operation with sequential partial stroke displacement strategy or creep mode. These limitations occur since the valve type is not able to open against high pressure differences.

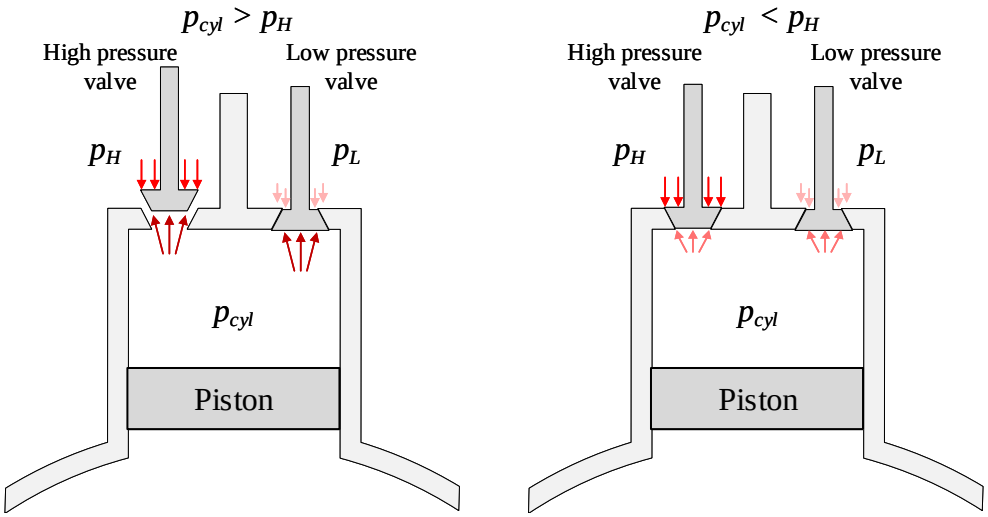

Figure 1.11: Schematic illustration of passive activation of the high pressure valve. The left plot illustrate opening and the right plot illustrate closing.

Actively activated valves are typically, but not limited to, spool type valves and are capable of opening against high pressure difference. Hence, this valve type can operate with all types of displacement strategies and self-start in motor mode. The main disadvantage of this type of valves is that they must be actively opened and closed. This means that it is more difficult to only activate the valves when the pressure drop across them is small. Requirements regarding valve timing and repeatability are therefore stricter compared to passively activated valves.

Independently of the valve type, the valves need to have appropriate valve characteristics such as high flow capacity, low switching time, low power consumption and high repeatability in order to facilitate high energy efficient operation. In [19, 20], these valve characteristics have been evaluated with respect to energy efficiency by simulation studies. The results show that it is essential to have valves with high flow capacity compared to the maximum flow running through the valves and low switching time. The shaft rotation time to the valve transition time ratio, time per revolution/valve transition time, should be in the range of 15 to 20 [19]. At Aalborg University, a research team has developed a general method for specifying the valve transition time requirements and the flow capacity requirements [26, 25]. The method shows that the valve requirements are stricter for partial stroke compared to full stroke displacement strategy. For the partial stroke

displacement strategy, the valve switching time should be below 1.7 % of the shaft revolution time and the valve pressure drop should be below 0.5 % of the machine pressure span for achieving energy efficiency above 95 % at 20 % displacement. To achive the same energy efficiency for the full stroke displacement strategy, the valve switching time should be below 20 % of the shaft revolution time and the valve pressure drop should be below 0.5 % of the machine pressure span.

Optimally, the valves should only be switched when the pressure difference across them is small. If a valve is opened too early or too late, the throttling losses during valve switching may increase significantly. A mistiming of only ± 2 ms for one valve can cause an increase in valve throttling losses by a factor of 8 [20]. This clearly shows the importance of accurate valve timing and valves with high repeatability. For passively opened valves, the activation of the valves happens automatically due to pressure forces. For actively activated valves, the timing must be done manually by a control signal. In the literature, there is still missing a general method for calculating the requirements regarding valve timing accuracy. It is among other reasonable to think that the operation speed will affect the requirements.

Prototype and commercially available valves for digital displacement machines
This section presents several prototype and commercially available valves which may have the potential of being used in digital displacement motors.

Artemis Intelligent Power Ltd. (AIP) is the pioneer in the digital displacement machine technology. Since the on/off valves are the key components, they have not disclosed any detailed information about the performance or the working principle of their valves. However, some information is possible to fined in patents filed by AIP [27, 28]. In general, AIP are using solenoid operated seat type poppet valves. Poppet valves are often used in digital displacement machines because of their large opening area that allows high flow rate for a relative small valve, the activation stroke is low which allows fast switching and the valve is capable of being passively opened. In 2006, AIP filed a patent for a solenoid operated poppet valve that was capable of opening against high pressure difference [29]. This valve concept retains the benefit of passive activation and still being able to operate with all types of displacement strategies and self-start in motor mode.

In 2007, Winkler and Scheidle [30] presented a pilot operated seat type valve for large flow rate with the capability of opening against high pressure difference. The presented valve utilizes the Hörbirger plate principle which has several annular rings at two opposite valve plates to form multiple metering edges. This principle allows a high flow rate for a small actuator stroke. The pilot valve is a 3/2 way spool type valve developed at Linz Center of Mechatronics (LCM). The nominal flow rate is 3.5 l/min at 5 bar pressure drop

and the switching time is about 1.6 ms. The main stage valve has a transition time below 2 ms when the pilot pressure is high. Due to a delay introduced by the pilot valve of about 1.6 ms, the entire switching time is 3.6 ms. The main stage valve has a measured flow rate of 90 l/min at 5 bar pressure drop and a measured leakage of 2.8 ml/min with 200 bar pressure drop. The valve can not be passively opened and has therefore increased demands to valve timing.

In 2010, Winkler et al. [31] presented a new pilot operated poppet valve with similar characteristics as presented in [30]. In the new valve, the Hörbirger plate is replaced by a novel concept based on multiple small poppets. The pilot valve is replaced by a 3/2 way valve with a higher flow rate. The new 3/2 way pilot valve is developed at LCM and has a flow rate of 10 l/min at 5 bar pressure drop and a transition time of 1-2 ms. The main stage valve has a flow capacity of 85 l/min and a transition time of about 1 ms. Due to the delay caused by the pilot stage, the entire switching time is approximately 3 ms.

A third valve developed at LCM is the FSVi4.1 [32]. This valve is a direct solenoid operated pressure compensated seat type poppet valve. The valve is capable of opening against high pressure difference and has no leakage. Measured results show switching time below 3 ms and a flow capacity of 5 l/min at 5 bar pressure drop across the valve. The valve is capable of switching at frequencies up to 200-500 Hz. The FSVi4.1 can be ordered for test applications in the prototype phase [33].

At Aalborg University, a research team has developed direct actuated seat type poppet valves for digital displacement machines with high power ratings. Both a moving coil actuator (MCA) [34, 35] and a moving magnet actuator (MMA) [36] have been optimized and tested. The valves have a flow capacity above 400 l/min at 5 bar pressure drop and switching time in the range of 2-6 ms. The valves are not capable of opening against high pressure difference.

The Bosch Rexroth WES valve is a commercially available valve [37]. The valve is a direct solenoid operated spool type valve with the capability of opening against high pressure difference. According to the data sheet, the switching time is below 5 ms and the flow capacity is 45 l/min at 5 bar pressure drop. The maximum switching frequency is only 10 Hz. This frequency may limit the operation speed in cases of using this valve type in high speed digital displacement machines.

Another valve developed in the industry is the pilot operated poppet valve from Diinef AS [38]. This valve is developed to be used in high torque low speed digital displacement motors. The pilot valve is a 3/2 way solenoid operated spool valve. The main drawback of this pilot valve is a minor leakage. However, the minor leakage is said to have a negligible influence on the performance and the energy efficiency of the motor. The valve switching time is 20 ms [18].

Table 1.1 gives an overview of the on/off valves that may be used in digital displacement machines. For more detailed information on fast switching on/off valves, see [25, 39, 33].

Table 1.1: Overview of on/off valves with the potential of being used in digital displacement machines. The table is inspired by [25].

Commercial valves	**Switching time**	**Flow at $\Delta p = 5$ bar**	**Leak free**
Bosch Rexroth WES [37]	< 5 ms	45 l/min	no
Bosch Rexroth SEC6 [33]	7-10 ms	7 l/min	yes
SUN DLV [33]	10 ms	7 l/min	yes
Bucher Hydraulics WS22GDA-10 [40]	< 21 ms	37 l/min	no
Diinef AS [38, 18]	20 ms	-	almost
LCM FSVi4.2 [32]	< 3 ms	5 l/min	yes
Prototype valves	**Switching time**	**Flow at 5 bar**	**Leak free**
Winkler et al. [30]	< 3.6 ms	90 l/min	no
Winkler et al. [31]	< 3 ms	85 l/min	no
Rømer et al. [34]	< 2.9 ms	1900[1] l/min	-
Nørgård et al. [35] (MCA)	< 3.5 ms	400[1] l/min	yes
Nørgård et al. [36] (MMA)	< 6 ms	510[1] l/min	yes

1.3.4 Control of Digital Displacement Machines

The dynamic behavior of digital displacement machines is changing based on the machine configuration (number of cylinders), displacement strategy and operation conditions (displacement ratio, speed and pressures). Also, cylinders are being activated and deactivated, which results in a non-continuous output signal. These features make model based feedback control of digital displacement machines complicated and non-conventional. This section gives an overview of controllers designed for digital displacement machines.

Ehsan et al. [10] are the first to present control strategies for digital displacement machines. The control strategy is based on the full stroke displacement strategy and the concept is to activate or deactivate the next cylinder based on knowledge about previously activated cylinders and the demand signal. The control method is implemented in a digital displacement pump that operated at 1500-2100 rpm. Both a pressure and flow control strategy is given. The presented control method has two key characteristics. The first characteristic is a quantification error duo to enabling or disabling the next cylinder chamber for an entire piston stroke. The quantification error is minimized by placing an accumulator close to the output valves. The second characteristic is a delay in the response

[1]Estimated flow

following a decision. An enabled cylinder will affect the output for a half shaft revolution after the decision is made. This delay is accounted for by predicting the decision-making process into the future by including a look-ahead time or angle. The control strategy is applied in an open-loop configuration. The results show that the proposed control strategy is robust and efficient.

Heikkilä et al. [41] propose a displacement controller for a digital hydraulic power management system (DHPMS) operating with the full stroke displacement strategy and at 1500 rpm. The DHPMS is a digital displacement machine with multiple independent controlled inputs and outputs. The principle of the proposed displacement controller is to convert a position reference, for example for a cylinder, into a volume displacement reference. The displacement error is minimized by choosing the best combination of idling, pumping and motoring cylinders. Experimental results show good open-loop tracking performance whenever the volume flow is sufficiently large [10]. Small flows are difficult to control. One way to increase the controllability of small flows is to increase the number of cylinders and the speed of the DHPMS while keeping the maximum flow fixed.

Armstrong and Yuan [17] describe a multi-level control method for speed control of a digital displacement machine operating at speeds ranging from -100 rpm to 100 rpm. The multi-level control method is based on the sequential partial stroke displacement strategy. The outer control level consists of a simple PI speed controller, which defines the desired motor torque. By using off-line optimization, the best cylinder combination of both motoring, pumping and idling cylinders are found to meet the desired motor torque. The best cylinder combination is updated with fixed time intervals. This control strategy is characterized by frequent switchings resulting in high valve throttling losses and flow and pressure peaks. However, the simulation results show good tracking performance at low motor speeds.

Sniegucki et al. [42] present a model predictive control approach for optimal torque control of a digital displacement machine. The nonlinear and discrete system behavior of the digital displacement machine is modeled using mixed logical dynamic system representation. The control performance depends on the optimization objective, sample size and prediction horizon. The presented optimization objective is a summed weighting of minimum set-point deviation, number of switching events and switching effort. The prediction horizon should be sufficiently large to be able to detect any constraint violations. The simulation results show that the torque output is close to the reference. Compared to using a delta-sigma modulator to generate the control signal for the full stroke displacement strategy or using pulse width modulation to generate the control signal for the partial stroke displacement strategy, the model predictive control strategy shows superior performance. One drawback of the model predictive controller is the large average solv-

ing time of 2 s per iteration, which makes the control strategy only suitable for off-line optimization unless the computational time is significantly reduced.

Research within the control design of digital displacement machines is often limited to open-loop systems with simplified load conditions and fixed speed operation. At Aalborg University, Pedersen [12] has therefore developed models describing the fundamental characteristics of the digital displacement units which can be used to design model based feedback controllers. These models include both continuous, discrete and hybrid dynamical system approximations. The continuous dynamical approximation is used to design a model based feedback controller for a digital displacement machine used in a wind turbine transmission [43]. The digital displacement motor operates at 1000-1200 rpm and with the full stroke displacement strategy. The results show that the continuous approximation is sufficient to describe the fundamental dynamics of the digital displacement motor if the number of cylinders and the displacement fraction are sufficiently high. Also, the continuous approximation is nonlinear in the time domain if the operation speed varies. In the case of applying linear control theory, the rotational speed of the digital displacement machine must, therefore, be lower bounded by the linearization point. Due to the high nonlinearities when operating at variable speed, the continuous approximation is only valid in a limited range of operation.

Johansen et al. [44] are the first to present a discrete dynamical approximation for fixed speed digital displacement machines. The discrete approximation is later extended by Pedersen et al. [45] to apply for variable speed units. In both cases, the digital displacement unit is operating with the full stroke displacement strategy. The discrete dynamical approximation has later been used to design a linear quadratic regulator (LQR) [46] and a linear quadratic gaussian (LQG) [47] controller for a digital hydraulic transmission used in a wind turbine. The hydraulic transmission consists of a conventional low speed fixed displacement pump and a variable displacement high speed digital displacement motor. The results show that both controllers can control the rotor speed similar to a conventional transmission. However, the LQG-controller with disturbance compensation does not improve the tracking performance compared to the LQR-controller. This means that the simpler LQR-controller, with the integral state, is sufficient to achieve accurate tracking performance.

The discrete dynamical approximation method is also extended for use with partial stroke [48] and sequential partial stroke displacement strategy [49]. In these cases, a model predictive controller is designed. The partial stroke displacement strategy is used on a motor operating at 100 rpm and the sequential partial stroke displacement strategy is used on a pump operating at 10 rpm. The reference signal is in both cases sinusoidal and with a period time of 50-60 s. The simulation results for the sequential partial stroke

displacement strategy show improved tracking capability compared to full and partial stroke operation [49]. The model predictive control allows the designer to specify the importance of energy consumption compared to output peaks. The results show great tracking performance when energy consumption is of low importance and reduced tracking performance when energy consumption is of high importance [48, 49].

The discrete dynamical approximation is fairly accurate for a high number of cylinders but has reduced accuracy for lower numbers due to larger phase shifts between cylinders. The approximation is also inaccurate for lower displacements. As for the continuous approximation, the rotational speed must be lower bounded by the linearization point in case of applying linear control theory on variable speed machines.

In [50], Pedersen et al. propose a hybrid dynamic approximation for digital displacement machines operating with the full stroke displacement strategy. The model includes the fundamental dynamic behavior of the digital displacement unit but is limited to operation in one direction of rotation with either pump or motor operation. In [51], Pedersen et al. propose a hybrid dynamic approximation for digital displacement machines operating with partial stroke and sequential partial stroke displacement strategy in all four quadrants. The model has high accuracy but is quite complex and, therefore, not suitable for use in stability analyses or control design theory. This is due to a large number of states and multiple jump maps and sets.

Summary

There is limited research within the field of control of low speed digital displacement machines. Pedersen et al. [48, 49] have designed pressure and flow controllers for low speed digital displacement motors and pumps operating with partial and sequential partial stroke displacement strategy. The input signal was, in both cases, a sinusoidal signal with a period time of 50 to 60 s. This period time is very high, compared to, for example, the period time used in winch systems during heave compensation. The period time of the vessel is typically in the range of 6 to 12 s. Armstrong and Yuan [17] have also designed a controller for low speed digital displacement machines. The controller is a simple velocity PI-controller and the used displacement strategy is the sequential partial stroke displacement strategy. The used reference speed is a sinusoidal signal with a time period of approximately 12 s. This controller may have the potential of being used in digital displacement winch drive systems. Still, more research must be done to examine if this PI-controller or other types of controllers have the motion and tension control performances that are needed to operate a winch system.

1.3.5 Development Trends for Digital Displacement Machines

The field of digital fluid power is characterized by only using on/off valves to control the output of a system [11]. Digital displacement machine technology is one part of this field. For a detailed description of the field of digital fluid power, see [11]. This section presents a summary of the history of digital displacement machine technology and the development and research trends.

In the 1980s, a research team at Edinburg University tried to develop a power take-off system for generating electricity out of wave energy [14]. The main challenge was to transform irregular, slow, high-force motion into constant high-speed motion suitable for driving a conventional generator. The most promising solution the research team could find was to use a hydraulic power take-off system. The hydraulic solution had three serious shortcomings: the power take-off system had to handle power in the megawatt range, the rotating machine had to be able to change displacement efficiently and with high bandwidth and, finally, the energy efficiency at partial load had to be improved [14]. The team solved those problems and the outcome of the work is the digital displacement machine technology and Artemis Intelligent Power Ltd.

Artemis Intelligent Power Ltd. was founded in 1994 and is a research and development company located in Edinburgh. The company is specialized in research, development and technology licensing associated with digital displacement machine technology. In 2010, Mitsubishi Heavy Industries (MHI) acquired AIP, but in October 2018, AIP announced that Danfoss Power Solution (Danfoss) had acquired the majority of shares in AIP. Artemis Intelligent Power is now a joint venture between Danfoss and MHI, with Danfoss as the majority shareholder. Today, AIP is working within the following applications: on and off-road vehicles, rail vehicles, and wind and wave power take-off systems.

Off-Road Vehicles

AIP has since the late 1990's worked with Danfoss Power Solution in using the digital displacement machine technology in off-road vehicles. AIP studied the energy losses in excavators and discovered that 70 % of the engine shaft power is lost as heat in the hydraulic system [52]. In July 2016, AIP reported that they had started the process of replacing the original axial piston pump in a 16-tonne excavator with their own E-dyn 96 digital displacement pump [53]. The project is co-funded by Scottish Enterprise [54]. In the first step, the modification is limited to a pump swap only. The results show that fuel consumption is reduced between 16 % and 21 % while at the same time, the productivity (cycle per hour) is increased by 10 % [54]. When operating in something called productivity mode, the productivity is increased by 28 % while the fuel consumption is reduced by 10 % [54]. By using a fully digital hybrid system, including hydraulic accumulators for

energy storage, it is estimated that the fuel consumption will be reduced by more than 50 % [52]. An experimental test on an internal combustion forklift truck shows a 40 % reduction of fuel consumption compared to a conventional hydrodynamic transmission [52].

On-Road Vehicles

In 1999 AIP formed a licensing agreement with Dana Incorporated to use the digital displacement machine technology in on-road vehicles [14]. This licensing agreement was sold to Bosch Rexroth in 2006 [14]. In parallel with the work done with Bosch Rexroth, AIP has developed a hydraulic series hybrid system for on-road vehicles. In the series hydraulic hybrid system, the traditional gearbox is replaced by a digital hydraulic transmission. The digital hydraulic transmission consists of a digital displacement pump that is directly connected to the combustion engine. The pump delivers working fluid to two digital displacement motors, which are directly connected to the driving wheels [55]. In 2008, the series hydraulic hybrid system was tested on a BMW 530i. The results show a 50 % fuel saving for the European Urban Cycle [55]. In addition to the series hydraulic hybrid system, AIP has, in cooperation with Lothian Buses and Alexander Dennis Ltd., also developed a parallel hydraulic hybrid system for recovering braking energy in a city bus [56]. A pre-study show that 32-35 % of the energy delivered by the engine is lost as heat in the brakes and 25 % in engine accessories as cooling fans [57]. The parallel hydraulic hybrid system consists of a digital displacement machine that is connected in parallel with the combustion engine. The digital displacement machine is used to store the braking energy in hydraulic accumulators. The recovered energy is later used to accelerate the bus. Based on validated simulation results, the system is predicted to reduce the fuel consumption by up to 27 % and with a payback time of around two to three years [58].

Wind Power Take-Off System

One of the most attractive fields of using digital displacement machines is in large hydraulic power take-off systems for wind turbines. In 2010, Mitsubishi Heavy Industries acquired AIP with the main purpose of using their digital displacement machine technology in wind turbines [59]. In the same year, AIP started to develop a 7 MW offshore wind turbine with a digital displacement hydrostatic transmission [60]. In January 2013, a 1.5 MW prototype started operation at Yokohama Dockyard & Machinery Works [60]. This is the world's first digital displacement hydrostatic transmission. The prototype is used for elemental tests of components such as hydraulic pistons, valves, cams and rollers.

The first 7 MW wind turbine with a digital displacement transmission was assembled at the land-based test facility at Hunterston test-site in 2014 and started testings in 2015

[61, 62]. The wind turbine consists of a 7 MW low speed ring-cam pump that delivers working fluid to two high speed 3.5 MW crank type piston motors. Each motor drives a generator. The energy efficiency of the digital displacement transmission is approximately 94 %, with 98 % for the low speed pump and 96 % for the high speed motor [63]. The rotor diameter is 167 m and the hub height is approximately 116 m from the average sea level [60]. A more in-depth analysis of the digital displacement hydrostatic transmission can be found in [64]. The second 7 MW wind turbine with digital displacement transmission is destined to operate as a floating wind turbine 20 km off the coast of Fukushima in Japan. This will be the world's largest floating wind turbine, and the largest wind turbine of any kind in Japan [62].

Wave Power Take-Off System

Digital displacement machines are well suited for wave energy converters due to their high energy efficiency over a wide range of operating conditions, fast response time, and its ability to integrate gas accumulators for energy storage [8]. AIP has together with Quoceant, a marine energy and technology consultancy, developed a technology called "Quantor" [65]. This development involves using digital displacement machine technology to transform the slow back and forth motion of waves into a reliable and cost-effective stream of electricity [65]. The project has received funds of £2.5 million from the Scottish agency Wave Energy Scotland to build and demonstrate a full-scale prototype that can work at sea [65].

Rail

In 2010, AIP, together with First ScotRail, analyzed the losses in trains [66]. The result shows that between 64 % and 73 % of the energy is lost through braking and transmission. Since 2013, AIP has worked with Ricardo and Bombardier on reducing fuel consumption in rail vehicles. They have developed a system where a digital displacement machine captures braking energy and stores it in a Ricardo flywheel and then uses the stored energy to accelerate the rail vehicle. According to Ricardo, the digital displacement rail transmission with flywheel energy storage are capable of reducing fuel consumption by 10 % [67]. This system won the top prize in "The Most Interesting initiative in safety and sustainability" category at The Rail Exec Club Awards on 29th November 2014 [67]. AIP has also worked with an alternative traction system. By using their digital displacement machine technology, they developed a new type of hydraulic transmission for diesel-powered rail vehicles for use in the parts of the rail network that are uneconomical to electrify. The hydraulic transmission consists of an E-dyn 96 digital displacement pump that delivers working fluid to an axle mounted digital displacement motor. A diesel engine drives the pump and accumulators are used to storing energy during braking and supplying energy

during acceleration [68]. The project is funded by the Rail Safety and Strategy Board and aims to reduce fuel consumption and reduce journey time by increasing the acceleration. The new traction system is planned to be installed and tested in a Chiltern Railways' Mark 3 DVT vehicle for three months starting from December 2017 [66]. The initial results show that the overall fuel consumption can be reduced by up to 30 % [69].

Tampere University of Technology

At Tampere University of Technology, a research team has further developed the digital displacement machine. By connecting more than two on/off valves to all cylinders, the digital displacement machine can have multiple independently controlled outlets. This novel solution is first presented in [70] and is later referred to as a digital hydraulic power management system (DHPMS). The DHPMS has the following functionalities: serving each outlet with arbitrary pressure levels, recovering energy from each outlet back to the prime mover, transferring power from one outlet to another with arbitrary pressure levels and energy storing and recovering from hydraulic accumulators independently of pressures [70]. The main challenges for the DHPMS are that the flow is strongly pulsating at partial displacement and that extremely fast and durable on/off valves are needed. In [71], the authors propose to use several fixed displacement pump/motors (e.g., gear type) instead of independently controlled pistons. The main goals of this concept are to achieve a smoother output flow and reduce the valve requirements. The first experimental test results from a piston type DHPMS with two independently controlled outlets are presented in 2010 [72]. The prototype is a modified six-piston boxer pump with a geometrical displacement of about 30 cm^3 [73]. The original check valves are replaced by prototype on/off valves with a flow capacity of 23 l/min at 5 bar pressure drop. The DHPMS is tested at speeds ranging from 500 rpm up to 1000 rpm and with pressures ranging from 20 bar up to 180 bar. The experimental results show that the total energy efficiency when pumping at full displacement is between 65 % and 85 % and between 80 % and 85 % when motoring at full displacement [72]. Note that the electrical losses in the valves are not included in the energy efficiency calculations. The energy efficiency is not as good as the results presented in Figure 1.9, mainly because of low flow capacity and leakage in the valves.

The measured characteristics of a second prototype DHPMS are presented in 2016 [73]. The second prototype is based on the same six-piston boxer pump, but the geometric displacement of each cylinder is decreased, the number of individually controlled outlets is increased to 5 outlets, and the prototype on/off valves are replaced by leak free commercial Bosch Rexroth SEC 3/3 poppet valves. The efficiency can still not reach the same results as shown in Figure 1.9, mainly because of the low flow capacity of the Bosch Rexroth

SEC 3/3 poppet valves. However, the reduced geometric displacement increases the flow resolution, the leak free on/off valves allows for effective use of accumulators as energy storage, and the number of outlets is increased to five.

The DHPMS can be used to design more energy efficient systems for off-road vehicles. In [41] the authors propose to use a DHPMS with two independently controlled outlets to control a double acting cylinder. The cylinder is directly connected to the DHPMS without the use of any throttling valves. The proposed controller is a displacement controller. The simulation results show the feasibility of using the direct connection between a cylinder and the DHPMS. The results also show high energy efficiency due to no throttling valves and very good open-loop control. The same system is later experimentally tested in [74]. The experimental results verified the earlier simulation results regarding feasibility and open-loop position tracking performance. On the other hand, small cylinder velocities should be avoided due to pulsating output flow from the DHPMS. Increasing the number of pistons in the DHPMS and the rotational speed while keeping the maximum flow fixed will improve the controllability at low cylinder velocities. Also, the energy efficiency is reduced due to leakage in the on/off valves and low flow capacity. However, the experimental results show the ability to convert energy from one outlet to another. This makes it possible to attach an accumulator for energy recovery.

The use of an accumulator for energy recovery in a displacement controlled DHPMS is investigated in [75] by simulations. An excavator's arm is used as a case study. The excavator's arm is controlled using a single acting cylinder directly connected to one of the outlets of the DHPMS. Another outlet is connected to a high pressure accumulator and used for energy storage. The results show that energy recovery is possible.

In [76], the authors present an experimental comparison analysis of a proportional valve controlled cylinder and a displacement controlled cylinder. For the proportional valve controlled cylinder, the system pressure is controlled by a DHPMS. For the displacement controlled cylinder, the cylinder is directly connected to the DHPMS similar to the system used in [41] and [74]. The results show that the displacement controlled cylinder uses 50 % less energy compared to the proportional valve controlled cylinder. On the other hand, the controllability is lower at low velocities.

A simulation study of a DHPMS with five independently controlled outlets is presented in [77]. The DHPMS is used to actuate two double acting cylinders on an excavator's arm. The cylinders are directly connected to the DHPMS. The fifth outlet is connected to an accumulator for use as energy storage. The simulation results show good open-loop control for both cylinders and that the accumulator can be used for energy recovery.

Purdue University

At Purdue University, researchers have focused on developing displacement strategies and analyzing valve parameters with respect to energy efficiency [19, 22, 21, 23, 20, 78]. This research has already been discussed in Section 1.3.2 and 1.3.3.

In [79], the author presents an algorithm that optimizes the valve timing during operation and an algorithm that detects the best displacement strategy for the current operation conditions. The following displacement strategies are included in the analysis: full stroke displacement strategy, partial stroke displacement strategy, full stroke flow limiting and partial stroke flow limiting. The optimal valve timing is found by measuring the input and output pressures and searching for pressure ripples. If there are any pressure ripples, the valve timing is adjusted to remove the ripples. Two different displacement switching algorithms are developed: one efficiency based and one ripple based. For more information, see [79].

Aalborg University

At Aalborg University, a research group has worked with the design and optimization of fast switching poppet valves for use in high speed digital displacement machines [80, 25]. This work is presented in Section 1.3.3. One important contribution of the work is a general method for specifying required valve switching time and flow capacity. At Aalborg University, a researcher has also developed models of digital displacement machines that can be used for model based feedback control design purposes [12]. Both continuous, discrete and hybrid dynamical system approximation are investigated. This work is described in Section 1.3.4.

Diinef AS

The company Diinef AS has developed a pilot operated valve, designed for use in high torque low speed digital displacement machines [38]. In May 2017, Diinef AS officially unveiled the world's first digital high torque low speed motor [81]. The motor is developed in cooperation with Imenco Bauer Hydraulics and described in [82].

In 2017, Diinef AS and Imenco Bauer Hydraulics joined MacGregor Norway in a project intenting to develop energy efficient hydraulic winch drive systems with the use of high torque low speed digital displacement motors [83]. In 2018, they presented a new displacement strategy for very low speed operations [18]. The new displacement strategy is called *creep mode* and can typically be used in winch systems during tensioning of the wire before lift-off.

1.4 Research Objectives

The work presented in this thesis aims to develop a controller for a secondary controlled high torque low speed digital displacement motor used in a winch drive system. The work can be divided into five research objectives that are based on the lack of research revealed by the state of the art.

Objective A: The digital displacement motor can achieve variable displacement by using different displacement strategies. Different displacement strategies have different transient and steady-state response. Objective A is to analyze the transient and steady-state response for the following displacement strategies: full stroke, partial stroke and sequential partial stroke displacement strategy.

Objective B: Objective B is to design and build a test rig for a high torque low speed digital displacement motor. The test rig shall be used to experimentally test the displacement strategies analyzed in research objective A and validate the used simulation model of the digital displacement motor.

Objective C: The digital displacement machine technology sets high requirements for the on/off valves. In order to operate with all displacement strategies investigated in objective A, the on/off valves must be of the actively activated valve type. Opening a valve too early or too late may result in a significant increase of the valve throttling losses. Objective C is therefore to investigate requirements regarding valve timing accuracy.

Objective D: Objective D is divided into two parts. The first part is to analyze winch operations and define performance requirements for the winch drive system. The second part is to use the results from objective A and select the displacement strategy that is most suited for use in the digital displacement winch drive systems. Also, a control strategy for four quadrant operation for the selected displacement strategy must be developed.

Objective E Objective E is to design controllers for the digital displacement winch drive system. The control system should use the displacement strategy chosen in Objective D. The aim is to adjust already developed control structures to fit to the digital displacement winch drive systems. If this is not possible, a new control structure should be developed.

1.5 Contribution

The main contributions of this thesis are:

- Definition of requirements regarding valve timing accuracy.
- Development of a new type of displacement strategy: partial stroke displacement strategy 2.

- Dynamic response analysis of a digital displacement motor operating at different displacement strategies: full stroke displacement strategy, partial stroke displacement strategy 1 (original version), partial stroke displacement strategy 2 (new version) and sequential partial stroke displacement strategy.
- Development of a test setup that can experimentally test digital operation on a high torque low speed digital displacement motor.
- Experimental test of full stroke displacement strategy, partial stroke displacement strategy and sequential partial stroke displacement strategy in low speed operations.
- Validation of the simulation model by experimental work.
- Development of switching logic between operation quadrants for a digital displacement motor operating with partial stroke displacement strategy 2.
- Development of motion controller and tension controller for the digital displacement winch drive system.

1.6 Reading Guidelines

Chapter 2 aims to present a detailed description of the digital displacement motor. The chapter begins with presenting the nonlinear simulation model of the digital displacement motor. Then the working principle of the full stroke, partial stroke and sequential partial stroke displacement strategy are described in detail. At the end, the valve requirements for the fast switching on/off valves are presented. First, a short summery of general valve requirements that can be found in the literature is given. Then requirements regarding valve timing accuracy are given. The given requirements regarding valve timing accuracy are based on the work published in paper C

Chapter 3 describes the experimental test rig, presents experimental test results and uses the experimental results to validate the nonlinear simulation model of the digital displacement motor presented in Chapter 2. This work is published in paper D.

Chapter 4 presents an analysis of the transient and steady-state response of the digital displacement motor operating with the displacement strategies described in Chapter 2. At the end of the chapter, the dynamic characteristics of each displacement strategy are discussed. The work presented in this chapter is published in paper D

Chapter 5 presents a preliminary winch drive study conducted in the beginning of the project. The aim of the presented work is to compare the use of conventional and digital displacement machines in a closed circuit winch drive system. This work is published in paper A and paper B.

Chapter 6 gives a description of different winch operation modes, different subsea lifting operations and defines performance requirements for winch drive systems. Parts of

the work presented in this chapter is published in paper E

Chapter 7 describes the designed controllers and shows the simulation results. Most of the work is presented in paper F but some of the work is presented in paper E.

Finally, the main conclusions are presented in Chapter 8 together with a proposal of future work.

Chapter 2

The Digital Displacement Motor

The digital displacement motor (DDM) technology has experienced increased interest in the last years due to their high energy efficiency potential. The working principle of the DDM is described in Section 1.3. This section presents a nonlinear simulation model of the DDM, four displacement strategies and important valve requirements.

2.1 Simulation Model of a Digital Displacement Motor

This section describes the nonlinear simulation model of a DDM. The simulation model is based on a radial piston type machine with the pistons uniformly distributed around the shaft. The model is inspired by the model presented in [80]. For simplicity, equations for the simulation model is derived for a single cylinder chamber, but the same method is used for all cylinders. A sketch of a single cylinder DDM is shown to the left in Figure 2.1.

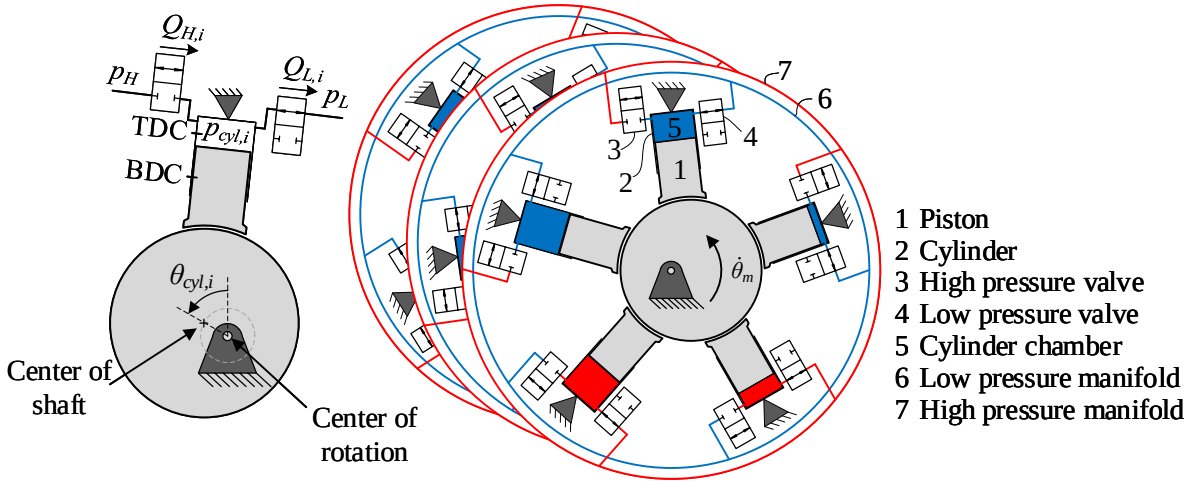

Figure 2.1: Sketch of single cylinder chamber (left side) and a 15 piston DDM (right side).

In this thesis, different numbers of cylinder chambers and different piston displacements will be used in different parts of the thesis. However, every simulation model is built up in the same manner. It is always assumed that the cylinder chambers are uniformly distributed around the same shaft. In cases with a high number of cylinder chambers, the cylinders can be uniformly distributed around the same shaft by stacking the cylinders in banks along the same shaft with the banks phase shifted in relation to each other. This solution is shown to the right in Figure 2.1. Another alternative may be to place several motors on the same gear ring with each piston movement phase shifted relative to each other.

The cylinder chambers can either be connected to a high or low pressure source. It is assumed that the high and low pressure sources have constant pressure levels and that friction and leakage in the DDM are negligible. The pressure dynamics in cylinder chamber i is calculated by using the continuity equation,

$$\dot{p}_{cyl,i} = \frac{\beta_{eff,i}}{V_{cyl,i}} \cdot \left(Q_{H,i} - Q_{L,i} - \dot{V}_{cyl,i} \right) \tag{2.1}$$

where $\beta_{eff,i}$ is the effective bulk modulus of the hydraulic fluid, $V_{cyl,i}$ is the cylinder chamber volume, $\dot{V}_{cyl,i}$ is the time derivative of cylinder chamber volume, $Q_{H,i}$ is the flow through the high pressure valve and $Q_{L,i}$ is the flow through the low pressure valve. The cylinder chamber volume, $V_{cyl,i}$, and its time derivative are given by Equation 2.2 and Equation 2.3 respectively.

$$V_{cyl,i} = V_0 + \frac{V_d}{2} \cdot (1 - \cos(\theta_{cyl,i})) \tag{2.2}$$

$$\dot{V}_{cyl,i} = \frac{V_d}{2} \cdot \sin(\theta_{cyl,i}) \cdot \dot{\theta}_m \tag{2.3}$$

where V_0 is the dead volume in the cylinder chamber, V_d is the piston displacement, $\theta_{cyl,i}$ is the shaft position relative to the piston position and $\dot{\theta}_m$ is the DDM shaft speed. Note that $\dot{\theta}_m = \dot{\theta}_{cyl,i}$. $\theta_{cyl,i}$ is called the local shaft position and is defined to be 0 rad when the piston is at TDC. Due to the phase shift between the cylinders, the local shaft position for cylinder number i is given by:

$$\theta_{cyl,i} = \theta_m + \frac{2 \cdot \pi}{N_c} \cdot (i - 1) \qquad\qquad i \in \{1, ..., N_c\} \tag{2.4}$$

where θ_m is the DDM shaft position and N_c is the number of cylinders. The volume flows through the valves, $Q_{H,i}$ and $Q_{L,i}$, are described by the orifice equation as shown in Equation 2.5 and Equation 2.6 respectively.

$$Q_{H,i} = \frac{u_{H,i}}{k_f} \cdot \sqrt{|p_H - p_{cyl,i}|} \cdot \text{sign}(p_H - p_{cyl,i}) \tag{2.5}$$

$$Q_{L,i} = \frac{u_{L,i}}{k_f} \cdot \sqrt{|p_{cyl,i} - p_L|} \cdot \text{sign}(p_{cyl,i} - p_L) \tag{2.6}$$

where $u_{H,i}$ and $u_{L,i}$ are the opening ratios of the high and low pressure valve ranging from 0 to 1, where 0 is fully closed and 1 is fully open. Both valves have the same flow-pressure coefficient, k_f, and the same transient response. The flow-pressure coefficient can be calculated based on experimental measurements or data given by the manufacturer,

$$k_f = \frac{\sqrt{\Delta p_{ref}}}{Q_{ref}} \tag{2.7}$$

where Q_{ref} is the flow trough the valve when the valve is fully open and with a pressure drop equal to Δp_{ref}. Q_{ref} is often called the valve flow capacity and specified at $\Delta p_{ref} = 5$ bar.

The transient response of the on/off valves is described by a second-order system,

$$\ddot{u}_{H,i} = u_{conH,i} \cdot \omega^2 - u_{H,i} \cdot \omega^2 - 2 \cdot \zeta \cdot \omega \cdot \dot{u}_{H,i} \tag{2.8}$$

$$\ddot{u}_{L,i} = u_{conL,i} \cdot \omega^2 - u_{L,i} \cdot \omega^2 - 2 \cdot \zeta \cdot \omega \cdot \dot{u}_{L,i} \tag{2.9}$$

where $u_{conH,i}$ and $u_{conL,i}$ are the desired valve positions for the high and low pressure valves, ω is the natural frequency of the valves, and ζ is the damping ratio. The desired valve positions, $u_{conH,i}$ and $u_{conL,i}$, are either 0 or 1 and is given by the chosen displacement strategy. Different displacement strategies and their valve actuation sequence is described in detail in Section 2.2.

The effective bulk modulus is calculated according to [84] as shown below.

$$\beta_{eff,i} = \frac{1}{\frac{1}{\beta_L} + \frac{\epsilon_g}{p_{cyl,i}^{(abs)}}} \tag{2.10}$$

where β_L is the bulk modulus of the liquid and ϵ_g is the volume fraction of undissolved gas. The volume fraction of undissolved gas is calculated as shown in Equation 2.11

$$\epsilon_g = \frac{1}{\left(\frac{1-\epsilon_{g0}}{\epsilon_{g0}}\right) \cdot \left(\frac{p_{atm}^{(abs)}}{p_{cyl,i}^{(abs)}}\right)^{-\frac{1}{\kappa}} + 1} \tag{2.11}$$

where ϵ_{g0} is the volume fraction of undissolved gas at atmospheric pressure, $p_{atm}^{(abs)}$ is the atmospheric pressure and κ is the specific heat ratio.

Finally, the torque contribution from each cylinder chamber is given by

$$T_{cyl,i} = \frac{V_d}{2} \cdot \sin(\theta_{cyl,i}) \cdot p_{cyl,i} \tag{2.12}$$

and the DDM output torque is the sum of the torque contribution from all cylinders

$$T_m = \sum_{i=1}^{N_c} T_{cyl,i} \tag{2.13}$$

2.2 Displacement strategies

The displacement of the DDM can be changed by using different displacement strategies. This section describes the valve activation sequence for the displacement strategies analyzed in this project: full stroke, partial stroke and sequential partial stroke displacement strategy. A general example of a DDM controller is shown in Figure 2.2. The input to

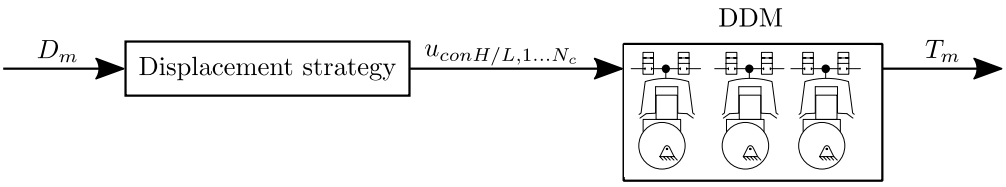

Figure 2.2: Schematic of open loop motor controller.

the controller is the desired DDM displacement ratio, D_m, and the output is the DDM torque. The displacement strategy is used to transform the desired displacement ratio into valve activation signals.

Note that in this section only motor operation is described, but the same strategy can also be used for pump operation.

2.2.1 Full Stroke Displacement Strategy

Full stroke displacement strategy (FSDS) is considered to be the simplest displacement strategy. The cylinder chambers are activated and deactivated for entire piston strokes. This means that the on/off valves are only switched when the pistons are close to TDC or BDC. In those positions, the valve flow is low, which results in a minimum of valve throttling losses when switching the valves. Also, the valves are timed only to be actuated when the pressure drop across them is small. The displacement of the DDM is changed by changing the number of active cylinder chambers.

Figure 2.3 illustrates the valve timing strategy for a single cylinder chamber. Through the first shaft revolution $[0 - 2\pi]$, the chamber is deactivated, and through the second revolution $[2\pi - 4\pi]$, the chamber is activated. Plot 1 shows the piston position, Plot 2 shows the opening ratios of the valves, Plot 3 shows the chamber pressure, Plot 4 shows the cylinder torque and Plot 5 shows the local shaft position. For an inactive cylinder chamber, the high pressure valve is kept closed and the low pressure valve is kept open, resulting in only a small torque contribution in the downstroke piston motion due to low chamber pressure. For an active cylinder chamber, the valves are switched close to TDC and BDC with the high pressure valve being open during the downstroke piston motion and the low pressure valve being open during the upstroke piston motion. The high chamber pressure during the downstroke piston motion results in a high torque

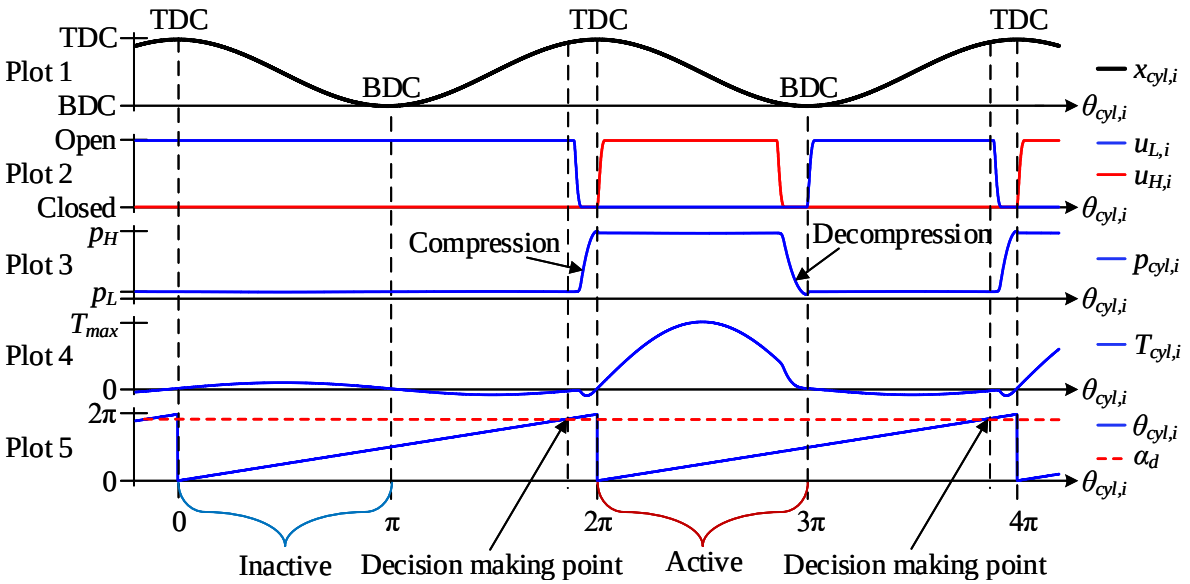

Figure 2.3: Valve timing schematics for the full stroke displacement strategy.

contribution.

It can also be seen that for the active cycle, the high pressure valve and low pressure valves are in closed position at the same time. This is done to compress and decompress the oil in the chamber in order only to switch the valves when the pressure difference is small. Switching the valves only when the pressure difference is small, results in a minimum of flow peaks, pressure peaks and valve throttling losses.

For each cylinder, the decision of activating or deactivating the cylinder chamber is taken at a fixed angle once every shaft revolution. This position is illustrated in Plot 5 in Figure 2.3 with the decision angle α_d (red dashed line). When $\theta_{cyl,i} = \alpha_d$, the decision of activating or deactivating cylinder chamber i for the next shaft revolution is taken. The desired displacement fraction, D_m, is normally a continuous signal ranging from 0 to 1 which corresponds to zero and full displacement respectively. The displacement fraction can be converted into a cylinder actuation sequence by a first-order delta-sigma modulator, which determines whether the current cylinder shall be active or inactive. This method was first proposed by Johansen et al. [85] and later used in several control papers [43, 46, 47, 45]. A block diagram of the proposed controller is shown in Figure 2.4.

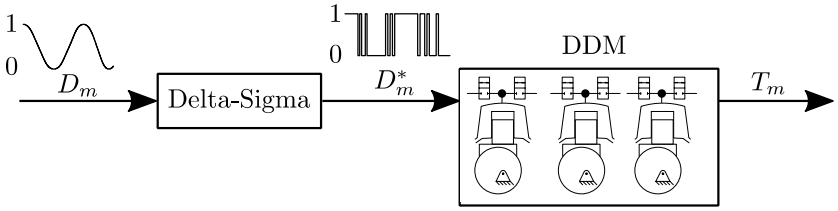

Figure 2.4: Schematic of open loop control system for FSDS.

Since the decision of activating or deactivating is taken at a fixed shaft position ahead of TDC, the sampling time, T_{sample}, for the delta-sigma modulator depends on the number of cylinders and the rotational speed.

$$T_{sample} = \frac{2 \cdot \pi}{\dot{\theta}_m \cdot N_c} \tag{2.14}$$

where $\dot{\theta}_m$ is the shaft speed and N_c is the number of cylinders. If the shaft speed is varying, the sampling time is also varying. A varying sampling time makes the control design more challenging.

2.2.2 Partial Stroke Displacement Strategy

In partial stroke displacement strategy (PSDS), all cylinder chambers are activated during every shaft revolution, but only in a portion of the downstroke piston motion. The displacement of the machine is changed by increasing or decreasing the active part. In this project, two versions of PSDS are investigated. The first version, PSDS 1, is the conventional version which is described in the literature. The second version, PSDS 2, is a development of the PSDS 1. PSDS 1 is based on operation with passively activated valves and are only capable of having one active period during the downstroke piston motion. PSDS 2 is based on operation with actively activated valves which makes it possible to reactivate a cylinder chamber and thereby have have more than one active period during the downstroke piston motion.

2.2.2.1 Partial Stroke Displacement Strategy 1

Figure 2.5 shows the valve timing strategy for a single cylinder chamber operating with PSDS 1. The red dashed line in the bottom plot shows the state change angle α. α describes at which local shaft position angle, $\theta_{cyl,i}$, the cylinder shall change state from active to inactive. If $\theta_{cyl,i} \leq \alpha$ the cylinder is active, else the cylinder is inactive.

For the situation shown in Figure 2.5, the state change angle is first set to $\alpha = \alpha_1 = \pi/2$ rad and the cylinder is active in the first half of the downstroke piston motion. This situation corresponds to 50 % displacement. After a small period, the state change angle is stepped up above the local cylinder angle, $\alpha = \alpha_2 = 3\pi/4$ rad. Increasing the state change angle after the cylinder has been deactivated, will not result in a reactivation of the cylinder due to the nature of the PSDS 1. Once the cylinder is deactivated, it can not be re-activated before the next shaft revolution.

As for the FSDS, the PSDS 1 also has a decompression phase and a compression phase in order only to switch the valves when the pressure difference across them is small. Switching the valves mid-stroke will result in higher flow throttling losses during

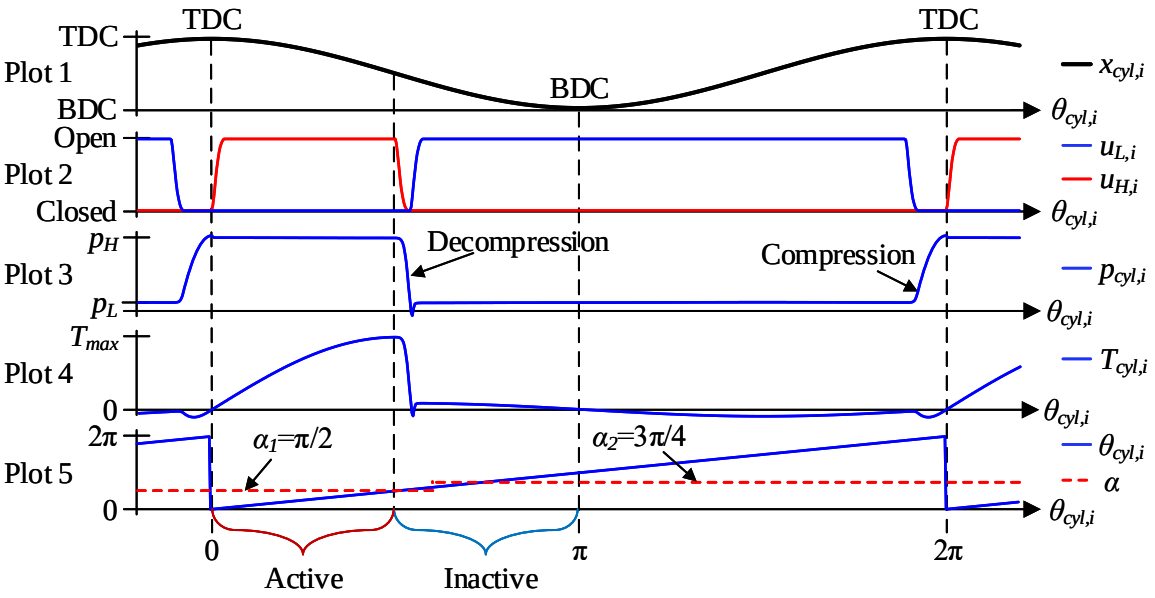

Figure 2.5: Valve timing schematics for the partial stroke displacement strategy 1.

switching compared to switching the valves closer to TDC or BDC. This is because the piston velocity and therefore also the flow is higher mid-stroke compared to closer to TDC or BDC.

The state change angle, α, is calculated based on the desired displacement ratio, D_m. The desired displacement ratio can be defined as the ratio between the intake volume during the active motoring period and the maximum intake volume [24]. Based on the calculation of the cylinder volume shown in Equation 2.2, the displacement ratio is calculated as shown below.

$$D_m = \frac{V_{cyl}(\alpha)}{V_{cyl}(\pi)} = \frac{\frac{V_d}{2} \cdot (1 - \cos(\alpha))}{\frac{V_d}{2} \cdot (1 - \cos(\pi))} = \frac{(1 - \cos(\alpha))}{2} \tag{2.15}$$

where $V_{cyl}(\alpha)$ is the intake volume during the active motoring period and $V_{cyl}(\pi)$ is the maximum intake volume. The state changing angle, α, is then calculated by rearranging Equation 2.15 as:

$$\alpha = \cos^{-1}(1 - 2 \cdot D_m) \tag{2.16}$$

The state change angle, α, is updated continuously until the state change is carried out. Figure 2.6 shows the block diagram of the open loop control system. Note that due to the decompression phase shown in Figure 2.5, the displacement fraction can not be as high as 1, because the last piston movement must be used to decompress the cylinder chamber.

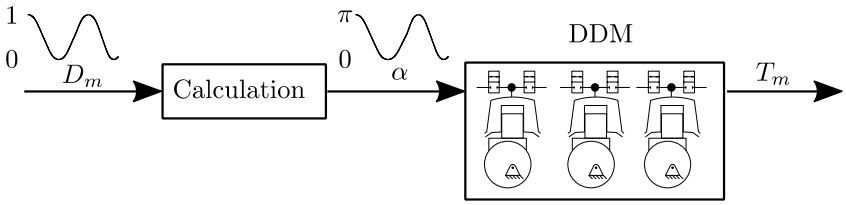

Figure 2.6: Schematic of open loop control for PSDS (equal for PSDS 1 and PSDS 2).

2.2.2.2 Partial Stroke Displacement Strategy 2

PSDS 2 is developed based on the PSDS 1. In PSDS 2, the cylinder is capable of being reactivated. Instead of only having one active period during the downstroke piston motion, the cylinder can be reactivated if the desired displacement ratio is changed, see Figure 2.7. For the illustrated situation, the state change angle is first set to $\alpha = \alpha_1 = \pi/2$ rad.

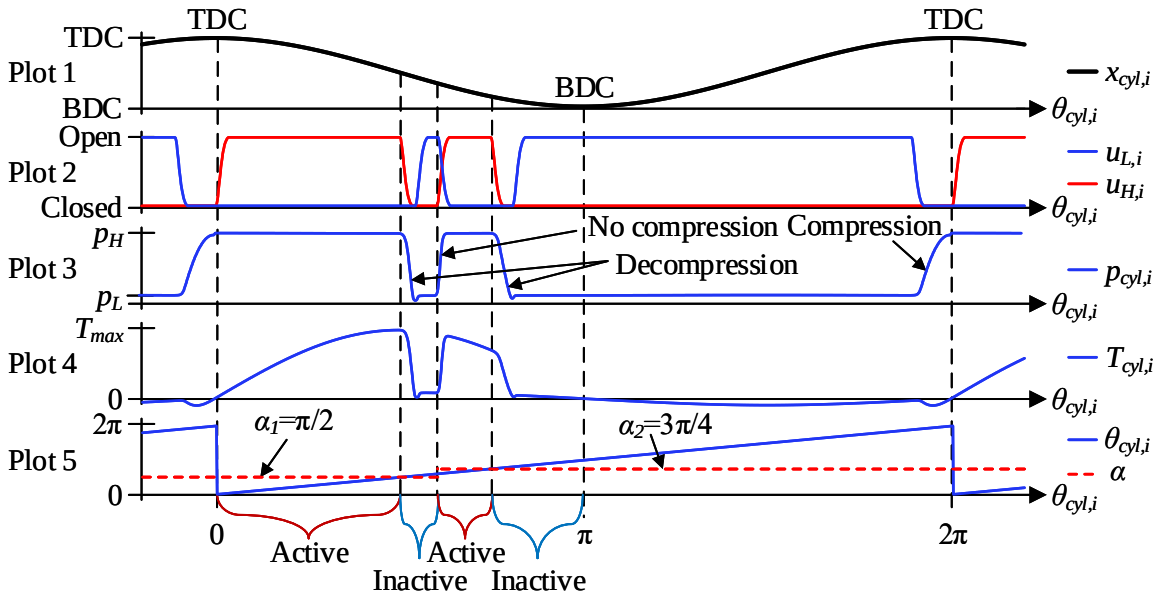

Figure 2.7: Valve timing schematics for the partial stroke displacement strategy 2.

When $\theta_{cyl,i} = \alpha_1$, the cylinder chamber changes state from active to inactive. After a small period, the state change angle is stepped up to $\alpha = \alpha_2 = 3\pi/4$ rad. Since $\theta_{cyl,i} < \alpha_2$, the cylinder is reactivated in the remaining shaft rotation up to $\theta_{cyl,i} = \alpha_2$.

When reactivating a cylinder, both valves are activated at the same time, opening the high pressure and closing the low pressure valve. This valve activation strategy is used because it is not possible to compress the oil in the cylinder chamber before opening the high pressure valve. The chamber oil can not be compressed because the cylinder volume is increasing due to the downward piston motion. Since both valves are activated at the same time, the high pressure valve must open against a high pressure difference, and the hydraulic fluid will flow directly from the high pressure source and into the low pressure source from the time the high pressure valve starts to open and until the low pressure valve is fully closed. This will result in higher valve throttling losses compared to switching the

valves when the oil in the chamber can be compressed or decompressed properly. The cylinder chamber may cavitate if the low pressure valve closes before the high pressure valve starts to open due to the downstroke piston motion. An anti-cavitation valve can be included to avoid the risk of cavitation in the case of poor timing of the valves.

2.2.3 Sequential Partial Stroke Displacement Strategy

In the sequential partial stroke displacement strategy (SPSDS), one combination of active and inactive cylinder chambers are used in a limited amount of time before a new cylinder combination is activated. The best cylinder combination can, for example, be found by an optimization algorithm or a search routine. This displacement strategy is characterized by frequently switchings and therefore lower efficiency compared to for example FSDS. In this section, only a short description of the SPSDS is given. A more detailed description can be found in [17].

For simplicity, a 5 cylinder DDM is used as an example when describing the concept of the SPSDS. For a 5 cylinder motor, the cylinder states can be described by a 5-bit binary number, where "1" indicates that the cylinder is active and connected to the high pressure source and "0" indicates that the cylinder is inactive and connected to the low pressure source. The left plot in Figure 2.8 shows the cylinder torque contribution from a 5 cylinder motor when all cylinders are activated for an entire shaft revolution. When $\theta_m = 4\pi/7$ rad, three chambers can potentially provide a positive torque, and

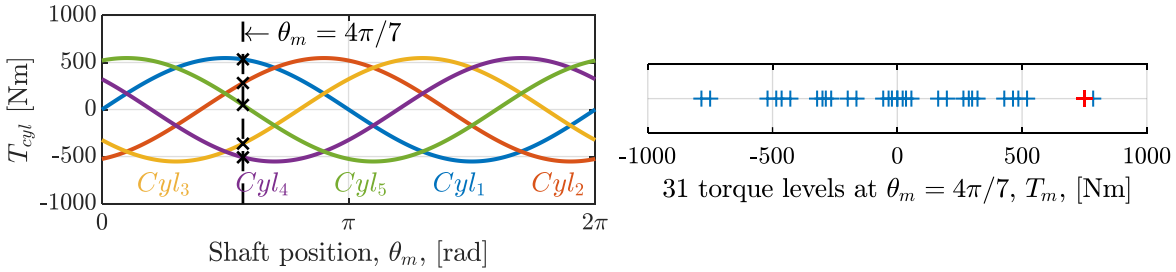

Figure 2.8: Cylinder torque (left plot) and possible torque levels at $\theta_m = 4\pi/7$ (right plot).

two chambers provide a negative torque. For a 5 piston motor, there are in all $2^{N_c} = 32$ possible cylinder configurations. At $\theta_m = 4\pi/7$ rad, the 32 possible cylinder configurations gives only 31 distinct output torques because all cylinders connected to the high pressure source and all cylinders connected to the low pressure source gives the same output torque, $T_m = 0$ Nm. The 31 distinct output torques when $\theta_m = 4\pi/7$ are shown in the right plot in Figure 2.8. The red point corresponds to activation of cylinder number 1 and 2 ($U_c = [1\ 1\ 0\ 0\ 0]$).

Rotating the motor shaft one revolution with the same cylinder configuration will result in a sinusoidal output torque. The cylinder configuration is therefore changed after

a short period, T_{update}, in order to meet the desired output torque. This is illustrated in the left side of Figure 2.9.

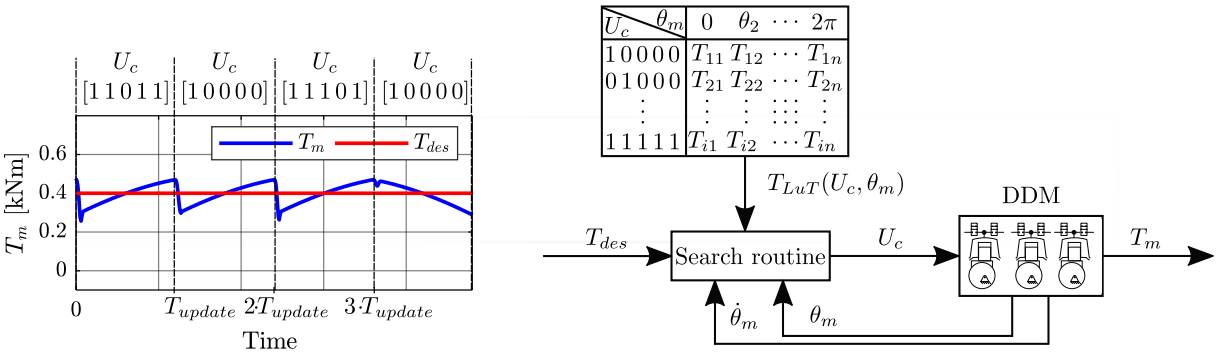

Figure 2.9: Schematic of open loop control for SPSDS.

The red line shows the desired motor torque and the blue line shows the actual motor torque. It can be seen that when the time is equal to T_{update}, $2 \cdot T_{update}$ and $3 \cdot T_{update}$, there is a step in the motor torque. These steps occur because the combination of active cylinder chambers is changed. The right side of Figure 2.9 shows the block diagram of the controller. In this work, a search routine is used to find the best cylinder configuration. The input to the system is the desired motor torque, and the output is the actual motor torque. The search routine finds the best cylinder configuration based on the desired motor torque, T_{des}, the current motor shaft position, θ_m, the motor shaft speed, $\dot{\theta}_m$, and a look-up table. The look-up table is estimated offline and describes the output torque, $T_{11\ldots in}$, for all possible cylinder configurations, U_c, at different shaft positions θ_m. In this work, the cylinder configuration, U_c, is updated every $T_{update} = 20$ ms and given by Equation 2.17.

$$U_c(k) = \arg\left(\min_{U_c}\left(\left|\overline{T}_{LuT}(\theta_m, U_c) - T_{des}\right|\right)\right) \tag{2.17}$$

where k is the sample index and $\overline{T}_{LuT}$ is the average output torque estimated from the look-up table over the interval of rotation which the valve configuration, $U_c(k)$, will be applied. The applied interval is defined as $[\theta_m, \theta_m + \Delta\theta_m]$ where $\Delta\theta_m = \dot{\theta}_m \cdot T_{update}$.

Figure 2.10 shows the result of the described controller for a 5 cylinder motor. The red line in the left plot shows the desired motor torque, T_{des}, and the blue line shows the actual motor torque, T_m. The right plot shows the torque contribution from every single cylinder (one color per cylinder). It can be seen that the cylinder configuration is frequently switched and that the best cylinder configuration includes both positive and negative torque contribution.

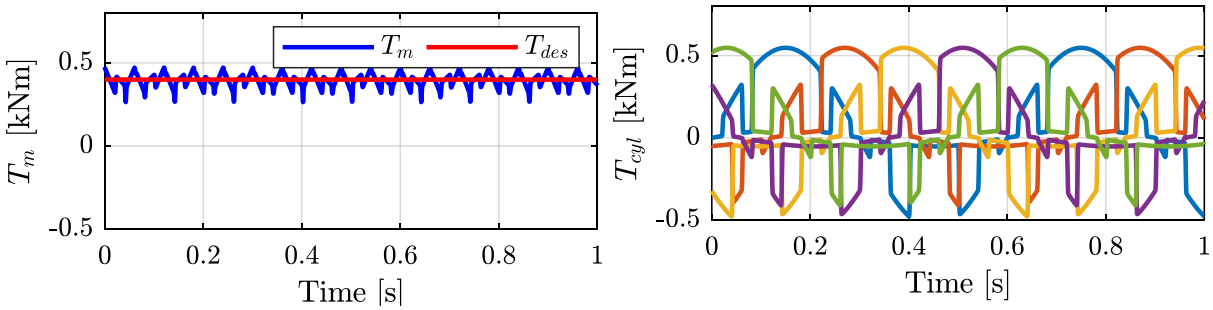

Figure 2.10: Example of DDM operation with SPSDS.

2.3 Valve Requirements

The most important components in the DDM are the on/off valves. One of the keys to achieving high energy efficiency are the on/off valve characteristics. In general, an on/off valve to be used in a DDM should have the following features [39]:

- low cost
- compact design
- high durability
- easy to replace
- low electrical power consumption
- zero leakage
- low switching time
- high flow capacity
- high repeatability and accuracy

A DDM needs two on/off valves per cylinder chamber. A high number of valves requires the valves to be cheap to keep the production costs of the DDM low and to be compact to reduce space requirement. Also, a high number of valves raises the risk of a system failure caused by a malfunction of one valve. The valves must, therefore, have high durability and be easy to replace. From an energy efficiency point of view, the valves should have low electric power consumption, low leakage (zero leakage is best), low switching time, high flow capacity and high repeatability and accuracy. The electrical power consumption should preferably be below 20 W [39], but this may be affected by the motor size. The valves should be leak tight to avoid leakage losses. Fast switching and high flow capacity is important to minimize flow throttling losses. High repeatability and accuracy is important to fully decompress and compress the pressure in the cylinder chamber before opening the valves in order to reduce compressibility losses and minimize flow and pressure peaks.

2.3.1 Flow capacity and response time

Rømer et al. [26] and Nørgård [25] have developed a method for finding the required flow capacity and switching time when operating with FSDS and PSDS 1. For FSDS, the result shows that it is possible to achieve energy efficiency higher than 95 % at 20 % displacement if the valve switching time is less then 20 % of the shaft revolution time, and the pressure drop across the valve is less than 0.5 % of the pressure drop across the machine at maximum valve flow. In order to achieve the same high energy efficiency when operating with PSDS 1, the valve switching time must be reduced to 1.67 % of the shaft revolution time. Note that the electrical energy consumed in the valves was not taken into account in this study. The switching time and flow capacity can be calculated as shown in Equation 2.18 and Equation 2.19.

$$T_s = T_{rev} \cdot \overline{T}_s \tag{2.18}$$

$$Q_{ref} = Q_{max} \cdot \frac{\sqrt{5\ \text{bar}}}{\sqrt{\Delta p_{machine} \cdot \overline{\Delta p}}} \tag{2.19}$$

where T_s is the switching time of the valve, T_{rev} is the time for one shaft revolution and $\overline{T}_s$ is the normalized switching time and equal to 20 % for FSDS and 1.67 % for PSDS 1. Q_{ref} is the valve flow with a pressure drop of 5 bar (also called flow capacity), Q_{max} is maximum flow through the valve ($Q_{max} = \frac{V_d}{2} \cdot \dot{\theta}_{m,max}$), $\Delta p_{machine}$ is the pressure difference across the machine and $\overline{\Delta} p$ is the normalized pressure drop and is equal to 0.5 % for both FSDS and PSDS 1.

Table 2.1 shows the required flow capacity and response time for a digital displacement motor with a cylinder displacement equal to $V_d = 50$ cc/rev, a pressure drop across the DDM of $\Delta p_{machine} = 200$ bar and operating at 10 rpm, 100 rpm and 1000 rpm.

Table 2.1: Required switching time and valve flow capacity.

Full stroke displacement strategy				
$\dot{\theta}_{m,max}$	10 rpm	100 rpm	1000 rpm	
T_s	1200 ms	120 ms	12 ms	(based on $\overline{T}_s = 20$ %)
Q_{ref}	3.5 l/min	35 l/min	350 l/min	(based on $\overline{\Delta} p = 0.5$ %)
Partial stroke displacement strategy 1				
$\dot{\theta}_{m,max}$	10 rpm	100 rpm	1000 rpm	
T_s	100 ms	10 ms	1 ms	(based on $\overline{T}_s = 1.67$ %)
Q_{ref}	3.5 l/min	35 l/min	350 l/min	(based on $\overline{\Delta} p = 0.5$ %)

It can be seen that the valve requirements are stricter for PSDS compared to FSDS.

Also, operation at higher speeds sets higher requirements for valve response time and flow capacity.

Note that the opening and closing profile of the valves will affect the efficiency of the digital displacement machine. In the method described above, a linear valve opening profile is assumed. The timing of the valves will also affect the efficiency of the DDM. The next section shows how mistiming of one valve will affect the energy efficiency.

2.3.2 Valve accuracy and repeatability

In addition to a proper valve timing strategy, it is important to have valves that are capable of operating according to the strategy. For example, opening a valve too early or too late may result in increased flow throttling losses and compressibility losses. Switching the on/off valves precisely is very important. In [20], the authors showed that the valve throttling losses were increased by a factor of approximately 8 when the actuation of the valves was off by 2 ms when operating at 3000 rpm, 300 bar, 57 % displacement and with valves capable of switching in 1 ms. The used displacement strategy was PSDS 1. This section aims to analyze the energy efficiency sensitivity to the mistiming of the valves. It also aims to describe the maximum mistiming that can be allowed without introducing significant losses. The work is presented in the paper C.

2.3.2.1 Analyzing Method

The piston speed is largest mid-stroke and smallest close to TDC and BDC. The valve flow will therefore have a similar flow profile. It is assumed that the energy efficiency is more sensitive to poor valve timing when the valve flow is high and also at lower displacements when the output power is low. In order to ensure that the most critical operation condition is covered, the effect of mistiming should be conducted along the entire piston stroke. For simplicity, when analyzing the sensitivity to mistiming of the valves, only motor operation and mistiming of one valve are considered. Figure 2.11 shows the valve timing strategy and relevant parameters used in this analysis. Plot 1 shows the piston position, Plot 2 shows the opening ratio of the high pressure valve and Plot 3 shows the opening ratio of the low pressure valve. θ_{delay1} is defined as the angle the shaft rotates between starting to close the high pressure valve and starting to open the low pressure valve. α is the control angle and describes at which local shaft position the high pressure valve shall start to close. The motor displacement can be calculated based on the control angle, α, as shown in Equation 2.15.

To evaluate the energy efficiency's sensitivity to mistiming of a valve, several simulations are conducted where α varies from α_{min} to α_{max}. At each step of α, the delay angle

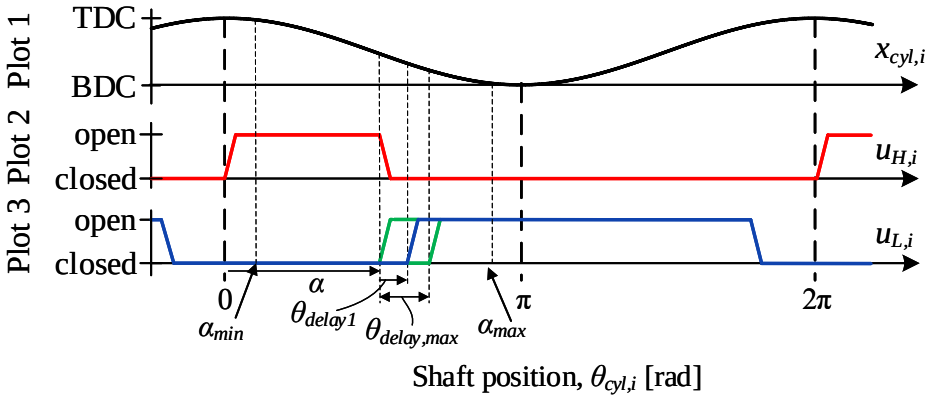

Figure 2.11: Simplified illustration of valve timing strategy when analyzing requirements regarding valve timing accuracy.

θ_{delay1} is varied from 0 rad up to $\theta_{delay,max}$, marked with two green lines in Plot 3 in Figure 2.11. At each simulation the energy efficiency is evaluated and saved. By using the saved values, the energy efficiency can be mapped for different values of α and θ_{delay1}. Based on the efficiency map, it is possible to evaluate which delay angle that gives the highest efficiency, and how early or late the low pressure valve can bee opened without reducing the energy efficiency significantly.

The maximum delay angle, $\theta_{delay,max}$, is defined as shown in Equation 2.20 and illustrated in Figure 2.12.

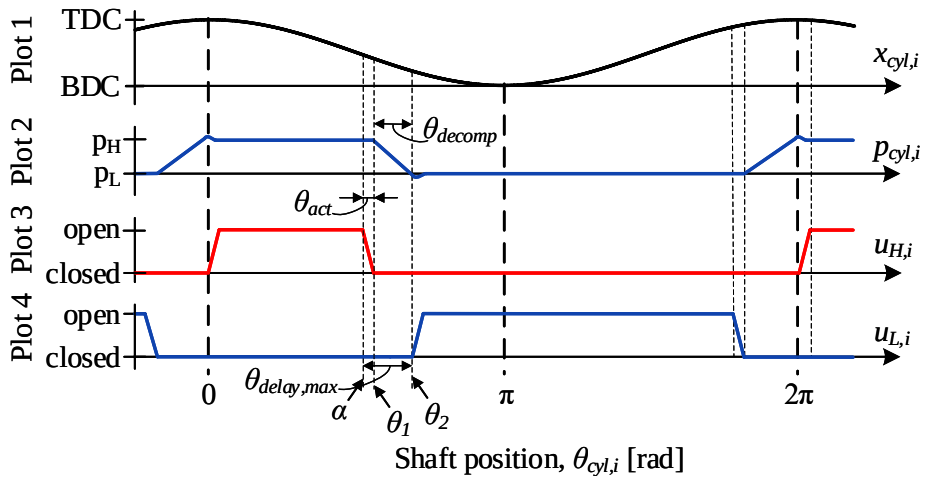

Figure 2.12: Illustration of $\theta_{delay,max}$.

$$\theta_{delay,max} = \theta_{act} + \theta_{decomp} \tag{2.20}$$

where θ_{act} is the angle the shaft rotates while closing the high pressure valve and θ_{decomp} is the angle the shaft needs to rotate in order to decompress the chamber oil from high pressure level down to the low pressure level. This definition is chosen in order to limit the number of simulations where the cylinder chamber cavitates, because if the delay angle

becomes too large, the cylinder chamber will cavitate. In a real system, cavitation can be avoided by for example connecting an anti-cavitation valve to every cylinder camber.

By knowing the valve switching time, T_s, and the motor speed, $\dot{\theta}_m$, θ_{act} is calculated as shown in Equation 2.21

$$\theta_{act} = T_s \cdot \dot{\theta}_m \tag{2.21}$$

For simplicity, the effective bulk modulus is set to $\beta_{eff} \approx \beta_L$ when estimating the decompression angle. The decompression angle, θ_{decomp}, can then be calculated as shown in Equation 2.22.

$$\theta_{decomp} = \theta_1 - \theta_2 \tag{2.22}$$

where θ_1 is calculated as shown in Equation 2.23 and θ_2 is calculated as shown in Equation 2.24.

$$\theta_1 = \alpha + \theta_{act} \tag{2.23}$$

$$\theta_2 = \cos^{-1}\left(\cos\left(\theta_1\right) + \frac{3 - \cos\left(\theta_1\right)}{\beta_L} \cdot \left(p_H - p_L\right)\right) \tag{2.24}$$

A more detailed derivation of the expression for θ_2 can be found in paper C. Note that the decompression angle is small when switching mid-stroke and larger when switching closer to TDC and BDC.

2.3.2.2 Results

The simulation parameters used in this analysis are listed in Table 2.2.

Table 2.2: Fixed simulation parameters.

Parameter	**Value**	**Description**
V_d	50 cc/rev	Cylinder displacement
V_0	50 cc/rev	Dead volume in cylinder
p_{HP}	220 bar	Constant high pressure source
p_{LP}	20 bar	Constant low pressure source
$\overline{T}_s$	1.67 %	Normalized valve transition time
$\overline{\Delta}p$	0.5 %	Normalized pressure drop
β_L	1.2 MPa	Bulk modulus liquid

Describing the valve characteristics by the normalized valve parameters $\overline{T}_s$ and $\overline{\Delta}p$, makes the simulation results valid for all speeds. This method has earlier been used in [26] and [25]. The switching time and valve flow capacity can be calculated as shown in Equation 2.18 and Equation 2.19 respectively.

The energy efficiency sensitivity of the digital displacement motor to the valve accuracy and repeatability is evaluated by performing a large number of simulations with different values of the control angle, α, and the timing delay angle, θ_{delay1}. The energy efficiency is evaluated for every simulation and saved together with the valve throttling losses. The energy efficiency is calculated as shown in Paper C. The control angle, α, is ranging from 40° to 154°, where 154° corresponds to full displacement. The timing delay angle, θ_{delay1}, is ranging from 0° to $\theta_{delay,max}$.

In Figure 2.13, the left plot shows the energy efficiency map and the right plot shows the valve throttling losses. The x-axis shows the control angle α and the y-axis shows the

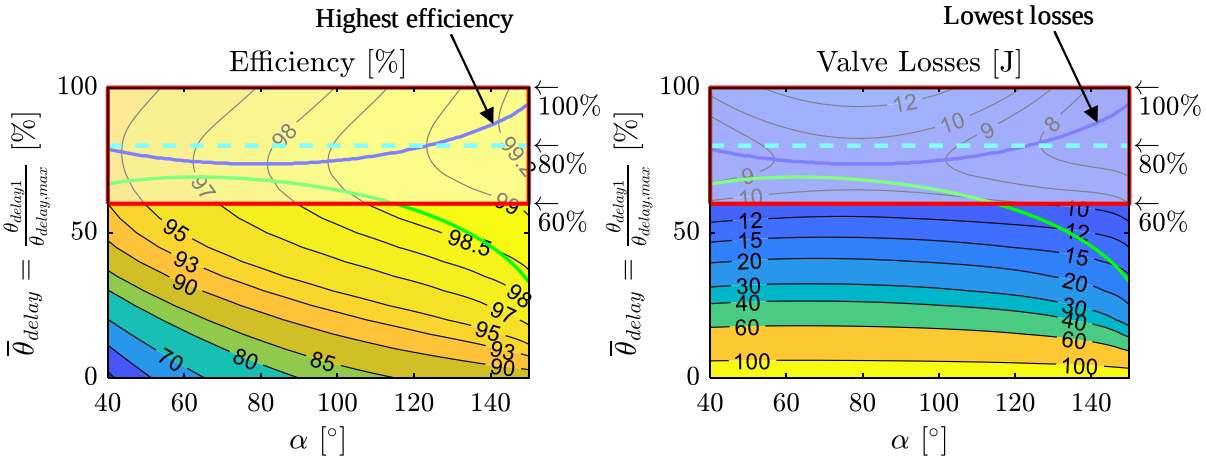

Figure 2.13: Efficiency and valve losses as a function of the state change angle and the delay angle.

normalized delay angle, $\overline{\theta}_{delay}$. The normalized delay angle is defined as $\overline{\theta}_{delay} = \frac{\theta_{delay1}}{\theta_{delay,max}}$.

From the plots, it can be seen that the energy efficiency is high and the valve throttling losses are low for high values of $\overline{\theta}_{delay}$. At lower values of $\overline{\theta}_{delay}$, the energy efficiency drops and the valve throttling losses increase significantly. The blue line marks the highest energy efficiency and lowest valve losses in the left and right plot respectively. It can be seen that the optimal delay angle varies with the control angle, α. In this simulation, the best delay angle is between 75 % and 95 % of $\theta_{delay,max}$, shown by the blue line. Note that a change in dead volume, valve flow capacity, valve transition time, valve motion profile or oil stiffness will change the optimal delay angle.

In the area below the green line, the low pressure valve starts to open before the high pressure valve is fully closed, resulting in increased flow throttling losses due to flow running directly from the high pressure source into the low pressure source. By further reducing the normalized delay angle, $\overline{\theta}_{delay}$, below the green line, the time where both valves are open simultaneously will increase and result in a significant increase of flow throttling losses.

Even though the optimal opening angle is known, the blue line in Figure 2.13, it is

not possible to actuate the valve at the exact optimal position every time. Some times it may open a little too early or too late. Simplifying the optimal delay angle to be $\overline{\theta}_{delay,opt} = 80$ %, marked with the cyan dotted line, the flow throttling losses will stay low, and the motor efficiency will stay high. Even though there is a delay in the timing of ±20 %, marked with the light area inside the red box in Figure 2.13, the valve throttling losses will remain low and the motor efficiency will remain high. Switching the low pressure valve within ±20 % of the simplified optimal delay angle, $\overline{\theta}_{delay,opt}$, is more demanding in high speed motors than low speed motors. By knowing the motor speed, $\dot{\theta}_m$, the delay in time can be calculated as shown in Equation 2.25 for various speeds.

$$T_{delay} = \frac{\pm 20\ \% \cdot \theta_{delay,max}\left(\alpha\right)}{\dot{\theta}_m} \tag{2.25}$$

In Figure 2.14, Equation 2.25 is used to calculate the allowable delay in time at different displacements and speeds. Note that the y-axis is scaled logarithmically. It can be seen

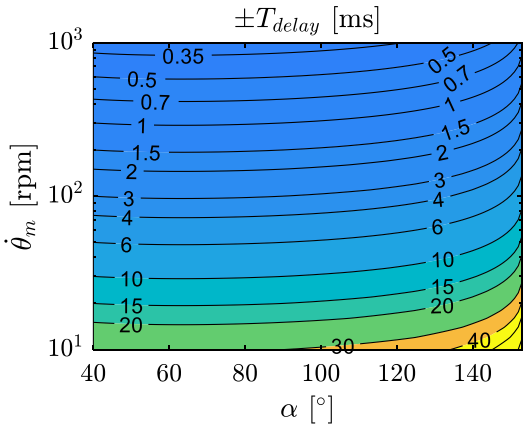

Figure 2.14: Acceptable deviation from optimal valve timing.

that the required accuracy and repeatability is stricter in high speed motors than in low speed motors. The requirements are also higher when switching mid stroke compared to close to BDC (α close to α_{max}). When operating at 1000 rpm, the low pressure valve should be opened within approximately ±0.3 ms from optimal opening time. When operating at 10 rpm, the requirements are not that strict, and the low pressure valve should open within approximately ±30 ms from the optimal opening time.

Chapter 3

Experimental Test Rig

A test rig has been built in order to validate the simulation model of the DDM and experimentally test the displacement strategies presented in Section 2.2. The test rig is designed to facilitate digital displacement operation on a single cylinder. It is assumed that all cylinders in a motor have the same characteristics. Therefore, only operation on a single cylinder is required to experimentally test a displacement strategy. Also, if the simulation model for a single cylinder is validated, then the entire DDM model is assumed to be valid. The test rig is based on a previously developed test rig at Aalborg University, Denmark [25].

This chapter presents the test rig, experimental results and validation of the simulation model. The simulation model is verified for operation with the displacement strategies FSDS, PSDS 1, PSDS 2 and SPSDS. The presented work is published in paper D.

3.1 Test Rig Description

The test rig is designed and built to test different digital displacement strategies. The test rig is based on a five cylinder Calzoni MR250 radial piston motor which has been modified to operate with digital displacement technology on one cylinder. Figure 3.1 shows a picture of the test rig. A permanent magnet synchronous electric machine is used as a load and to control the rotational speed. The control block is used to supply the modified radial piston motor with appropriate pressures and volume flows. The control block is supplied by a 250 kW variable displacement pump station, not shown in the picture. The power cabinet contains power supplies, valve drivers, data acquisition system, and control system.

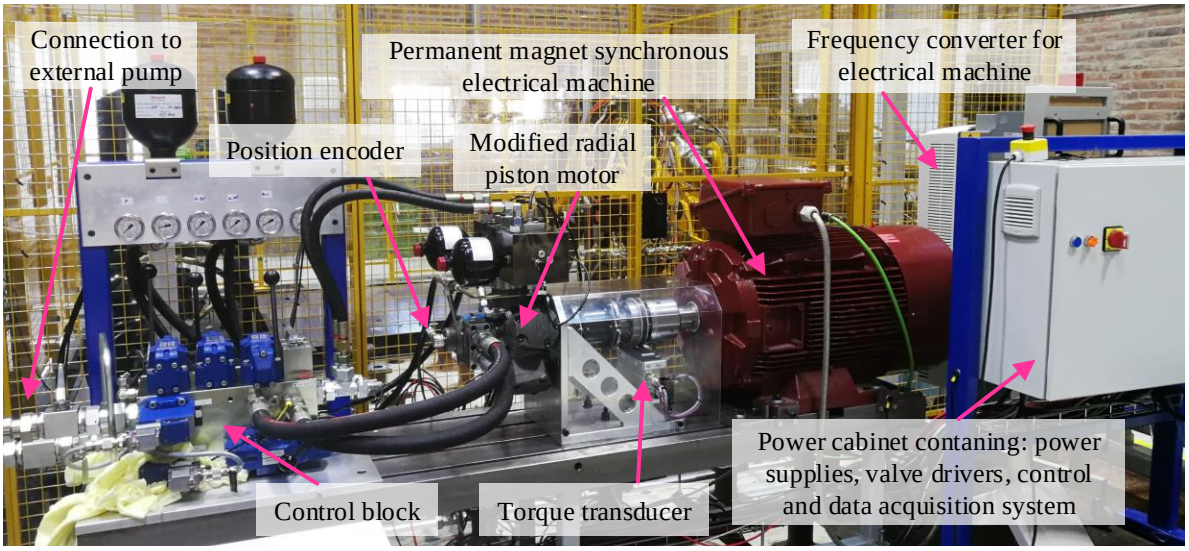

Figure 3.1: Test rig.

3.1.1 Modification of the Hydraulic Motor

The hydraulic motor is modified to operate with the digital displacement technology on a single cylinder. The cylinder has been modified by blocking the original oil supply to the cylinder chamber and replace it with two on/off valves mounted in a custom made valve block. Figure 3.2 shows the modified hydraulic motor with the custom made valve block. In addition to the two on/off valves, the valve block is equipped with two accumulators, three pressure sensors and a pressure relief valve with anti-cavitation function. The on/off valves (1) and (2) are normally open WES type valves from Bosch Rexroth with a flow capacity of 45 l/min at 5 bar pressure drop and a switching time below 5 ms. The hydraulic accumulators are 0.7-L diaphragm type from Bosch Rexroth. The low pressure accumulator (3) is pre-pressurized with 5 bar and the high pressure accumulator (4) is pre-pressurized with 80 bar. In total three pressure transmitters are mounted on the valve block. They measure the pressure in the low pressure source (5), high pressure source (6) and in the cylinder chamber (7). For safety reasons, a pressure relief valve with anti-cavitation function (8) is connected to the cylinder chamber to avoid dangerous high cylinder chamber pressures and cavitation. A new top cover (10) for the modified cylinder has been designed and manufactured. The new top cover was designed to block the original oil connection (12) between the port plate and the cylinder chamber, and to create a new oil connection to the valve block.

There is also mounted an encoder and torque transducer on the motor shaft for shaft position measurements and torque measurements respectively. The position encoder and torque transducer is not shown in Figure 3.2 but can be seen in Figure 3.1. The position encoder is an incremental Scancon encoder with 5000 ppr. The torque transducer is an HBM T12 inductive torque transducer.

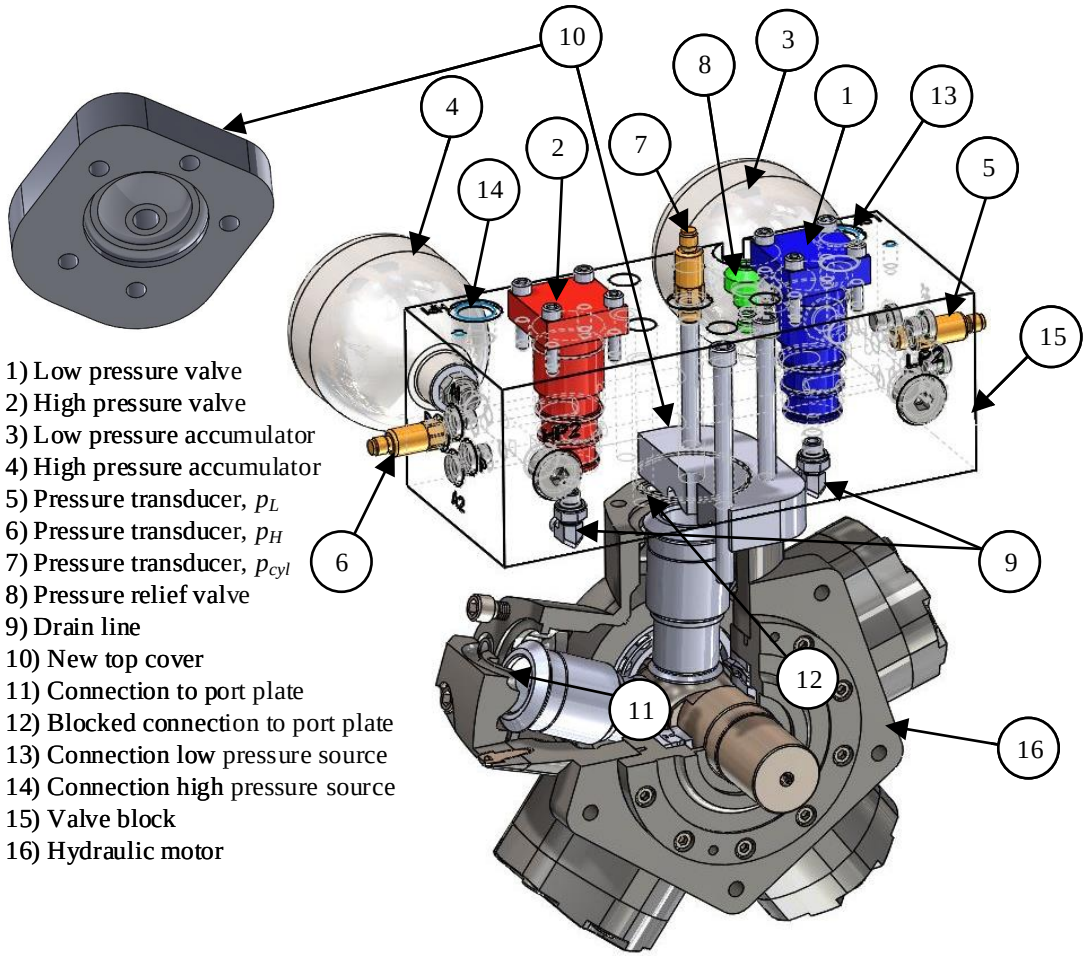

Figure 3.2: Illustration of the modified radial piston motor.

Table 3.1 lists all parts used in the valve block.

Table 3.1: Part list for the custom made valve block and motor shown in Figure 3.2.

Description	Part number	Ordering code	Manufacturer
On/off valve	1 and 2	3WES 8 P1XK/AG24CK50/V	Bosch Rexroth
Accumulator	3 and 4	HAD-0.7-250-1x/50Z06A-1N111-BA	Bosch Rexroth
Pressure transducer	5	HM 20-2x-100-H-K35	Bosch Rexroth
Pressure transducer	6 and 7	HM 20-2x-400-H-K35	Bosch Rexroth
Pressure relief valve	8	PLC053 393000K179	Parker
Hydraulic motor	16	MR250D-P1Q1N1C1N07 00	Delivered by Parker

3.1.2 Hydraulic Diagram

The hydraulic diagram for the test rig is shown in Figure 3.3. The hydraulic diagram is divided into three main parts; control block, valve block and the unmodified cylinders. The control block delivers desired pressures and flows to the valve block and the unmodified cylinder chambers. The control block is designed to facilitate pumping, motoring and

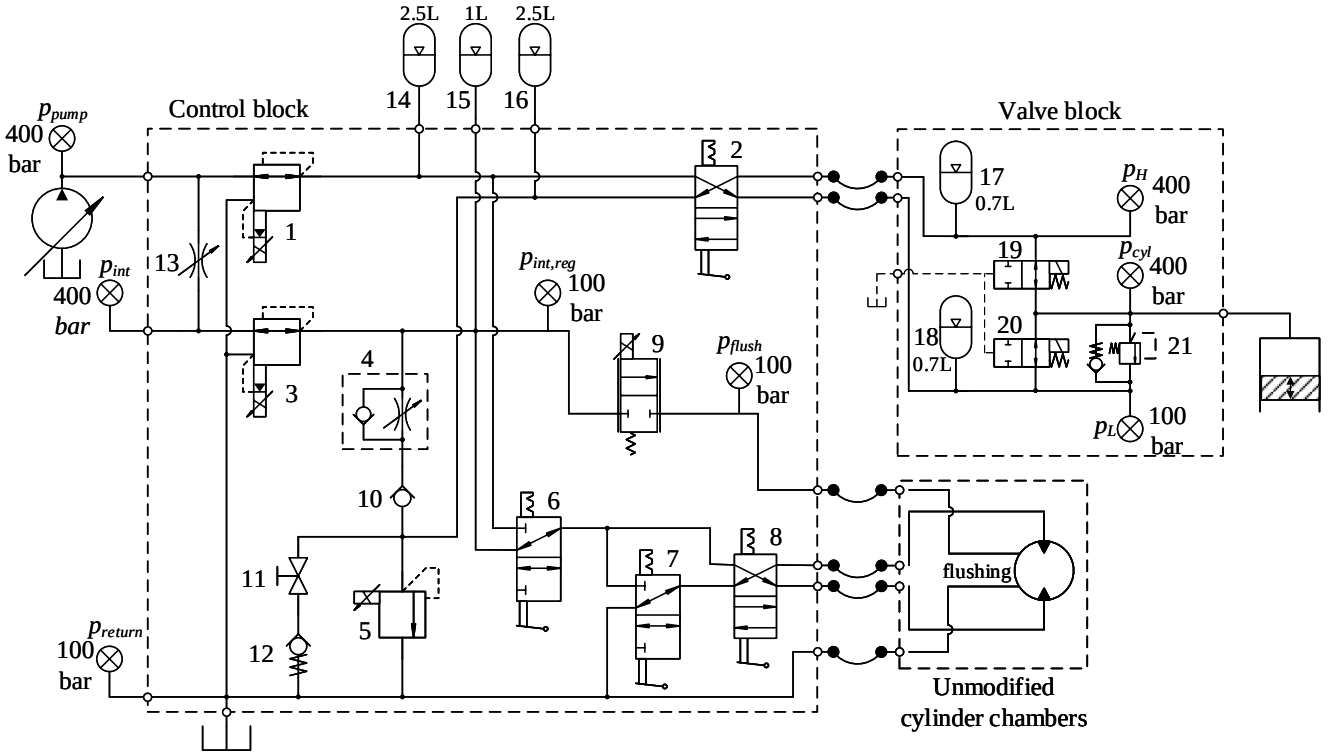

Figure 3.3: Hydraulic diagram for the test rig.

idling (inactive) operation on the modified cylinder. In this study, only the motor operation is used, and therefore, only the motor operation will be described. Pump operation is described in [86].

The pressure reduction valves (1, 3) are used to control the pressure level in the high pressure line, p_H, and in the intermediate pressure line, $p_{int,reg}$. The high pressure line is used to supply the modified cylinder chamber. The intermediate pressure line is used to supply the four remaining cylinder chambers and for flushing of the machine casing by using the flow control valve (9). During motor operation, the 4/2 directional control valve (2) is set opposite of drawn, the gate valve (11) is open, the pressure relief valve (5) is set to high pressure level and the remaining cylinder chambers are short circuited by setting the 3/2 directional control valve (7) opposite of drawn. The accumulators are used to reduce the pressure oscillations introduced by the digital displacement operation.

3.2 Experimental Work and Model Validation

The test rig has been used to validate the simulation model and experimentally test operation with FSDS, PSDS and SPSDS. The simulation model has been validated by comparing experimental results with simulation results. Table 3.2 shows the opening and closing angles used in both the experimental work and in the simulation model. Note that HPV and LPV are abbreviations for high pressure valve and low pressure valve

respectively. Table 3.3 shows the operation conditions. The simulation parameters are set to match the parameters in the experimental test setup and are shown in Table 3.4.

Table 3.2: Activation angles.

	FSDS	PSDS	SPSDS
Open HPV	0°	0°	60°
Open LPV	180°	90°	125°
Close HPV	154°	90°	120°
Close LPV	338°	338°	60°

Table 3.3: Operation conditions.

Description	Symbol	Value
Operation speed	$\dot{\theta}_m$	100 rpm
High pressure level	p_H	110 bar
Low pressure level	p_L	10 bar

Table 3.4: Simulation parameters.

Parameter	**Symbol**	**Value**	**Unit**
Piston chamber displacement	V_d	50	cc/rev
Cylinder chamber dead volume	V_0	130.8	cc
Number of pistons	N_c	1	–
Switching time on/off valves	T_s	5	ms
Flow-pressure coefficient	k_f	$1.2 \cdot 10^6$	$\sqrt{\text{Pa}} \cdot \text{s/m}^3$
Bulk modulus liquid	β_L	1.2	GPa
Volume fraction of undissolved gas at $p_{atm}^{(abs)}$	ϵ_{g0}	0.01	–

3.2.1 Full Stroke Operation

Figure 3.4 shows measured and simulated results of the cylinder pressure p_{cyl} (red line) and cylinder torque T_{cyl} (blue line) during full stroke operation as a function of the shaft angle position. Note that the cylinder is at TDC for $\theta_m = j \cdot 2\pi$ rad and at BDC for $\theta_m = \pi + j \cdot 2\pi$ rad $\forall j \epsilon \mathbf{Z}$ where $\mathbf{Z}$ is a set of positive and negative integers. The left plot

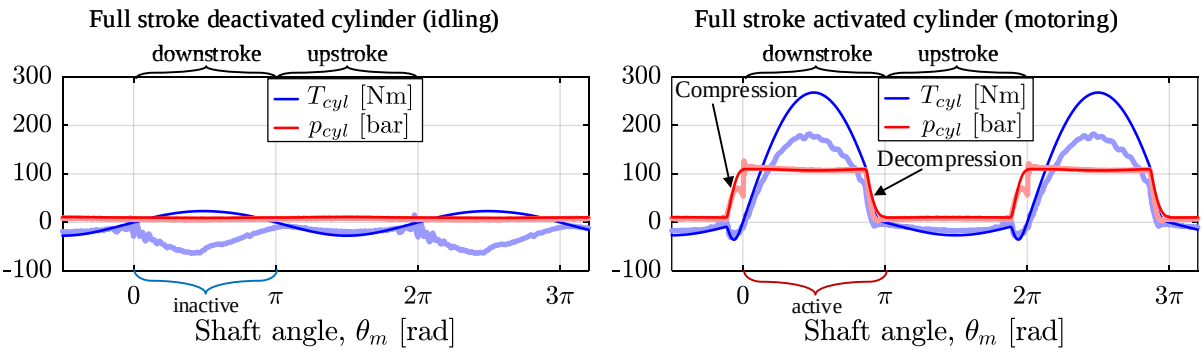

Figure 3.4: Experimental and simulation results for idling and full stroke motor operation (light colors are experimental results and dark colors are simulation results).

shows an inactive cylinder operation and the right plot shows an active full stroke motor operation. The light colors show the experimental results and the dark colors show the simulation results.

For the inactive cylinder, the simulated chamber pressure matches the measured pressure. The simulated output torque matches the measured torque in the upstroke phase but deviates in the downstroke phase. Some of the negative measured torque may be due to friction in the motor, but most of it is produced by the unmodified cylinder chambers. As mentioned earlier, the four unmodified cylinder chambers are short circuited with a 1-L accumulator (15) connected to the short circuit line as shown in the hydraulic diagram in Figure 3.3. If all five cylinders had been short circuited, the fluid volume in the short circuited line would be relatively constant when rotating the radial piston motor. Since one cylinder is disconnected, there will be a difference in the amount of fluid going in and out of the unmodified cylinders. When the modified cylinder is in the downstroke phase, more fluid will go out of the unmodified cylinders than in. When the modified cylinder is in the upstroke phase, more fluid will go in to the unmodified cylinders than out. The 1-L accumulator is therefore used to store excess fluid in the downstroke phase and deliver fluid in the upstroke phase. This will result in a varying pressure in the short circuited line. The measured pressure in the short circuited line is shown by the black line in Figure 3.5. It can be seen that the pressure is higher in the downstroke phase than in the upstroke phase. The high pressure in the downstroke phase results in a negative torque contribution from the unmodified cylinders. This torque contribution has been simulated by using the measured pressure. The green line, denoted $T_{cyl,sim}$, shows the simulated torque from the unmodified cylinders added to the simulated cylinder torque. Now when the negative torque produced by the unmodified cylinders is included, the simulated and experimental measured torque is a close fit. This can be seen by comparing the green and light blue colored lines. The precharge pressure of the 1-L accumulator (15) is 20 bar. A precharge pressure of 20 bar is unnecessarily high and should have been reduced to reduce the torque contribution from the unmodified cylinders.

In the active full stroke motoring cycle, shown to the right in Figure 3.4, the measured and simulated torque have the same trends. The simulated torque is a good match in the upstroke phase, but the measured torque has a lower magnitude in the downstroke phase due to the negative torque produced by the unmodified cylinders. The green line in the right plot in Figure 3.5 shows the simulated cylinder torque when the torque contribution from the unmodified cylinders is included, $T_{cyl,sim}$. The results show that the simulated and measured torque is a good match when the negative torque from the unmodified cylinders is included in the simulation results. The simulated cylinder pressure matches the measured pressure quite well, except for small deviations in the compression and

decompression phase, seen in the right plot in Figure 3.4. It can be seen that in the experimental work, the chamber fluid does not compress fully up to the high pressure level in the compression phase and decompresses slightly faster in the decompression phase. The poor compression and decompression phases may occur due to leakage in the modified cylinder or leakage in the on/off valves. In the simulation model, it was originally assumed that the cylinder and the on/off valves are leak free. Assuming that the cylinder is leak free does not reflect reality. Some leakage is expected in order to reduce friction between moving parts in the hydraulic motor. By including some leakage in the simulation model, the simulated pressure matches very well with the measured. The improvement can be seen in the compression and decompression phase in the right plot in Figure 3.5.

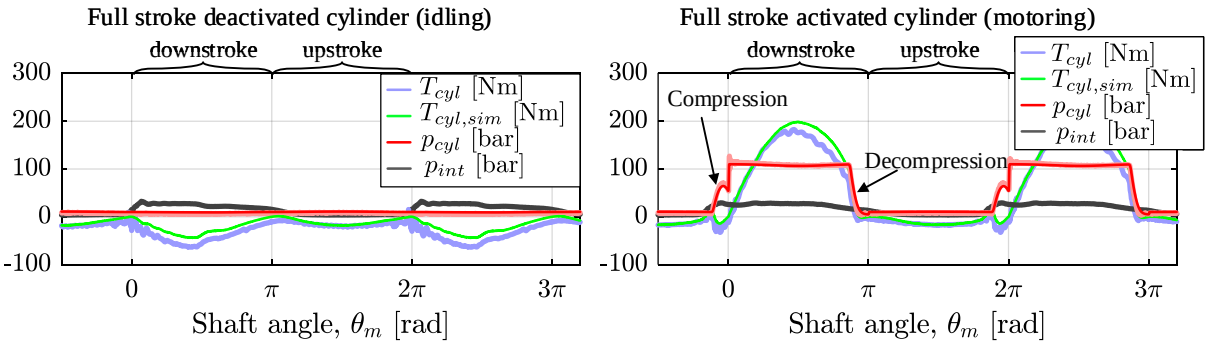

Figure 3.5: Experimental and simulated results for full stroke motor operation when the simulation model is modified to include leakage in the cylinder chamber and the negative torque produced by the unmodified cylinders.

The leakage is included as shown in Equation 3.1.

$$Q_L = \frac{w \cdot h^3}{12 \cdot \mu \cdot L} \cdot (p_{cyl} - p_d) \tag{3.1}$$

where w is the width of the leakage path, h is the height of the leakage path, L is the length of the leakage path, μ is the viscosity of the hydraulic fluid and p_d is the drain pressure. The width of the leakage path is calculated as $w = \pi \cdot d_{cyl}$, where d_{cyl} is the diameter of the cylinder chamber. The height of the leakage path is adjusted until the simulated pressure matches the measured pressure. The used height is set to $25.5 \cdot 10^{-6}$ m and the drain pressure is set to $p_d = 5$ bar.

3.2.2 Partial Stroke and Sequential Partial Stroke Operation

The left plot in Figure 3.6 shows the measured and simulated results for PSDS 1 motor operation and the right plot shows measured and simulated results for SPSDS motor operation. The red line shows the chamber pressure and the blue line shows the cylinder

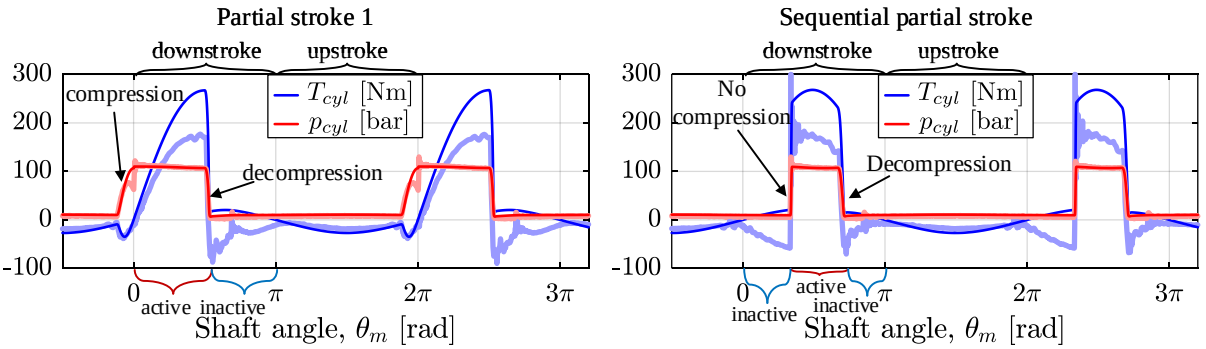

Figure 3.6: Experimental and simulated results for partial stroke and sequential partial stroke motor operation (light colors are experimental results and dark colors are simulation results).

torque. Light colors are experimental results and dark colors are simulation results. When operating with the PSDS 1 the cylinder chamber is deactivated at $\theta_{cyl} = \pi/2$ rad. Deactivating a chamber at this position corresponds to the most critical switching position due to maximum piston velocity and, therefore, the highest valve flow. It can be seen that the measured and simulated chamber pressures match quite well, except in the compression phase and some small oscillations right after $\theta = 0$ rad and $\theta = 2\pi$ rad. The error in the compression phase occurs due to leakage in the cylinder chamber as discussed earlier in Section 3.2.1. In the downstroke phase, the measured and simulated cylinder torques have the same characteristics but with a deviation in the magnitude. This deviation is expected to occur due to the negative torque introduced by the unmodified cylinder chambers, also discussed in Section 3.2.1. In the upstroke phase, the measured and simulated output torques match well.

In the SPSDS, shown to the right in Figure 3.6, there is no compression phase, because the cylinder chamber is activated during the downstroke piston motion. Hence, the cylinder volume is increasing and the cylinder fluid can therefore not be compressed by the piston motion. The high pressure valve is opened at the same angle as the low pressure valve is closed. The measured and simulated pressures match very well. The measured and simulated output torques match very well in the upstroke phase but deviate in the downstroke phase due to the negative torque introduced by the four unmodified cylinder chambers. However, the torque characteristics are the same, except for some oscillations in the measured torque.

The PSDS 2 is quite similar to the PSDS 1, except that in PSDS 2, the cylinder can be reactivated. Reactivation of a cylinder is shown in the SPSDS operation. The PSDS 2 is therefore considered as a combination of the PSDS 1 and the SPSDS. If the simulation model is valid for the PSDS 1 and the SPSDS, it is also assumed that it is also valid for the PSDS 2.

Figure 3.7 shows the measured results and the simulation results for the PSDS 1

and the SPSDS when leakage and the negative torque contribution from the unmodified cylinders are included in the simulation model. The plots show that the measured and simulated results match well.

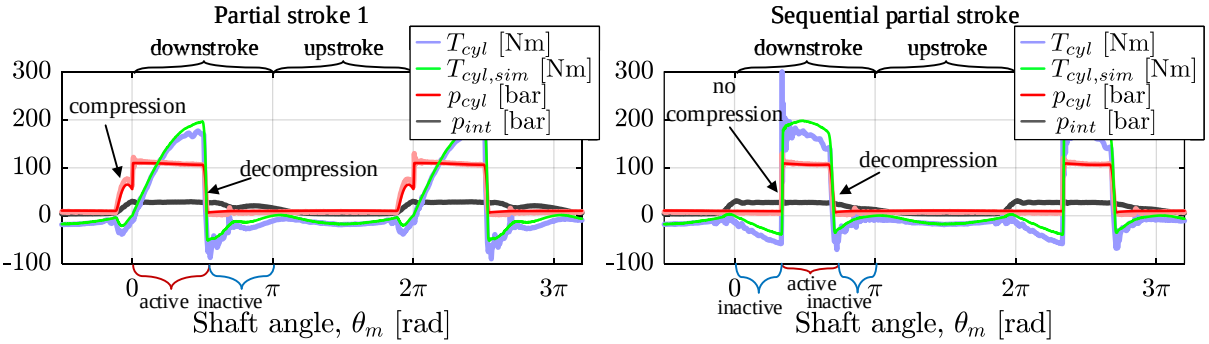

Figure 3.7: Experimental and simulated results for partial stroke and sequential partial stroke motor operation when the simulation model is modified to include leakage in the cylinder chamber and the negative torque produced by the unmodified cylinders.

3.3 Discussion

In the experimental measurements, there is some uncertainty due to sensor accuracy and alignment of shaft position and piston position in the modified cylinder chamber. The piston position is not measured but estimated based on the shaft position measurements. The piston position is an essential parameter considering proper activation of the on/off valves. The piston position was aligned with the shaft position measurements by comparing measured and simulated results of the output torque and cylinder pressure. A possible deviation in the range of a few degrees is therefore assumed.

There is also uncertainty in the valve switchings. The valve positions are not measured, and therefore it is not known exactly when the valves are switched. However, since the motor is operating at a low speed, approximately 100 rpm corresponding to 600 ms pr revolution, a valve that opens a few milliseconds too late or too early will not significantly affect the results. This is also verified by the valve accuracy analysis conducted in Section 2.3.2.

By comparing the measured and simulated results, it has been shown that the results match quite well except for some deviation in the pressure expectedly due to leakage in the cylinder and some deviation in the torque due to negative torque introduced by the four unmodified cylinder chambers. In this project, the simulation model is used to analyze the dynamic behavior of a digital displacement machine and to test controllers. The output torque is therefore essential. By modifying all cylinders, it is assumed that the measured output torque will be closer to the simulated output torque because the effect

of the unmodified cylinders is removed. The deviation between measured and simulated pressure is largest in the compression phase and only small in the decompression phase. Since the compression phase occurs close to TDC, an error in the chamber pressure at this position will have a very small influence on the cylinder torque. This is seen in Equation 2.12. When $\theta_{cyl,i} = j \cdot 2\pi \ \forall \, j \, \epsilon \, \mathbf{Z}$ the cylinder torque is 0 Nm. The simulation model is therefore assumed to be a valid model of the digital displacement motor when considering the output torque.

Chapter 4

Dynamic Response Analysis

The dynamic response characteristics of a DDM are among others affected by the displacement strategy, operation speed, number of cylinders and the displacement ratio. Knowledge about the dynamic response characteristics is highly relevant considering control design. The displacement strategy and the number of cylinders should therefore be chosen in order to meet the operation requirements of the driven application.

This chapter gives a detailed analysis of the transient and steady-state behavior of a DDM operating with different displacement strategies, FSDS, PSDS 1, PSDS 2 and SPSDS, respectively. This analysis also examines how the shaft speed, the number of cylinders and the displacement ratio affect the dynamic response. The work presented in this chapter is published in paper D.

The simulation parameters used in this chapter are as shown in Table 4.1. Those parameters apply as long as nothing else is specified.

Table 4.1: Simulation parameters used in the transient and steady-state response analysis.

Parameter	**Symbol**	**Value**	**Unit**
Piston chamber displacement	V_d	50	cc/rev
Cylinder chamber dead volume	V_0	50	cc
Number of pistons	N_c	15	–
Switching time on/off valves	T_s	5	ms
Flow-pressure coefficient	k_f	$1.2 \cdot 10^6$	$\sqrt{\text{Pa}} \cdot \text{s/m}^3$
Bulk modulus liquid	β_L	1.2	GPa
Volume fraction of undissolved gas at $p_{atm}^{(abs)}$	ϵ_{g0}	0.01	–

4.1 Full Stroke Displacement Strategy

In the FSDS the cylinders are enabled and disabled on a stroke by stroke basis. This section describes the transient and steady-state characteristics of the DDM operating with FSDS.

4.1.1 Transient Response for the Full Stroke Displacement Strategy

The decision of either activating or deactivating the cylinder chamber is made ahead of TDC, as described in Section 2.2. Since the chamber is activated or deactivated for an entire piston stroke, this decision will affect the output torque until the piston reaches BDC. Hence, the motor shaft has to rotate more than a half revolution to change displacement fully. As a result, the response time is affected by the shaft speed. This analysis starts, therefore, by analyzing the transient behavior in the shaft position domain.

Figure 4.1 shows the step response in the shaft position domain. The left plot shows the step-up response when the displacement fraction, D_m, is stepped from 0 up to 0.25, 0.5, 0.75 and 1. The right plot shows the step-down response when the displacement fraction is stepped from 1 down to 0.75, 0.5, 0.25 and 0. The step is applied at $\theta_m = 0$ rad.

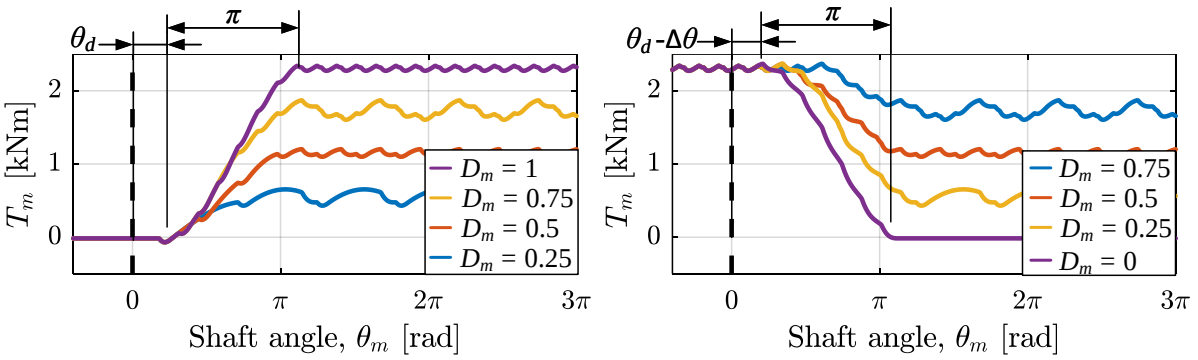

Figure 4.1: Transient response FSDS in position domain.

When stepping up, there is a small delay before the torque starts to rise. This delay angle occurs since the decision of activating or deactivating the cylinder is made ahead of the compression phase. Right before the torque starts to rise, there is a small drop in the torque due to the compression phase in the first activated cylinder. The response angle when stepping up is $\theta_{FSup} = \theta_d + \pi$. The delay angle, θ_d, is calculated as $\theta_d = 2 \cdot \pi - \alpha_d$ where α_d is the position where the decision of activating or deactivating the next cylinder is taken, as shown in Figure 2.3.

When stepping down, there is also a delay before reducing the motor torque. When stepping down to 0 displacement, the delay occurs because the decision of activating or

deactivating the cylinder is made ahead of the decompression phase, similar to the delay in the step-up case. When stepping down to $D_m > 0$ there is an extended delay. However, the response angle when stepping down is equal in all plotted cases. The response angle is calculated as $\theta_{FSdown} = \theta_d - \Delta\theta + \pi$, where $\Delta\theta$ is the phase shift between the cylinders and given by $\Delta\theta = 2 \cdot \pi / N_c$.

The step-up and step-down response angles are in some cases less than the maximum response angles, θ_{FSup} and θ_{FSdown}. Examples of this phenomena can be seen in Figure 4.2 and is a result of the nature of the delta-sigma modulator.

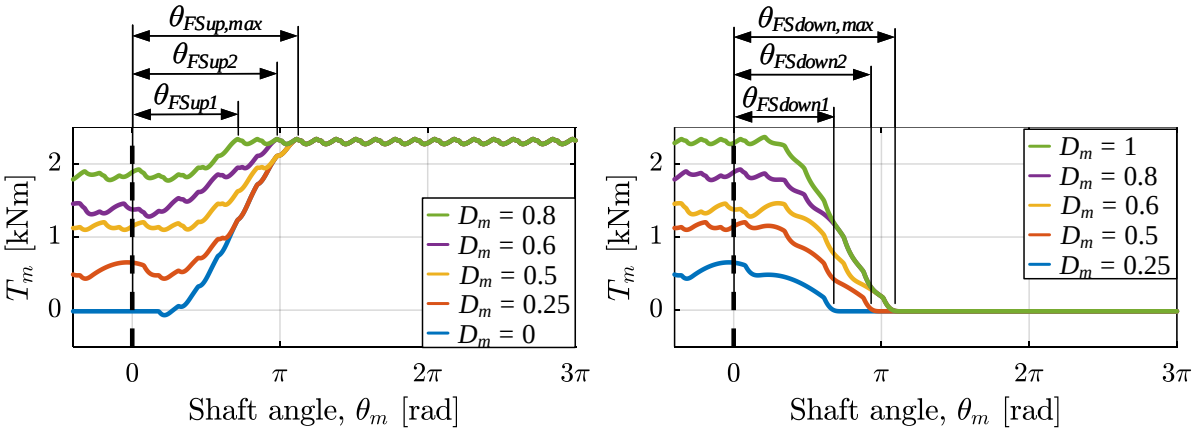

Figure 4.2: Transient response FSDS with variable response angle.

For the simulated case, it can be seen that the response angle when stepping up deviates from the maximum response angle for the green and purple line. When stepping down, the step response angle deviates from the maximum response angle for the blue and red line.

As shown above, the step response can be expressed as a function of the shaft position. The step response time will therefore be highly affected by the shaft speed and operation at variable speed will result in variable response time. Figure 4.3 shows the step response in the time domain when stepping the displacement fraction from 0 up to 1 at various speeds.

The results show that the response time is decreasing at higher shaft speeds. Assuming that the response angle is always at the maximum, the response time is inversely proportional to the shaft speed.

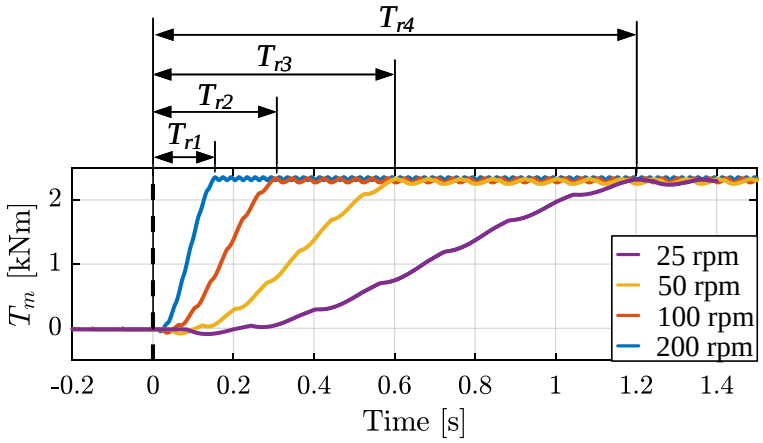

Figure 4.3: Transient response FSDS in time domain operating at various speeds.

4.1.2 Steady-State Response for the Full Stroke Displacement Strategy

When operating with the FSDS, the steady-state characteristics depend on the number of cylinders, the displacement fraction and the shaft speed. Already in Figure 4.1, it can be seen that the steady-state torque tends to oscillate. In this section it is discussed how the number of cylinders, the shaft speed and the displacement fraction affect the steady-state torque.

The left plot in Figure 4.4 shows the steady-state torque in the shaft position domain for DDMs with a various number of cylinders and equal maximum motor displacement. The displacement ratio is set to $D_m = 0.5$ for all motors. The right plot shows the steady-state torque from a 15 cylinder DDM operating at various displacement fractions. From the left plot, it can be seen that the amplitude of the torque oscillations can be

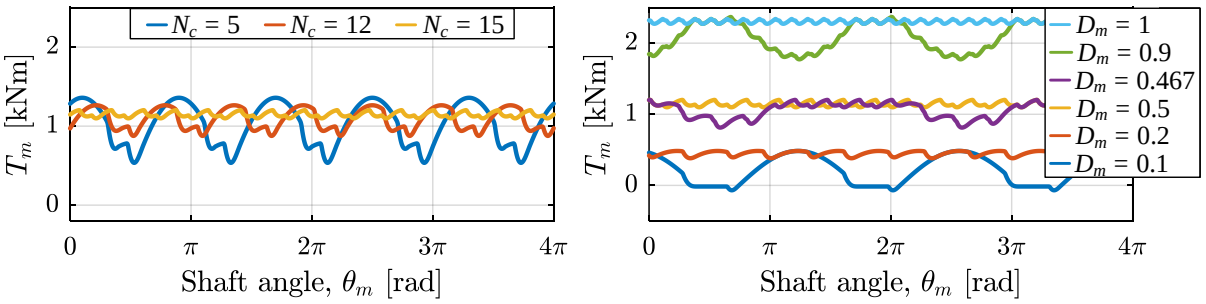

Figure 4.4: Steady-state response FSDS with various number of cylinders (left plot) and at various displacements (right plot).

reduced by increasing the number of cylinders. From the right plot, it can be seen that for some selected displacements, for example, $D_m = 1$, $D_m = 0.5$ and $D_m = 0.2$, the output torque is relatively smooth. On the other hand, only a small change in the displacement may change the cylinder actuation sequence and result in significant torque variations,

see $D_m = 0.1$, $D_m = 0.462$ and $D = 0.9$. A significant torque peak or drop may not be very critical in high speed motors due to a very short duration, but more critical in very low speed motors where the exposure time is much longer. Off course, the inertia of the load will also affect the impact of a torque peak or drop. The number of smooth outputs can be increased by increasing the number of cylinders.

The frequency of the torque oscillations is affected by the rotational shaft speed and the number of cylinders. The effect of changing the shaft speed can be seen in Figure 4.3 where the frequency of the steady-state oscillations is clearly increased when increasing the speed. The effect of changing the number of cylinders can be seen in the left plot in Figure 4.4, where the frequency is increased when increasing the number of cylinders.

4.2 Partial Stroke Displacement Strategy

In the PSDS the cylinders are activated in only a portion of the downstroke piston motion and deactivated in the remaining part. This section describes the transient and steady-state characteristics for both the PSDS 1 and the PSDS 2. The transient response is different for the two displacement strategies, but the steady-state response is the same.

4.2.1 Transient Response for the Partial Stroke Displacement Strategy 1

In PSDS 1, the cylinders can only have one active period during the downstroke piston motion. Hence, the motor needs to rotate in order to increase displacement, similar to the FSDS. Therefore, the step response is constant in the shaft position domain but will vary with shaft speed in the time domain. Figure 4.5 shows the step response in the shaft position domain. In the left plot, the displacement fraction is stepped up from 0.1 to 0.25,

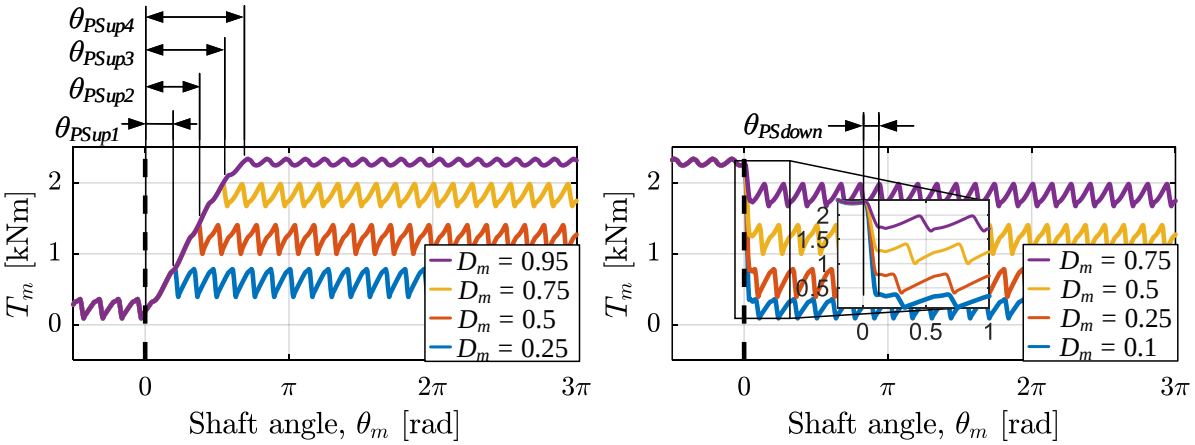

Figure 4.5: Transient response PSDS 1 in position domain.

0.5. 0.75 and 0.95. In the right plot, the displacement is stepped down from 0.95 to 0.75, 0.5, 0.25 and 0.1. The step is applied at $\theta_m = 0$ rad.

From the left plot, it can be seen that there is no delay before increasing the torque, but the step-up response angle is affected by the magnitude of the applied step. A small step gives a small response angle. In fact, the relation between a change in the state change angle, $\Delta\alpha$, and the response angle, θ_{PSup}, is 1:1, or $\Delta\alpha = \theta_{PSup}$.

It can be seen that the step-down response angle is much lower than the step-up response angle. The step-down response angle is affected both by the response time of the valves and the angle the shaft needs to rotate in order to decompress the cylinders. Assuming that the on/off valves are fast compared to the time it takes for the shaft to rotate the angle needed to decompress the oil, the response angle is approximately equal to $\theta_{PSdown} \approx \theta_{decomp}$, where θ_{decomp} is the decompression angle.

Figure 4.6 shows the step response in the time domain at various speeds. The left plot shows the step-up response when the displacement ratio is stepped from 0.1 to 0.95. The right plot shows the step-down response when the displacement ratio is stepped down from 0.95 to 0.1. It can be seen that the step-down response is much faster than the

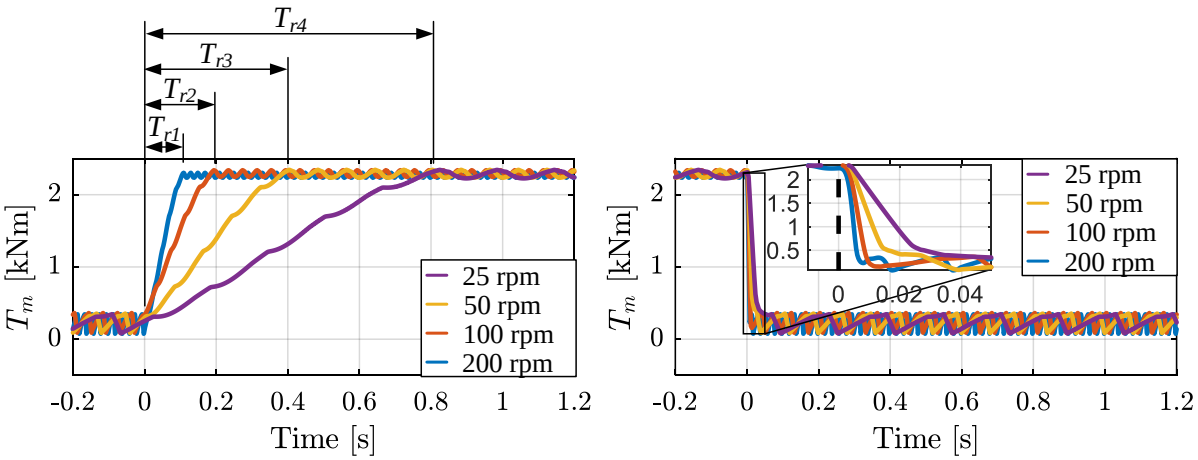

Figure 4.6: Transient response PSDS 1 in time domain operating at various speeds.

step-up response. Also, by comparing the step-up response times, marked with T_{r1}, T_{r2}, T_{r3} and T_{r4}, it can bee seen that the response time is inversely proportional to the speed. The step-up response time is equal to the time it takes to rotate the step-up response angle (θ_{PSup}). The step-down response time is equal to the time it takes to rotate the step-down response angle (θ_{PSdown}).

4.2.2 Transient Response for the Partial Stroke Displacement Strategy 2

In the PSDS 2, the cylinder chambers can be reactivated and have more than one active period during the downstroke piston motion. In PSDS 1, the step-up response time is much larger than the step-down response time. The PSDS 2 has the same step-down characteristics as PSDS 1, but the step-up characteristics are changed. With the PSDS 2, the step-up response time is much lower than for the PSDS 1 and it is not affected by the motor speed nor the magnitude of the displacement step. This is shown in Figure 4.7. The left plot shows a step response in the time domain when stepping up at various

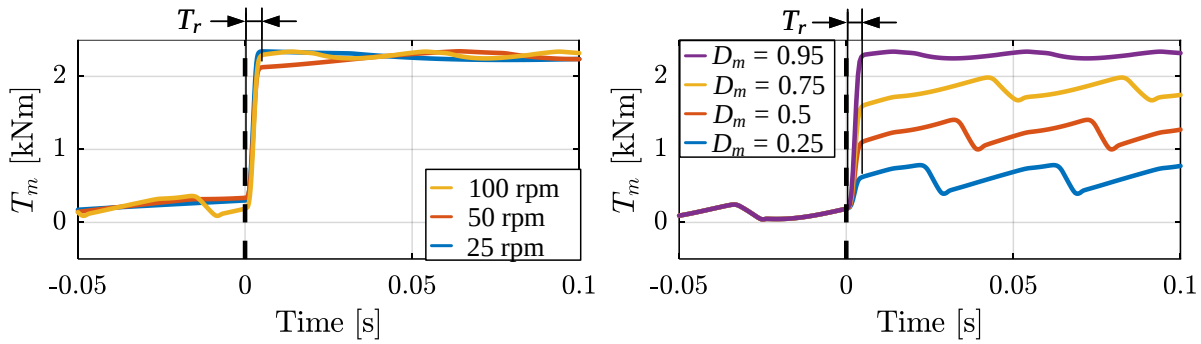

Figure 4.7: Transient response PSDS 2 in time domain at various speeds and displacement step up to various displacements.

speeds, and the right plot shows the step response in the time domain when stepping up to various displacement ratios with the shaft speed kept constant.

The left plot shows that the step-up response time is equal at various speeds. The step response is approximately equal to the response time of the on/off valves which in this simulation is $T_s = 5$ ms. The right plot shows that the response time is equal regardless of the magnitude of the displacement step, unlike the PSDS 1.

4.2.3 Steady-State Response for the Partial Stroke Displacement Strategy

The steady-state response for the PSDS 1 and PSDS 2 is the same and characterized by small ripples. The ripples occur because the cylinders are deactivated mid-stroke. The shape is constant in the shaft position domain, but the frequency will vary with the shaft speed in the time domain. Therefore, the steady-state torque shape is analyzed in the position domain.

The amplitude of the ripples is affected by the used displacement ratio and the displacement of the cylinders. The left plot in Figure 4.8 shows the steady-state torque at different displacement ratios, and the right plot shows the steady-state torque for DDMs

with a various number of cylinders and equal maximum motor displacement. Hence, the cylinder displacement is different in order to have the same maximum motor displacement. The left plot shows that maximum amplitude occurs when operating at 50 %

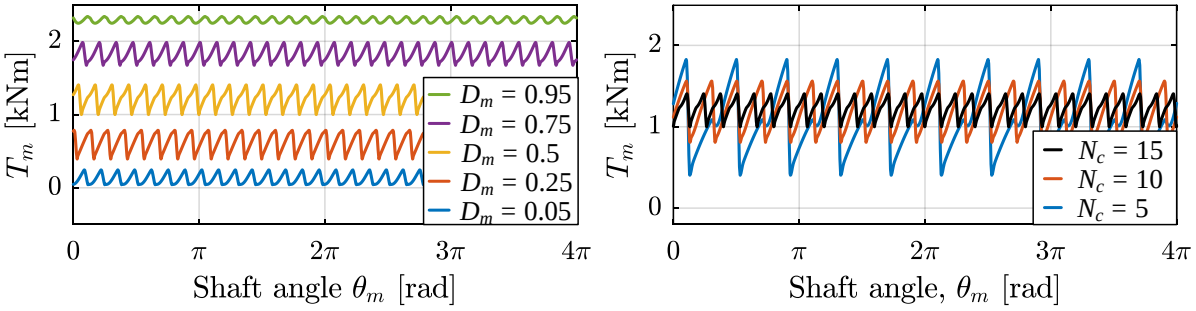

Figure 4.8: Steady-state response PSDS 1 and PSDS 2 at various displacements (left plot) and with various number of cylinders (right plot).

displacement. 50 % displacement corresponds to changing the cylinder state from active to inactive when $\theta_{cyl,i} = \pi/2$. From Equation 2.12, it can be seen that it is in this position, the torque contribution is at its highest. Therefore, deactivating a cylinder at this position, results in the highest possible torque ripple. The smoothest output torque occurs when operating with very high or very low displacement ratios, meaning that the valves are switched close to TDC or BDC where the torque contribution from each cylinder is low. From the right plot, it can be seen that the amplitude is reduced when the number of cylinders is increased. Meaning that the cylinder displacement is reduced and therefore also the torque contribution from each cylinder. The frequency of the ripples is increased when the number of cylinders is increased. The frequency of the torque ripples is also affected by the shaft speed. Increased shaft speed results in increased frequency. This can best be seen in the left plot in Figure 4.6.

4.3 Sequential Partial Stroke Displacement Strategy

In SPSDS the cylinders are activated in limited periods. The activation sequence is found by a search routine. This section presents the transient and steady-state response characteristics of a DDM operating with the SPSDS.

4.3.1 Transient Response for the Sequential Partial Stroke Displacement Strategy

The transient response of the SPSDS is constant in the time domain and affected by the response time of the on/off valves. The step-up and step-down response in the time

domain is shown in Figure 4.9 when operating at 100 rpm. The step-up and step-down response have no delay and are equal and independent of the magnitude of the step.

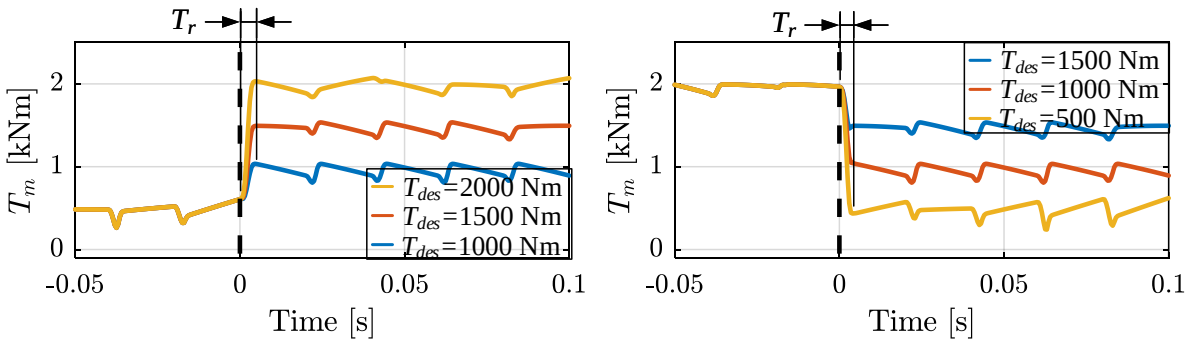

Figure 4.9: Transient response of the SPSDS in time domain.

Figure 4.10 shows the step response when the DDM is operating at different speeds, 100 rpm, 50 rpm and 25 rpm respectively. The results show that the step response time is not affected by the speed.

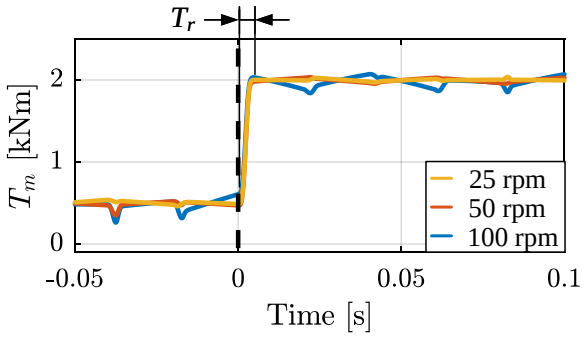

Figure 4.10: Transient response of the SPSDS in time domain when operating at various speeds.

4.3.2 Steady-State Response for the Sequential Partial Stroke Displacement Strategy

The steady-state torque tends to oscillate when operating with the SPSDS. The torque ripples are affected by the motor speed, the number of cylinders and also the update frequency of the controller. In Figure 4.11 the desired torque is set to 2000 Nm. The left plot shows the steady-state torque when the DDM is operating at various speeds, 100 rpm, 50 rpm and 25 rpm respectively. The results show that the amplitude of the torque ripples tend to increase with the shaft speed.

The middle plot in Figure 4.11 shows the steady-state torque for two motors with equal maximum motor displacement but a different number of cylinders. The red line shows the output torque from a 7 piston motor and the blue line shows the output torque

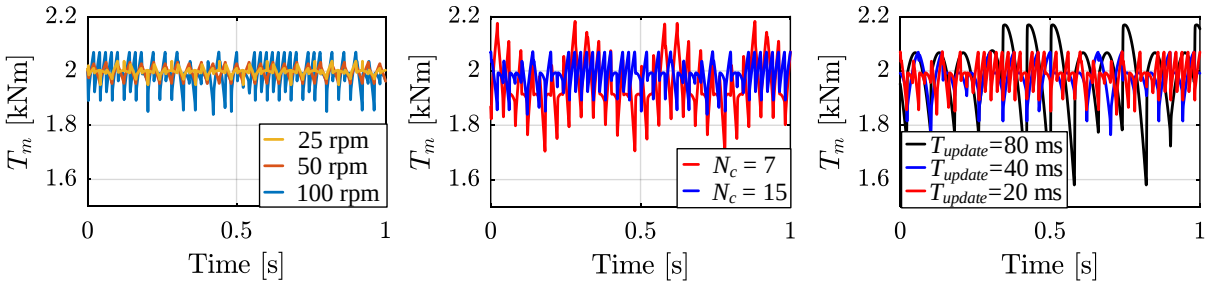

Figure 4.11: Steady-state response SPSDS at various shaft speeds (left plot), with various number of cylinders (mid plot) and various controller update frequencies (right plot).

from a 15 piston motor. It can be seen that the torque ripples are reduced when the number of cylinders is increased. This reduction in torque ripples occurs because the number of possible cylinder configurations is affected by the number of cylinders (2^{N_c}). By increasing the number of cylinders, the number of distinctive output levels will also be increased. Hence, the probability of finding a valve configuration that meets the desired output torque is increased.

The right plot in Figure 4.11 shows the steady-state torque when the controller update frequency varies. The controller update time is set to 80 ms for the black line, 40 ms for the blue line and 20 ms for the red line. A reduction in the torque ripples can be seen when the controller update time is changed from 80 ms and down to 40 ms. A further reduction in the torque ripples can be seen when the update time is decreased down to 20 ms. In addition the frequency of the torque ripples is increased when the valve controller is updated more frequently.

Both the left and right plot in Figure 4.11 show that it is beneficial with many controller updates per shaft revolution to reduce the amplitude of the torque ripples. Meaning that if the speed is high, the update time should be low. If the speed is reduced, the update time does not need to be that low.

The search routine used in this work is shown in Equation 2.17. Another search routine may also affect the torque ripples. It is not in the scope of this work to further investigate other search routines.

4.4 Discussion

In this section, the transient and steady-state response of the analyzed displacement strategies are discussed. In Figure 4.12, both the input signal and the output torque is plotted when a sinusoidal input signal with increasing frequency is given. The operation speed is set to 50 rpm. In order to be able to compare the output torque to the input signal, the values on the y-axis are normalized. The normalization is done by dividing the output torque and motor displacement by its maximum value, $T_m/T_{m,max}$ and $D_m/D_{m,max}$

respectively. The DDM is operating with the FSDS in Plot 1, the PSDS 1 in Plot 2, the PSDS 2 in Plot 3 and the SPSDS in Plot 4.

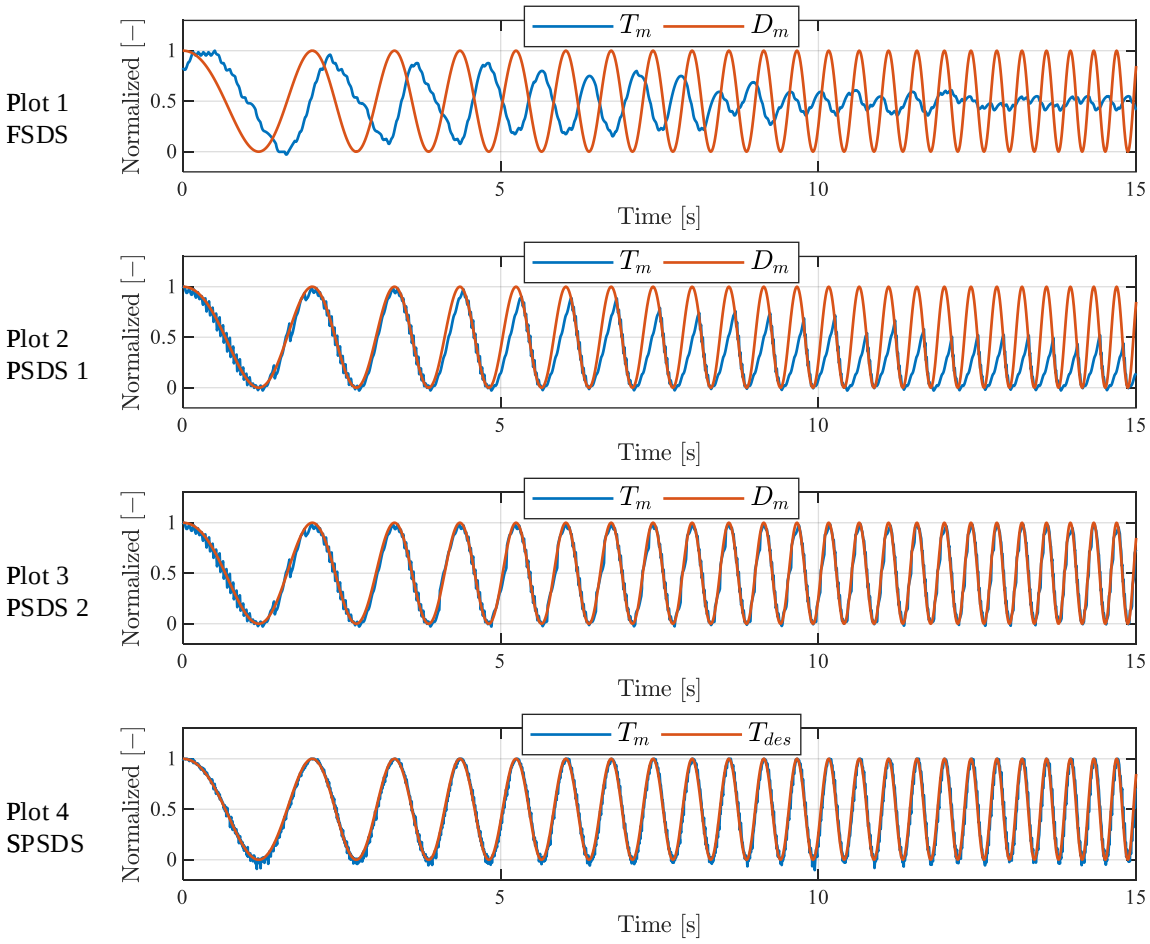

Figure 4.12: DDM torque response with a sinusoidal input signal operating at 50 rpm.

As shown earlier, the transient response when operating with FSDS is known to have a delay in the response. Also, the response time is highly affected by the operation speed. These effects can be seen in Plot 1. At low frequencies, the output torque is phase shifted to the input signal due to the delay. When increasing the frequency, the amplitude of the output torque starts to decrease because of the high response time at low operation speeds. By increasing the operation speed, the time delay will be reduced and the amplitude will reach 1 for a higher input frequency. Therefore, FSDS is most suited for use in high speed operations due to the delay in the transient response and the fact that the response time is highly affected by the speed.

The response time of the DDM when operating with the PSDS 1 is highly affected by the operation speed, similar to the FSDS. However, the response of the PSDS 1, shown in Plot 2 in Figure 4.12, is much better than for FSDS, especially at low input frequencies. This improvement is because the PSDS 1 does not have any delay and the step up response time is affected by the magnitude of the step. A small step has a low response time. The

PSDS 1 is also known to have much lower response time when stepping down compared to stepping up. This characteristic is seen when increasing the input frequency. The output torque follows the input signal in the torque reduction phase but rises too slow in the torque increasing phase. The output torque tends to oscillate with small ripples. The magnitude of the ripples can be reduced by increasing the number of cylinders. The frequency is affected both by the number of cylinders and the operation speed. A small number of cylinders will result in large magnitude of the ripples and should be avoided. Since the step-up response time is highly affected by the operation speed, this displacement strategy should only be used for medium and high speed operations. The controllability is considered to be higher than for the FSDS.

The PSDS 2 can have more than one active period in the downstroke piston motion. This feature results in a response time that no longer is affected by the operation speed but is closer to the response time of the on/off valves. The third plot in Figure 4.12 shows that the PSDS 2 has high controllability and follows the input signal very well, also at higher frequencies. The small torque ripples seen for the PSDS 1 can also be seen for the PSDS 2 (best seen at low input frequencies).

The SPSDS is characterized by frequent switchings. Plot 4 in Figure 4.12 shows that the output torque follows the input signal very well. The output torque has some small ripples. Those ripples are smaller than for the PSDS but will be increased if the speed increases, the number of cylinders is reduced or the controller update frequency decreases. The SPSDS is best suited for low operation speeds, because it is hard to keep the number of controller updates per shaft revolution high when the speed is high.

The main characteristics of the investigated displacement strategies are summarized in Table 4.2. In general, the FSDS and PSDS 1 have low controllability at low loads and are therefore most suited for high speed applications. The PSDS 2 and the SPSDS have high controllability at low operation speeds and are therefore suited for low speed applications.

Table 4.2: Summary of transient and steady-state characteristics.

		FSDS	**PSDS 1**	**PSDS 2**	**SPSDS**
Transient response	Delay-time	Some delay due to decision angle ahead of TDC	No delay	No delay	No delay
	Response time	Affected by shaft speed	Affected by shaft speed and displacement step	Affected by valve response time	Affected by valve response time
	Overshoot	No overshoot	No overshoot	No overshoot	No overshoot
Steady-state response	Magnitude of torque ripples	Affected by displacement ratio & number of cylinders	Affected by displacement ratio & number of cylinders	Affected by displacement ratio & number of cylinders	Affected by shaft speed, controller update rate & number of cylinders
	Frequency of torque ripples	Affected by shaft speed & number of cylinders	Affected by shaft speed & number of cylinders	Affected by shaft speed & number of cylinders	Affected by controller update rate

Chapter 5

Preliminary Winch Drive Study

A preliminary winch drive study was conducted at the beginning of this project. The preliminary study has two main focuses. The first focus is to investigate the potential of increasing energy efficiency in hydraulic winch drive systems by using digital displacement machines. Since digital displacement machines are known to have a pulsating output torque, the second focus is to examine if digital displacement machines can provide reasonable controllability of the winch. In order to examine if digital displacement machines can increase energy efficiency in winch drive systems, both a conventional and digital winch drive system is studied. Both winch drive systems are of the closed circuit type. Note that the winch drive system with digital hydraulic machines analyzed in this chapter is not the same as the system referred to as the digital displacement winch drive system described in Section 1.2. The digital displacement winch drive system analyzed in this chapter is referred to as the full digital displacement winch drive system. The work presented in this chapter is based in the work published in paper A and paper B.

A 20 tonnes winch with a drum capacity of 3600 m of wire is used as a case study. This chapter presents the preliminary winch drive study. First, the mechanical winch system is presented. Then, the conventional and full digital displacement winch drive systems are presented. Finally, the simulation results are presented and discussed.

5.1 Mechanical Winch System

The simulated winch system is shown in Figure 5.1. In this preliminary winch study, all lifting operations are conducted in air with a maximum traveling distance of 10 m and with a small amount of wire payed out. Since the simulated traveling distance is low, it is assumed that the inertia of the system is constant and that the entire lifting operation is conducted on only one wire layer. Since only one wire layer is used, the winch radius is considered to be constant. Since only a small amount of the wire is payed out,

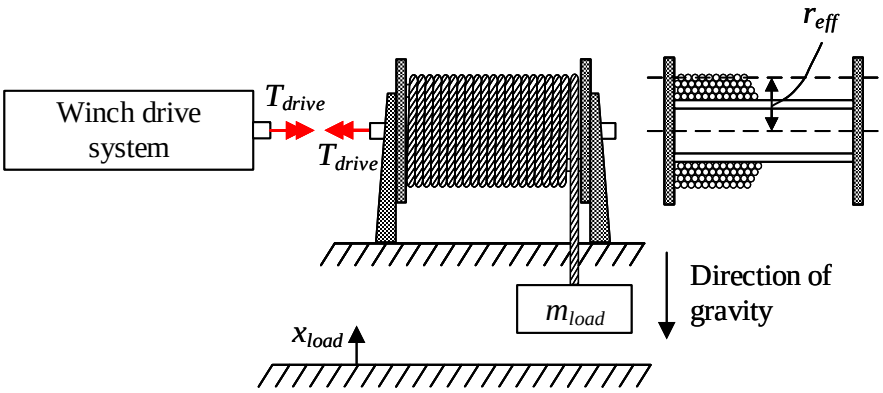

Figure 5.1: Illustration of mechanical winch system.

it is assumed that the wire elasticity is neglectable. Friction in the winch drum is also neglected.

The equation of motion for the winch drum is shown in Equation 5.1

$$\ddot{\theta}_d = \frac{T_{drive} - m_{load} \cdot g \cdot r_{eff}}{J_{eff}} \tag{5.1}$$

where T_{drive} is the drive torque acting on the winch drum, m_{load} is the mass of the payload, r_{eff} is the radius of the outer wire layer, g is the acceleration of gravity and J_{eff} is the effective mass moment of inertia relative to the drum shaft. The effective mass moment of inertia is calculated as shown in Equation 5.2:

$$J_{eff} = m_{load} \cdot r_{eff}^2 + J_{winch} + J_{drive} \tag{5.2}$$

where J_{winch} is the mass moment of inertia of the drum and the wire on the drum and J_{drive} is the mass moment of inertia of the winch drive system relative to the drum shaft. The driving torque, T_{drive}, for each drive system is given in the following two sections.

5.2 The Conventional Winch Drive System

The conventional winch drive system is a closed circuit system with one variable displacement over center axial piston pump and two variable displacement axial piston motors, as illustrated in Figure 5.2. There is also included a charge pump to ensure a minimum pressure in Line A and Line B. The pressure relief valve connected to Line A is included to avoid high pressures that may damage the system. The axial piston pump has a maximum displacement of 500 cc/rev and delivers working fluid to the two motors. Each motor has a maximum displacement of 250 cc/rev. The pump is driven at a constant speed of 1800 rpm and can deliver pressure up to 350 bar. The motor torque is transfered to the winch drum through a gearbox and a pinion and gear ring. The gear ring is mounted directly on the winch drum but this is not shown in Figure 5.2. The gearbox and the pinion and gear ring have a total gear ratio of 156.

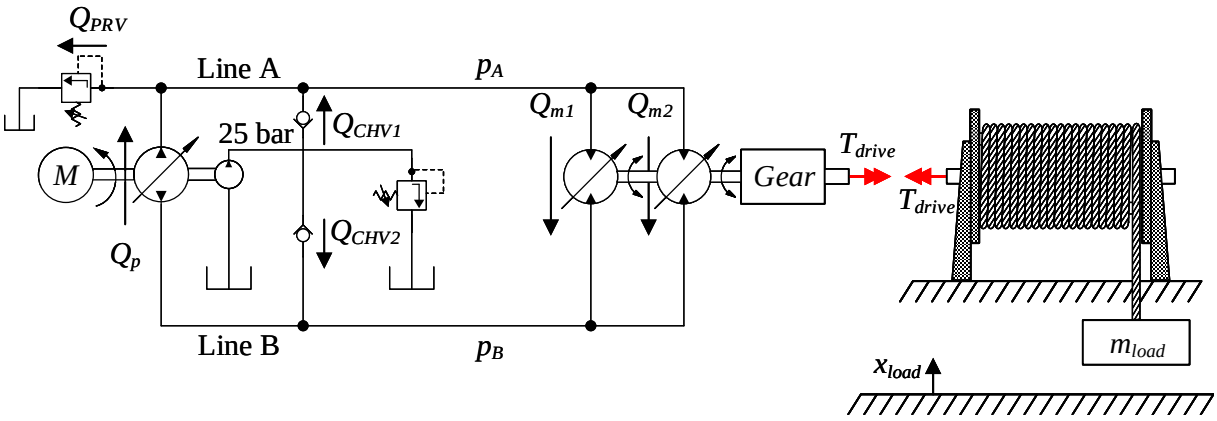

Figure 5.2: Illustration of conventional winch drive system.

5.2.1 Simulation Model

The driving torque acting on the winch drum is calculated as shown in Equation 5.3.

$$T_{drive} = 2 \cdot \frac{(p_A - p_B) \cdot V_{gm}}{2 \cdot \pi} \cdot i_{gear} \cdot \eta_{hmm} \cdot \eta_{gear} \tag{5.3}$$

where p_A is the pressure in Line A, p_B is the pressure in Line B, V_{gm} is the displacement of each motor ($V_{gm} = V_{gm1} = V_{gm2}$), i_{gear} is the total gear ratio of the gearbox and the pinion and gear ring, η_{hmm} is the hydromechanical efficiency of the motors and η_{gear} is the total efficiency of the gearbox and the pinion and gear ring. η_{gear} is in this study assumed to be 95 %. The hydromechanical efficiency is found by interpolation between measured data from a representative axial piston machine. The pressures in Line A and Line B are calculated by integrating the pressure gradients calculated in Equation 5.4 and Equation 5.5 respectively.

$$\dot{p}_A = \frac{\beta}{V_A} \cdot (Q_p - Q_{PRV} + Q_{CHV1} - Q_m) \tag{5.4}$$

$$\dot{p}_B = \frac{\beta}{V_B} \cdot (Q_m + Q_{CHV2} - Q_p) \tag{5.5}$$

where β is the effective bulk modulus of the oil, V_A is the volume in Line A, V_B is the volume in Line B, Q_p is the pump flow, Q_m is the summed motor flow ($Q_m = Q_{m1} + Q_{m2}$), Q_{PRV} is the flow through the pressure relief valve, Q_{CHV1} is the flow through check valve 1 and Q_{CHV2} is the flow through check valve 2. The bulk modulus is in this analysis assumed to be constant. The following equations describe the flow through the pump and the motors.

$$Q_p = \frac{\dot{\theta}_p \cdot V_{gp}}{2 \cdot \pi} \cdot \eta_{vp} \tag{5.6}$$

$$Q_m = 2 \cdot \frac{\dot{\theta}_m \cdot V_{gm}}{2 \cdot \pi} \cdot \frac{1}{\eta_{vm}} \tag{5.7}$$

where $\dot{\theta}_p$ is the shaft speed of the pump, $\dot{\theta}_m$ is the shaft speed of the motors, V_{gp} is the displacement of the pump, η_{vp} is the volumetric efficiency of the pump and η_{vm} is the volumetric efficiency of the motors. The volumetric efficiencies of the pump and motors are found by interpolation between measured data from a representable axial piston machine. The dynamic response of the pump and motors is described by a first order system.

$$\dot{V}_g = \frac{V_g - V_{gc}}{\tau} \tag{5.8}$$

where V_g is the current displacement of the machine, V_{gc} is the desired displacement and τ is the time constant.

5.2.2 Control System

The control strategy for the conventional winch drive system is to have an open loop controller for the motor and a closed loop controller for the pump. The main purpose for the open loop motor controller is to provide a motor displacement that keeps the pressure drop across the motors relatively close to a desired pressure drop. By ignoring leakage in the pump and motors and assuming that the flows in the pressure relief valve and the check valves are zero, the drum speed is proportional to the pump outlet if the displacement of the motors is kept constant. The main purpose of the closed loop pump controller is, therefore, to control the motion of the winch drum. The controller is illustrated in Figure 5.3.

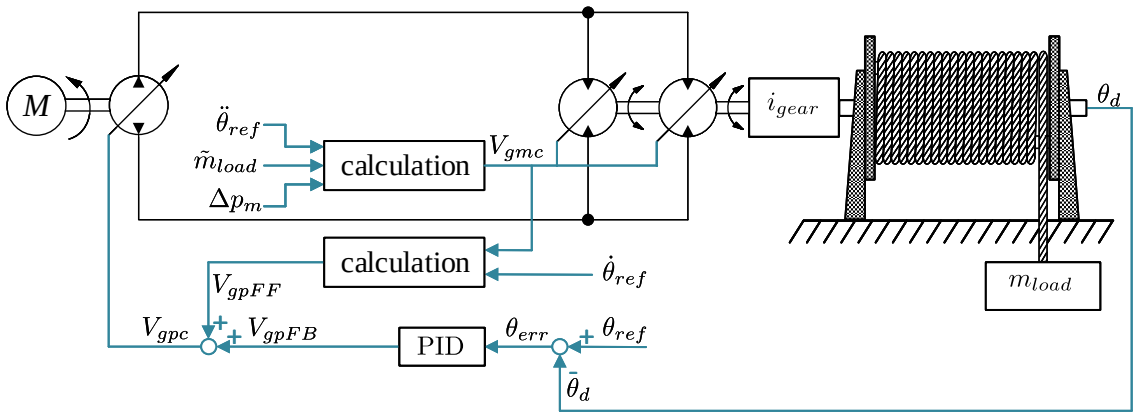

Figure 5.3: Illustration of control system for the conventional winch drive system.

The desired motor displacement, V_{gmc}, is calculated based on measured values of the payload, $\tilde{m}_{load}$, a reference acceleration of the winch drum, $\ddot{\theta}_{ref}$, and a desired pressure drop across the motor Δp_m, as shown in Figure 5.3 and in Equation 5.9.

$$V_{gmc} = \frac{(\ddot{\theta}_{ref} \cdot J_{eff} + \tilde{m}_{load} \cdot g \cdot r_{eff}) \cdot 2 \cdot \pi}{\Delta p_m \cdot i_{gear}} \cdot \frac{1}{2} \tag{5.9}$$

The term $\frac{1}{2}$ occurs because the drive systems have two motors and V_{gmc} is the desired displacement for each of the motors.

The closed loop pump controller has a position feedback controller and a feedforward controller. Assuming that the motors have no leakage the feedforward reference flow can be calculated based on Equation 5.7 as shown in Equation 5.10.

$$Q_{ref} = \frac{\dot{\theta}_{ref} \cdot i_{gear} \cdot V_{gmc}}{\pi} \tag{5.10}$$

By rearranging Equation 5.6, the feedforward signal, V_{gpFF}, can be calculated as

$$\begin{aligned} V_{gpFF} &= \frac{2 \cdot \pi \cdot Q_{ref}}{\dot{\theta}_p} \\ &= \frac{2 \cdot \left(\dot{\theta}_{ref} \cdot i_{gear} \cdot V_{gmc}\right)}{\dot{\theta}_p} \end{aligned} \tag{5.11}$$

The feedback control signal for the pump is calculated by

$$V_{gpFB} = \theta_{err} \cdot k_p + \dot{\theta}_{err} \cdot k_d + \int \theta_{err} \cdot k_i \ dt \tag{5.12}$$

where θ_{err} is the position error of the winch drum and k_p, k_d and k_i are the controller gains for the PID-controller. Finally the desired pump displacement is calculated as shown in Eq. 5.13.

$$V_{gpc} = V_{gpFB} + V_{gpFF} \tag{5.13}$$

5.3 The Full Digital Displacement Winch Drive System

This section presents the simulation model and the control system for the full digital displacement system. The full digital displacement winch drive system consists of a high speed digital displacement pump (DDP) and a low speed digital displacement motor (DDM) connected in a closed circuit system as shown in Figure 5.4. The low speed DDM is directly connected to the winch drum without any gearing. The DDP is driven at a constant speed of 1800 rpm. Two gas accumulators are connected to each line, Line A and Line B, in order to smooth out any flow and pressure peaks. The DDP and DDM are two radial piston type machines with 9 and 42 cylinders respectively. Both the pump and the motor are operating with the full stroke displacement strategy.

5.3.1 Simulation model

The DDP and the DDM are simulated based on the single cylinders shown in Figure 5.5. The left illustration shows cylinder number i in the DDP and the right illustration shows

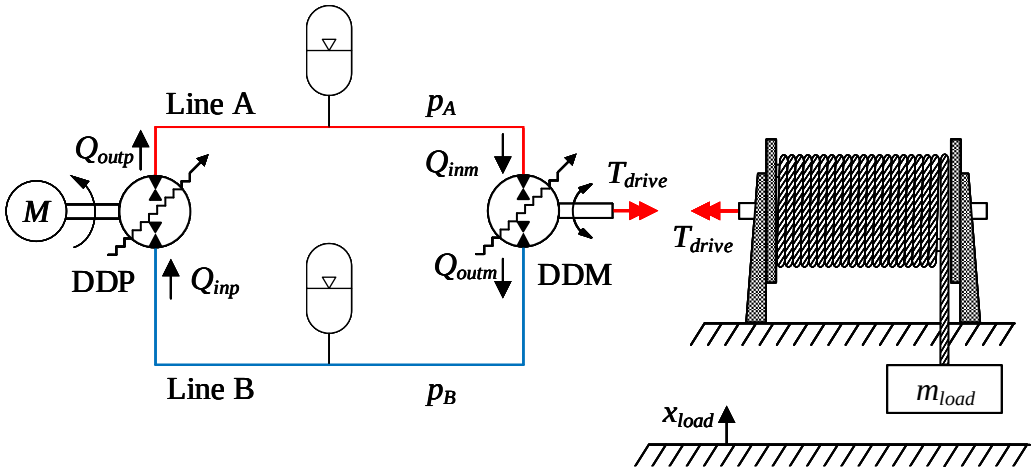

Figure 5.4: Illustration of the full digital displacement winch drive system.

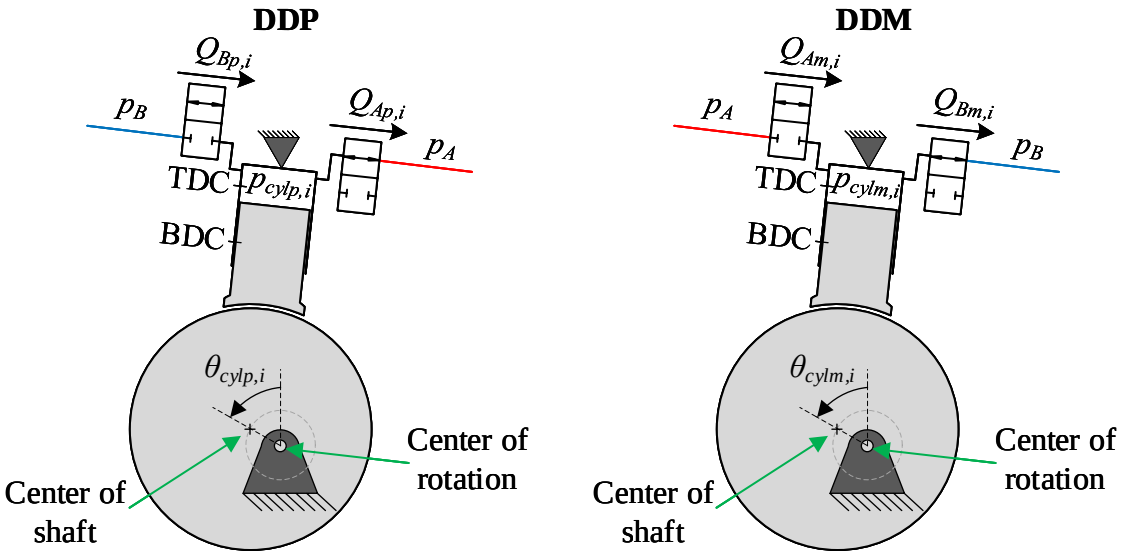

Figure 5.5: Illustration of cylinder number i in the DDP (left) and DDM (right).

cylinder number i in the DDM. The simulation model of the DDP and DDM is built up by the same principle as shown in Section 2.1, except that in this preliminary study, the bulk modulus is assumed to be constant. The input and output flows from the digital displacement machines, illustrated in Figure 5.4 and Figure 5.5, are given by:

$$Q_{inp} = \sum_{i=1}^{9} Q_{Bp,i} \tag{5.14}$$

$$Q_{outp} = \sum_{i=1}^{9} Q_{Ap,i} \tag{5.15}$$

$$Q_{inm} = \sum_{i=1}^{42} Q_{Am,i} \tag{5.16}$$

$$Q_{outm} = \sum_{i=1}^{42} Q_{Bm,i} \tag{5.17}$$

and the driving torque is given by:

$$T_{drive} = \sum_{i=1}^{42} T_{cylm,i} \tag{5.18}$$

The pressure build up in pressure Line A is calculated as shown in Equation 5.19.

$$\dot{p}_A = \frac{\beta}{V_A} \cdot \left(Q_{outp} - Q_{inm} - \dot{V}_{accA} \right) \tag{5.19}$$

where V_A is the volume in Line A and accumulator A and $\dot{V}_{accA}$ is the rate of change of the accumulator volume. $\dot{V}_{accA}$ is positive if the volume is expanding and is calculated as shown in Equation 5.20

$$\dot{V}_{accA} = \dot{p}_A \cdot \frac{V_{accAg}}{n_{accA} \cdot p_A} \tag{5.20}$$

where V_{accAg} is the gas volume in accumulator A and n_{accA} is the polytropic exponent. By substituting Equation 5.20 into Equation 5.19, the pressure dynamics in Line A can be expressed as shown below.

$$\dot{p}_A = \frac{\beta}{V_A} \cdot \frac{Q_{outp} - Q_{inm}}{1 + \frac{\beta \cdot V_{accAg}}{V_A \cdot n_{accA} \cdot p_A}} \tag{5.21}$$

The pressure dynamics in Line B is calculated in the same manner as for Line A and is shown in Equation 5.22.

$$\dot{p}_B = \frac{\beta}{V_B} \cdot \frac{Q_{outm} - Q_{inp}}{1 + \frac{\beta \cdot V_{accBg}}{V_B \cdot n_{accB} \cdot p_B}} \tag{5.22}$$

5.3.2 Control system

The control system for the full digital displacement winch drive system is divided into two, similarly as for the conventional winch drive system, with an open loop motor controller and a closed loop pump controller. The main purpose for the open loop motor controller is to keep a desired pressure drop across the DDM. The main purpose for the closed loop pump controller is to control the motion of the winch drum. The control structure is illustrated in Figure 5.6.

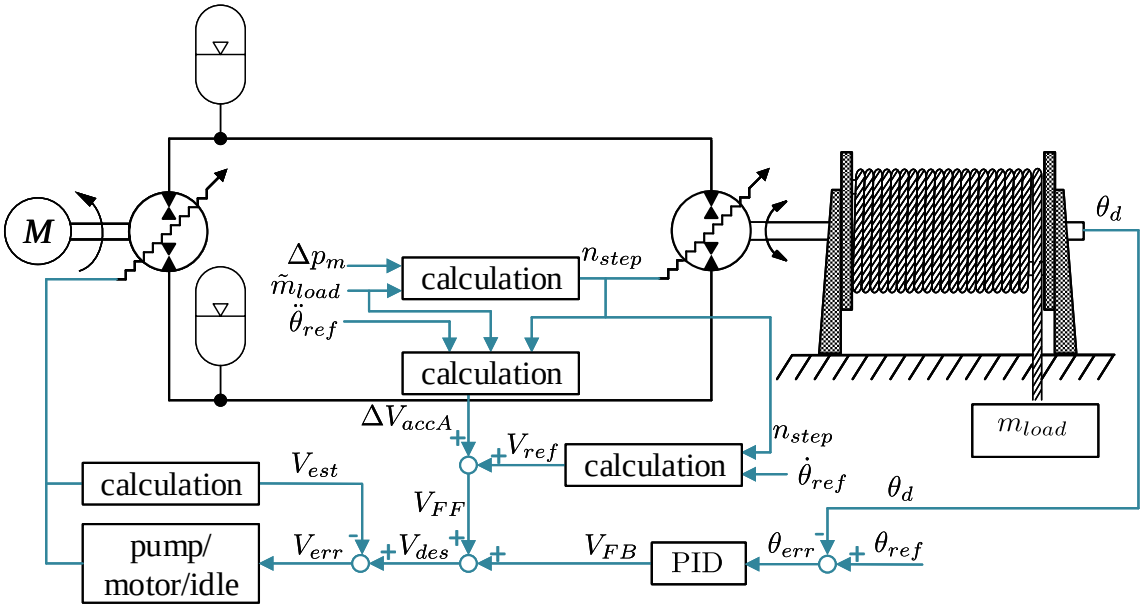

Figure 5.6: Illustration of the control structure for the full digital displacement winch drive system.

Motor controller

The output of digital displacement machines is known to pulsate. In order to ensure a relatively smooth output torque, the 42 cylinders in the DDM are divided into 14 packages or cylinder banks with three cylinders in each bank. The three cylinders in each bank are equally spaced around the shaft. This principle is illustrated in Figure 5.7 where a 6 cylinder motor is divided into two cylinder banks, one bank marked with yellow pistons and one with green pistons.

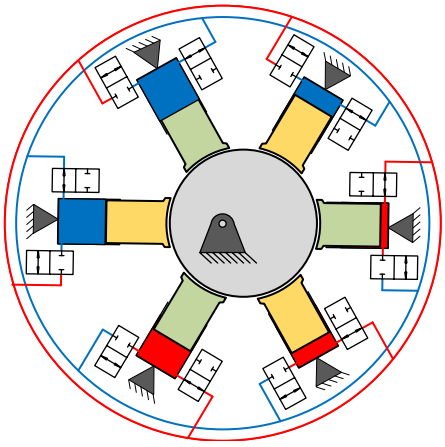

Figure 5.7: Illustration of a 6 cylinder digital displacement machine divided into two cylinder banks with 3 cylinders in each bank. One of the cylinder banks is marked with yellow pistons and the other bank is marked with green pistons.

The open loop motor controller controls the number of cylinder banks that shall be active. The number of active banks, also called n_{step}, is calculated based on measurements

of the payload, $\tilde{m}_{load}$, and a desired pressure drop across the DDM, Δp_m, as shown in Equation 5.23

$$n_{step} \approx \frac{T_{load,est}}{T_{cylbank}} = \frac{\tilde{m}_{load} \cdot g \cdot r_{eff}}{\Delta p_m \cdot T_{step}}, \qquad \text{round off to nearest integer} \tag{5.23}$$

where T_{step} is the torque delivered from one bank with a pressure drop of 1 Pa across the machine. $n_{step} = 1$ corresponds to one active bank, $n_{step} = 2$ corresponds to two active banks and so on.

Pump controller

The pump controller is based on the displacement controller first introduced in [41]. The controller is mainly developed for use in DHPMSs but can also be used in DDPs. The controller estimates the desired volume the pump shall deliver and the volume the pump has delivered. If the desired volume is more than a half piston displacement higher than the delivered volume, the next cylinder is set to pump. If the desired volume is more than a half piston displacement below the delivered volume, the next cylinder is set to motor. If the displacement error is in between, the next cylinder is deactivated. This control strategy is illustrated in Figure 5.8, where V_{des} is the desired volume, V_{est} is the delivered volume and V_{dp} is the piston displacement in one of the cylinders in the DDP.

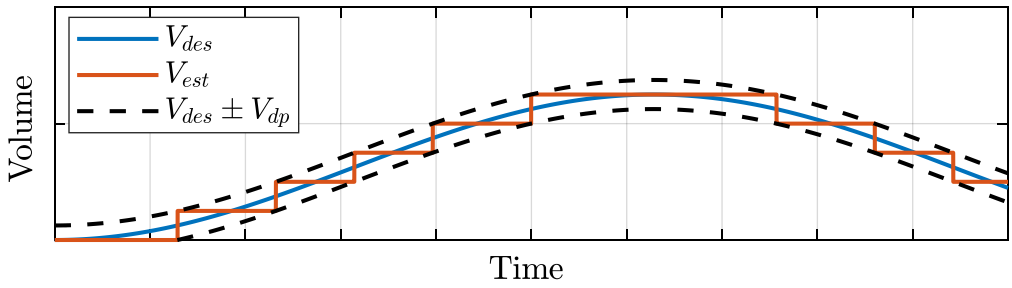

Figure 5.8: Example of the DDP displacement controller.

When the delivered volume, V_{est}, is stepped up, the DDP is pumping and delivers fluid to Line A. When V_{est} is stepped down, the DDM is motoring and removes fluid from Line A.

The already delivered volume is estimated based on the piston displacement, V_{dp}, and the number of cylinders that already have been pumping, n_{pump}, and motoring, n_{motor}.

$$V_{est} = (n_{pump} - n_{motor}) \cdot V_{dp} \tag{5.24}$$

In a real system, it is reasonable to assume that there will be leakage in the DDP and DDM. In order to account for this, an integral term can be added when designing the desired volume, V_{des}.

In this study, the desired volume is the sum of a feedforward signal, V_{FF}, and a feedback signal V_{FB}. The feedforward signal consists of two parts, V_{ref} and ΔV_{accA}, and is calculated as shown in Equation 5.25.

$$V_{FF} = V_{ref} + \Delta V_{accA} \tag{5.25}$$

where V_{ref} is called the reference volume and is the volume the motor needs to displace to follow the reference position of the drum. The reference volume is estimated based on the reference speed of the drum and the known displacement of the DDM. V_{ref} is calculated by integrating Equation 5.26.

$$\dot{V}_{ref} = \frac{V_{dm} \cdot n_{step} \cdot 3 \cdot \dot{\theta}_{ref}}{2 \cdot \pi} \tag{5.26}$$

where V_{dm} is the piston displacement for one of the cylinders in the DDM and $\dot{\theta}_{ref}$ is the reference speed of the drum. The DDM will normally be running at a constant displacement. In order to accelerate and decelerate the payload, the pressure in Line A has to be increased or decreased. When changing the pressure in Line A, the accumulator volume will also change. The second part in the feedforward controller accounts for variations in the accumulator volume when accelerating and decelerating the payload. This volume change is called ΔV_{accA} and is calculated in Equation 5.27

$$\Delta V_{accA} = \frac{\Delta p_A \cdot V_{accAg0}}{n_{accA} \cdot p_{A0}} \tag{5.27}$$

where p_{A0} is the initial pressure in Line A, V_{accAg0} is the gas volume in accumulator A at the initial pressure p_{A0} and Δp_A is the change in pressure in order to accelerate or decelerate the payload. Δp_A is calculated as shown in Equation 5.28.

$$\Delta p_A = \frac{\ddot{\theta}_{ref} \cdot J_{eff}}{T_{step} \cdot n_{step}} \tag{5.28}$$

The feedback volume is calculated by Equation 5.29.

$$V_{FB} = \theta_{err} \cdot k_p + \dot{\theta}_{err} \cdot k_d + \int \theta_{err} \cdot k_i \ dt \tag{5.29}$$

The decision of either pumping or idling the next cylinder is taken by evaluating Equation 5.30

$$V_{err} = V_{des} - V_{est} \quad \Rightarrow \quad \begin{cases} \text{pumping} & \text{if} \quad V_{err} > V_{dp}/2 \\ \text{idling} & \text{if} \quad -V_{dp}/2 \leq V_{err} \leq V_{dp}/2 \\ \text{motoring} & \text{if} \quad V_{err} < -V_{dp}/2 \end{cases} \tag{5.30}$$

5.4 Simulation Results

The simulation results are presented in two parts. The first part compares the conventional winch drive system and the full digital displacement winch drive system from an energy efficiency point of view. The second part examines the controllability of the full digital displacement system. Recall that in this study, the wire elasticity is neglected. The payload motion has therefore a linear relation to the drum motion. Hence, $x_{load} = \theta_d \cdot r_{eff}$. To get a clearer understanding of the simulation results, only the payload motion is plotted and not the drum motion.

The simulation parameters can be found in paper A.

5.4.1 Energy Efficiency Considerations

The energy consumption of the two systems are evaluated for operation with two different load cases. In the first load case, the mass of the payload is set to 18000 kg. The payload is lifted 10 m. The velocity is ramped up to 1 m/s with a ramp time of 2 s. In the second load case, the mass of the payload is set to 4000 kg and the payload's velocity is ramped up to 1.5 m/s with a ramp time of 3 s. The two load cases are summarized in Table 5.1.

Table 5.1: Load cases.

	Load Case 1	Load Case 2
Mass of load	18000 kg	4000 kg
Hoisting distance	10 m	10 m
Max speed	1 m/s	1.5 m/s
Ramp time	2 s	3 s

The input and output power is calculated as shown below.

$$P_{in} = T_{El} \cdot \dot{\theta}_p \tag{5.31}$$

$$P_{out} = T_{drive} \cdot \dot{\theta}_d \tag{5.32}$$

where T_{El} is the torque needed to drive the pump, $\dot{\theta}_p$ is the pump speed, T_{drive} is the driving torque acting on the winch drum and $\dot{\theta}_d$ is the drum speed. The losses are found by subtracting the output power from the input power, $P_{loss} = P_{in} - P_{out}$.

Load Case 1

Figure 5.9 shows the simulation results of the payload position, payload speed and the tracking error for the conventional winch drive system (CWD), left hand side, and the full digital displacement winch drive system(FDWD), right hand side. The sub-plots from

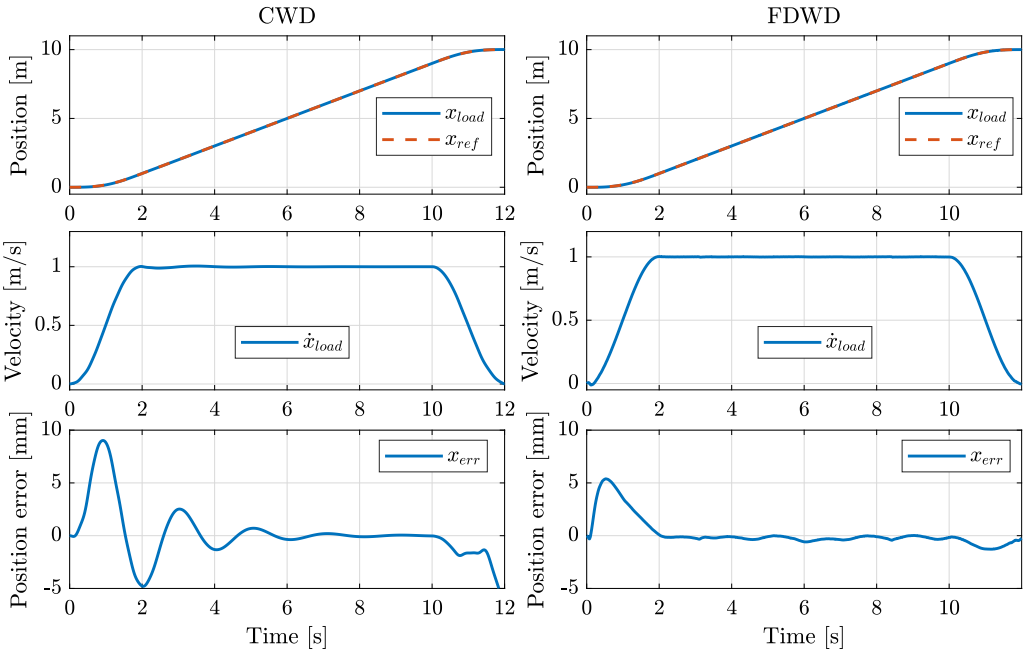

Figure 5.9: Simulation results for load case 1.

top to bottom show the simulated payload position together with the reference position, the load speed and finally the position error. The simulated payload position follows its reference position well, both for the CWD and the FDWD. The largest tracking error occurs when accelerating the load and is 9 mm for the CWD and 5.4 mm for the FDWD. The tracking error for both the CWD and the FDWD is close to zero when the winch runs with constant speed.

Figure 5.10 shows the simulation result of the power and energy consumption. The

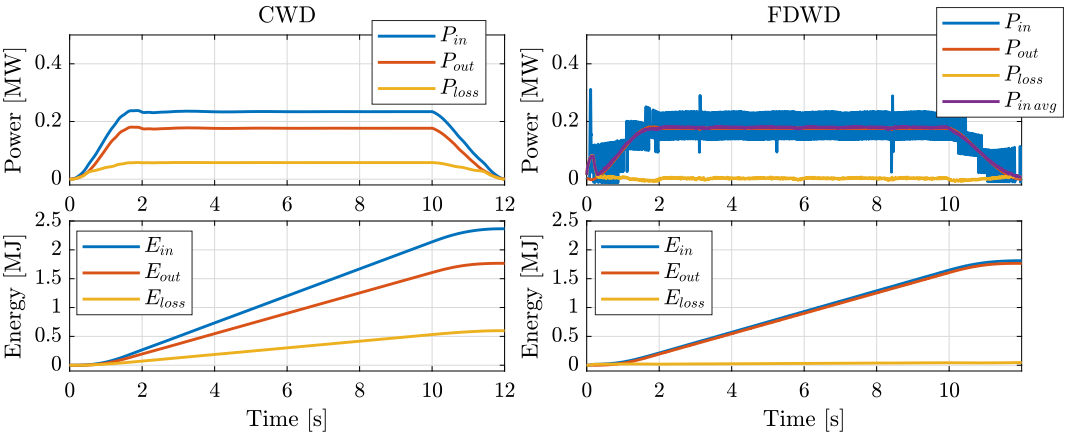

Figure 5.10: Simulation results for power and energy consumption in load case 1.

top sub-plots show the input power, output power and the power losses of the hydraulic system and the bottom sub-plots show the input energy, output energy and the energy losses. The purple line in the top right plot is a filtered version of the input power, blue line.

When driving with constant speed of 1 m/s and a payload equal to 18000 kg, the input power to the CWD is approximately 234 kW and the output power is approximately 176 kW, resulting in a loss equal to 58 kW. The input power to the FDWD is heavily oscillating because of the nature of the DDP. The DDP enables and disables pistons on a stroke by stroke basis which results in the input power oscillations. The same peaks occur in the pump flow, but the accumulators connected to line A and B smooth out the peaks. The mean input power to the FDWD when operating at constant speed is 181 kW and the mean loss is only 5 kW.

In the bottom sub-plots in Figure 5.10, it can be seen from the yellow line that the energy losses are much larger for the CWD than for the FDWD. The total energy consumed by the CWD is 2365 kJ and the loss is 599 kJ which results in a total system efficiency equal to 75 %. The total system efficiency for the FDWD is 97 % where the total consumed energy is 1813 kJ and the energy loss is only 47 kJ.

Load Case 2

Figure 5.11 shows the simulation results of the payload position, payload speed and tracking error for the CWD, left hand side, and the FDWD, right hand side. The results show

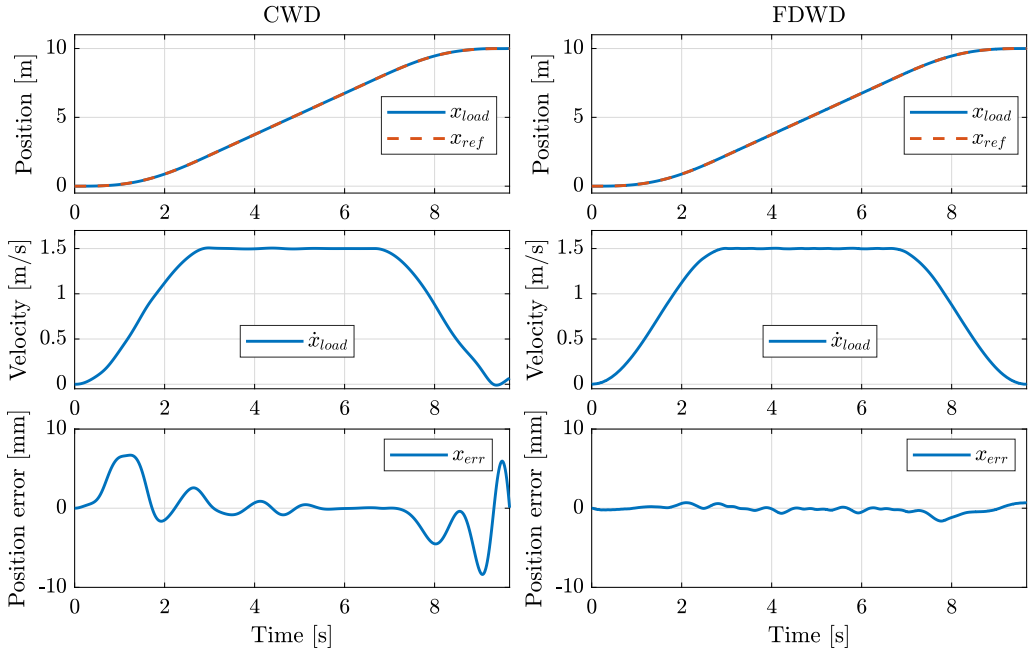

Figure 5.11: Simulation results for load case 2.

that both drive systems follow their position and speed references well. The position error for the CWD tends to oscillate when accelerating and decelerating the load but stabilizes around zero when running at constant speed. The largest tracking error for the CWD is -8.4 mm and only -1.6 mm for the FDWD.

Figure 5.12 shows the power and energy consumption. The results show that the input

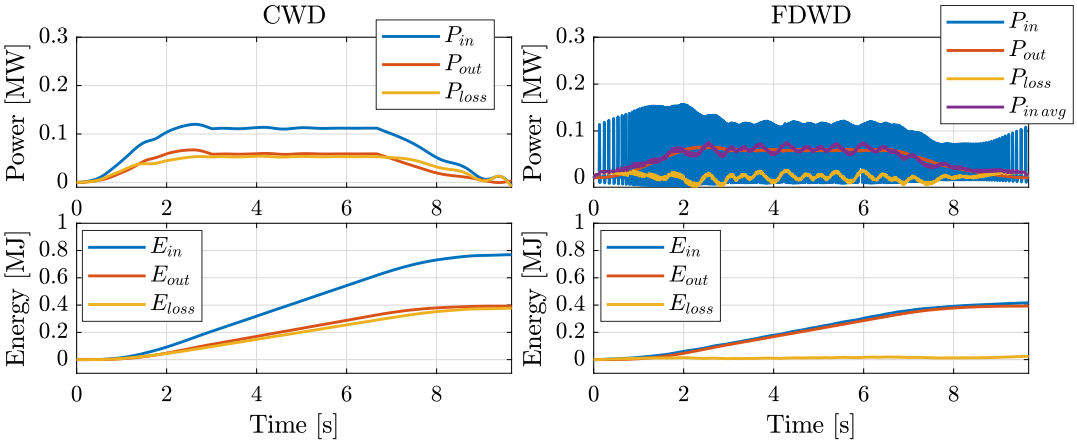

Figure 5.12: Simulation results for power and energy consumption in load case 2.

power to the CWD is approximately 112 kW and the output power is 59 kW when driving with a constant speed of 1.5 m/s. For the FDWD the input power is heavily oscillating, but the mean value is approximately 61 kW. The total consumed energy for the simulated trajectory is 769 kJ for the CWD and only 417 kJ for the FDWD. The losses are 377 kJ for the CWD and only 25 kJ for the FDWD. This gives a total efficiency for the entire simulated trajectory equal to 51 % for the CWD and 94 % for the FDWD.

Discussion

In this section, the presented results are summarized and further discussed. Some of the most important results are summarized in Tab. 5.2 The total system efficiency for the

Table 5.2: Energy efficiency considerations summarized results.

	Load case 1		**Load case 2**	
	CWD	FDWD	CWD	FDWD
Input power at constant speed	234 kW	181 kW	112 kW	61 kW
Power losses at constant speed	58 kW	5 kW	50 kW	1 kW
Total energy consumed	2365 kJ	1813 kJ	769 kJ	417 kJ
Total energy losses	599 kJ	47 kJ	377 kJ	25 kJ
Total efficiency	75 %	97 %	51 %	94 %
Largest tracking error	9 mm	5.4 mm	-8.4 mm	-1.6 mm

CWD is 75 % in load case 1 and 51 % in load case 2 and the maximum position error is 9 mm and -8.4 mm respectively. The CWD has 24 percent points higher efficiency when operating with the heavy load compared to the light load. The energy efficiency for the FDWD is also higher when operating with the heavy load, but the change in efficiency is not that big. When reducing the load from 18000 kg down to 4000 kg, the efficiency for the FDWD is reduced by only 3 percent points. When operating with constant speed,

the position error for the CWD tends to converge towards zero, while the position error for the FDWD tends to oscillate with a small amplitude. These small oscillations are affected by control parameters, accumulator properties and the number of pistons in the DDP and the DDM.

The FDWD consumes approximately 550 kJ less than the CWD when operating load case 1. If the same load was supposed to be hoisted 3000 m, the FDWD would use 165 MJ less energy than the CWD. For one short lifting operation, the saved energy is not that much, but for a winch that is frequently used over time and with long lifting distances, the savings can be significant.

This study shows that there is a significant improvement in efficiency when using the FDWD. Neither leakage and friction losses in the DDP and the DDM nor power consumption of the on/off valves are included in this study. The real efficiency will therefore be lower than for the simulated system. Because the increase in efficiency is so high, especially when operating small loads, and knowing that previous studies show that digital hydraulic units have high efficiency for a wide range of operations [15], it is realistic to expect that the efficiency for the FDWD will remain significantly higher than CWD even when all losses are included.

5.4.2 Feasibility study

The feasibility of the FDWD is evaluated by conducting various relevant test cases. For a winch, it is obviously important to be able to hoist and lower a payload. The ability to hoist a heavy and light payload has already been shown in Figure 5.9 and Figure 5.11. The ability to lower a payload is shown in the first test case in this section. Since the cylinders in the DDP and the DDM are activated and deactivated, the output flow and output torque can be pulsating, especially when running with very low displacements. Therefore, the second test case presents results where a light payload is hoisted at a very low speed. In the third test case, an error in measurements of the mass of the payload is introduced to investigate the robustness of the controller. Normally, the same motor displacement can be used during short lifting operations, but for longer lifting operations it can be appropriate to change displacement due to changes in the load acting on the winch drum. The load acting on the winch drum can, for example, change when lifting a payload into or out of the water. In the last test case, the simulation results show the effect of changing motor displacement during a hoisting situation.

Lowering of a payload

Figure 5.13 shows the simulation results when lowering a payload equal to 18000 kg a distance of 10 m. The velocity of the load is ramped down to -1 m/s with a ramp time of

2 s. When lowering the load, the DDP acts like a motor and the DDM acts like a pump.

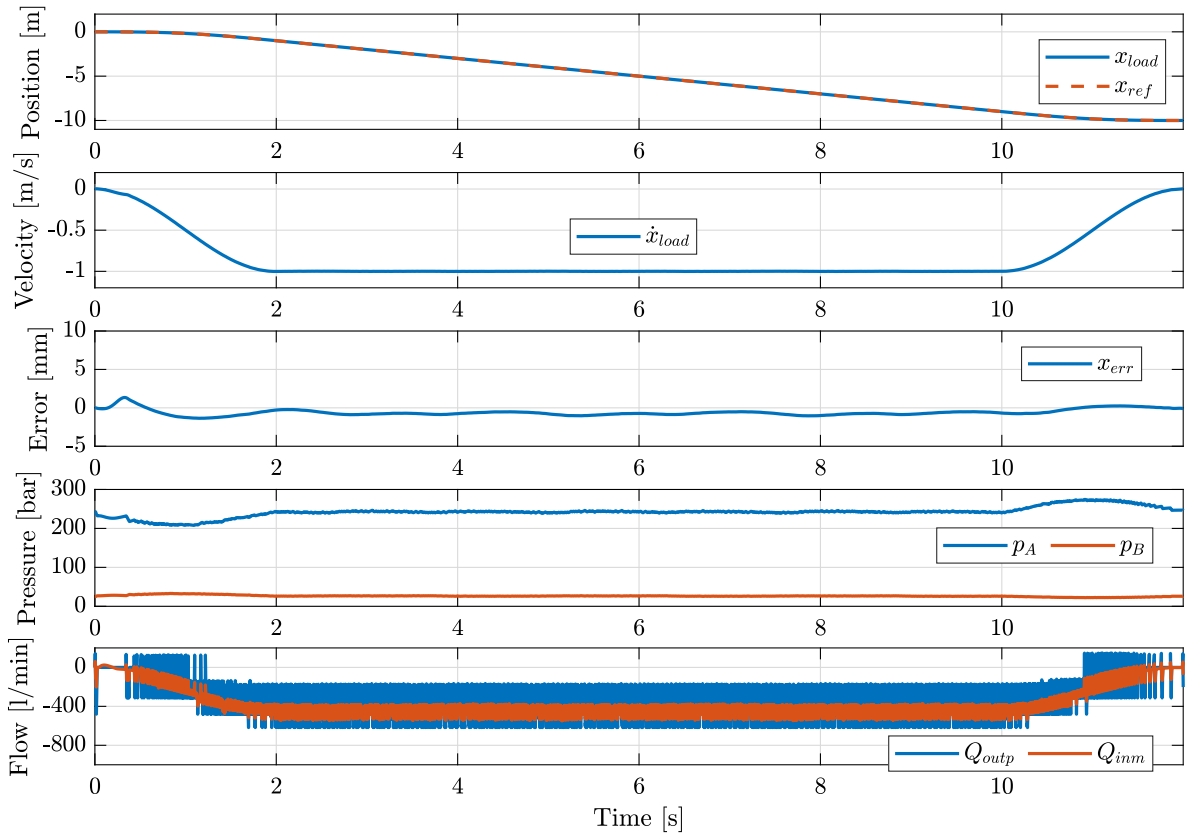

Figure 5.13: Simulation results of lowering with $m_{load} = 18000$ kg.

The simulation results show that the payload follows the reference position well. The tracking error is kept below 1.5 mm for the entire test case.

Hoisting light payloads at low speed

Every single cylinder in the DDP is controlled individually on a stroke by stroke basis, which results in flow ripples when running at partial displacements. In the closed circuit system studied in this analysis, two accumulators are connected to Line A and Line B to smooth out flow and pressure ripples. However, one critical scenario is when the required pump flow is low. This scenario occurs when the speed and the payload's mass is low. Therefore, in this test, the payload is set to 4000 kg and maximum speed is set to 0.2 m/s. The payload is hoisted 5 m and the speed is ramped up to 0.2 m/s in 2 s. Figure 5.14 shows the simulation results.

The results do not show any oscillations in the payload velocity. The payload follows the reference trajectory well with the tracking error less than 2 mm. The tracking error is close to 0 mm when the winch runs with constant speed. The simulated pump flow shows that there are times where no cylinders are pumping, $Q_{outp} = 0$ l/min. The average frequency of pumping cylinders is only 7 Hz.

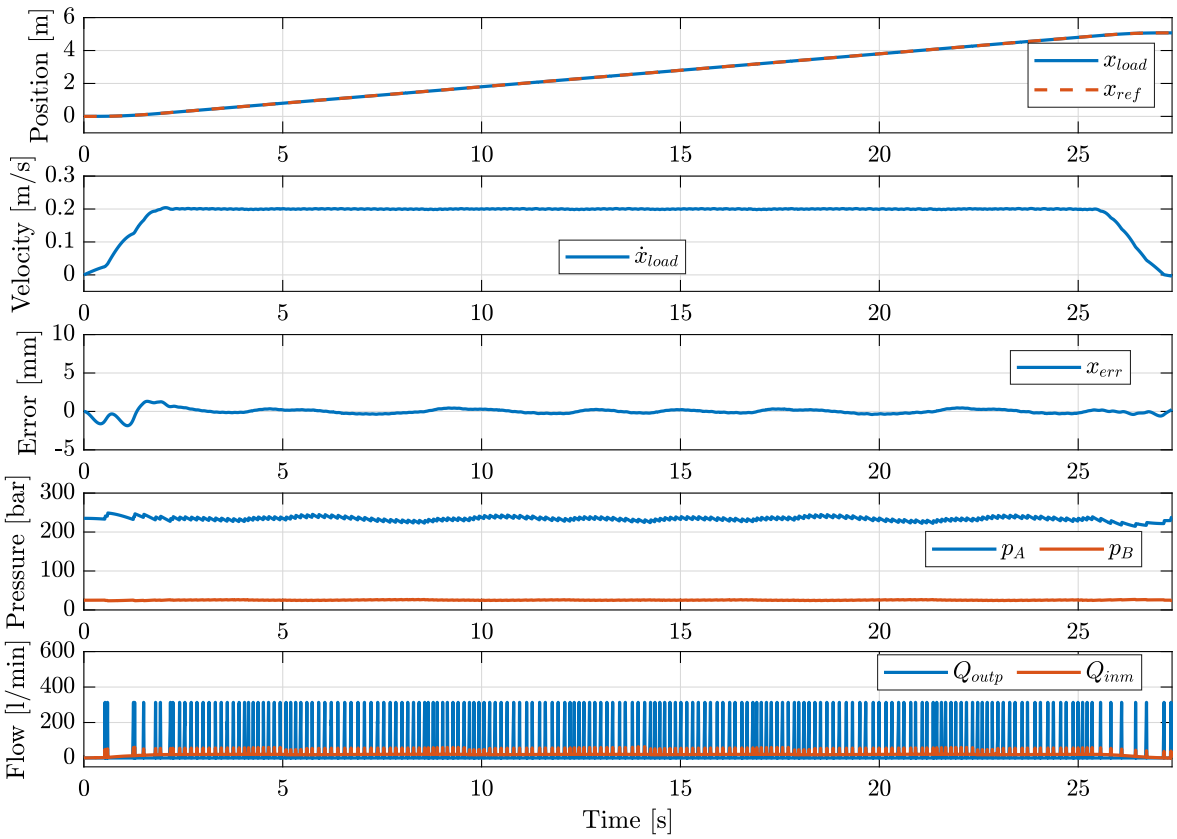

Figure 5.14: Simulation results of hoisting with a light payload at low speed, $v_{max} = 0.2$ m/s and $m_{Load} = 4000$ kg.

Error in load measurement

The motor displacement is calculated based on a desired pressure drop across the motor and measurements of the payload. In this test, an error in the payload measurements is introduced to investigate the robustness of the control system. The actual payload is set to 18000 kg, but the measured value used in the controller is only 80 % af the actual load. The payload is hoisted 10 m and the velocity is ramped up to 1 m/s with a ramp time of 2 s. The simulation results are shown in Figure 5.15.

This test case is similar to the case shown in Figure 5.9 except for the error in the load measurements. The simulation results show that an error in the payload measurements gives almost the same results as in Figure 5.9 but the maximum tracking error is increased to 7.4 mm. Due to the measurement error, the calculated motor displacement is only $n_{step} = 11$ compared to $n_{step} = 13$ for the case without any measurements error. The difference in motor displacement results in a higher pressure in Line A and a lower pump flow, but the position tracking performance remains almost unchanged.

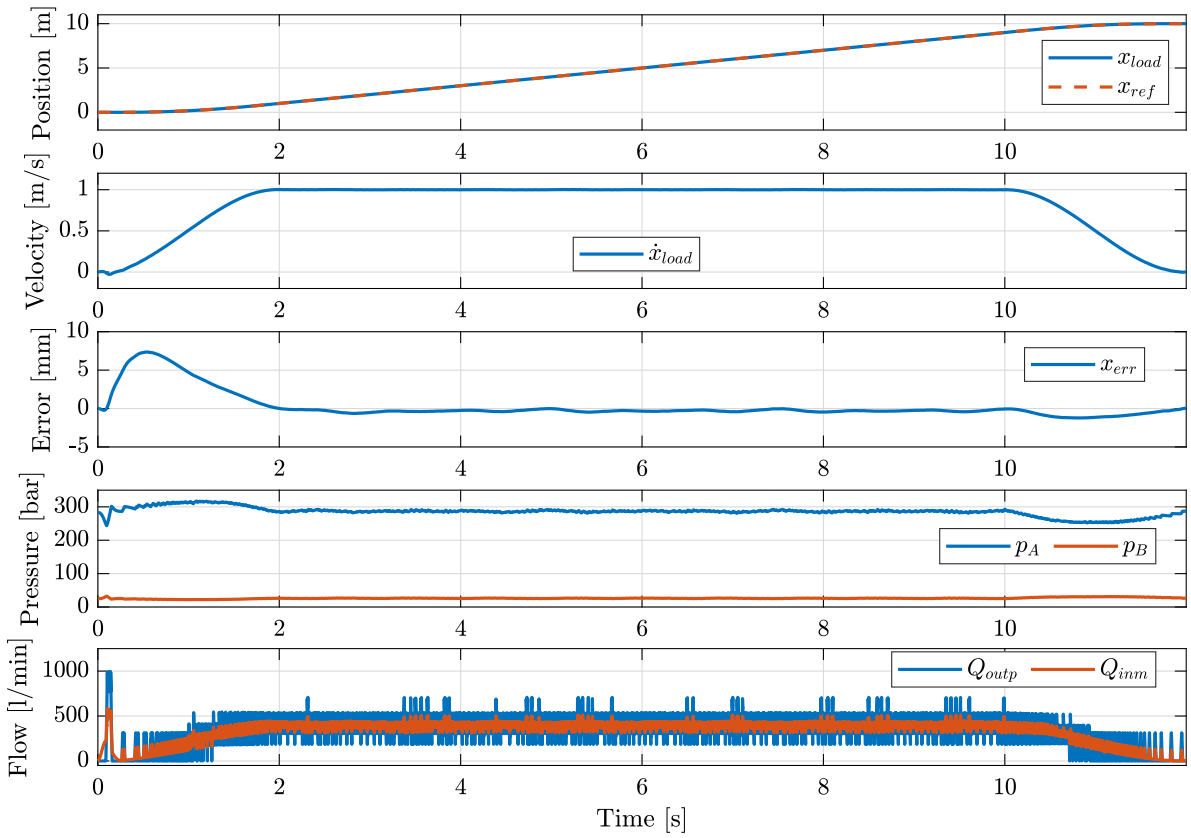

Figure 5.15: Simulation results of hoisting a load with measured load equal 80 % of the real load and where $m_{Load} = 18000$ kg.

Change of Motor Displacement

The studied winch has a capacity of 3600 m of wire. In cases where the load is lifted or lowered several hundreds of meters, the load acting on the winch drum will vary. The load can vary because the mass of the wire will act as an extra load when lowering or because the load is lowered into water. In cases like this, the motor must be able to change displacement during operation. Figure 5.16 shows results from hoisting of a constant load equal to 15000 kg with a change in motor step from $n_{step} = 11$ to $n_{step} = 14$ after 4 s.

The motor starts to change displacement after 4 s. The time it takes to change motor displacement depends on the motor speed. The motor has to rotate more than a half shaft revolution to fully change displacement. When hoisting the payload with 1 m/s, the motor response time is approximately 4.4 s.

When changing motor displacement, the tracking error drops to -3 mm, but approximates zero when the motor displacement is fully changed. In the pressure plot, it can be seen that the pressure in Line A decreases when the motor displacement is increased. It can also been seen that the pump flow and motor flow increase.

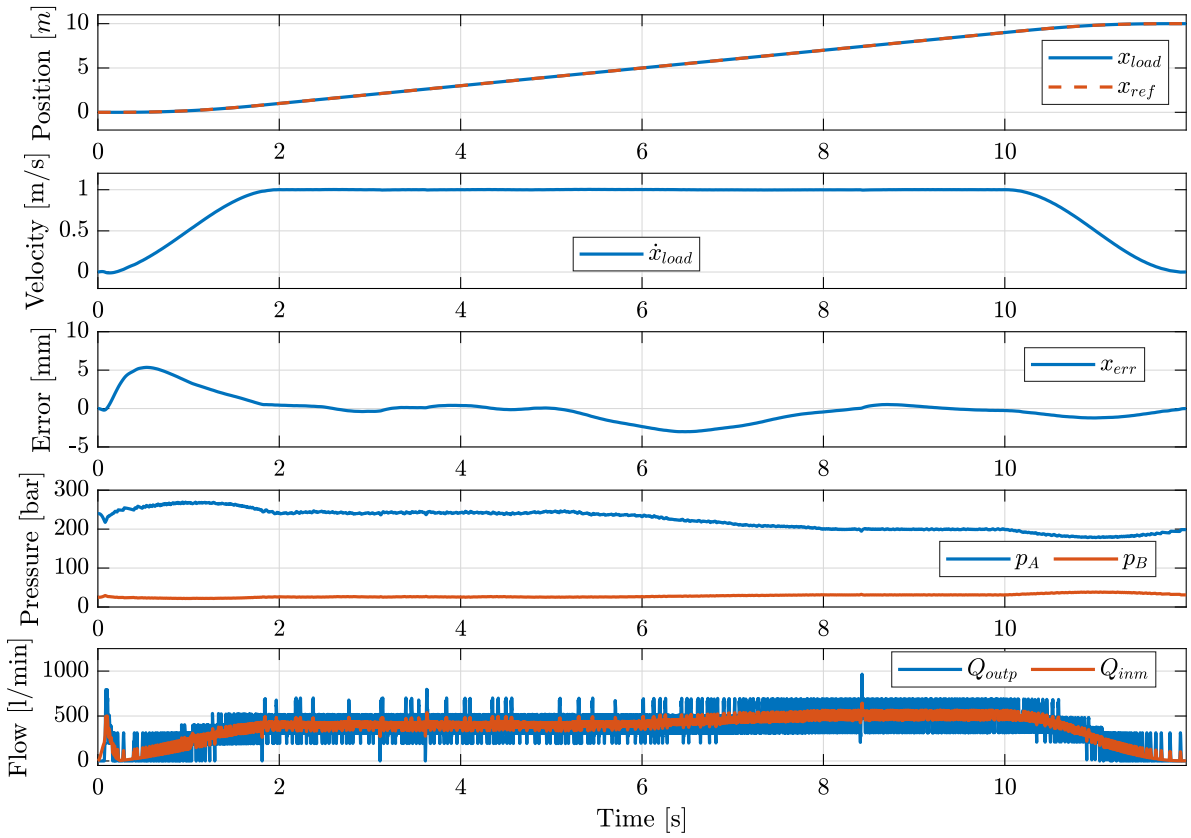

Figure 5.16: Simulation results of hoisting a load when changing motor step from step 11 to step 14 with $m_{Load} = 15000$ kg.

Summary

This simulation study investigates the feasibility of using a digital hydraulic winch drive system on a 20000 kg hydraulic offshore winch. Handling of heavy and light payloads has been investigated in addition to handling errors in load measurements and a change in motor displacement during operation.

The simulation results show that DDPs and DDMs have the potential of driving a winch with high precision and controllability in a wide range of speeds and loads. The largest tracking error was 7.4 mm and occurred when an error in the measured load was introduced. Even though the digital displacement machines are known to have pulsating outputs, the winch motion was smooth and with high controllability.

Chapter 6

Winch System

This chapter gives a general description of typical offshore winch operation systems, typical subsea lifting operations, and requirements related to these operation systems and lifting operations. Based on this description, a set of tests which can be used to test new control systems is presented. Finally, the nonlinear simulation model of the winch system is presented.

6.1 Offshore Winch Operation Modes

An offshore winch is normally controlled by a human operator that operates a joystick, as illustrated in Figure 6.1. By actuating the joystick, the operator controls the winch drum

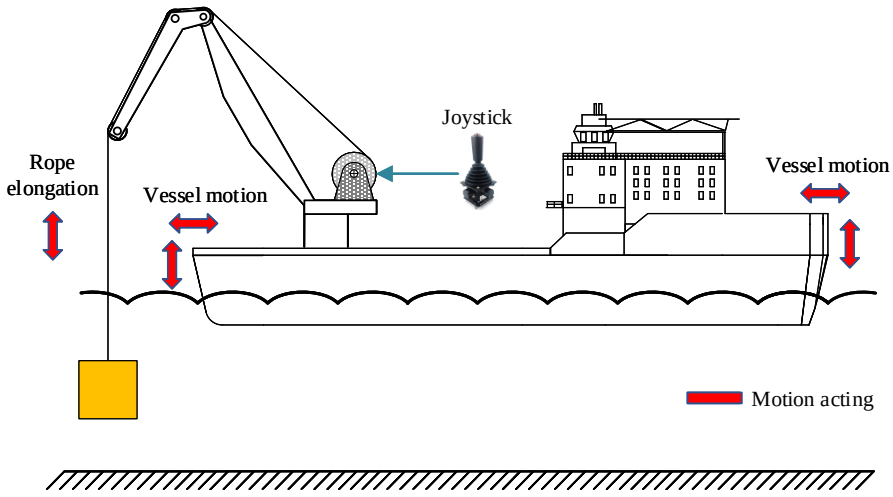

Figure 6.1: Schematic illustration of operator mode. The figure is inspired by [87].

motion. In harsh weather, the vessel will heave due to the waves and wind. This heave motion puts high demands on the operator. The payload should be handled without any dangerous motions or sway. In general, the payload should be lifted slowly and landed slowly with small impact forces.

Additional systems can be used to ease the operation and increase the weather window. Recall that the weather window is a set of weather conditions, for example wind speed, wave hight and wave period, that must not be exceeded during operation. Examples of additional systems are active heave compensation, constant tension, and passive heave compensation systems.

6.1.1 Active Heave Compensation System

Active heave compensation system (AHC) is a winch controller that compensates for the unwanted vertical vessel motion. The payload motion is decoupled from the vessel motion by paying in or out wire rope to oppose the vessel motion. This means that the winch operator can use the joystick to control the payload motion relative to a ground fixed point, which will ease the landing operation on, for example, a fixed platform or the seabed. Figure 6.2 shows a schematic illustration of the working principle of the AHC system.

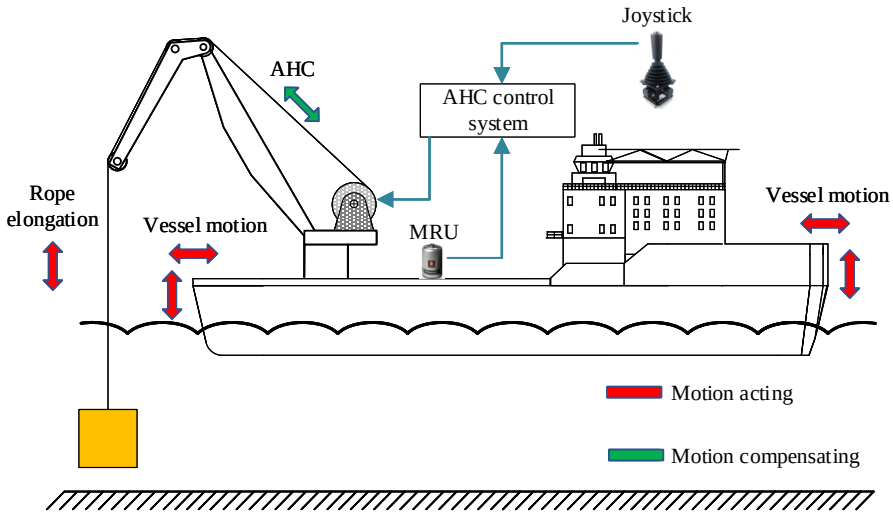

Figure 6.2: Schematic illustration of AHC system. The figure is inspired by [87].

The AHC system normally utilizes a MRU to measure the unwanted vessel motion and actively controls the winch drum to counteract this motion. The MRU is located at the floating vessel and utilizes information from an accelerometer and a gyroscope to determine the motion of the vessel [88].

One of the advantages of AHC systems is that the feedback signal is not limited to vessel heave motion. The feedback signal can also be based on the difference between the motion of two vessels which can be used during vessel-to-vessel lifting operations. In that case, the motion of both vessels needs to be measured.

The AHC system should optimally decouple all of the vessel's heave motion from the motion of the payload. In the literature there are simulation studies of AHC systems

that show compensation efficiencies of 84 % [89], 90-95 % [90], 95 % [91], 97.5 % [92] and 99 % [93]. The compensation efficiency is among other affected by the vessel motion, payload shape and mass of the payload. It is therefore hard to compare compensation performance and put a number on the required compensation efficiency. However, based on input from offshore winch manufacturers, the AHC system should at least reduce the payload motion down to ±5-10 cm, independent of the vessel motion, payload shape and the mass of the payload.

The AHC system is typically used during subsea landing and to reduce dynamical forces in case of resonance when lowering trough the water column. AHC systems can also be used during lift-off from the seabed but should be used with caution. The payload might sink into the soil resulting in a suction force during lift-off. This suction force may lead to overloading of the lifting appliance during lift-off. AHC systems shall therefore only be used during lift-off in combination with load measurements [87]. Also, caution must be taken regarding wear and heating of the wire in bends around sheaves.

6.1.2 Constant Tensioning System

Constant tension (CT) system, also called active cable tension system, is a winch controller that keeps the wire tension at a given pre-set value regardless of vessel motion. Figure 6.3 shows a schematic illustration of the working principle.

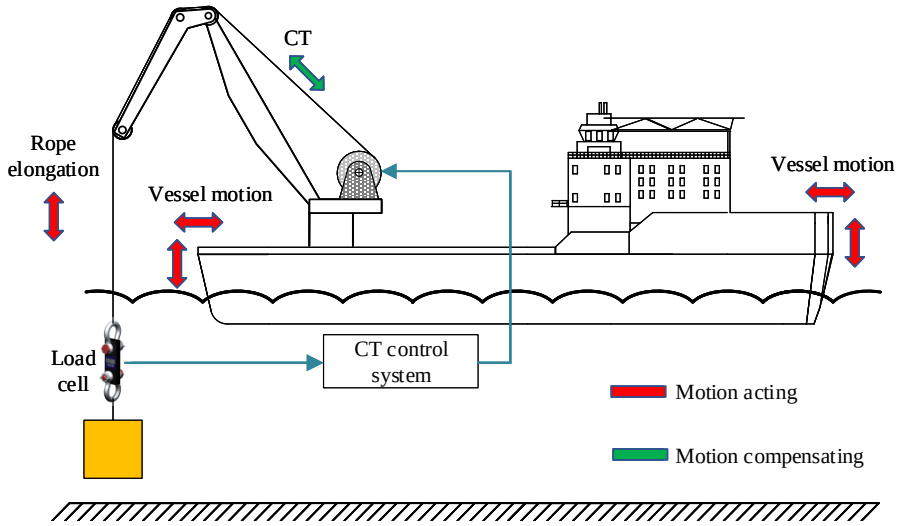

Figure 6.3: Schematic illustration of CT system. The figure is inspired by [87].

A load cell is normally used to measure the wire tension and a control system is used to keep the wire tension equal to the pre-set value. If the measured value deviates from the pre-set value, the winch will pull in or pay out rope to maintain the pre-set value.

The CT system is not suited for use in combination with light payloads relative to the maximum SWL due to low wire tension. Based on inputs from offshore winch manufac-

turers, the compensation error should be below the force needed to overcome the friction in the winch drum. The lowest friction force occurs when the mass of the payload is 0 kg. For the system studied in this thesis, the error in wire tension should be below 8 kN.

The CT system is typically used during lift-down and lift-off at the seabed. In case of suction forces during lift-off, the desired rope tension can be gradually increased until lift-off. Since the rope tension is controlled, the risk of overloading the winch system is at a minimum. In addition to subsea lifting operations, the CT system can also be used during lift-off from another floating vessel and in buoy-laying and positioning operations [87]. As for the AHC system, the CT system must be used with caution regards wear and heating of the winch rope in bends around sheaves.

6.1.3 Passive Heave Compensation System

Passive heave compensation system (PHC) is not a control system, but an application that can be used instead or in combination with an AHC and CT system. A PHC system is basically a spring and damper system. One example of a PHC system is shown in Figure 6.4 and consists of a hydraulic cylinder and an accumulator. The PHC is placed

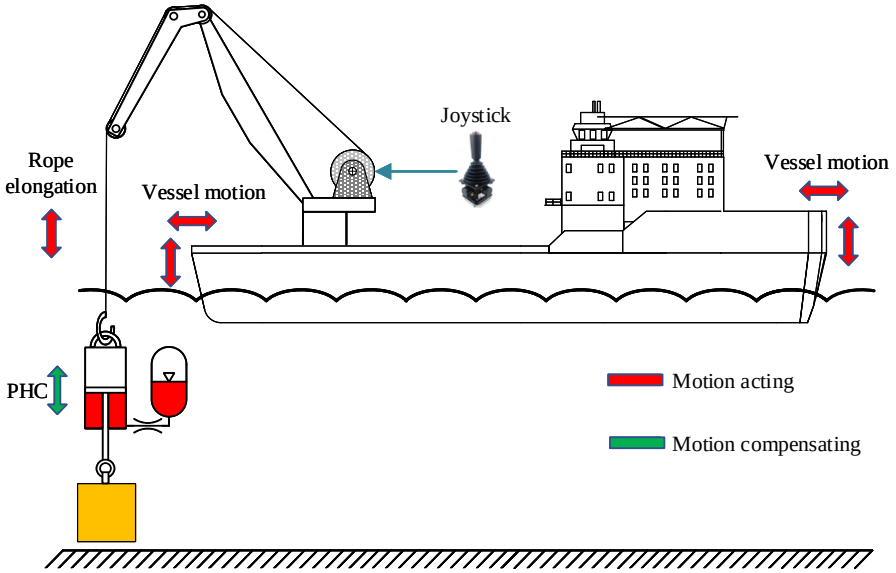

Figure 6.4: Schematic illustration of PHC system. The figure is inspired by [87].

between the crane hook and the payload. If the vessel heaves upwards, the cylinder fluid will be pushed into the accumulator due to inertia forces and drag forces on the payload and thereby extend the cylinder and compensate for the heave motion.

The PHC system must be tuned for the specific lifting operation. Spring and damping characteristics can be changed by changing valves, oil level and accumulator pressure. In some cases, the spring and damper characteristics may also be changed during the lifting operation [87].

The PHC system is typically used to [87]:

- Prevent slack wire.
- Reduce peak loads during splash zone crossing.
- Protect the lifting appliance and the payload from forces caused by vessel motions when lowering or hoisting through the water column.
- Avoid resonance in deep water operation.
- Maintain constant wire tension during lift-off.

The compensation efficiency is affected by the payload geometry, payload density, sea state, and the surrounding medium of the payload. The PHC system is most efficient in high heaves and for objects submerged in water with large drag forces and a low weight in water. The compensation efficiency may vary from 0 % up to 95 % [94]

6.2 Subsea Lifting Operations

Subsea lifting operations can normally be divided into three main operations; deployment, recovery and relocation of payloads on the seabed [87]. Each of those lifting operations can be further broken down into phases or steps. When planning a lifting operation, each step must be well defined and further divided into sub-steps. Figure 6.5 illustrates the three main subsea lifting operations. The vessel position is controlled by a dynamic positioning system that controls thrusters to keep the vessel at the desired location.

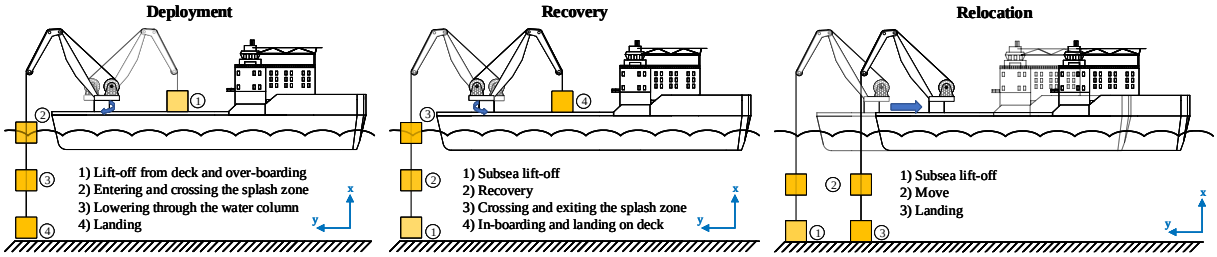

Figure 6.5: Subsea operations.

In general, high variation of dynamic forces on the winch rope and payload should be avoided. In case of lift-off, the rope should be gently tensioned and the payload should be gently accelerated. In case of lift-down, the payload should be landed with a low speed to avoid high impact forces and high variations in the rope tension. Further down in this section, the challenges related to each lifting operation shown in Figure 6.5 are described in detail. The descriptions are based on the work presented in [87] and inputs given from offshore winch manufacturers. Note that the descriptions are not exhaustive, and not all information may be relevant for all types of payloads.

6.2.1 Deployment

In a deployment operation, a payload is moved from the deck and down to the seabed. The deployment operation can be divided into four steps:

1: Lift-off from deck and over-boarding
The main challenges in a lift-off sequence from deck and over-boarding are to control the horizontal movement of the payload and avoid collision with other objects. The operation requires a skilled operator. In this case, the AHC and CT mode are normally not used. It is very important to center the winch hook above the payload to avoid a horizontal shift at lift-off. The operator must slowly tension the wire to ensure that the winch hook and payload are aligned properly. Also, bumpers and guides may be used to avoid collision with other equipment or the vessel itself. When maneuvering the payload overboard, guide lines can be used to control the rotation of the object.

2: Entering and crossing the splash zone
The splash zone is defined as the part of the water column where the variation of the sea surface level affects the payload. This zone extends from the sea surface and down to approximately 50 m below the sea surface. It is in the splash zone that the highest forces acting on the payload and the lifting appliance are expected to be found. Quick changes of buoyancy, added mass and slamming loads caused by the interaction between payload and waves, can result in high dynamic forces and slack slings or slack winch wire. Slack slings or wire may be followed by high snap loads. The lowering speed through the splash zone must, therefore, be carefully assessed.

When crossing the splash zone, the winch should be controlled by a highly skilled operator. The AHC and CT system is normally not used. When the payload is close to the sea surface, the crane operator tries to compensate for the vessel heave motion and cross the sea surface at a low speed, typically in the range of 0.2-0.3 m/s. Once the bottom of the payload has crossed the sea surface, it should be kept within the water to avoid slamming loads and dampen any pendulum movements. A PHC system may be used to reduce the dynamic forces and avoid slack slings.

When lowering through the splash zone, the load acting on the wire will change due to buoyancy, drag force, wave induced loads and flooding of the payload. For hollow payloads, there should be included time for free flooding. Unfortunately, a remotely operated underwater vehicle (ROV) has limited operation capability in the splash zone and the visual observation capability is therefore limited. Flooding is sometimes conducted through small vent holes, which makes the flooding time consuming. The payload should therefore be lowered down to a depth of approximately 50 m, out of the wave zone, for

visual inspection by a ROV to confirm that venting is fully completed before the load is further lowered. In addition, care must be taken regarding tilting of the payload due to trapped air and that the center of gravity and center of buoyancy may not be located vertically above each other.

3: Lowering through the water column

This step involves lowering the payload from the splash zone and down to a safe distance above the seabed or the structure the payload shall be landed on. The main challenges related to this step are stable lowering and the risk of resonance. The payload should be lowered at a pre-defined speed to avoid any wobbling motion and to ensure that the payload has the strength to withstand the drag forces related to motion in water.

When lowering through the water column, the natural frequency of the lifting appliance will change due to increasing wire length. If the natural frequency of the system is close to or equal to the frequency of the vessel's heave motion, the heave motion of the payload will significantly increase, resulting in increased dynamic forces. If the payload and the lifting appliance is sized to withstand the increased dynamical forces, the payload can be lowered without taking any actions. If not, the winch can operate in AHC mode in the period where the natural frequency of the lifting appliance is close to the heave frequency. Another solution is to use a PHC system to change the natural frequency of the lifting appliance and thereby fully avoid the risk of resonance. According to [95], the resonance period of the lifting appliance can be calculated by

$$T_0 = 2 \cdot \pi \cdot \sqrt{\frac{m_{load} + m_a + \delta \cdot m_w \cdot L_1}{K}} \tag{6.1}$$

where m_{load} is the mass of the payload, m_a is an inertia included when the payload is submerged in water, δ is an adjustment factor, m_w is the mass of wire per meter, L_1 is the length of the payed out wire and K is the combined stiffness of the crane boom, wire rope and other contributions if there are any.

When approaching the seabed, the payload should be stopped in a safe height above the highest subsea installation or the seabed and in a vertical offset from the landing position. Then, guide wires or clump weights might be used to control the orientation and position of the payload during landing.

4: Landing

The payload can be landed directly on the seabed, or on a previously installed platform or installation. The payload should be landed smoothly with low speeds, typically below 0.1-0.15 m/s, to avoid high impact forces. High impact forces may result in damage on the payload or already installed equipment. In case of vessel heave motion, the payload may

bounce up and down with high impact forces unless the heave motion is compensated. The heave motion can be compensated for by using AHC, CT or PHC systems. When using AHC system, the payload motion is decoupled from the vertical vessel motion and the winch operator can control the payload motion relative to the seabed. The winch operator should slowly lower the payload and keep attention to the wire tension. When the payload touches the ground, the wire tension should be slowly reduced to zero. Fast unloading of the wire may cause the vessel to roll backward and thereby snap the wire. When using CT during landing, the desired wire tension is set slightly below the tension needed to hold the weight of the payload in water. This will ensure a low impact force during landing. When the payload is in contact with the seabed, the wire tension is slowly decreased by reducing the set point of the wire tension.

Payloads placed at the seabed tend to sink into the soil. The lifting force needed to free the structure depends on the content of the soil and also the impact force during landing. The impact force should therefore be as low as possible.

During landing, a ROV is normally used for visual monitoring of the motion and orientation of the payload. Guide wires connected by a ROV can be used to control the orientation and position of the payload. Lift and guide equipment can be released by, e.g., acoustic release systems, ROV operable hook, ROV shackle or by ROV cutting tools.

6.2.2 Recovery

In a recovery operation, a payload is recovered from the seabed and lifted up to the deck. The recovery operation can be divided into four steps:

1: Subsea lift-off

Lift-off from the seabed may be challenging due to suction forces and trapped mud in the payload. Some seconds or minutes may be required to free the payload from suction. Lift-off from the seabed is normally conducted in CT mode. The desired wire tension is sett to, for example, 20 % above the payload's weight in water. When the payload is lifted to a safe distance above the seabed, the CT system is deactivated and the load motion is controlled by the winch operator. AHC can also be used during lift-off. When using AHC mode, the operator must slowly hoist the payload. Because of the motion controller, the operator must keep attention to the wire tension measurements to avoid overloading the lifting appliance because of suction loads or trapped mud.

2: Hoisting through the water column

In this step, the payload is lifted from a safe distance above the seabed and close to but below the splash zone. As for lowering through the water column, care must be taken

regarding resonance, stability, and drag forces acting on the payload. For more information, see step 3 in Section 6.2.1.

3: Crossing and exiting the splash zone
When hoisting through the splash zone, special care must be taken when exiting the water. Trapped water will increase the payload's weight in the air which may result in overloading of the lifting appliance. Therefore, time must be included for draining the payload for water. The payload should be slowly lifted out of the water, but once the payload is free, it should be hoisted to a safe height above the waves to avoid slamming loads and slack slings. Exiting the splash zone is normally conducted by a skilled operator without the use of any additional modes. A PHC system may be used to reduce the dynamic forces and avoid slack slings.

4: In-boarding and landing on deck
In-boarding and landing on deck can be described as demanding and brutal, and require a highly skilled crane operator. In-boarding and landing on deck should be carried out relatively fast. If the vessel rolls back and forth a few times, the load starts to build up a pendulum movement which makes the landing operation even more demanding. Care must be taken to avoid uncontrolled swinging of the payload and collision with other objects. When the load is in the water, guide lines can be attached to the payload by an ROV to control the orientation in the air. This step is normally carried out by the operator without the use of AHC or CT.

6.2.3 Move

In a move operation, a payload is moved from one location to another. The move operation can be divided into three steps:

1: Subsea lift-off
This step is described in step 1 in Section 6.2.2.

2: Move
Movement covered in this step is typically horizontal movement of payloads located close to but in a safe distance from the seabed. The move is normally conducted by relocating the floating vessel. During relocation, the orientation and position of the load can be controlled by guide wires attached to the payload. Care must be taken to avoid twisting of the wires. The guide wire winches should be in CT mode, and the orientation and position of the payload are controlled by the tension of the guide wires. For a move with-

out the use of guide wires, the orientation of the payload may be controlled by the vessel heading or by using more than one lifting appliance.

3: Landing
This step is described in step 4 in Section 6.2.1.

6.3 Safety

All lifting appliances should be provided with safety systems to reduce the risk of damaging the payload, lifting appliance, other equipment or personnel within the working area. Winches used offshore should generally be provided with at least but not limited to the following features [96]:

- Brakes
- Overload protection systems
- Hook limiting switch
- Safety valves in the hydraulic system
- Emergency stop system
- Slack wire rope detection

Brakes
In normal operation, the braking energy during lowering is absorbed by the drive system, either a hydraulic or electric motor. For safety reasons, the winch should also be equipped with a mechanical brake. The mechanical break shall be designed to not introduce shock loads on the system. Every time the joystick is in natural position, the brakes shall be automatically activated unless AHC or CT is active. The braking system shall also be activated upon failure of the power supply or control system.

When starting with a hanging load with the brakes activated, there should be no drop before lift. A drop in the payload position before lift is an uncontrolled motion which can result in damage of equipment, payload or personnel.

Overload protection system
Overload of a lifting appliance may result in disasters like crane structure collapse and flipping of ships. The overload protection system shall protect against overloading by reducing the load-carrying capacity and allowing the hook to be pulled away from the winch. Overloading can occur due to hook being entangled to a moving object like a ship, a load sucked to the seabed, heave compensation system that is not working properly or other issues.

There are two types of overload protection systems; manual and automatic. Man-

ual overload protection system is manually actuated by the winch operator and shall reduce the lifting capacity to 10 % - 25 % of its rated capacity. The automatic overload protection system shall be automatically actuated when the load exceeds the rated capacity of the lifting appliance and shall keep the tension in the wire rope at the rated capacity.

Hook limiting switches
The winch shall be equipped with upper and lower switches in order to stop the winch hook from collision with other parts of the lifting appliance and keeping the at least 3 turns of wire on the drum.

Safety valves in hydraulic system
The hydraulic system must be equipped with pressure relief or load holding valves to prevent unwanted movement in case of hose rupture. The valves must be mounted directly on the actuator.

Emergency stop
A manual operated emergency stop must be provided in order to stop dangerous winch drum movements or unintended movements caused by a fault in the control system. Activating the emergency stop shall stop the winch movement and activate the brakes in a safe manner.

Slack wire rope detection
Slack wire rope at the drum can result in improper spooling and may occur due to high rotational speed of the winch. The slack wire rope detection system shall stop the winch such that the rope can be re-tightened before automatically returning to operation.

This is only a review of some of the safety functions that offshore winches can be provided with. Other examples are load indicator, audible warning alarm, emergency lowering of loads, etc.

6.4 Test Case Design

Based on the description given in Section 6.2, three critical steps are identified when considering subsea lifting operations:

- Lift-down and lift-off from deck.
- Crossing the splash zone.
- Lift-down and lift-off from the seabed.

The dynamic characteristic of the lifting appliance is affected by the payload mass, the

surrounding medium of the payload and the amount of payed out wire. During landing and lift-off from the deck, the payload is operated in air with a low amount of the wire payed out. Hence the lifting appliance is relatively stiff. During landing and lift-off at deep waters, the dynamic characteristics are changed since a high amount of the wire is payed out and the surrounding medium is water. Therefore, both performance of winch operation in air with a small amount of the wire payed out and at deep waters with a high amount of the wire payed out should be tested.

During landing and lift-off from the deck and crossing the splash zone, the winch is normally operated by a skilled operator without the use of AHC or CT systems. High motion control is therefore important. During landing and lift-off from the seabed, both AHC and CT systems may be used, and both motion control and wire tension control is important. In this section, three test cases are designed in order to test the required performance of the winch system.

Test Case 1 imitates a lift in air without the use of AHC or CT system. Test Case 2 imitates a landing situation on the seabed with the use of the AHC system. Test Case 3 imitates a landing situation on the seabed with the use of the CT system. In the second and third test case, it is assumed that the vessel heaves up and down due to waves. Wave motions are irregular and random in shape, height, length and speed. It is assumed that the vessel has a similar motion and that the motion can be described by the Pierson-Moskowitz wave spectrum [97]. The operation window is typically limited by wave height and wave period. Normally, deck operations are not conducted in waves higher than 2.5 m. In subsea lifting operations, the allowable wave hight depends on the wave period and also the payload. In Test Case 2 and Test Case 3, it is assumed that the vessel heaves with a significant wave height of $H_s = 1.3$ m and a typical wave period of $T_p = 9$ s. The vessel motion is calculated using the method described in [98]. Figure 6.6 shows an example of the heave motion of the vessel with $H_s = 1.3$ m and $T_p = 9$ s.

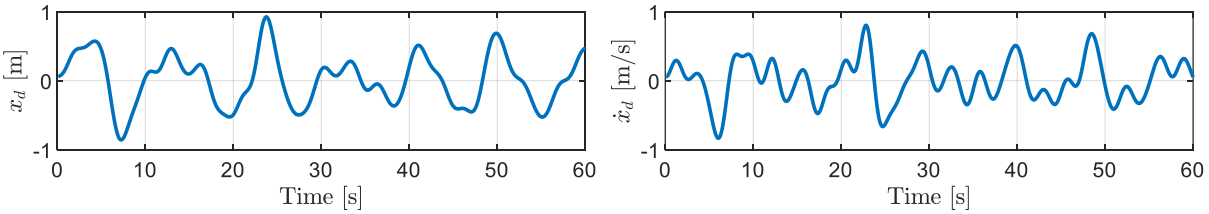

Figure 6.6: Example of vessel motion described by Pierson-Moskowitz wave spectrum with $H_s = 1.3$ m and $T_p = 9$ s. The left plot shows vessel position and the right plot shows vessel velocity.

6.4.1 Test Case 1: Motion Control at Deck with External Force Disturbance

Test Case 1 imitates a lifting operation where the payload is lifted in the air. The payload starts from a hanging load and is hoisted 10 m and then lowered back to its initial position with a trapezoidal velocity profile. During the lifting operation, an external force is applied to the payload in order to test the resistance to external force disturbance. In a real lifting operation, such external force can typically occur during water exit and entry or in case of collision with other objects. The external force is set to 50 % of the force needed to hold the payload at rest.

This test case should be tested both with a payload mass equal to 75 % of max SWL and equal to 5 % in order to test motion tracking performance both for heavy and light payloads. The vessel motion is set to zero. The vessel motion will affect the control performance and should also be tested. However, it is assumed that the vessel motion will have small influence compared to the external load, so in this test case, the vessel motion is assumed to be zero.

Figure 6.7 shows an example of the reference trajectory and the external force. The external force, F_{ext}, is shown in the upper plot, the payload position, x_{pl}, is shown in the middle plot and the payload speed, $\dot{x}_{pl}$, is shown in the bottom plot. The external force is applied as a negative force, acting in the downward direction, in the hoisting phase and as a positive force, acting in upward direction, in the lowering phase.

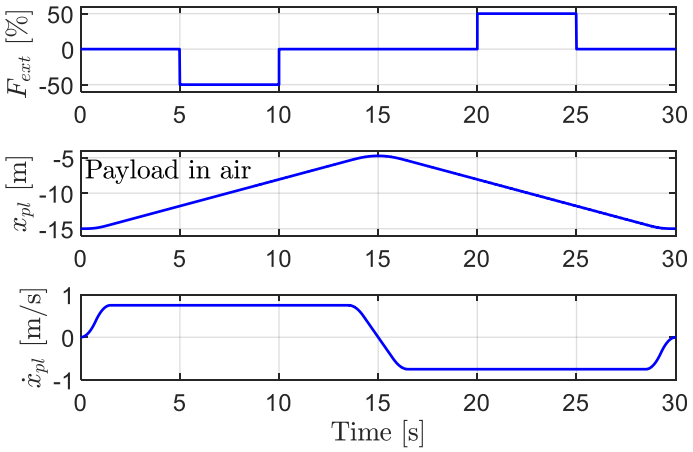

Figure 6.7: Illustration of Test Case 1.

6.4.2 Test Case 2: Landing on the Seabed in AHC Mode

Test Case 2 imitates a landing sequence on the seabed by using AHC. The water depth is set to 1000 m. The purpose of this test case is to test motion tracking performance at deep

waters. A landing situation is chosen in order to test the motion tracking performance with heavy and light payloads. Heavy payloads are tested before landing and no payload is tested after landing.

The mass of the payload is set to max SWL. The landing speed should be below 0.15 m/s and the maximum compensation error for the AHC system should be less than ±5 cm.

Figure 6.8 illustrates an example of the payload position, upper plot, and the drum position, lower plot, during the landing sequence. First, the winch starts with zero velocity

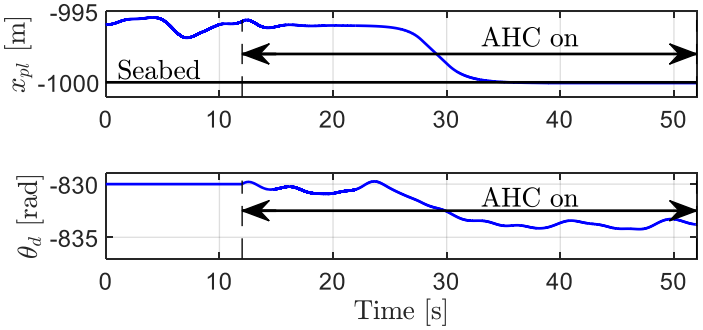

Figure 6.8: Illustration of Test Case 2.

and the payload follows the heave motion of the vessel in a safe height above the seabed. Then the AHC mode is activated and the payload is stabilized at a constant depth, or payload motion smaller than ±5 cm. After the payload has stabilized, the crane operator starts to lower the payload. When the payload touches the seabed, the wire tension is slowly reduced by paying out more wire. Recall that a fast relief of wire tension may cause the vessel to roll backwards which may result in a snap load in the wire. When the wire tension is zero, the winch should continue operating in AHC mode in order to test the motion tracking performance for zero payloads at deep waters.

6.4.3 Test Case 3: Landing on the Seabed in CT Mode

Test Case 3 imitates a landing sequence at the seabed by using CT mode. The purpose is to test the wire tension control performance at deep waters. A landing situation is chosen in order to test wire tension control at high tension and low tension. High tension is tested before landing and low tension is tested after landing.

The mass of the payload is set to max SWL. The preset value of the tension is set slightly below the weight of the payload in water. The wire tension error for the CT mode should be less than 8 kN and the impact force during landing must be low.

Figure 6.9 illustrates an example of the desired wire tension, F_{ref}, payload position, x_{pl}, and drum position, θ_d, during landing in CT mode. The drum will pay wire in and out in order to compensate for the vessel heave motion and the payload will land smoothly.

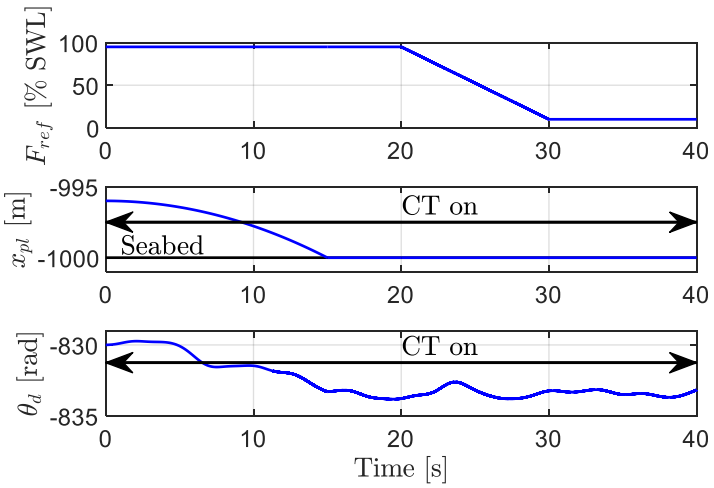

Figure 6.9: Illustration of Test Case 3.

The wire tension is kept constant until the load has landed. When the load has landed, the wire tension is slowly reduced to avoid the vessel from rolling. When the wire tension is reduced to 10 % of maximum SWL, the desired wire tension is kept constant in order to test controllability at low wire tensions.

6.5 Simulation model of the winch

In this project, a winch with max SWL equal to 20000 kg is used as a case study. The winch is a single drum winch type with a drum capacity of 3600 m of wire. The winch is driven by a digital displacement winch drive system consisting of a digital displacement motor with 42 cylinders directly connected to the winch drum through a pinion and gear ring as described in Section 1.2. The 42 cylinders can be distributed on multiple motors placed around the gear ring on the winch drum. For simplicity, in the simulation model, it is assumed that all cylinders are placed on one motor with the cylinders uniformly distributed around the motor shaft.

The simulated system is shown in Figure 6.10. r_d is the drum radius, r_{eff} is the effective radius of the outer wire layer, w_d is the drum width and m_{load} is the mass of the payload. This section describes the nonlinear winch model. The DDM is simulated as shown in Section 2.1.

6.5.1 Assumptions

The dynamics of the winch system depend on the payload's position and mass. In operation, the wire rope is either payed out or in causing variations in the rotational inertia and a variation in the effective drum radius due to switching between wire layers. For the simulated winch, the inner wire layer, which has the smallest radius and therefore the

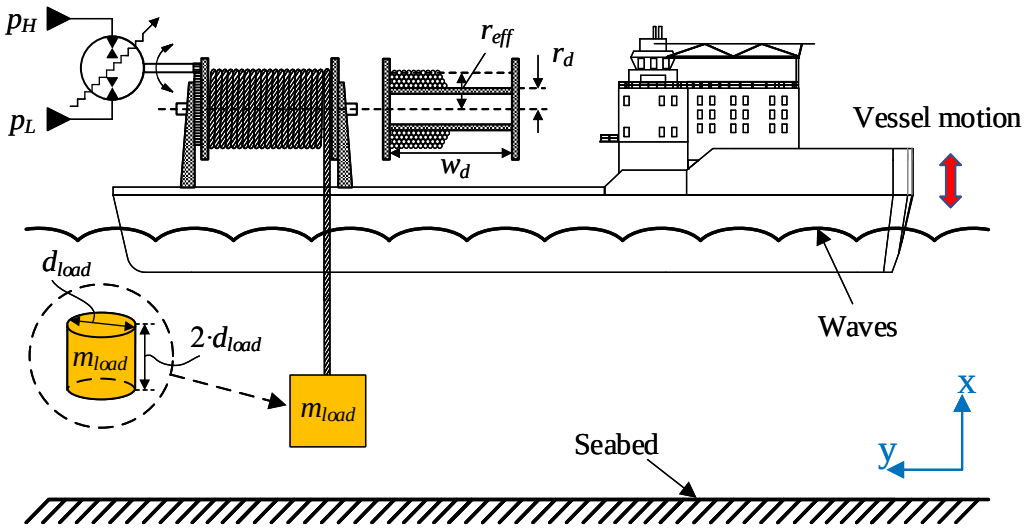

Figure 6.10: Offshore winch simulation system.

smallest storing capacity, has a capacity of 186 m. This length is significant larger than the distance the payload is moved in the three test cases. Hence, it is assumed that all simulations are carried out without changing wire layer. Due to this the effective drum radius is assumed to be constant in the test cases. Of course, the effective radius can vary between different test cases, depending on the length of the payed out wire. However, the rotational inertia of the drum is always modeled as a function of the length of the wire payed out.

The wire will be stretched due to its own mass and the mass of the payload. The wire and the payload will also be exposed to horizontal forces caused by sea currents and wind loads, which again will result in horizontal movement. The difference between the real vertical payload position and the unstretched condition has two contributions: vertical geometric displacement due to curvature of the cable and the vertical elastic displacement due to stretching of the cable [95]. The total vertical cable stiffness is therefore a combination of the wire elastic stiffness and the geometric stiffness [95]. For simplicity, the sea current and wind load are considered to be negligible in this study. Hence, the horizontal drift of the payload is zero and the vertical payload position is only affected by the wire elongation. The wire elongation is included in the simulation model by simulating the wire as a mass-spring-damper system.

The floating vessel will move due to wave induced motion. In this study, only vertical motion is considered. The dynamics of the payload is affected by the motion of the vessel, but it is assumed that the motion of the vessel is not affected by the motion of the payload. This simplification is based on the following assumptions [95]:

- Mass of the payload is much smaller than the displacement of the vessel.
- The payload's contribution to the mass moment of inertia around center of gravity is much smaller than the vessel moment of inertia.

For heavy lifts where the weight of the payload is more than 1-2 % of the vessel displacement, typically more than 1000 tonnes, the coupled dynamics of the vessel and the payload must be considered [95].

Ocean waves are irregular and random in shape, height, length and velocity. It is assumed that the vessel has an equal vertical motion and that the motion can be described by the Pierson-Moskowitz wave spectrum [97] as described in [98] and discussed in Section 6.4.

The seabed dynamics are affected by the content of the soil. The main objective of this thesis is to develop a control system for the proposed digital displacement winch drive system. It is therefore assumed that modeling the seabed as a spring- and damper system is sufficient to show the control performance of the winch. In case the landing or lift-off phase is of special interests, a more realistic seabed model can be implemented.

When the load is submerged in water, an inertia is added to the payload. This inertia is often referred to as added mass and occurs because the payload must accelerate some volume of surrounding water as it moves. The added mass is affected by the payload geometry, motion amplitude and the rate of submergence [95]. In this project, the payload is either fully submerged or not submerged at all. For simplicity, the added mass is in this work considered to be constant.

For simplicity, the simulation model is only valid for operations in air or when the payload is fully submerged in water. Hence, the simulation model is not valid in the splash zone. Forces that occurs during water entry or exit are:

- Varying buoyancy force.
- Varying drag force.
- Slamming force.
- Wave excitation force.
- Water exit force.
- Wave damping force.
- Varying added mass.

The non-linear winch model takes into account the following:

- Inertia of drum, wire and payload.
- Wire elongation.
- Heave motion of the floating vessel.
- Buoyancy of the wire and the payload.
- Viscous drag force in water.
- Friction in drum bearings.
- Seabed dynamics.

6.5.2 Nonlinear winch model

The mechanical winch system consists of the winch drum, wire rope and the payload. The simulation model is based on the model described in [93] and derived based on the dynamic model schematic, the free body diagram and the kinetic diagram shown in Figure 6.11. The wire is modeled as a mass-spring-damper system and the seabed is modeled as

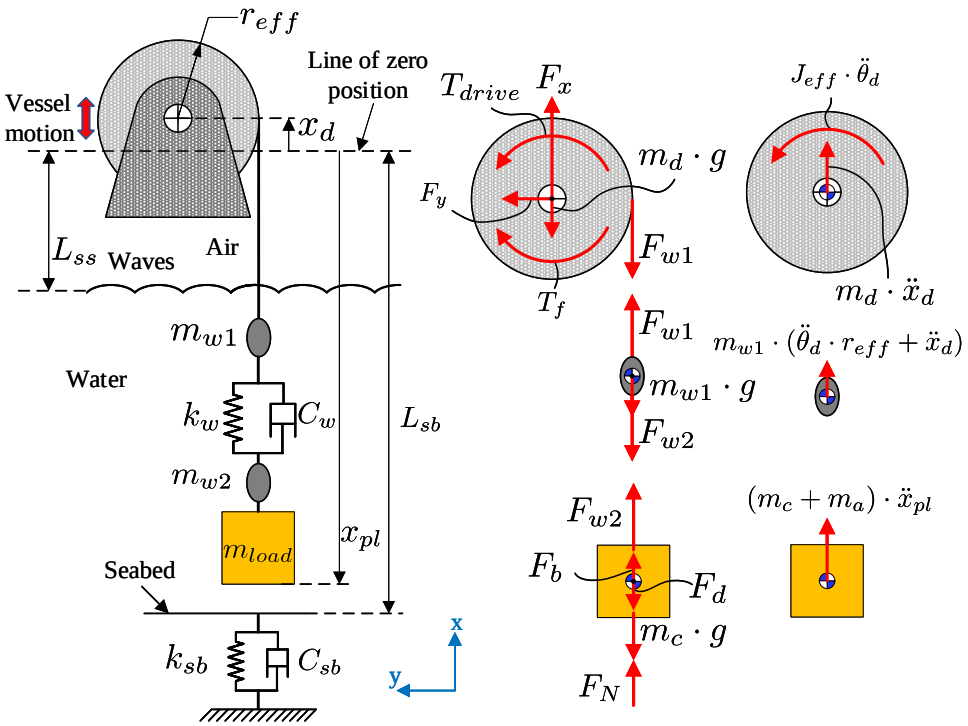

Figure 6.11: System dynamics (left figure), free body diagram (middle figure) and kinetic diagram (right figure).

a spring-damper system, shown in the dynamic model schematic. Note that the payload position is calculated from the center of the drum when the vessel is at rest, marked by the *line of zero position* in Figure 6.11. The payload position is negative when the payload is below the line of zero position. The length down to the sea surface is $L_{ss} = 20$ m and the length down to the seabed is $L_{sb} = 1000$ m. Based on the free body diagram and the kinetic diagram, Newton's second law of motion is used to describe the rotational motion of the drum and the vertical motion of the payload.

$$\sum M = J_{eff} \cdot \ddot{\theta}_d = T_{drive} - T_f - F_{w1} \cdot r_{eff} \tag{6.2}$$

$$\sum F_x = (m_c + m_a) \cdot \ddot{x}_{pl} = F_{w2} + F_b + F_N - F_d - m_c \cdot g \tag{6.3}$$

where T_{drive} is the driving torque acting on the drum, T_f is the friction torque in the drum bearings, F_{w1} is the wire force in the upper wire section, F_{w2} is the wire force in the lower wire section, r_{eff} is the effective radius of the outer wire layer, J_{eff} is the effective mass moment of inertia relative to the drum shaft, m_c is the mass of the combined load, m_a is

the added mass, F_b is the buoyancy force, F_d is the drag force, F_N is the interaction force between the payload and the seabed and g is the acceleration of gravity.

The driving torque is given by the digital displacement winch drive system. It is assumed that there is no slack and no friction between the pinion and the gear ring. The driving torque can then be calculated as shown in Equation 6.4.

$$T_{drive} = T_m \cdot N_{gear} \tag{6.4}$$

where N_{gear} is the gear ratio between the pinion and the gear ring and T_m is the motor torque.

The friction torque in the drum bearings, T_f, is assumed to be a combination of coulomb and viscous friction and is calculated as shown in Equation 6.5.

$$T_f = \underbrace{(m_d \cdot g + F_{w1}) \cdot r_b \cdot \mu_c \cdot \tanh(\dot{\theta}_d \cdot 1000 \text{ s})}_{T_{coulomb}} + \underbrace{\mu_v \cdot r_b \cdot \dot{\theta}_d}_{T_{viscous}} \tag{6.5}$$

where m_d is the mass of the drum and the mass of the wire rolled onto the drum, r_b is the radius of the drum bearings, μ_c is the coulomb friction coefficient and μ_v is the viscous friction coefficient. The coulomb friction coefficient is approximated as $\mu_c = 0.1$ and the viscous friction coefficient is approximated as $\mu_v = 1000$ Ns/rad. The term $\tanh(\dot{\theta}_d \cdot 1000 \text{ s})$ is implemented to avoid a step in the coulomb friction torque when passing through 0 rpm. However, this friction model is only an approximation and may not reflect the exact friction characteristics.

From the dynamic model schematic shown in Figure 6.11, it can be seen that the wire is divided into two point masses, m_{w1} and m_{w2}, with a spring and damper in between. The connection between the upper wire section and the winch drum, and the connection between the lower wire section and the payload are assumed to be rigid. Hence, the motion of the upper wire section is a combination of the vertical motion of the vessel and the rotation of the drum, $\ddot{x}_{w1} = \ddot{\theta}_d \cdot r_{eff} + \ddot{x}_d$. The motion of the lower wire section is equal to the payload motion, $\ddot{x}_{w2} = \ddot{x}_{pl}$ The upper wire forces, F_{w1}, is calculated by using Newton's second low of motion on the upper wire section as shown in Equation 6.6. The lower wire force, F_{w2} is calculated as the force from the spring-damper-system describing the wire elasticity as shown in Equation 6.7.

$$F_{w1} = m_{w1} \cdot (\ddot{\theta}_d \cdot r_{eff} + \ddot{x}_d) + m_{w1} \cdot g + F_{w2} \tag{6.6}$$

$$F_{w2} = \underbrace{(\theta_d \cdot r_{eff} + x_d - x_{pl}) \cdot k_w}_{F_{spring}} + \underbrace{(\dot{\theta}_d \cdot r_{eff} + \dot{x}_d - \dot{x}_{pl}) \cdot C_w}_{F_{damper}} \tag{6.7}$$

where $\ddot{x}_d$ is the vertical acceleration of the vessel, k_w is the spring stiffness of the wire and C_w is the damping coefficient of the wire. Note that Equation 6.7 is only valid when the wire is stretched. If the wire is slack, the wire force is $F_{w2} = 0$ N. The spring stiffness is

calculated based on the wire E-modulus, E_w, wire cross-section area, A_w, and the length of the payed out wire, L_w, as shown in Equation 6.8. The damping force is introduced to compensate for internal friction in the wire rope. The damping coefficient is defined as 10 % of the spring stiffness and calculated in Equation 6.9. However, this wire model is only a rough estimation and may not reflect the exact characteristics of the wire.

$$k_w = \frac{E_w \cdot A_w}{L_w} \tag{6.8}$$

$$C_w = \frac{k_w}{10} \tag{6.9}$$

Note that Equation 6.9 does not give the correct unit of the damping coefficient. The correct unit is Ns/m.

The payload is exposed to buoyancy when submerged in water and a viscous drag force during motion. The buoyancy force includes the buoyancy of the payload and the submerged wire. The buoyancy force, F_b, and drag force, F_d, are calculated as shown in Equation 6.10 and Equation 6.11 respectively.

$$F_b = \rho_{sea} \cdot g \cdot (V_{pl} + V_w) \tag{6.10}$$

$$F_d = \frac{1}{2} \cdot \rho_{sea} \cdot C_d \cdot A_{pl} \cdot \dot{x}_{pl}^2 \cdot \text{sign}(\dot{x}_{pl}) \tag{6.11}$$

where ρ_{sea} is the sea water density, V_{pl} is the volume of the payload, V_w is the volume of the submerged wire, C_d is the drag force coefficient and A_{pl} is the projected cross-section area of the payload normal to the motion. Note that the buoyancy and drag force are only applied when the payload is submerged in water. For the payload considered in this project, shape shown in Figure 6.10, the drag coefficient is $C_d = 0.85$ [95]. The term $\text{sign}(\dot{x}_{pl})$ is included to get the correct sign of the drag force.

The seabed is modeled as a spring-damper system. The seabed interaction force, F_N, is calculated as shown below.

$$F_N = (-x_{pl} - L_{sb}) \cdot k_{sb} - \dot{x}_{pl} \cdot C_{sb} \tag{6.12}$$

where k_{sb} is the spring stiffness for the seabed, C_{sb} is the damping coefficient for the seabed and L_{sb} is the length from the line of zero payload position, shown in Figure 6.11, and down to the seabed. The spring stiffness is set to $k_{sb} = 4000000$ N/m and the damping coefficient is set to $C_{sb} = 1000000$ Ns/m. This results in an over damped system if the mass of the payload is 20000 kg.

The effective mass moment of inertia varies as a function of the mass of the wire on the drum. It is assumed that the wire is uniformly distributed around the drum. The effective mass moment of inertia is calculated as shown in Equation 6.13.

$$J_{eff} = J_d + \underbrace{\frac{1}{2} \cdot m_{wd} \cdot (r_d^2 + r_{eff}^2)}_{J_{wire}} + J_m \cdot N_{gear}^2 \tag{6.13}$$

where J_d is the mass moment of inertia of the drum, m_{wd} is the mass of the wire rolled onto the drum, J_m is the mass moment of inertia of the DDM and N_{gear} is the gear ratio of the pinion and gear ring.

The combined mass, m_c, consists of the mass of the payload, m_{load}, hook, m_{hook}, and the lower wire section, m_{w2}. The combined mass is calculated as shown in Equation 6.14.

$$m_c = m_{load} + m_{hook} + m_{w2} \tag{6.14}$$

The added mass, m_a, is calculated as shown in Equation 6.15.

$$m_a = \rho_{sea} \cdot C_A \cdot V_R \tag{6.15}$$

where C_A is the added mass coefficient and V_R is the reference volume. The added mass coefficient is set to $C_A = 0.72$ and the reference volume is $V_R = V_{pl}$ for the payload shape considered in this project [95].

Chapter 7

Control design

This chapter presents controllers for the digital displacement winch drive system. The winch should be able to operate both in operator mode, AHC mode and CT mode. The operator mode and AHC mode require a motion controller while the CT mode requires a tension controller.

Multiple motion controllers for hydraulic winch drive systems have been proposed in the literature. The proposed controllers are often designed for use in open circuit systems. In [99], the authors presented a combination of a position feedback and velocity feedforward AHC controller for an open circuit winch drive system. In [93], the authors proposed a cascade controller to improve motion tracking performance for an open circuit systems. The cascade controller used a PI controller in the inner velocity loop and a P controller in the outer position loop. The nonlinearities in conventional open circuit winch drive systems reduce the tracking performance for linear controllers. Several nonlinear controllers have been proposed to improve the tracking performance. Examples are: model predictive controller [100], sliding mode controller [101, 102] and adaptive controller [103]. Other approaches to increase the heave compensation performance are to use measurements of the wave amplitude as a feed forward compensator within the AHC system [104] or to predict the heave motion and use this prediction as a part of the control strategy for the AHC system [105, 106].

Most of the designed tension controllers that can be found in the literature are also for open circuit systems. In [99], the authors presented a closed loop wire tension feedback loop with a P controller for an open circuit winch system. The designed controller was experimentally tested by lifting a 400 kg payload from a moving platform. In [107], the authors compared the performance of a PID controller to a fuzzy P + ID controller in a towing winch. The controllers were implemented in an open circuit winch drive system. The simulation results showed that the fuzzy P + ID controller was able to reduce the mean squared error by 57 % and 39 % in a towing situation compared to the PID controller

when the desired wire tension was set to 50 kN and 30 kN respectively. The peak error was also reduced by 60 % and 58 % when the desired tension was set to 50 kN and 30 kN respectively. An alternative solution has been presented in [108]. In stead of actively controlling the proportional valve in the CT mode, it was proposed to implement a short cut valve that maintains a desired pressure drop across the motor. The desired pressure drop can be controlled to meet a desired wire tension. The motor will pay out wire if the load torque is greater than the available driving torque and pull in wire if the load torque is lower than the available driving torque.

This chapter presents in all four motion controllers and one tension controller for the digital displacement winch drive system. The designed controllers are then tested on the test cases designed in Section 6.4 and their performances are evaluated. This chapter is divided into six sections. The first section discloses the selection of the used displacement strategy. The second section presents a simplified simulation model of the entire digital displacement winch drive system. The simplified simulation model is further used in the third section to design the motion controllers. The fourth section presents a simple PI tension controller used in the CT mode. The fifth section presents the simulation results of all designed controllers. Finally, the sixth section discusses the motion controllers regarding performance, robustness and implementation issues. The presented work is published in paper E and paper F.

7.1 Selection of displacement strategy

The choice of displacement strategy is important. Every displacement strategy has its characteristics. The winch drive system must be able to operate at low speeds with frequent starts and stops and frequent changes in the direction of rotation. Based on the work presented in Chapter 4, both the PSDS 2 and the SPSDS are found to be suitable for use in a winch drive system due to high controllability at low speeds. The SPSDS is known to switch the valves and reactivate the cylinder chambers more often than the PSDS 2. It is therefore assumed that the PSDS 2 has higher energy efficiency and is, therefore, the selected displacement strategy.

Note that the focus of this project is to design a controller that can be used when high controllability of the winch is important, e.g. landing, lift-off or crossing the splash zone. When the controllability is of less importance, e.g. during deep water lowering, another displacement strategy with higher energy efficiency, like the FSDS, may be used. It is out of the scope for this project to develop controllers with optimal displacement strategies for all phases in all lifting operations. However, the designed controller can be used in all operation phases, but there may be more suitable displacement strategies that gives a

higher energy efficiency.

One of the benefits of the DDM, is that the decompression and compression phase can be optimized for all operation conditions. Developing an optimized compression and decompression phase is not in the scope of this work and is, therefore, not implemented. In this study, when changing state from active to inactive, the low pressure valve is opened when the high pressure valve is fully closed. When reactivating a cylinder, the high pressure valve and the low pressure valve are actuated at the same time. This strategy will result in unnecessary high flow peaks and flow throttling losses. One technique of optimizing the decompression and compression phase have been investigated in [79].

Winch operation requires a drive system that is able to operate in all four quadrants. Normally, quadrant 1 is used during hoisting and quadrant 3 during lowering but in special cases, like driving with an empty hook or in AHC mode, quadrant 2 and quadrant 4 may also be used. The four quadrants are illustrated in Figure 7.1. The green arrows show

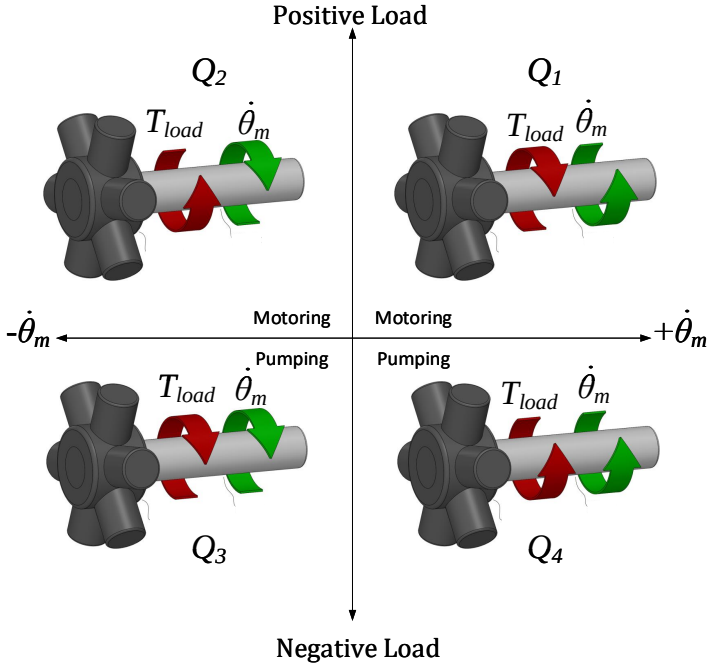

Figure 7.1: Four quadrant operation.

the direction of rotation and the red arrows show the direction of the load torque. Q_1 is quadrant 1, Q_2 is quadrant 2 and so on. In Q_1 and Q_2 the DDM is operating as a motor, hence the load torque acts in the opposite direction of the speed. In Q_3 and Q_4 the DDM is operating as a pump, hence the load torque and the speed act in the same direction.

In the PSDS 2, the valve timing strategy shown in Figure 2.7 in Section 2.2.2 is only valid for operation in Q_1. Each quadrant requires a unique valve timing strategy. Figure 7.2 shows a simplified schematic illustration of the valve timing strategy for all four quadrants. The top graph shows the piston position and the next four graphs show the valve timing sequence for operation in quadrant 1 to 4 respectively. The red line shows

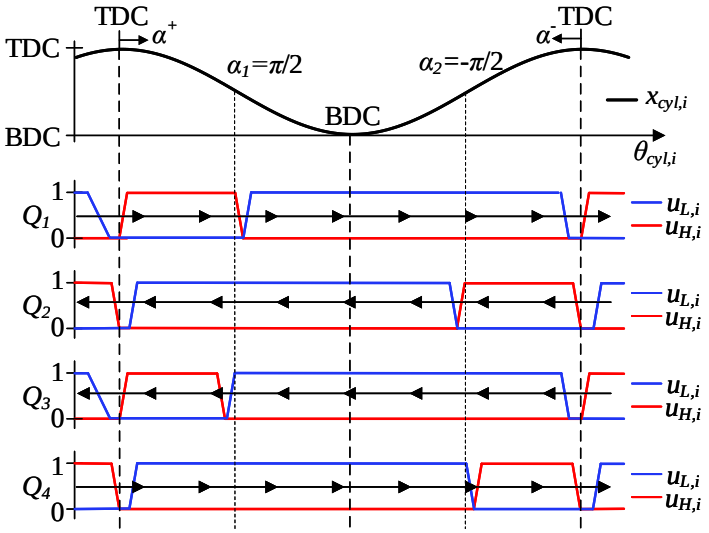

Figure 7.2: Valve timing sequence for four quadrant operation.

the opening ratio of the high pressure valve and the blue line shows the opening ratio of the low pressure valve. The black line with arrows shows the direction of rotation. Arrows pointing to the right indicates positive direction and arrows pointing to the left indicates negative direction of rotation. Note that in Q_1 and Q_3, the control angle, α_1, is used to switch cylinder state and in Q_2 and Q_4 the control angle, α_2, is used to switch cylinder state.

A schematic illustration of the motor controller is shown in Figure 7.3. The input to

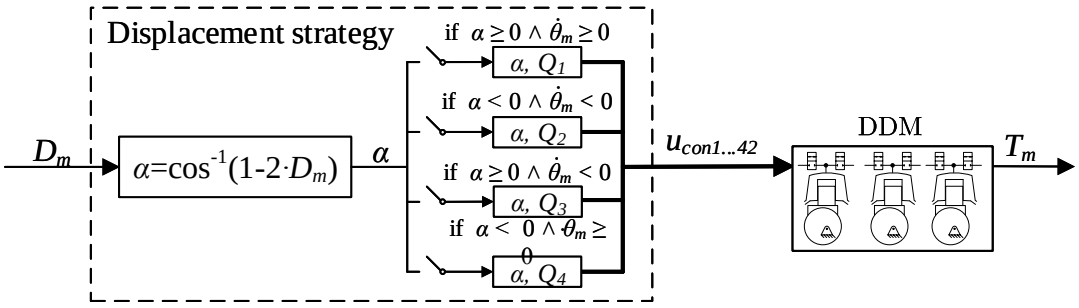

Figure 7.3: Motor controller.

the controller is the desired displacement ratio, D_m, and the output is the motor torque, T_m. The state change angle, α, is calculated based on the desired displacement fraction by using Equation 2.16. The valve timing strategy, Q_j where $j = 1...4$, is selected by a switching controller. Based on given conditions, the proper valve activation strategy is selected. The given conditions are shown in Equation 7.1.

$$Q = \begin{cases} Q_1 & \text{if} \quad \alpha \geq 0 \quad \wedge \quad \dot{\theta}_m \geq 0 \\ Q_2 & \text{if} \quad \alpha < 0 \quad \wedge \quad \dot{\theta}_m < 0 \\ Q_3 & \text{if} \quad \alpha \geq 0 \quad \wedge \quad \dot{\theta}_m < 0 \\ Q_4 & \text{if} \quad \alpha < 0 \quad \wedge \quad \dot{\theta}_m \geq 0 \end{cases} \tag{7.1}$$

where $\dot{\theta}_m$ is the motor velocity. The state change angle and the valve activation strategy are then sent to the on/off valves on the DDM which results in an output torque of the motor.

7.2 Model Simplification

In order to design model based controllers, the nonlinear models for the DDM, presented in Section 2.1, and for the mechanical winch system, presented in Section 6.5, are simplified. In the simplified model, the wire elasticity is neglected and the motor torque is approximated to be linear to the motor displacement. The new simplified free body diagram and the kinetic diagram, where the elasticity of the wire is neglected, are shown in Figure 7.4.

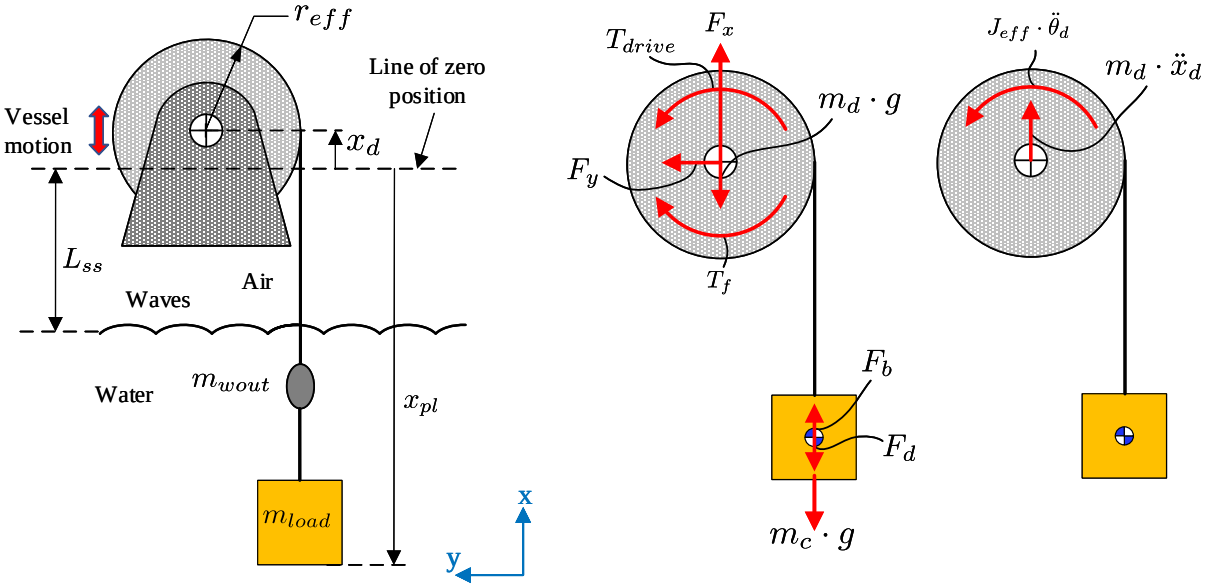

Figure 7.4: Simplified system dynamics, free body diagram and kinetic diagram.

The equation of motion for the winch drum is derived based on the free body diagram and the kinetic diagram as shown in Equation 7.2.

$$\overline{J}_{eff} \cdot \ddot{\theta}_d = \overline{T}_{drive} - r_{eff} \cdot (m_c \cdot g + F_d - F_b) - \overline{T}_f \tag{7.2}$$

where overline indicates that the parameter is a simplified version of the real parameter. The driving torque is given by the hydraulic motor. In this simplified model, the driving torque is assumed to be linear to the input signal, D_m, and expressed by:

$$\overline{T}_{drive} = \frac{\Delta p_{motor} \cdot V_m}{2 \cdot \pi} \cdot N_{gear} \cdot D_m \tag{7.3}$$

where $\Delta p_{motor} = p_H - p_L$ is the pressure difference across the motor, V_m is the maximum motor displacement, N_{gear} is the gear ratio between the pinion and the gear ring and D_m is the displacement ratio ranging from -1 to 1.

In order to validate the simplified driving torque, the driving torque from the simplified model, $\overline{T}_{drive}$, is compared to the driving torque from the nonlinear model, T_{drive}, when a sinusoidal input signal with increasing frequency is given. The motor is running at 50 rpm and the results are shown in Figure 7.5. The blue line shows the driving torque from

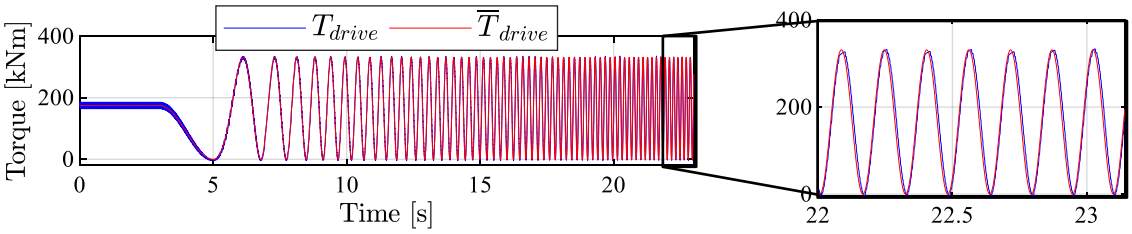

Figure 7.5: Comparison between simple model and non-linear model of the driving torque.

the nonlinear model, and the red line shows the driving torque from the simplified model. The simulation results show that the simplified model is a sufficient representation of the nonlinear model, even at high input frequencies. However, the output torque from the nonlinear model tends to oscillate, while the output torque from the simplified model is smooth. This is best seen in the first 5 s of Figure 7.5 where the blue line looks thick due to the oscillating output torque caused by fast switching between active and inactive cylinder chambers.

The simplified friction torque is calculated as shown in Equation 7.4.

$$\overline{T}_f = (m_{tot} \cdot g + F_d - F_b) \cdot r_b \cdot \mu_c \cdot \text{sign}\left(\dot{\theta}_d\right) + \mu_v \cdot r_b \cdot \dot{\theta}_d \tag{7.4}$$

where m_{tot} is the mass of the winch drum, payload and the wire.

The simplified effective mass moment of inertia relative to the drum shaft, $\overline{J}_{eff}$, is calculated as shown in Equation 7.5

$$\overline{J}_{eff} = J_d + \frac{1}{2} \cdot m_{wd} \cdot \left(r_d^2 + r_{eff}^2\right) + J_m \cdot N_{gear}^2 + (m_{load} + m_{wout}) \cdot r_{eff}^2 \tag{7.5}$$

where m_{wout} is the mass of the payed out wire.

7.3 Motion controller

This section presents the design of the motion controllers. The goal of the motion controller is to make the winch drum follow a given reference trajectory. In operator mode, the reference trajectory is generated by operating the joystick. In AHC mode, the measured vessel motion is subtracted from the joystick signal. A schematic illustration of the control strategy is shown in Figure 7.6.

The displacement controller transforms the reference trajectory into a desired displacement ratio. The displacement strategy transforms the desired displacement ratio

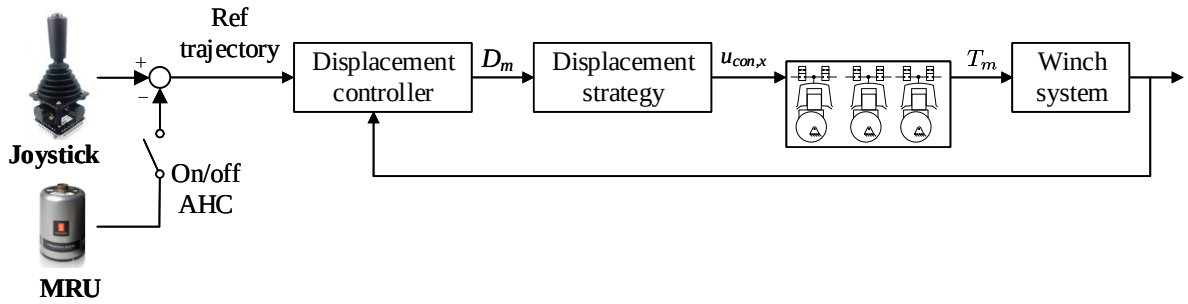

Figure 7.6: Schematic illustration of the control structure for the motion controller

into valve control signals. Then the valves activates and deactivates the cylinder chambers which results in an output torque that drives the winch.

This section presents four displacement controllers. The first three controllers are also presented in paper F and the fourth controller is presented in paper E.

7.3.1 Base Controller

The dynamical model of the winch system, shown in Equation 7.2, can be rearranged to a more general form.

$$\begin{aligned}
\overline{J}_{eff} \cdot \ddot{\theta}_d &= \overline{T}_{drive} - r_{eff} \cdot (m_c \cdot g + F_d - F_b) - \overline{T}_f \Downarrow \\
\ddot{\theta}_d &= \frac{\frac{\Delta p_{motor} \cdot V_m}{2 \cdot \pi} \cdot N_{gear}}{\overline{J}_{eff}} \cdot D_m - \frac{r_{eff} \cdot (m_c \cdot g + F_d - F_b)}{\overline{J}_{eff}} - \frac{\overline{T}_f}{\overline{J}_{eff}} \\
&= b \cdot D_m - f
\end{aligned} \tag{7.6}$$

where

$$b = \frac{\frac{\Delta p_{motor} \cdot V_m}{2 \cdot \pi} \cdot N_{gear}}{\hat{J}_{eff}} \tag{7.7}$$

$$f = \frac{r_{eff} \cdot (m_c \cdot g + F_d - F_b)}{\overline{J}_{eff}} + \frac{\overline{T}_f}{\overline{J}_{eff}} \tag{7.8}$$

If the parameters b and f were exactly known, the following control law would have given optimal tracking performance.

$$D_{m,opt} = \frac{u_n + f}{b} \tag{7.9}$$

with the nominal controller

$$u_n = \ddot{\theta}_{ref} - c_2 \cdot \dot{e} - c_1 \cdot e \tag{7.10}$$

where $e = \theta_d - \theta_{ref}$ and θ_{ref} is the reference position for the drum. c_1 and c_2 are controller gains and must be positive. Inserting the optimal control law, given in Equation 7.9, into

Equation 7.6 results in the following closed loop response.

$$\begin{aligned}\ddot{\theta}_d &= b \cdot D_{m,opt} - f \\ &= b \cdot \frac{u_n + f}{b} - f \\ &= u_n \Downarrow \end{aligned} \tag{7.11}$$

$$\begin{aligned}\ddot{\theta}_d &= \ddot{\theta}_{ref} - c_2 \cdot \dot{e} - c_1 \cdot e \\ \ddot{\theta}_d - \ddot{\theta}_{ref} + c_2 \cdot \dot{e} + c_1 \cdot e &= 0 \\ \ddot{e} + c_2 \cdot \dot{e} + c_1 \cdot e &= 0 \end{aligned} \tag{7.12}$$

where the position error, e, will converge to zero exponentially.

In reality, the parameters b and f are not known exactly because of unmodeled dynamics, uncertainties in the simulation parameters and other disturbances. Therefore, only an approximation of the control law can be implemented:

$$D_m = \frac{u_n + \hat{f}}{\hat{b}} \tag{7.13}$$

where $\hat{}$ indicates that the parameter is estimated based on system knowledge and state measurements. Inserting our best approximation of the control law, shown in Equation 7.13, into Equation 7.6 gives the following closed loop response:

$$\begin{aligned}\ddot{\theta}_d &= b \cdot D_m - f \\ &= b \cdot \frac{u_n + \hat{f}}{\hat{b}} - f \\ &= \frac{b}{\hat{b}} \cdot u_n + \frac{b}{\hat{b}} \cdot \hat{f} - f \\ &= u_n - \left(f - \frac{b}{\hat{b}} \cdot \hat{f} + u_n \cdot \left(1 - \frac{b}{\hat{b}} \right) \right) \\ &= u_n - \Delta_{b,f}, \qquad \text{where} \quad \Delta_{b,f} = \left(f - \frac{b}{\hat{b}} \cdot \hat{f} + u_n \cdot \left(1 - \frac{b}{\hat{b}} \right) \right) \end{aligned} \tag{7.14}$$

where $\Delta_{b,f}$ is called the model error and represents the error dynamics between the estimated model and the real system.

The control law presented in Equation 7.13 is referred to as the base controller (BC). Assuming that the model error is small, the control performance will be good.

7.3.2 Sliding Mode Disturbance Controller

The base controller presented in the previous section is not optimal due to the model error. The goal of this section is, therefore, to present a compensator, u_c, that will cancel the model error. The compensator is designed by using a sliding mode disturbance compensator (SMDC).

First, the control law in Equation 7.13 is modified to include the compensator, u_c.

$$D_{m,SMC} = \frac{u_n + u_c + \hat{f}}{\hat{b}} \tag{7.15}$$

Inserting the new control law into Equation 7.6 gives the following closed loop dynamics.

$$\begin{aligned}
\ddot{\theta}_d &= b \cdot D_{m,SMC} - f \\
&= b \cdot \frac{u_n + u_c + \hat{f}}{\hat{b}} - f \\
&= \frac{b}{\hat{b}} \cdot u_n + \frac{b}{\hat{b}} \cdot u_c + \frac{b}{\hat{b}} \cdot \hat{f} - f \\
&= u_n + u_c + \left(\frac{b}{\hat{b}} \cdot \hat{f} - f + (u_n + u_c) \cdot \left(\frac{b}{\hat{b}} - 1 \right) \right) \\
&= u_n + u_c + \Delta_{b,f,SMC}
\end{aligned} \tag{7.16}$$

where

$$\Delta_{b,f,SMC} = \left(\frac{b}{\hat{b}} \cdot \hat{f} - f + (u_n + u_c) \cdot \left(\frac{b}{\hat{b}} - 1 \right) \right) \tag{7.17}$$

$\Delta_{b,f,SMC}$ is the model error. The aim of the compensator, u_c, is to compensate for the model error such that

$$\ddot{\theta}_d = u_n, \text{ for } u_c \to -\Delta_{b,f,SMC} \tag{7.18}$$

The compensator is designed by following the structure in [109]. The model parameters, f and b, are unknown but assumed to be bounded. The bounds are given by the following equations.

$$|\hat{f} - f| \leq F \tag{7.19}$$

and

$$0 < b_{min} \leq b \leq b_{max} \tag{7.20}$$

$$\Downarrow$$

$$\beta^{-1} \leq \frac{b}{\hat{b}} \leq \beta \tag{7.21}$$

where

$$\beta = \frac{b_{max}}{b_{min}} \tag{7.22}$$

A time-varying sliding surface is defined by Equation 7.23 and its derivative by Equation 7.24

$$s = \dot{\theta}_d - z \tag{7.23}$$

$$\dot{s} = \ddot{\theta}_d - \dot{z} \tag{7.24}$$

where $\dot{z}$ is chosen to $\dot{z} = u_n + u_c + \nu_{SMC}$ and $\nu_{SMC} = L \cdot \text{sign}(s)$. Inserting for $\ddot{\theta}_d$, given in Equation 7.16, and $\dot{z}$ into Equation 7.24 gives:

$$\begin{aligned} \dot{s} &= u_n + u_c + \Delta_{b,f,SMC} - u_n - u_c - \nu_{SMC} \\ &= \Delta_{b,f,SMC} - L \cdot \text{sign}(s) \end{aligned} \tag{7.25}$$

The condition for sliding mode is $s = 0$. A Lyapunov function is used to investigate if sliding occurs. The Lyapunov function is chosen as shown in Equation 7.26 and its derivative is shown in Equation 7.27.

$$V(s) = s^2/2 \tag{7.26}$$

$$\dot{V}(s) = s \cdot \dot{s} \tag{7.27}$$

Inserting Equation 7.25 for $\dot{s}$ results in

$$\dot{V}(s) = s \cdot (\Delta_{b,f,SMC} - L \cdot \text{sign}(s)) \tag{7.28}$$

If the constraint $\dot{V}(s) \leq -\eta \cdot |s|$ with $\eta > 0$ can be fulfilled, it may be concluded that $s \to 0$ as $t \to T < \infty$, whereafter sliding occurs i.e. $s = 0$ for $t \geq T$. The gain L in Equation 7.28 must be chosen such that $\dot{V}(s) \leq -\eta \cdot |s|$ will always apply. Based on Equation 7.28 and knowing that $s \cdot \text{sign}(s) = |s|$, the gain L must be chosen to satisfy Equation 7.32.

$$\dot{V}(s) = s \cdot (\Delta_{b,f,SMC} - L \cdot \text{sign}(s) \leq -\eta \cdot |s| \Downarrow \tag{7.29}$$

$$L \cdot |s| \geq \eta \cdot |s| + |s| \cdot |\Delta_{b,f,SMC}|_{max} \Downarrow \tag{7.30}$$

$$L \geq \eta + |\Delta_{b,f,SMC}|_{max} \Downarrow \tag{7.31}$$

$$\begin{aligned} L &\geq \eta + \left| \frac{b}{\hat{b}} \cdot \hat{f} - f + (u_n + u_c) \cdot \left(\frac{b}{\hat{b}} - 1 \right) \right|_{max} \\ &\geq \eta + \left| \left(\hat{f} - f \right) + \left(u_n + u_c + \hat{f} \right) \cdot \left(\frac{b}{\hat{b}} - 1 \right) \right|_{max} \end{aligned} \tag{7.32}$$

From Equation 7.19 and Equation 7.21 it is known that $|\hat{f} - f| \leq F$ and $\left| \frac{b}{\hat{b}} \right|_{max} = \beta$. Based on those relations, Equation 7.32 can be rewritten as shown in Equation 7.33.

$$L \geq \eta + F + \left| u_n + u_c + \hat{f} \right| \cdot (\beta - 1) \tag{7.33}$$

Choosing L large enough will ensure sliding mode within a finite time.

For sliding to occur, $s = 0$ for $t > T$, will also require that $\dot{s} = 0$, see [109]. By using that $\dot{s} = 0$ for $t \geq T$ and Equation 7.25, an equivalent controller, u_{eq} is designed as shown below.

$$\begin{aligned} 0 &= \Delta_{b,f,SMC} - L \cdot \text{sign}(s) \Downarrow \\ u_{eq} &= L \cdot \text{sign}(s) = \Delta_{b,f,SMC} \end{aligned} \tag{7.34}$$

In the ideal case, the compensator controller, u_c, should be chosen to $u_c = -u_{eq}$. Inserting this controller will introduce a chattering problem due to the term sign(s). Therefore, a continuous approximation, u_{av}, of the equivalent controller is implemented. The equivalent controller can be continuously approximated by use of, for example, a low pass filter as shown in [102] or a tanh-function as shown in [110]. However, in this project, the equivalent controller is approximated as shown in Equation 7.35.

$$u_{av} = -L \cdot \text{sat}(s, \epsilon) \tag{7.35}$$

where

$$\text{sat}(s, \epsilon) = \frac{s}{|s| + \epsilon}, \text{ where } \epsilon > 0 \tag{7.36}$$

The designed controller will give the following system response:

$$\ddot{\theta}_d = u_n + u_c + \Delta_{b,f,SMC} \approx u_n \tag{7.37}$$

with

$$u_c = -u_{av} \approx -\Delta_{b,f,SMC} \tag{7.38}$$

The control parameter L and ϵ shall be chosen based on a compromise between tracking performance and control effort in addition to satisfying Equation 7.33.

7.3.3 Adaptive Controller

The adaptive controller (AC) is also based on the BC. Instead of compensating for the model error, as done in the SMDC, the aim of the AC is to remove the model error by adjusting the simulation parameters. Assuming that the estimated simulation parameters $\hat{f}$ and $\hat{b}$ will adapt to f and b, the response shown in Equation 7.12 will occur. For the AC, the control law given by Equation 7.13 is applied and the model parameters are adjusted as described in this section.

A gradient based adaption law is used to adjust the model parameters. The controller is designed by following the structure of a self-tuning controller described in [111]. First, the winch system dynamics shown in Equation 7.6 is rewritten in vector form as shown below.

$$\begin{aligned} \ddot{\theta}_d &= b \cdot D_m - f \\ &= \underbrace{\begin{bmatrix} D_m & -1 \end{bmatrix}}_{\mathbf{W}} \cdot \underbrace{\begin{bmatrix} b \\ f \end{bmatrix}}_{\mathbf{a}} \\ &= \mathbf{W} \cdot \mathbf{a} \end{aligned} \tag{7.39}$$

The estimated system dynamics is calculated by Equation 7.40.

$$\begin{aligned}\ddot{\hat{\theta}}_d &= \hat{b} \cdot D_m - \hat{f} \\ &= \mathbf{W} \cdot \hat{\mathbf{a}}\end{aligned} \tag{7.40}$$

where $\hat{\mathbf{a}}$ consists of the estimated parameters $\hat{b}$ and $\hat{f}$. The prediction error is defined as

$$\begin{aligned}e_{pre} &= \ddot{\hat{\theta}}_d - \ddot{\theta}_d \\ &= \mathbf{W}\cdot\hat{\mathbf{a}} - \mathbf{W}\cdot\mathbf{a} \\ &= \mathbf{W}\cdot\tilde{\mathbf{a}}, \text{ where } \tilde{\mathbf{a}} = \hat{\mathbf{a}} - \mathbf{a}\end{aligned} \tag{7.41}$$

The implemented gradient based adaption law is shown in Equation 7.42.

$$\dot{\hat{\mathbf{a}}} = -p_0 \cdot \mathbf{W}^T \cdot e_{pre} \tag{7.42}$$

where p_0 is a positive controller gain.

The convergence of the estimated parameters is investigated by using a Lyapunov function. The Lyapunov function is chosen as shown in Equation 7.43 and its derivative is shown in Equation 7.44.

$$V = \tilde{\mathbf{a}}^T \cdot \tilde{\mathbf{a}} \tag{7.43}$$

$$\dot{V} = 2 \cdot \tilde{\mathbf{a}}^T \cdot \dot{\tilde{\mathbf{a}}} \tag{7.44}$$

It is assumed that the real system parameters are constant, or at least varying very slowly compared to the estimated parameters, hence $\dot{\hat{\mathbf{a}}} \approx \dot{\tilde{\mathbf{a}}}$. Using this relation and Equation 7.41, Equation 7.42 can be written as

$$\dot{\tilde{\mathbf{a}}} = -p_0 \cdot \mathbf{W}^T \cdot \mathbf{W} \cdot \tilde{\mathbf{a}} \tag{7.45}$$

Inserting this for $\dot{\tilde{\mathbf{a}}}$ in Equation 7.44 results in

$$\dot{V} = -2 \cdot p_0 \cdot \tilde{\mathbf{a}}^T \cdot \mathbf{W}^T \cdot \mathbf{W} \cdot \tilde{\mathbf{a}} \tag{7.46}$$

Equation 7.46 shows that $\dot{V}$ is at least negative semi-definite and implies that the gradient based parameter estimator is always stable. V is the squared parameter error and is never increasing, $\dot{V} \leq 0$. The convergence of the estimated parameters to the true parameters depends on the signals in $\mathbf{W}$. Since the reference trajectory is a part of the signals in $\mathbf{W}$, the reference trajectory will affect the convergence of the estimated parameters. As long as the signals in $\mathbf{W}$ are non-zero, the prediction error, e_{pre}, will converge to zero. However, this does not mean that the estimated parameters, $\hat{\mathbf{a}}$, converges to the real system parameters $\mathbf{a}$. This only means that for the given input signal, both the model and the real system gives the same output, $\ddot{\hat{\theta}}_d = \ddot{\theta}_d$. For example, for a constant input

signal, D_m = constant, there may be several solutions for $\hat{b}$ and $\hat{f}$ that gives the same output result. If a variable input signal is given, then there will be fewer solutions for $\hat{b}$ and $\hat{f}$ that gives the same output as the real system. This means that the probability for the model parameters to converge to its real values is higher when a variable input signal is given.

7.3.4 PID Controller

The last motion controller is a PID controller. This controller is included to examine if the more advanced controllers designed can improve the tracking performance. The PID controller is implemented as shown in Equation 7.47.

$$D_{m,PID} = -k_d \cdot \dot{e} - k_p \cdot e - k_i \cdot \overline{e} \tag{7.47}$$

where $e = \dot{\overline{e}}$.

7.4 Tension controller

The tension controller is used in CT mode. The goal of the tension controller is to provide a constant tension in the wire rope. Figure 7.7 shows a schematic illustration of the tension controller.

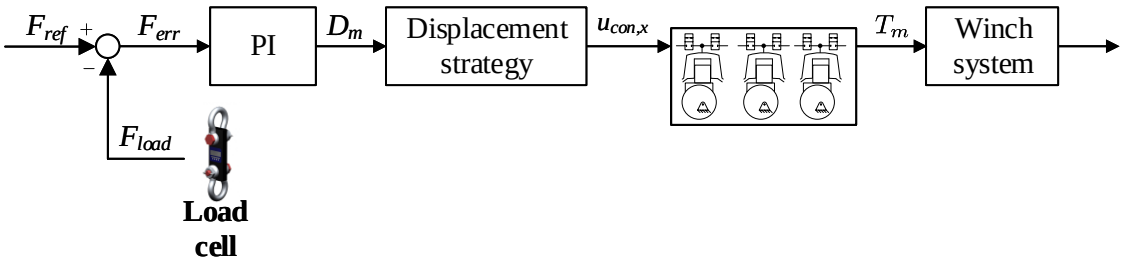

Figure 7.7: Schematic illustration of the tension controller.

The desired displacement ratio, D_m, is controlled by a PI controller with a wire tension feedback signal. The desired displacement is transformed into valve activation signals by the displacement strategy. Then the cylinder chambers are activated and deactivated according to the valve control signals in order to keep a constant tension in the winch wire.

The displacement ratio is calculated as shown in Equation 7.48

$$D_{m,CT} = k_p \cdot F_{err} + k_i \cdot \overline{F}_{err} \tag{7.48}$$

where $F_{err} = F_{ref} - F_{load}$ is the wire tension error and $F_{err} = \dot{\overline{F}}_{err}$.

7.5 Simulation Results

The designed controllers are tested on the test cases described on Section 6.4. The motion controllers are used in Test Case 1 and Test Case 2. The tension controller is used in Test Case 3.

7.5.1 Test Case 1

Test Case 1 imitates a lift in air where the payload first is lifted 10 m and then lowered back to its initial position. During the hoisting phase and lowering phase, an external force is applied to the payload to test the controllers robustness against external force disturbance. The test case is conducted with two different loads. In the first load case, the payload's mass is 15000 kg and in the second load case it is 1000 kg.

Figure 7.8 shows the simulation results from load case 1, $m_{load} = 15000$ kg, when using all motion controllers. Plot 1 shows the drum position and the reference trajectory, Plot 2 shows the tracking error, Plot 3 shows the payload position, Plot 4 shows the payload speed and Plot 5 shows the lower wire force, F_{w2}, and the external force, F_{ext}. Note that the tracking error in Plot 2 is transformed from the rotation domain and into the translation domain by multiplying the error in radians by the effective radius, $\theta_{err} \cdot r_{eff}$. This is done to get a better understanding of the magnitude of the tracking error.

In general, the simulation results in Plot 1, Plot 3, Plot 4 and Plot 5 are relatively equal for all controllers. The payload is lifted and lowered 10 m with a trapezoidal velocity profile. The external force is applied as a negative force, downwards direction, after 5 s and as a positive force after 15 s. The load is applied in 5 s for each case. Plot 4 shows that there is a small drop or peak in the payload velocity when the external force is applied and removed.

The most interesting plot is Plot 2 where the tracking error is plotted. For the PID controller, it can be seen that a tracking error occurs when accelerating and decelerating the payload, driving through 0 rpm and when the external force is applied and removed. The tracking performance of the BC is characterized with a steady-state error when driving with constant speed and some small oscillations when accelerating and decelerating the payload and driving through 0 rpm. The steady-state tracking error is very small and hard to see when no external load is applied. When the external load is applied, the steady-state error is increased. The SMDC and the AC have no steady-state error. The tracking error have some small oscillations when accelerating and decelerating the payload and when driving through 0 rpm. When the external force is applied or removed, only a small peak can be seen in the tracking error for both the SMDC and the AC.

The simulation results of load case 2, $m_{load} = 1000$ kg, is shown in Figure 7.9. As for

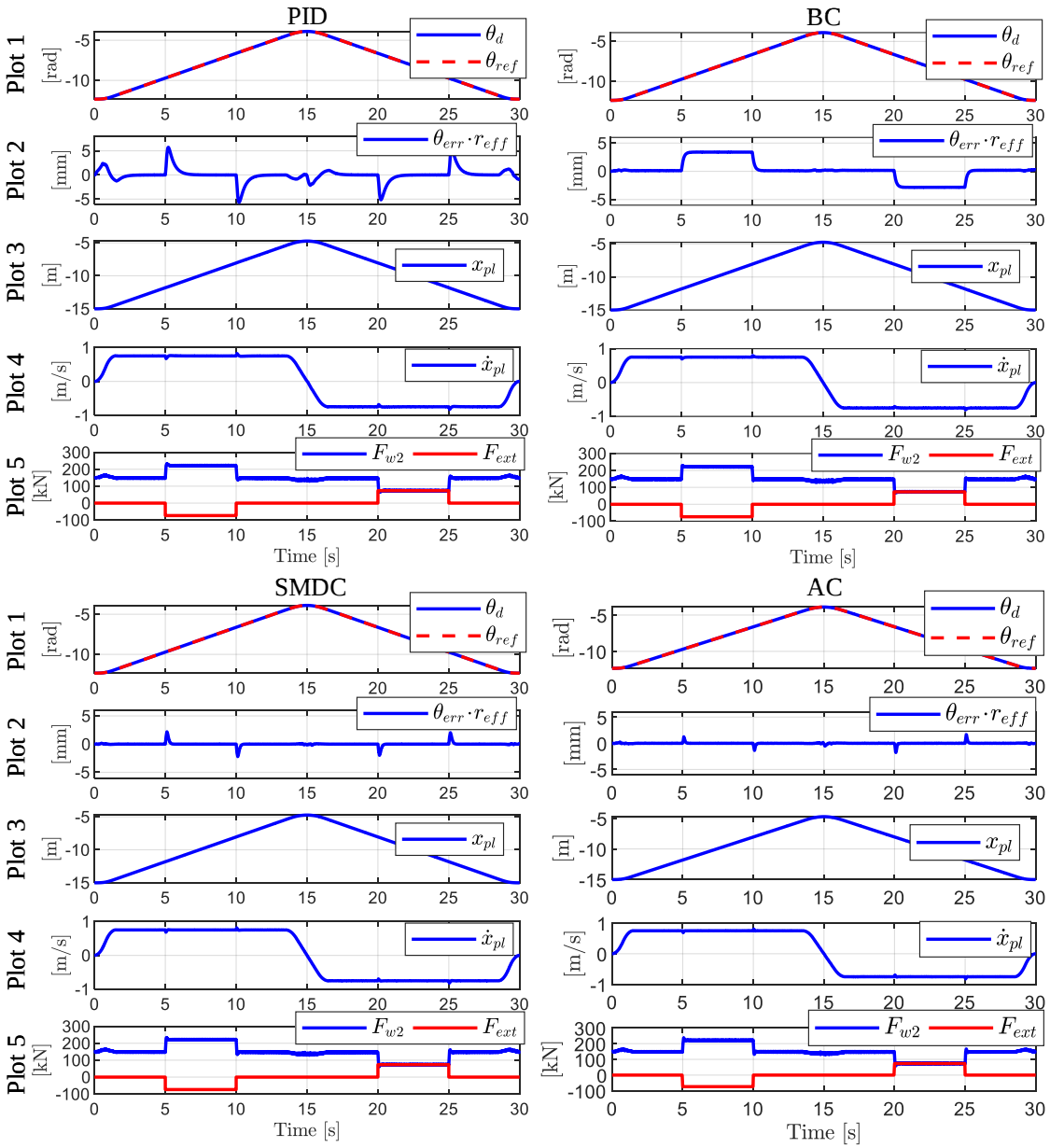

Figure 7.8: Simulation results Test Case 1 and load case 1 ($m_{load} = 15000$ kg).

load case 1, the simulation results in Plot 1, Plot 3, Plot 4 and Plot 5 are relatively equal for all controllers. The most interesting plot is Plot 2. For the PID controller, a small tracking error can be seen when accelerating and decelerating the payload, driving through 0 rpm and when the external load is applied and removed. For the BS, a steady-state error can be seen when driving with constant speed. There is a step in the steady-state error when the external force is applied. Also, a step in the steady-state error can be seen after approximately 18 s. This step occurs because the motor changes operation quadrant. For the SMDC and the AC, the tracking performance is very good with only small tracking errors when accelerating and decelerating the payload, driving through 0 rpm and when the external force is applied and removed.

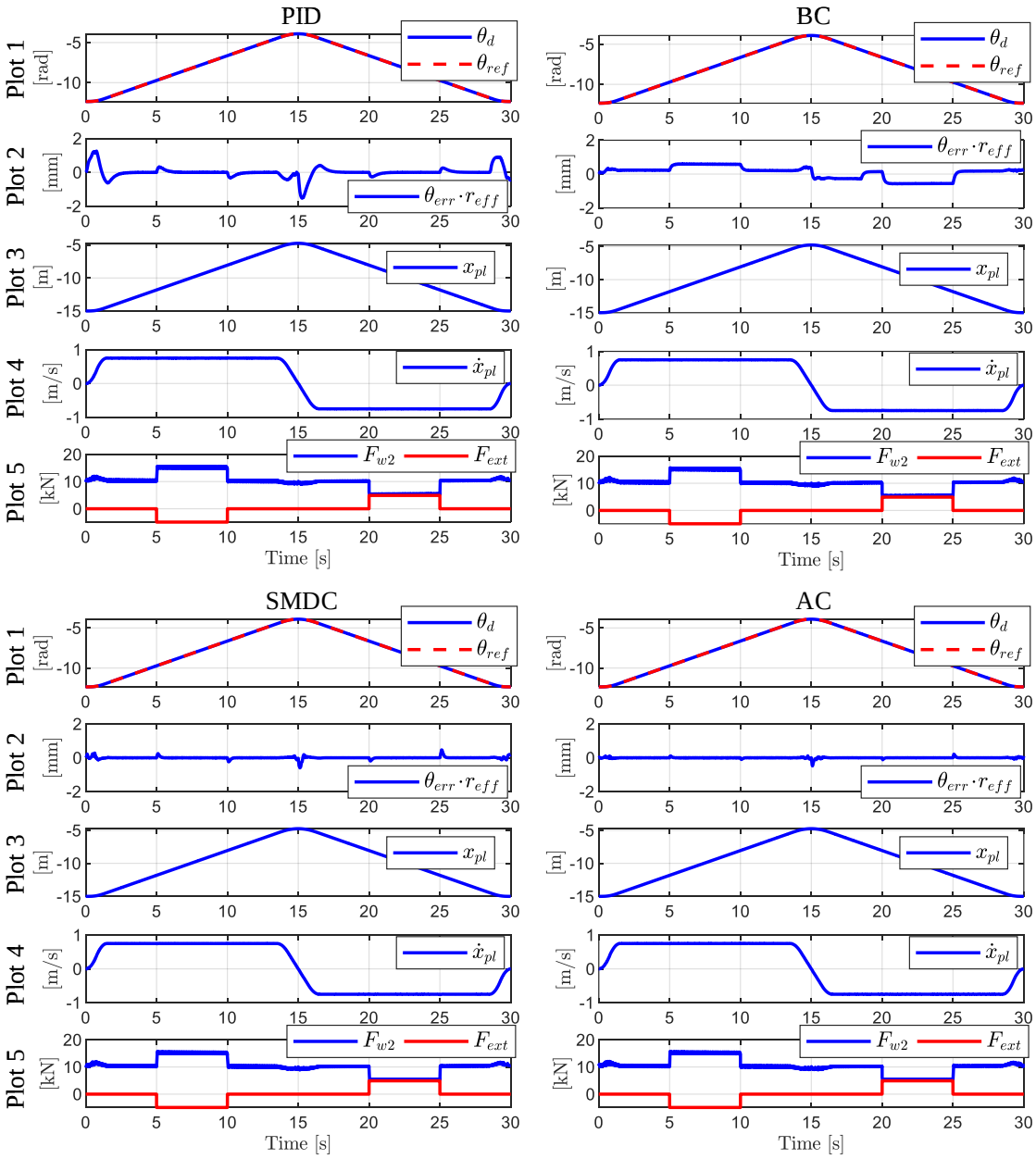

Figure 7.9: Simulation results Test Case 1 and load case 2 ($m_{load} = 1000$ kg).

Discussion

Figure 7.10 shows the tracking error for all controllers in the same plot. The upper plot shows the tracking error from load case 1 and the lower plot shows the tracking error for load case 2. It can be seen that the tracking performance is better for the SMDC and the AC compared to the PID and the BC. The SMDC and the AC is very robust against external forces added to the payload. Only a small peak or drop can bee seen in the tracking error. For the PID controller, the tracking error peaks are higher than for the SMDC and the AC. The BC controller has also a higher tracking error than the SMDC and the AC in addition to the steady-state error.

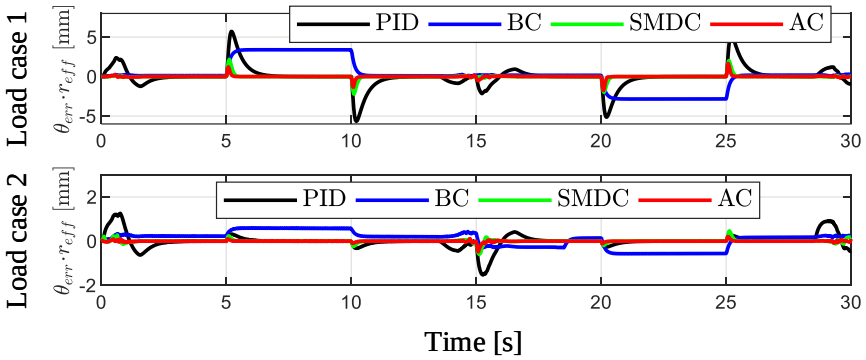

Figure 7.10: Tracking error for load case 1 and load case 2.

7.5.2 Test Case 2

Test Case 2 imitates a landing situation at the seabed by using the AHC mode. The simulation results for both the PID controller, the BC, the SMDC and the AC are shown in Figure 7.11. Plot 1 shows the drum position and the reference trajectory, Plot 2 shows the tracking error, Plot 3 shows the payload position, Plot 4 shows the payload velocity together with the vessel velocity and Plot 5 shows the lower wire force, F_{w2}, together with the seabed interaction force, F_N. Note that the tracking error in Plot 2 is transformed from the rotation domain into the translation domain by multiplying the error in radians by the effective radius, $\theta_{err} \cdot r_{eff}$.

The payload starts at approximately -995 m and is landed at the seabed at -1000 m. In the first 10 s, the drum is at rest and the payload moves up and down with the vessel motion. This can be seen in plot 4 where the payload speed matches the vessel speed. After 10 s, the AHC system is activated and the payload is stabilized at a constant depth. Hence, the payload speed approaches 0 m/s and the payload position is almost constant. The zoomed window in Plot 3 shows the payload position in 15 s after the AHC system is activated. After 30 s, the lowering phase starts. The payload touches the seabed after approximately 52 s and the winch drum keeps paying out wire in order to slowly remove the tension in the wire rope. The wire tension is fully removed after approximately 62 s.

The simulation results show that all controllers provide high controllability. The AHC system is capable of reducing the payload motion to below ± 1 cm for all controllers. This can be seen in the zoomed window in Plot 3. The SMDC and the AC show the best compensation efficiency. For the SMDC and the AC, the payload is stabilized at a constant depth when the time approaches 30 s.

The tracking error is shown in Plot 2. All controllers have a step in the tracking error when starting the AHC mode. This step occurs because the vessel motion is subtracted instantaneously from the reference trajectory. This results in a step in the desired drum position and therefore also a step in the tracking error. A smoother start-up of the AHC

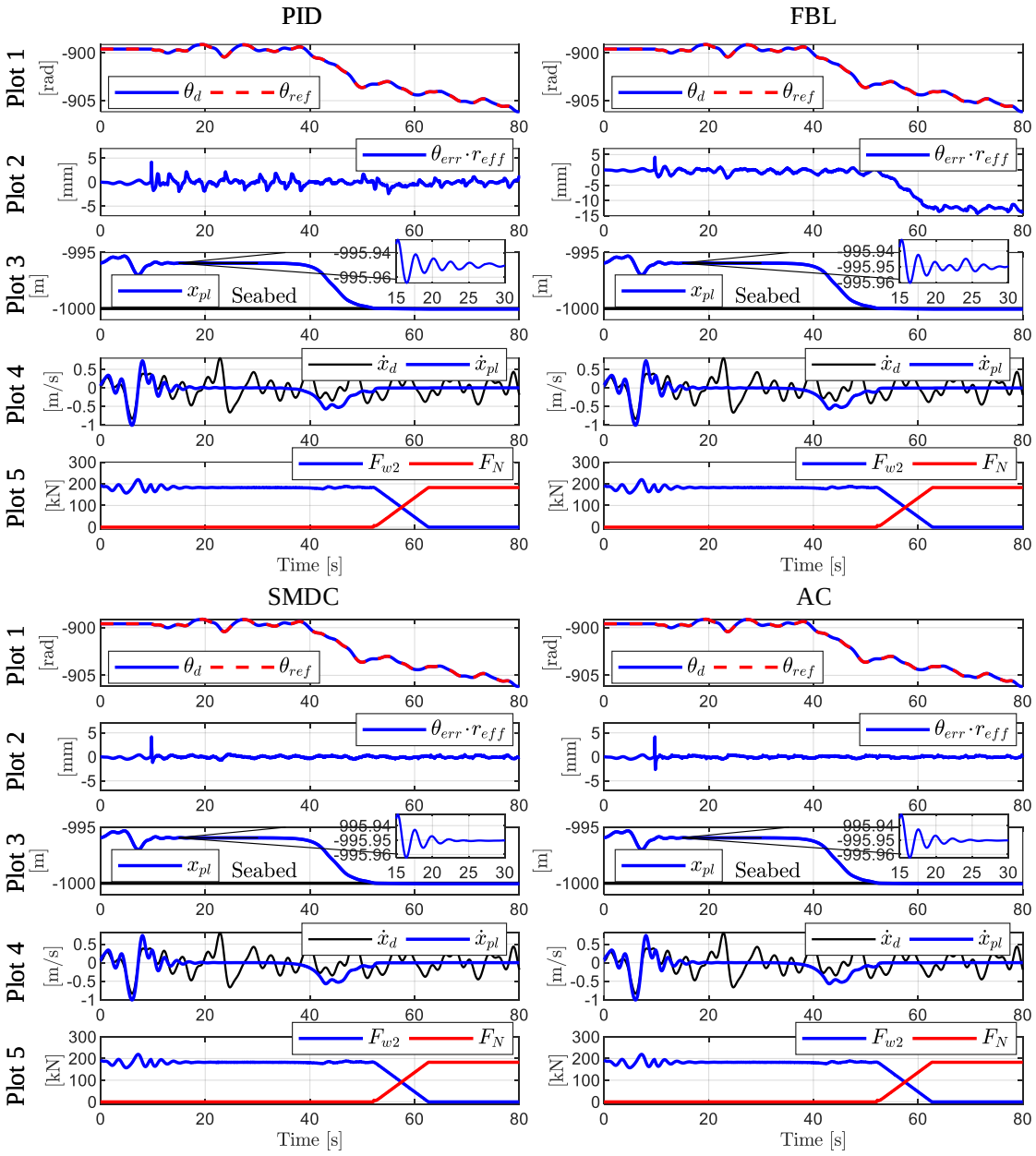

Figure 7.11: Simulation results Test Case 2.

mode will reduce the tracking error when starting the AHC mode. After the AHC mode is activated, the tracking performance is worst for the BC and best for the SMDC and the AC. The tracking error is below ±2 mm for the PID controller and below ±1 mm for the SMDC and the AC. The tracking error for the BC differs from the others controllers when the payload touches the ground. This is because the estimated parameters $\hat{b}$ and $\hat{f}$ used in the BC do not include the interaction force between the payload and the seabed. The model and the real system is therefore not the same after the payload touches the ground which results in increased tracking error.

The payload is in all cases landed with a low landing speed, less than 0.1 m/s, resulting in a low impact force.

Discussion

Figure 7.12 shows the tracking error from all controllers plotted in the same plot. The results show that the SMDC and the AC have the best controllability and that the BC controller has the worst controllability due to the high error that occurs after the payload touches the seabed. However, the high tracking performance for the SMDC and the

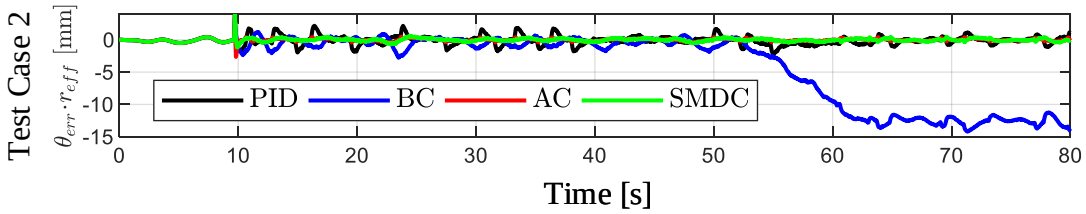

Figure 7.12: Tracking error Test Case 2.

AC comes at the cost of high controller effort and more frequent reactivation of cylinder chambers. This is shown in Figure 7.13 where the torque contribution from every single cylinder is plotted for a selected time period, from 48 s to 50 s respectively. The plotted cylinder contributions represent the typical characteristics. Multiple vertical lines with the same color consecutively indicate that the cylinder is reactivated multiple times. It can be seen that the cylinders for the PID controller and BC are reactivated less often than the SMDC and the AC. The SMDC is the controller that reactivates cylinders most often. Reactivation of cylinder chambers introduces losses in the system and should be minimized.

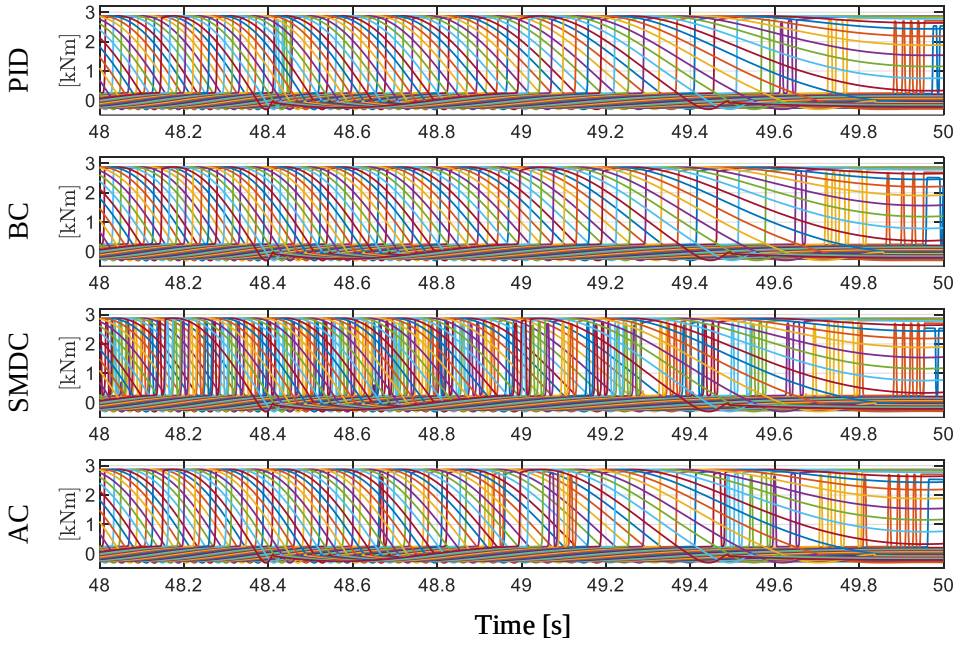

Figure 7.13: Torque contribution from each cylinder chamber in Test Case 2.

7.5.3 Test Case 3

Test Case 3 imitates landing of a 20000 kg payload at the seabed with the use of the CT mode. Figure 7.14 shows the simulation results. The desired tension F_{ref} is set to 99.5 % of the payload's weight in water. Plot 1 shows the lower wire force, F_{w2}, the desired wire

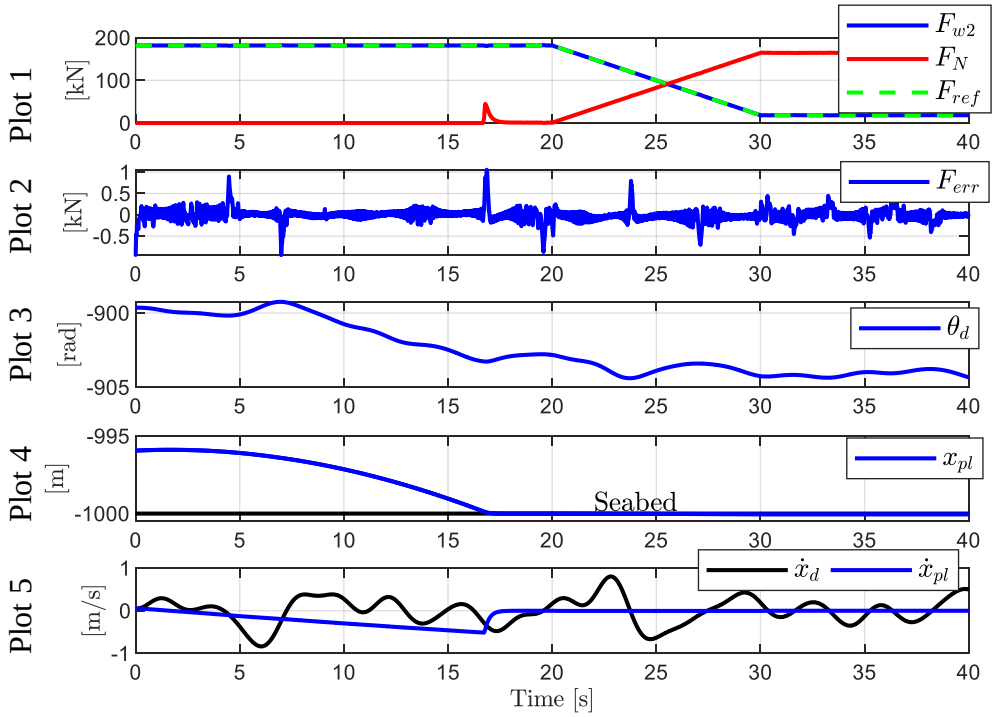

Figure 7.14: Simulation result Test Case 3.

tension, F_{ref}, and the seabed interaction force, F_N, Plot 2 shows the tracking error, Plot 3 shows the drum position, Plot 4 shows the payload position and Plot 5 shows the payload velocity together with the velocity of the vessel.

The simulation results show that the wire tension follows the desired wire tension well. The tracking error is kept below 1 kN which is less than the 8 kN requirement. The payload is landed after approximately 17 s at a velocity of approximately -0.5 m/s. This is a relatively high speed, but the impact force, shown by the peak in the red line in Plot 1, is relatively low. After 20 s, the wire tension is slowly reduced. In Plot 4 and Plot 5 it can be seen that the payload has a smooth motion without any disturbance from the vessel motion.

The desired wire tension is close to the wire tension needed to keep the payload at rest in water. However, the payload's landing speed is still quite high. This is because the simulated payload is solid with a mass density of 6200 kg/m^3. This results in a low buoyancy and drag force relative to the mass of the payload. Also, if the payload had been positioned closer to the seabed before starting the CT mode, the payload would not reach the same high speed.

If the diameter of the payload is doubled and the mass is kept constant, the mass density will be reduced to 1550 kg/m^3. This will result in a higher drag force and a higher buoyancy force in addition to a lower wire tension and lower payload velocity. This is shown in Figure 7.15 where the light colors show the simulation results when the payload diameter is doubled. The desired wire tension is in both cases set to 99.5 % of

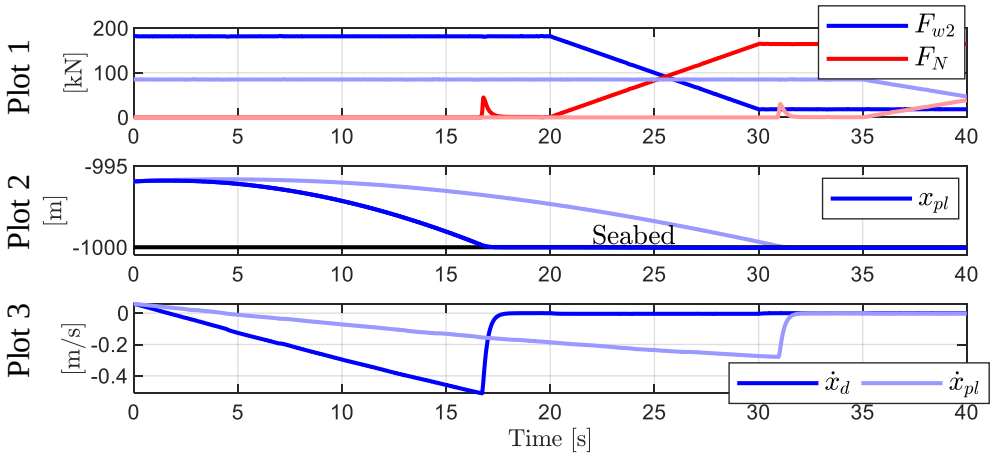

Figure 7.15: Simulation result Test Case 3 where the dark colors show results from the original system and the light colors show results when the payload diameter is doubled.

the wire tension needed to hold the payload in water. It can be seen that the landing speed for the payload with double diameter is halved. The reduced landing speed results in reduced impact force during landing. This can be seen by comparing the peak in the dark red line, occurring after 17 s, to the peak in the light red line, occurring after 31 s, in Plot 1.

The impact force during landing shown in Figure 7.14 is low, even though the landing speed is relatively high. One of the reasons that the impact force is low, is that most of the weight of the payload is held by the wire and the buoyancy force. However, the seabed dynamics also affects the impact force. The seabed stiffness depends, off course, on the content of the soil. In the simulated case, when the payload is placed at the seabed with slack wire, the payload sinks 4 cm into the seabed. If the stiffness is increased by a factor of 10, the impact force will be as shown by the light red color in Plot 1 in Figure 7.16. Note that the damping ratio is kept constant. It can be seen that the impact force is increased. However, the impact force is still below the interaction force between the payload and seabed when the wire is slack.

The damping ratio of the seabed will also affect the impact force during landing. If the seabed is assumed to be underdamped, the payload may bounce back up when it hits the ground. This situation is shown in Figure 7.17. The light colors show simulation results when the damping ratio is set to 0.5 with the mass of the payload equal to 20000 kg. The original damping ratio is 1.75 with a mass of the payload equal to 20000 kg. It can be

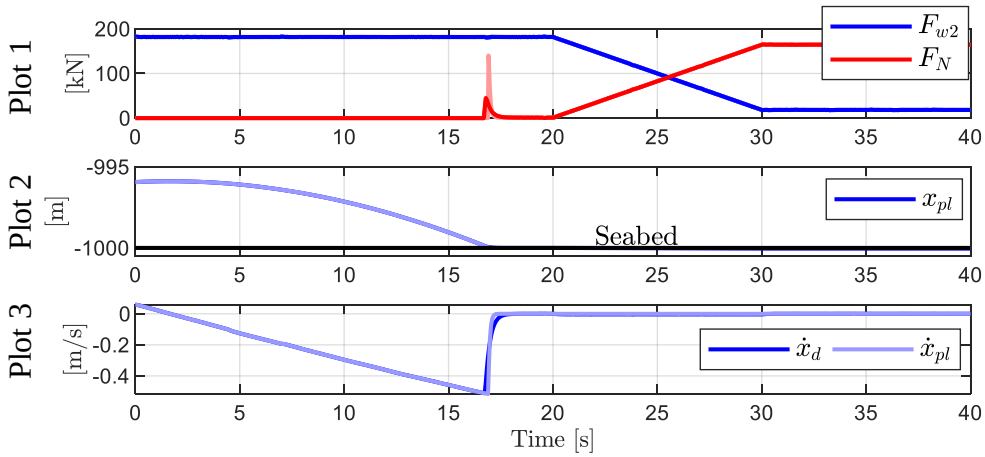

Figure 7.16: Simulation result Test Case 3 where the dark colors show results from the original system and the light colors show results when the seabed stiffness is increased by a factor of 10 and the damping ratio is kept constant.

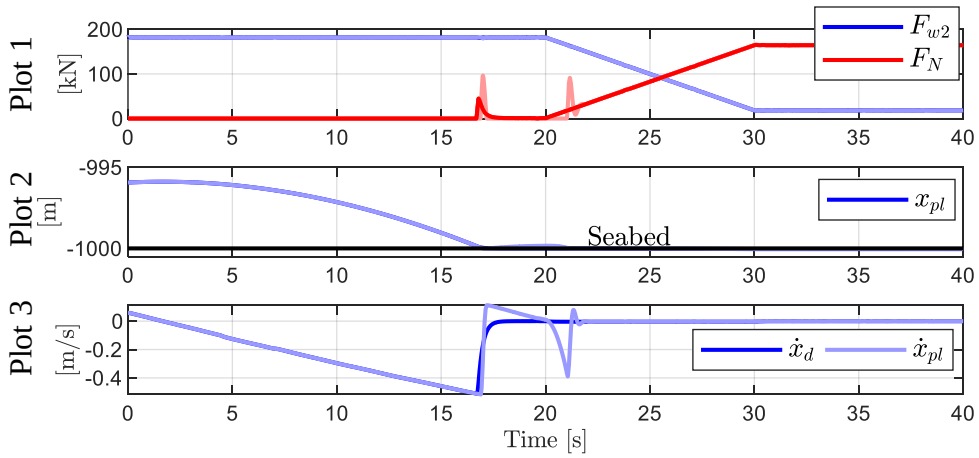

Figure 7.17: Simulation result Test Case 3 where the dark colors show results from the original system and the light colors show results when the seabed dynamic is underdamped.

seen that the impact force during landing is higher when the damping ratio is reduced. For the case where the damping ratio is reduced, light colors, it can also be seen that the payload velocity becomes positive after the payload touches the ground. This means that the payload is lifted from the ground. This can also be seen in Plot 2, where the payload position increases after the payload hits the ground. The peak that occurs in the interaction force between the payload and the seabed after 21 s, shown in the light red line in Plot 1, is because the payload hits the ground for the second time.

The simulation results of the tension controller show that the controllability is high and the tracking error is less than the requirement of 8 kN. The disturbance from the vessel motion and the interaction force from the seabed have a small influence on the tracking error. The impact force is also low. However, the impact force is affected by the content of the soil and also the payload itself. A stiff seabed and payload will have higher

interaction force than a more soft seabed and payload.

7.6 Discussion

This section discusses the motion controllers with respect to performance, robustness and implementation challenges. The tension controller is not included in this section. The results from the tension controller are shown in Section 7.5.3.

7.6.1 Performance

All motion controllers showed good controllability and good tracking performance, however there are some differences. The simulation results show that the tracking performance for the SMDC and the AC is better than the tracking performance for the PID and the BC controller. When operating with constant speed, the tracking error for the SMDC, AC and PID controllers approached zero while the BC has a steady-state error. The high tracking performance for the SMDC and the AC result in higher control effort and thereby more frequent reactivation of cylinder chambers. The SMDC reactivates the cylinders most often.

This simulation study shows that the digital displacement winch drive system can achieve good tracking performance. The good tracking performance reduces the payload motion below $\pm$ 1 cm for all controllers when the AHC system is activate. This motion is below the requirement of $\pm$ 5 cm. However, a perfect tracking of the reference signal does not necessarily result in perfect heave compensation. For successful implementation of the AHC system, it is important to measure or estimate the vessel motion precisely and in real time. The applied reference trajectory must reflect the real vessel motion. An error in the reference signal will result in a compensation error.

7.6.2 Robustness

The robustness against external forces for the motion controllers is tested by applying an external force in Test Case 1. The results show that the SMDC and AC are very robust against external forces, while the PID controller and the BC are less robust. The SMDC and the AC have a maximum tracking error below 2 mm when applying the external load in load case 1. The PID and the BC have a maximum tracking error of 5.5 mm and 3.5 mm respectively.

7.6.3 Implementation

All controllers require a reference trajectory of the drum position and velocity in addition to measurements of the drum position and velocity. The BC, SMDC and the AC also need reference trajectory of the acceleration. Also, the BC and the SMDC require measurements of the payload's mass while the AC requires measurements of the drum acceleration.

The BC requires only two control parameters while the PID controller requires three. In addition, the BC requires system knowledge due to the estimation of the system parameters. On the other hand, the tracking performance of the PID controller is affected by the mass of the payload, which may increase the complexity of tuning the PID controller. The AC has three control parameters while the SMDC has four. The control parameter p_0 in the AC is relatively easy to tune by trial and error. However, p_0 should not be chosen too small or too large. A low value may result in a slow convergence of the model parameters and a large value may result in an oscillatory behavior and slow convergence. Tuning of the control parameters L and ϵ in the SMDC is also relatively simple. Several combinations gives satisfactory results but one should remember that L must be chosen to satisfy Equation 7.33. A large value of L and a small value of ϵ result in good tracking performance but also high control effort with frequent reactivation of cylinder chambers. L and ϵ should therefore be chosen based on a compromise between tracking performance and control effort.

The convergence of the estimated parameters in the AC and also the stability of the system is depending on the signals in the system, $\mathbf{W}$, which consists of the desired displacement ratio, D_m. For example, when lowering the load several thousand meters, the desired displacement ratio will be relatively constant and the estimated parameters, $\hat{b}$ and $\hat{f}$ may not converge to its real values. This may result in an unstable system. If the AC controller is implemented in a real system, one should include a safety function that resets the model parameters estimated by the gradient based adaption law, shown in Equation 7.42, to the parameters estimated for the BC if the deviation becomes too large.

Chapter 8

Conclusion

The work presented in this thesis focuses on the design of a control system for a digital displacement winch drive system. The digital displacement winch drive system consists of a high torque low speed DDM directly connected to the winch drum through a pinion and gear ring. The DDM is supplied by a high and low pressure source, in a so called secondary controlled system.

Objective A was to analyze the transient and steady-state response for the full stroke, partial stroke and sequential partial stroke displacement strategy. During this work, the partial stroke displacement strategy was further developed into a second version. This new version was also included in the transient and steady steady-state response analysis. The results of the analysis showed that the transient response of the full stroke displacement strategy and partial stroke displacement strategy 1 are highly affected by the operation speed. If high controllability is important, those two displacement strategies are most suited for use in high speed motors. The transient response of both the partial stroke displacement strategy 2 and the sequential partial stroke displacement strategy are not affected by the shaft speed and provides high controllability at low speeds. The steady-state response for all displacement strategies is affected by the number of cylinders, the desired displacement ratio and the shaft speed.

Objective B was to design and build an experimental test setup that can be used to validate simulation models and experimentally test displacement strategies in a high torque low speed digital displacement motor. The experimental test setup consists of a modified radial piston motor. The motor is modified to operate with the digital displacement technology on a single cylinder. All the displacement strategies investigated in Objective A have been experimentally tested, and the simulation model of the DDM has been validated.

Objective C was to investigate requirements regarding valve timing accuracy. For the DDM to operate with high energy efficiency and low pressure and torque peaks, it

is essential with accurate switching of the on/off valves. A valve that opens too early or too late will introduce unnecessarily high energy losses and pressure and flow peaks in the system. The results showed that the required accuracy is stricter for high speed operation compared to low speed operation. For example, the valves should be activated within ± 0.3 ms when operating at 1000 rpm and within ± 30 ms when operating at 10 rpm.

One of the reasons why control design of DDMs differs from traditional hydraulic motors is that the same displacement ratio can be achieved by multiple displacement strategies. Also, different displacement strategies have different characteristics. Objective D was, therefore, to study subsea winch operations and design performance requirements for the winch drive system. The presented work showed that a winch drive system must handle frequent starts and stops, frequent change in the direction of rotation, full four quadrant operation and low speed operation. In addition, the winch drive system must provide good motion and tension control. Based on those requirements and the work presented in Objective A, a suitable displacement strategy for use in a digital displacement winch drive system was selected. Both the partial stroke displacement strategy 2 and the sequential partial stroke displacement strategy can provide high controllability at low speeds, four quadrant operations and frequently change the direction of rotation. However, the partial stroke displacement strategy 2 was considered to be the most suited displacement strategy because the sequential partial stroke displacement strategy is known to switch the valves most often resulting in the lowest energy efficiency.

A displacement strategy converts the desired motor displacement into valve activation signals. For the partial stroke displacement strategy 2, one unique valve timing strategy is needed for each operation quadrant. A control system for switching between operation quadrants has therefore been developed. The developed switching controller selects the proper operation quadrant based on the direction of rotation of the DDM and the desired displacement ratio.

Objective E was to design a full controller for the digital displacement winch drive system. In all, four motion controllers and a wire tension controller have been designed. All controllers utilize the partial stroke displacement strategy 2. The motion controllers are a conventional PID controller, a PD controller with feedback linearization also called the base controller, a sliding mode disturbance controller and an adaptive controller. The PID controller and the base controller showed the lowest robustness to external force disturbance and the poorest controllability performance. The sliding mode disturbance controller and the adaptive controller showed very good motion tracking performance. However, the high tracking performance resulted in increased controller effort in the form of more often reactivation of cylinder chambers, especially for the sliding mode disturbance compensator. The tension controller is a PI controller with wire tension feedback. The

simulation results showed good controllability for the tension controller.

The work presented in this thesis shows that the proposed digital displacement winch drive system is suited for driving offshore winches. The secondary controlled DDM has shown good controllability, both for motion control and wire tension control. The proposed digital displacement winch drive system includes the benefits from both the conventional open and closed circuit hydraulic systems. Those benefits are the potential of regenerating braking energy, the possibility of using one hydraulic power unit to supply multiple actuators in addition to improve the energy efficiency of existing systems.

8.1 Future Work

The work presented in this thesis considers control development. The controllers have been tested in simulations. The next step should be to modify all the cylinders on a conventional hydraulic motor and experimentally test the designed controllers. Also, the energy efficiency of the partial stroke displacement strategy 2 and the sequential partial stroke displacement strategy should be examined.

The designed controller utilizes one displacement strategy during operation. However, there might be cases where it is beneficial to utilize different displacement strategies in different parts of a lift. For example, when hoisting through the water column controllability may be of low importance and energy efficiency may be of high importance. In that case, it may be beneficial to use the full stroke displacement strategy during the hoisting phase and another displacement strategy when controllability is of high interest, like for example, during landing. This is something that should be investigated in the future in order to show the full potential of the digital displacement winch drive system.

Recently there has been a trend of replacing hydraulic drive systems with electric drive systems. In the future, it will be interesting to compare an electric winch drive system to a digital hydraulic winch drive system.

Bibliography

[1] Offshore cranes. https://www.macgregor.com/Products-solutions/products/offshore-and-subsea-load-handling/offshore-cranes/. Accessed: 25-01-2019.

[2] Xingui Liang and Tapio Virvalo. What's wrong with energy utilization in hydraulic cranes. In *The 5th international conference on fluid power transmission and control*, 2001.

[3] JK Woodacre, RJ Bauer, and RA Irani. A review of vertical motion heave compensation systems. *Ocean Engineering*, 104:140–154, 2015.

[4] Pat Jones. Maximizing hydraulic efficiency. https://www.design-engineering.com/features/maximizing-hydraulic-efficiency/, 2012. Accessed: 14-08-2019.

[5] Hydra-Tech Pumps. Hydraulic circuits, open vs. closed. https://hydra-tech.com/hydraulic-circuits-open-vs-closed/, 2017. Accessed: 14-08-2019.

[6] When to apply digital HTLS motors. https://www.diinef.com/technology-benefits. Accessed: 20-06-2019.

[7] Staffa motor, fixed and dual displacement radial piston motors. http://www.hydrofitgroup.com/pdf/staffaproductpverview.pdf. Accessed: 20-06-2019.

[8] Grégory S. Payne, Uwe B.P. Stein, Mohammad Ehsan, Niall J. Caldwell, and Win Rampen. Potential of digital displacement hydraulics for wave energy conversion. In *Proceedings of the sixth European wave and tidal energy conference, Glasgow*, 2005.

[9] G. S. Payne, A. E. Kiprakis, M. Ehsan, W. H. S. Rampen, J. P. Chick, and A. R. Wallace. Efficiency and dynamic performance of digital displacement^{TM} hydraulic transmission in tidal current energy converters. *Proceedings of the Institution of Mechanical Engineers, Part A: Journal of Power and Energy*, 221(2):207–218, 2007.

[10] Md. Ehsan, W. H. S. Rampen, and S. H. Salter. Modeling of Digital-Displacement Pump-Motors and Their Application as Hydraulic Drives for Nonuniform Loads . *Journal of dynamic systems, measurement, and control*, 122(1):210–215, 2000.

[11] Matti Linjama. Digital fluid power: State of the art. In *12th Scandinavian International Conference on Fluid Power, Tampere, Finland, May*, pages 18–20, 2011.

[12] Niels Henrik Pedersen. *Development of Control Strategies For Digital Displacement Units*. Ph.d. thesis, Aalborg University, Denmark, August 2018.

[13] How it works. `https://www.diinef.com/technology`. Accessed: 20-06-2019.

[14] Win Rampen. The Development of Digital Displacement Technology. In *Proceedings of the ASME/BATH Symp. on Fluid Power & Motion Control*, pages 11–16, 2010. keynote address.

[15] Win Rampen. Gearless Transmissions for Large Wind Turbines - The History and Future of Hydraulic Drives. *Artemis Intelligent Power Ltd.*, 2006.

[16] Michael A. Holland. *Design of Digital Pump/Motor and Experimental Validation of Operating Strategies*. Ph.D. thesis, Purdue University, Indiana, USA, August 2012.

[17] Brian S. R. Armstrong and Qinghui Yuan. Multi-level control of hydraulic gerotor motors and pumps. In *2006 American Control Conference*, pages 8–pp. IEEE, 2006.

[18] Henrik B. Larsen, Magnus Kjelland, Anders Holland, and Per N. Lindholdt. Digital Hydraulic Winch Drives. In *BATH/ASME 2018 Symposium on Fluid Power and Motion Control, Bath, UK*, pages V001T01A028–V001T01A028. American Society of Mechanical Engineers, 2018.

[19] Kyle Joseph Merrill. *Modeling and Analysis of Active Valves Control of a Digital Pump-Motor*. Ph.D. thesis, Purdue University, Indiana, USA, August 2012.

[20] Kyle J. Merrill, Farid Y. Breidi, and John Lumkes. Simulation Based Design and Optimization of Digital Pump/Motors. In *ASME/BATH 2013 Symposium on Fluid Power and Motion Control*, pages V001T01A045–V001T01A045. American Society of Mechanical Engineers, 2013.

[21] K. Merrill, M. Holland, and J. H. Lumkes. Analysis of digital pump/motor operating strategies. In *Proceedings of the 52nd National Conference on Fluid Power*, 2011.

[22] K. Merrill and J. Lumkes. Operating strategies and valve requirements for digital pump/motors. In *Proceedings of the 6th FPNI-PhD Symposium, West Lafayette*, pages 249–258, 2010.

[23] Farid Breidi, Tyler Helmus, and John Lumkes. High Efficiency Digital Pump/Motor. In *2015 Fluid Power Innovation & Research Conference (FPIRC15)*, 2015.

[24] Niels Henrik Pedersen, Per Johansen, and Torben Ole Andersen. Challenges with respect to control of digital displacement hydraulic units. *Modeling, Identification and Control*, 39(2):91–105, 2018.

[25] Christian Nørgård. *Design, optimization and testing of valves for digital displacement machines*. Ph.D. thesis, Aalborg University, 2017.

[26] Daniel Rømer, Per Johansen, Henrik C Pedersen, and Torben Ole Andersen. Analysis of valve requirements for high-efficiency digital displacement fluid power motors. In *8th International Conference on Fluid Power Transmission and Control, ICFP 2013*, pages 122–126. World Publishing Cooperation, 2013.

[27] Toshihide Noguchi, Haruhiko Hirano, Shinji Kawabata, Masayuki Shimizu, Toshikazu Hayashi, Uwe Stein, Gordon Voller, and William Rampen. Poppet valve, hydraulic machine, and power generating apparatus of renewable-energy type, December 21 2016. EP 3 106 724 A1.

[28] Stephen Laird, Onno Kuttler, and Luke Wadsley. Fluid distribution valve, May 19 2010. EP 2 187 104 B1.

[29] Uwe Bernhard Pascal Stein. Fluid-working machine, June 24 2014. US Patent 8,757,583.

[30] Bernd Winkler and Rudolf Scheidl. Development of a fast seat type switching valve for big flow rates. *The Tenth Scandinavian International Conference on Fluid Power, SICFP'07, Tampere, Finland*, 2:137–146, 2007.

[31] Bernd Winkler, Andreas Ploeckinger, and Rudolf Scheidl. A novel piloted fast switching multi poppet valve. *International journal of fluid power*, 11(3):7–14, 2010.

[32] Thomas Zehetbauer, Paul Foschum, Andreas Plöckinger, and Bernd Winkler. Advancement and demonstration of the new generation of LCM's FSVi4.1. In *Proceedings of The Ninth Workshop on Digital Fluid Power, Aalborg, Denmark*, 2017.

[33] Bernd Winkler. Recent advances in digital hydraulic components and applications. In *Proceedings of The Ninth Workshop on Digital Fluid Power, Aalborg, Denmark*, 2017.

[34] Daniel Beck Roemer, Per Johansen, Michael Møller Bech, and Henrik C Pedersen. Simulation and experimental testing of an actuator for a fast switching on-off valve suitable to efficient displacement machines. In *9th JFPS International Symposium on Fluid Power*. Japan Fluid Power System Society, 2014.

[35] Christian Nørgård, Michael M Bech, Jeppe H Christensen, and Torben Ole Andersen. Modeling and validation of moving coil actuated valve for digital displacement machines. *IEEE Transactions on Industrial Electronics*, 65(11):8749–8757, 2018.

[36] Christian Nørgård, Esben L Madsen, Janus MT Joergensen, Jeppe H Christensen, and Michael M Bech. Test of a novel moving magnet actuated seat valve for digital displacement fluid power machines. *IEEE/ASME Transactions on Mechatronics*, 23(5):2229–2239, 2018.

[37] Rexroth Bosch Group. Directional spool valves, direct operated, with solenoid actuation, fast switching. Datasheet. Edition:2014-08.

[38] American Society of Mechanical Engineers. *An Approach to Digital Distributor Valves in Low Speed Pumps and Motors*, volume ASME/BATH 2014 Symposium on Fluid Power and Motion Control of *Fluid Power Systems Technology*, 09 2014. V001T01A041.

[39] Bernd Winkler, Andreas Plöckinger, and Rudolf Scheidl. State of the art in digital valve technology. In *Proceedings–The Seventh Workshop on Digital Fluid Power*, pages 151–163, 2015.

[40] Miikka Ketonen and Matti Linjama. High flowrate digital hydraulic valve system. In *Proceedings of The Ninth Workshop on Digital Fluid Power, Aalborg, Denmark*, 2017.

[41] Mikko Heikkilä and Linjama Matti. Direct connection of digital hydraulic power management system and double acting cylinder - a simulation study. In *Proceedings of The Fourth Workshop on Digital Fluid Power, Linz, Austria*, September 2011.

[42] Mateusz Sniegucki, Markus Gottfried, and Uwe Klingauf. Optimal Control of Digital Hydraulic Drives using Mixed-Integer Quadratic Programming. *IFAC Proceedings Volumes*, 46(23):827–832, 2013. 9th IFAC Symposium on Nonlinear Control Systems.

[43] Niels H Pedersen, Per Johansen, and Torben O Andersen. Feedback Control of Puls-Density Modulated Digital Displacement Transmission using a Continuous Approximation. *IEEE/ASME Transactions on Mechatronics*, 2018. Under 3rd revision.

[44] Per Johansen, Daniel B. Roemer, Torben O. Andersen, and Henrik C. Pedersen. Discrete Linear Time Invariant Analysis of Digital Fluid Power Pump Flow Control. *Journal of Dynamic Systems, Measurement, and Control*, 139(10):101007, 2017.

[45] Niels H Pedersen, Per Johansen, and Torben O Andersen. Event-driven control of a speed varying digital displacement machine. In *ASME/BATH 2017 Symposium*

on Fluid Power and Motion Control, pages V001T01A029–V001T01A029. American Society of Mechanical Engineers, 2017.

[46] Niels H Pedersen, Per Johansen, and Torben O Andersen. LQR Feedback Control Development for Wind Turbines Featuring a Digital Fluid Power Transmission System. In *9th FPNI Ph. D. Symposium on Fluid Power*, pages V001T01A024–V001T01A024. American Society of Mechanical Engineers, 2016.

[47] Niels H Pedersen, Per Johansen, and Torben O Andersen. Optimal control of a wind turbine with digital fluid power transmission. *Nonlinear Dynamics*, 91(1):591–607, 2018.

[48] Niels Henrik Pedersen, Per Johansen, and Torben Ole Andersen. Model Predictive Control and Discrete Analysis of Partial Stroke Operated Digital Displacement Unit. In *2018 Global Fluid Power Society PhD Symposium (GFPS)*, pages 1–9. IEEE, 2018.

[49] Niels Henrik Pedersen, Per Johansen, Anders Hedegaard Hansen, and Torben Ole Andersen. Model Predictive Control of Low-Speed Partial Stroke Operated Digital Displacement Pump Unit. *Modeling, Identification and Control*, 39(3):167–177, 2018.

[50] Niels Henrik Pedersen, Per Johansen, Torben O Andersen, and Rudolf Scheidl. Nonlinear hybrid control oriented modelling of a digital displacement machine. In *Proceedings of the 9th Workshop on Digital Fluid Power, Aalborg, Denmark*, pages 7–8, 2017.

[51] Niels H Pedersen, Per Johansen, and Torben O Andersen. Four Quadrant Hybrid Control Oriented Dynamical System Model of Digital Displacement® Units. In *BATH/ASME 2018 Symposium on Fluid Power and Motion Control*, pages V001T01A039–V001T01A039. American Society of Mechanical Engineers, 2018.

[52] Diesel's demise is a long way off for off-road vehicles. `http://www.artemisip.com/diesels-demise-is-a-long-way-off-for-off-road-vehicles/`. Accessed: 20-06-2019.

[53] Excavator development program. `http://artemis.armadillojam.co.uk/hybrid-hydraulic-excavator/`. Accessed: 25-05-2018.

[54] Matthew Green, Jill Macpherson, Niall Caldwell, and WHS Rampen. DEXTER: The Application of a Digital Displacement® Pump to a 16 Tonne Excavator. In *BATH/ASME 2018 Symposium on Fluid Power and Motion Control, Bath, UK*, pages V001T01A047–V001T01A047. American Society of Mechanical Engineers, 2018.

[55] Karl-Eirik Rydberg. Energy Efficient Hydraulic Hybrid Drives. *The 11th Scandinavian Conference on Fluid Power, SICFP'09*, June 2009.

[56] Jamie Taylor, Win Rampen, Alasdair Robertson, and Niall Caldwell. DIGITAL DISPLACEMENT® HYDRAULIC HYBRIDS. In *Presented at the JSAE Annual Congress on*, 2011.

[57] Automotive. `http://www.artemisip.com/sectors/automotive/`. Accessed: 20-06-2019.

[58] Jamie Taylor, Win Rampen, Daniel Abrahams, and Andrew Latham. Demonstration of a digital displacement hydraulic hybrid bus. In *Proceedings 2015 JSAE Annual Congress*. Yokohama, 2015.

[59] MHI acquires Artemis Intelligent Power, a UK venture company, to secure unique hydraulic power drive technology. `https://www.mhi.com/news/story/1012031389.html`. Accessed: 08-05-2018.

[60] Masahide Umaya, Toshihide Noguchi, Michiya Uchida, Masaaki Shibata, Yasuhiro Kawai, and Ryosuke Notomi. Wind Power Generation - Development status of Offshore Wind Turbines -. *Mitsubishi Heavy Industries Technical Review*, 50(3):29, 2013.

[61] Wind turbine assembly starts. `http://www.artemisip.com/wind-turbine-assembly-starts/`. Accessed: 25-05-2018.

[62] Fukushima forward. `http://www.artemisip.com/fukushima-forward/`. Accessed: 25-05-2018.

[63] Mitsubishi launches 7mw turbine. `https://www.windpowermonthly.com/article/1109873/mitsubishi-launches-7mw-turbine`. Accessed: 14-08-2019.

[64] Masashi Sasaki, Atsushi Yuge, Toshikazu Hayashi, Hiroshi Nishino, Michiya Uchida, and Toshihide Noguchi. Large Capacity Hydrostatic Transmission with Variable Displacement. *The 9th International Fluid Power Conference, Aachen, Germany*, 9, March 2014.

[65] Edinburgh technology duo secure £2.5 million to turn wave power into electricity. `http://www.artemisip.com/edinburgh-technology-duo-secure-2-5-million-turn-wave-power-electricity/`. Accessed: 25-05-2018.

[66] Rail. `http://www.artemisip.com/sectors/rail/`. Accessed: 25-05-2018.

[67] Saving fuel in rail vehicles. http://www.artemisip.com/saving-fuel-in-rail-vehicles/. Accessed: 25-05-2018.

[68] Artemis set to test alternative traction system. http://www.artemisip.com/artemis-set-test-alternative-traction-system/. Accessed: 25-05-2018.

[69] Digital displacement cuts energy use. http://www.artemisip.com/wp-content/uploads/2019/03/190325-Railway-Gazette-case-study.pdf. Accessed: 25-08-2019.

[70] Linjama Matti and Kalevi Huhtala. Digital pump-motor with independent outlets. *The 11th Scandinavian Conference on Fluid Power, SICFP'09, Lindköping, Sweden*, June 2009.

[71] Linjama Matti and Jyrki Tammisto. New alternative for digital pump-motor-transformer. In *The Second Workshop on Digital Fluid Power, Linz, Austria*, pages 49–61, November 2009.

[72] Mikko Heikkila, Jyrki Tammisto, Mikko Huova, M Huhtala, and Matti Linjama. Experimental evaluation of a piston-type digital pump-motor-transformer with two independent outlets. *Fluid Power and Motion Control, Bath, England*, pages 83–98, 2010.

[73] Mikko Heikkilä, Jyrki Tammisto, Linjama Matti, and Kalevi Huhtala. Digital hydraulic power management system - measured characteristics of a second prototype. In *Proceedings of the Eight Workshop on Digital Fluid Power, DFP16, Tampere, Finland*, pages 69–81, May 2016.

[74] Mikko Heikkilä and Matti Linjama. Displacement control of a mobile crane using a digital hydraulic power management system. *Mechatronics*, 23(4):452–461, 2013.

[75] Mikko Heikkilä and Matti Linjama. Hydraulic Energy Recovery in Displacement Controlled Digital Hydraulic System. In *13th Scandinavian International Conference on Fluid Power; June 3-5; 2013; Linköping; Sweden*, pages 513–519. Linköping University Electronic Press, 2013.

[76] Mikko Heikkilä, Matti Karvonen, Matti Linjama, Seppo Tikkanen, and Kalevi Huhtala. Comparison of Proportional Control and Displacement Control Using Digital Hydraulic Power Management System. In *ASME/BATH 2014 Symposium on Fluid Power and Motion Control*, pages V001T01A026–V001T01A026. American Society of Mechanical Engineers, 2014.

[77] Mikko Heikkilä, Linjama Matti, and Kalevi Huhtala. Digital Hydraulic Power Management System with Five Independent Outlets - Simulation Study of Displacement Controlled Excavator Crane. *The 9th International Fluid Power Conference, 9, Aachen, Germany*, March 2014.

[78] K.J. Merrill, M.A. Holland, and J.H. Lumkes. Efficiency analysis of a digital pump/-motor as compared to a valve plate design. In *7th International Fluid Power Conference: Workshop Proceedings, Aachen, Germany, Mar*, pages 22–24, 2010.

[79] Farid El Breidi. *Investigation of digital pump/motor control strategies*. Ph.D. thesis, Purdue University, Indiana, USA, August 2016.

[80] Daniel Beck Rømer. *Design and optimization of fast switching valves for large scale digital hydraulic motors*. Ph.D. thesis, Department of Energy Technology, Aalborg University, 2014.

[81] Worlds first digital htls motor at norshipping 2017. `https://www.diinef.com/single-post/2017/09/26/Worlds-first-digital-HTLS-motor-at-Nordshipping`. Accessed: 20-06-2019.

[82] Per Lindholdt, Henrik B. Larsen, and AS Diinef. Digital distributor valves in low speed motors–practical approach. In *Proceedings of The Ninth Workshop on Digital Fluid Power, Aalborg, Denmark*, 2017.

[83] Macgregor granted maroff support for digiwin project. `https://www.diinef.com/single-post/2015/11/28/Time-is-Money`. Accessed: 20-06-2019.

[84] Michael Rygaard Hansen. In Compendium *Fluid Mechanics*. Department of Engineering, University of Agder, Norway, Lecture notes MAS126, 2015; pp. 28–30.

[85] Per Johansen, Daniel Beck Roemer, Torben Ole Andersen, and Henrik C Pedersen. Delta-sigma modulated displacement of a digital fluid power pump. In *7th Workshop on Digital Fluid Power*, pages 1–9. LCM GmbH, 2015.

[86] Christian Nørgård, Jeppe H Christensen, and Michael M Beck. Test rig for valves of digital displacement machines. In *Proceedings of The Ninth Workshop on Digital Fluid Power, Aalborg, Denmark*, 2017.

[87] DNV GL. *DNVGL-RP-N201 Lifting Appliances used in subsea operations*, 6 2017.

[88] Kongsberg Maritime AS. *MRU 5th generation - Motion reference for any need*, 11 2013.

[89] Liujun Li and Shaojun Liu. Modeling and simulation of active-controlled heave compensation system of deep-sea mining based on dynamic vibration absorber. In *2009 International Conference on Mechatronics and Automation*, pages 1337–1341. IEEE, 2009.

[90] J. T. Hatleskog and M. W. Dunnigan. Active Heave Crown Compensation Sub-System. In *OCEANS 2007-Europe*, pages 1–6. IEEE, 2007.

[91] Philip Bennett. Active heave: The benefits to operations as seen in the north sea. In *SPE/IADC drilling conference*. Society of Petroleum Engineers, 1997.

[92] Umesh A. Korde. Active heave compensation on drill-ships in irregular waves. *Ocean engineering*, 25(7):541–561, 1998.

[93] Peter Gu, Ahmed Ahmed Walid, Yousef Iskandarani, and Hamid Reza Karimi. Modeling, simulation and design optimization of a hoisting rig active heave compensation system. *International Journal of Machine Learning and Cybernetics*, 4(2):85–98, 2013.

[94] T. Martinsen and A. Totland. *The Engineers Guide, Second Edition*. Safelink AS, Norway: 68, 70-5, 2012.

[95] DNV GL. *DNVGL-RP-N103 Modelling and analysis of marine operation*, 7 2017.

[96] DNV GL. *DNVGL-ST-0378 Standard for offshore and platform lifting appliances*, 5 2016.

[97] Willard J Pierson and Lionel Moskowitz. A proposed spectral form for fully developed wind seas based on the similarity theory of sa kitaigorodskii. *Journal of geophysical research*, 69(24):5181–5190, 1964.

[98] Sondre Sanden Tordal, Per-Ove Løvsland, and Geir Hovland. Testing of wireless sensor performance in vessel-to-vessel motion compensation. In *IECON 2016-42nd Annual Conference of the IEEE Industrial Electronics Society*, pages 654–659. IEEE, 2016.

[99] Magnus B. Kjelland and Michael R. Hansen. Offshore Wind Payload Transfer Using Flexible Mobile Crane. *Modeling, Identification and Control*, 36(1):1–9, 2015.

[100] Zhou Entao, Yang Wenlin, and Lin Junzhe. Predictive control of hydraulic winch motion control. In *2009 2nd IEEE International Conference on Computer Science and Information Technology*, pages 1–4. IEEE, 2009.

[101] Stian Skjong and Eilif Pedersen. Model-based control designs for offshore hydraulic winch systems. *Ocean Engineering*, 121:224–238, 2016.

[102] Lasse Schmidt, Torben O Andersen, Per Johansen, and Henrik C Pedersen. A Robust Control Concept for Hydraulic Drives Based on Second Order Sliding Mode Disturbance Compensation. In *ASME/BATH 2017 Symposium on Fluid Power and Motion Control*, pages V001T01A033–V001T01A033. American Society of Mechanical Engineers, 2017.

[103] Lasse Schmidt, Torben O Andersen, Henrik C Pedersen, and Michael M Bech. An Arbitrary Order Adaptive Control Structure With Application to a Hydraulic Winch Drive. In *ASME/BATH 2017 Symposium on Fluid Power and Motion Control*, pages V001T01A035–V001T01A035. American Society of Mechanical Engineers, 2017.

[104] Tor A. Johansen, Thor I. Fossen, Svein I. Sagatun, and Finn G. Nielsen. Wave synchronizing crane control during water entry in offshore moonpool operations - experimental results. *IEEE Journal of Oceanic Engineering*, 28(4):720–728, 2003.

[105] Jorg Neupert, Tobias Mahl, Bertrand Haessig, Oliver Sawodny, and Klaus Schneider. A heave compensation approach for offshore cranes. In *2008 American Control Conference*, pages 538–543. IEEE, 2008.

[106] Markus Richter, Eckhard Arnold, Klaus Schneider, Johannes K. Eberharter, and Oliver Sawodny. Model predictive trajectory planning with fallback-strategy for an active Heave Compensation system. In *2014 American Control Conference*, pages 1919–1924. IEEE, 2014.

[107] Qi Chen, Wei Li, and Genshe Chen. FUZZY P+ID Controller for a Constant Tension Winch in a Cable Laying System. *IEEE Transactions on Industrial Electronics*, 64(4):2924–2932, 2016.

[108] Thuong Kim Than, Ivar Langen, and Oddvar Birkeland. Modelling and simulation of offshore crane operations on a floating production vessel. In *The Twelfth International Offshore and Polar Engineering Conference, Kitakyushu, Japan*. International Society of Offshore and Polar Engineers, 2002.

[109] J. Komsta, J. Adamy, and P. Antoszkiewicz. Input-output linearization and integral sliding mode disturbance compensation for electro-hydraulic drives. In *2010 11th International Workshop on Variable Structure Systems (VSS)*, pages 446–451, June 2010.

[110] Michael Rygaard Hansen, Torben Ole Andersen, and Henrik Clemmensen Pedersen. Robust control of a hydraulically actuated manipulator using sliding mode control. In *Fluid Power Transmission and Control ICFP'2005*, pages 864–868, 2005.

[111] Jean-Jacques E. Slotine and Weiping Li. *Applied nonlinear control*. Prentice hall Englewood Cliffs, NJ, 1991.

Paper A

The Potential of a Digital Hydraulic Winch Drive System

Sondre Nordås, Morten Kjeld Ebbesen and Torben Ole Andersen

This paper has been published as:

S. Nordås, M. K. Ebbesen, and T. O. Andersen. The Potential of a Digital Hydraulic Winch Drive System. In *The Proc. of The Ninth Workshop on Digital Fluid Power*, Aalborg, Denmark, 2017.

The Potential of a Digital Hydraulic Winch Drive System

Sondre Nordås*, Morten Kjeld Ebbesen* and Torben Ole Andersen**

*University of Agder
Faculty of Engineering and Science
Jon Lilletunsvei 9, 4879 Grimstad, Norway

** Aalborg University
Faculty of Engineering and Science
Pontoppidanstræde 101, 9220 Aalborg East, Denmark

Abstract **– Digital hydraulic piston pumps and motors have shown the potential of improving efficiency in hydraulic systems. Two independently controlled fast switching on/off valves are connected to each piston chamber and allows for optimal valve timing and independent piston control. Each piston chamber is only pressurized when necessary, resulting in losses that almost scale with motor and pump displacement. This simulation study investigates the potential of using digital hydraulic pumps and motors to increase efficiency in a hydraulic offshore auxiliary winch with a safe working load equal to 20000 kg. One digital hydraulic winch drive system and one conventional hydraulic winch drive system are simulated hoisting two different loads. The payload in the first load case is 18000 kg and the payload in the second load case is 4000 kg. The efficiency and control performance of the two different winch drive systems are then evaluated. The simulation results show that digital hydraulic winch drive systems have the potential of increasing efficiency of hydraulic offshore winches.**

A.1 INTRODUCTION

Hydraulic winches are widely used for various offshore lifting operations. They are for example used in cranes for deck to deck lifting operations, loading and unloading of supply vessels and subsea lifting operations, but they can also be used at the drill floor for small lifting operations.

The working environment on an offshore drilling unit is harsh and sets high requirements for all offshore equipment. The equipment should be light, small in volume and have a minimum of downtime. For example, every extra pound of weight increases the

cost of structural material by 1 - 5$, the platform deck area has a value of approximately 600 - 6 000 $\$/ft^2$ and the cost of a production shutdown ranges from 37500 $\$/h$ for small Gulf of Mexico platforms to 187500 $\$/h$ for large North Sea platforms [1]. Hydraulic actuation systems have normally been used, but because of environmental issues, more energy efficient systems are now required. Electric solutions tend to replace hydraulic solutions in rotational applications. Electrical solutions offer higher efficiency, no risk of oil leakage, high position accuracy, and few maintenance tasks [2]. The benefits of electric motors have to be weighed up against the key features of hydraulic systems. Key features of hydraulic motors and systems are for example high torque density, they can operate in stall conditions without damage, it is easy and efficient to store energy in accumulators, they are tolerant of shock loads due to the compressibility of the hydraulic oil, and the fluid carries away the generated heat to a heat exchanger placed at a convenient place [2]. New research has shown that in addition to the already mentioned benefits of hydraulic motors, the new digital hydraulic pump and motor technology also has the potential of designing highly efficient systems.

Digital hydraulic pump and motor technology can for example be applied to hydraulic hybrid buses and cars [3, 4], tidal current energy converters [5], hydraulic actuated booms [6, 7, 8], and wind turbines [9]. The piston chambers in a digital hydraulic pump (DHP) or a digital hydraulic motor (DHM) can be controlled individually to operate in pump, motor or idle mode. In idle mode, the low-pressure valve is kept open an entire shaft revolution. Hence, a piston chamber in idle mode is never pressurized and leakage losses and friction losses are therefore minimized. Displacement of a DHM is controlled by changing the ratio of pistons running in motor mode and idle mode resulting in losses that scales more with displacement compared to traditional variable displacement piston machines and allowing for high efficiency even at partial displacement.

A.2 SIMULATION MODEL

In this paper, two different winch drive systems are simulated, one conventional hydraulic winch drive system (CHWDS) and one digital hydraulic winch drive system (DHWDS). Both winch drive systems are driving the same winch drum with two different load cases. In the first load case, the payload is equal to 18000 kg and lifted 10 m. The velocity is ramped up to 1 m/s with a ramp time of 2 s. For the second load case, the payload is equal to 4000 kg and lifted 10 m. The velocity is ramped up to 1.5 m/s with a ramp time of 3 s. The two load cases are summarized in Tab. A.1.

Table A.1: Simulation parameters

	Load Case 1	Load Case 2
Mass of load	18000 kg	4000 kg
Hoisting distance	10 m	10 m
Max speed	1 m/s	1.5 m/s
Ramp time	2 s	3 s

A.2.1 Modeling of the Winch

Figure A.1 shows all relevant winch elements. The winch has a drum capacity of 3600 m of wire and a safe working load of 20000 kg. In this study the inertia of the winch and wire wound onto the drum is assumed to be constant because the simulated traveling distance is small compared to the total wire length. It is also assumed that only the outer wire layer is used. Hence the winch radius, r_{winch}, is considered to be constant. Neither friction in the drum nor elasticity in the wire are included.

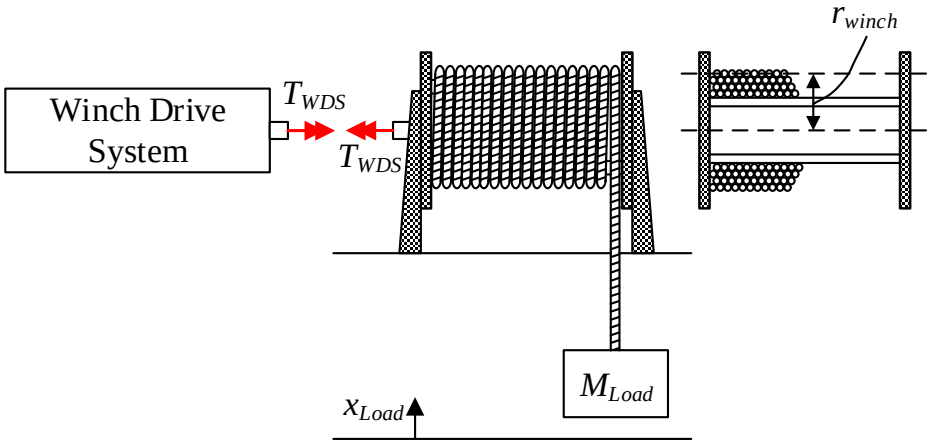

Figure A.1: Mechanical system

The equation of motion for the winch is shown in Eq. A.1.

$$\ddot{\theta}_{drum} = \frac{T_{WDS} - M_{Load} \cdot g \cdot r_{winch}}{J_{eff}} \tag{A.1}$$

where T_{WDS} is the torque from the winch drive system acting on the drum, M_{Load} is the mass of the payload, g is acceleration of gravity, r_{winch} is the radius of the outer winch layer, and J_{eff} is the effective mass moment of inertia. The effective mass moment of inertia is calculated as shown in Eq. A.2.

$$J_{eff} = M_{Load} \cdot r_{winch}^2 + J_{winch} + J_{WDS} \tag{A.2}$$

where J_{winch} includes the inertia of the drum and the wire wound onto the drum and J_{WDS} is the inertia of the drive system that is mechanically connected to the winch drum. The

drive torque, T_{WDS}, for the two different winch drive systems are given in the following sections.

A.2.2 Modeling of the Conventional Hydraulic Winch Drive System

The conventional hydraulic winch drive system is a closed circuit system with one variable displacement over center axial piston pump delivering working fluid to two variable displacement axial piston motors. Figure A.2 illustrates the simulated CHWDS. Line A is the high-pressure side of the motor and line B is the low-pressure side. In addition to the main pump, a smaller pump is installed to ensure that the pressure in line A and line B stays above 25 bar. This external circuit is modeled as a constant pressure source of 25 bar. The main axial piston pump has a displacement of 500 cc/rev and the two axial piston motors have a displacement of 250 cc/rev. The pump is driven at a constant velocity equal to 1800 rpm and can deliver pressure up to 350 bar.

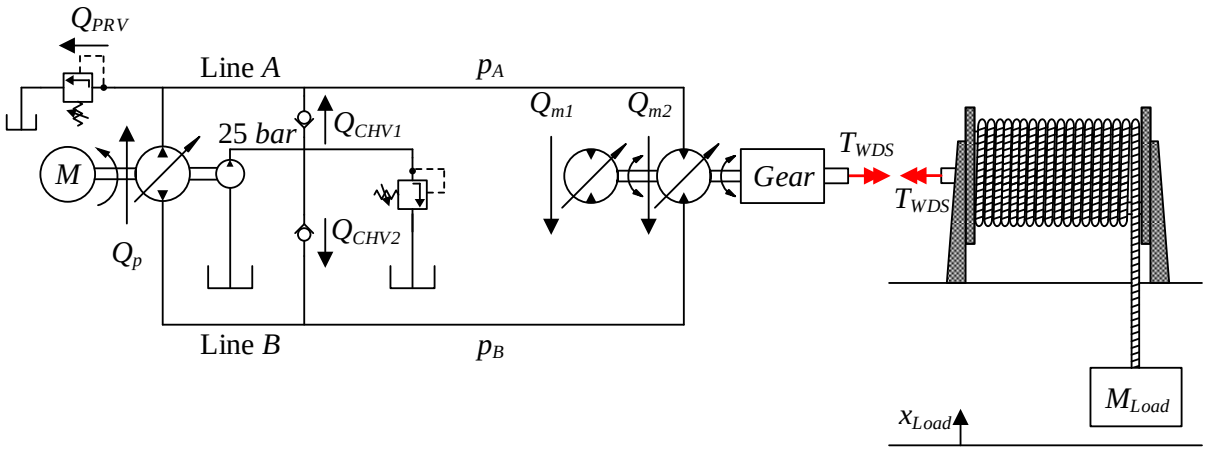

Figure A.2: Conventional hydraulic winch drive system

The torque delivered to the winch drum from the drive system is calculated as shown in Eq. A.3.

$$T_{WDS} = 2 \cdot \frac{(p_A - p_B) \cdot V_{gm}}{2 \cdot \pi} \cdot i_{gear} \cdot n_{hmm} \cdot n_{gear} \tag{A.3}$$

where p_A is the pressure in line A, p_B is the pressure in line B, V_{gm} is the common displacement of the motors, i_{gear} is the gear ratio, n_{hmm} is the hydromechanical efficiency of the motors, and n_{gear} is the efficiency of the gear box. The hydromechanical efficiency is found by linear interpolation between measured data for a representative axial piston motor. The pressure in line A and line B is calculated by integrating the pressure gradients calculated as shown in Eq. A.4 and Eq. A.5 respectively.

$$\dot{p}_A = \frac{\beta}{V_A} \cdot (Q_p - Q_{PRV} + Q_{CHV1} - Q_m) \tag{A.4}$$

$$\dot{p}_B = \frac{\beta}{V_B} \cdot (Q_m + Q_{CHV2} - Q_p) \tag{A.5}$$

where β is the bulk modulus of the oil, V_A and V_B are the volume in line A and B respectively, Q_p is the pump flow, Q_m is the total motor flow ($Q_m = Q_{m1} + Q_{m2}$), Q_{PRV} is the flow through the pressure relief valve connected to line A, Q_{CHV1} and Q_{CHV2} are the flows through the two check valves.

The following equations describe the flow through the pump and the motors:

$$Q_p = \frac{\dot{\theta}_p \cdot V_{gp}}{2 \cdot \pi} \cdot n_{vp} \tag{A.6}$$

$$Q_m = 2 \cdot \frac{\dot{\theta}_m \cdot V_{gm}}{2 \cdot \pi} \cdot \frac{1}{n_{vm}} \tag{A.7}$$

where $\dot{\theta}_p$ is the speed of the pump, V_{gp} is the pump displacement, n_{vp} is the volumetric efficiency of the pump, n_{vm} is the volumetric efficiency of the motors, and $\dot{\theta}_m$ is the speed of the motors.

The dynamic response of the swash plate for the axial piston pump and motors is described by a first order system as shown in Eq. A.8.

$$\dot{V}_g = \frac{V_g - V_{gc}}{\tau} \tag{A.8}$$

where V_g is the current displacement, V_{gc} is the desired displacement and τ is the time constant.

A.2.2.1 Control system

The control system for the CHWDS is divided into two different control systems, one for the motors and one for the pump. The motors have a simple open-loop controller, and the pump has a feedforward controller and a feedback controller. The desired motor displacement is calculated based on a measured value of the load, a reference acceleration of the winch drum and a desired pressure drop across the motor as shown in Eq. A.9.

$$V_{gmc} = \frac{(\ddot{\theta}_{ref} \cdot J_{eff} + \widetilde{M}_{Load} \cdot g \cdot r_{winch}) \cdot 2 \cdot \pi}{\Delta p_m \cdot i_{gear}} \cdot 0.5 \tag{A.9}$$

where $\ddot{\theta}_{ref}$ is the reference acceleration for the winch drum, $\widetilde{M}_{Load}$ is the measured value of the payload and Δp_m is the desired pressure drop across the motors.

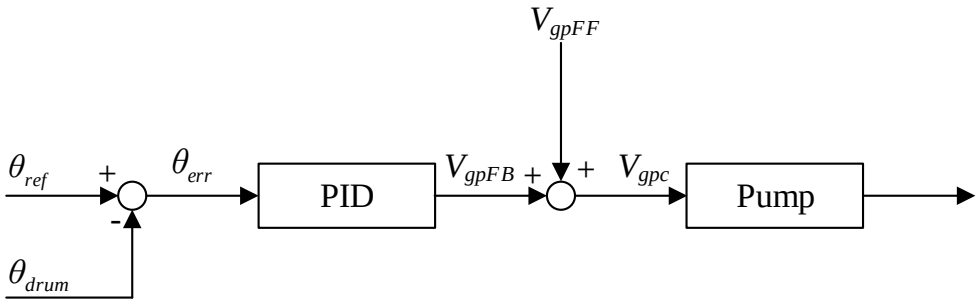

Figure A.3: Pump controller

The pump has a position feed-back controller and a flow feed-forward controller as shown in Fig. A.3

Assuming that the volumetric efficiency for the pump is equal to one, the feed-forward pump displacement is calculated by rearranging Eq. A.6 as shown in Eq. A.10.

$$\begin{aligned} Q_{ref} &= \frac{V_{gpFF} \cdot \dot{\theta}_p}{2 \cdot \pi} \\ &\Downarrow \\ V_{gpFF} &= \frac{2 \cdot \pi \cdot Q_{ref}}{\dot{\theta}_p} \\ &= \frac{2 \cdot \pi \left(\frac{\dot{\theta}_{ref} \cdot i_{gear} \cdot V_{gmc}}{2 \cdot \pi} \right) \cdot 2}{\dot{\theta}_p} \\ &= \frac{\dot{\theta}_{ref} \cdot i_{gear} \cdot V_{gmc} \cdot 2}{\dot{\theta}_p} \end{aligned} \tag{A.10}$$

where $\dot{\theta}_{ref}$ is the reference velocity of the winch drum and $\dot{\theta}_p$ is the pump speed. The feed-back control signal is calculated as shown in Eq. A.11.

$$V_{gpFB} = \theta_{err} \cdot k_p + \dot{\theta}_{err} \cdot k_d + \int \theta_{err} \cdot k_i \ dt \tag{A.11}$$

where θ_{err} is the position error of the winch drum and k_p, k_d and k_i are the controller gains for the PID-controller. Finally the desired pump displacement is calculated as shown in Eq. A.12.

$$V_{gpc} = V_{gpFF} + V_{gpFB} \tag{A.12}$$

A.2.3 Modeling of the Digital Hydraulic Winch Drive System

The digital hydraulic winch drive system consists of a DHP, DHM, and two gas accumulators connected in a closed circuit system, as shown in Fig. A.4. The DHP is driven

by an electrical motor running at a constant velocity of 1800 rpm. The DHM is directly connected to the winch drum without a gear box. The DHP and the DHM are two radial piston units with respectively 9 and 42 cylinders. Both units are controlled by using sequential flow diverting strategy, meaning that the entire cylinder displacement has to be used when selecting pump or motor mode. The on/off valves are only switched when the piston is close to top dead center (TDC) and bottom dead center (BDC) when the flow is low. The actuation is timed in conjunction with the piston movement to minimize the pressure difference when switching the valves. This maximizes the efficiency and minimizes pressure peaks and flow peaks. The two gas accumulators are used to smooth out the pressure and flow peaks in line A and B.

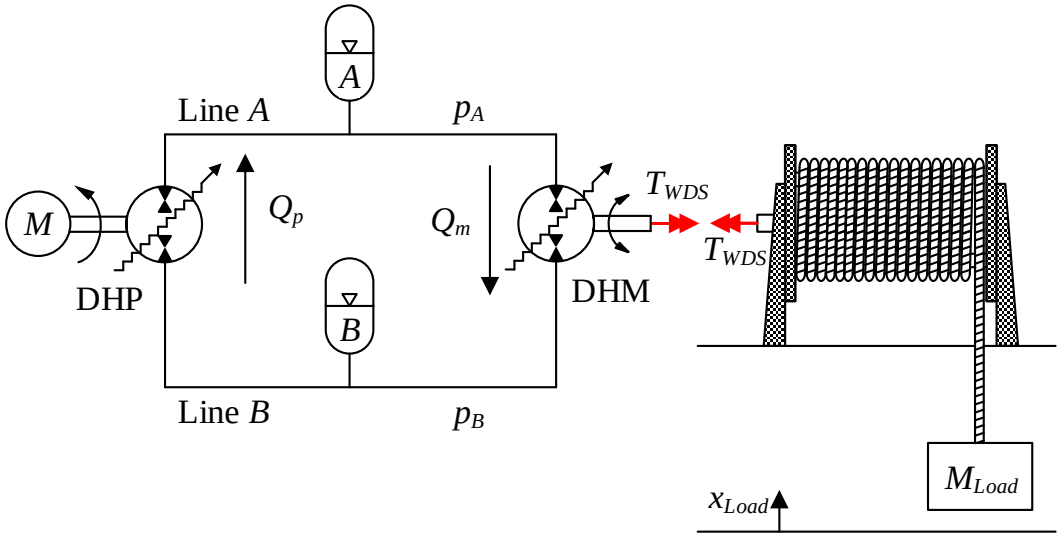

Figure A.4: Digital hydraulic winch drive system

A.2.3.1 Modeling of the Digital Hydraulic Pump and Motor

It is assumed that the cylinder configuration is the same for both the DHP and the DHM. For simplicity, only calculations for one of the pistons in the DHM are shown in this section, but the same method is used for all of the pistons, both for the DHM and DHP. The contribution from all the cylinders are summed up in Eq. A.20 to Eq. A.22. The on/off valves are assumed to be leak free, and the DHP and DHM models do not include any friction or leakage.

Figure A.5 shows the cylinder configuration for one cylinder. The continuity equation is used to calculate the pressure gradient in the cylinder as shown in Eq. A.13.

$$\dot{p}_{cyl} = \frac{\beta}{V_{cyl}} \cdot \left(Q_A - Q_B - \dot{V}_{cyl} \right) \tag{A.13}$$

where β is the effective bulk modulus of the oil, V_{cyl} is the cylinder volume, Q_A and Q_B

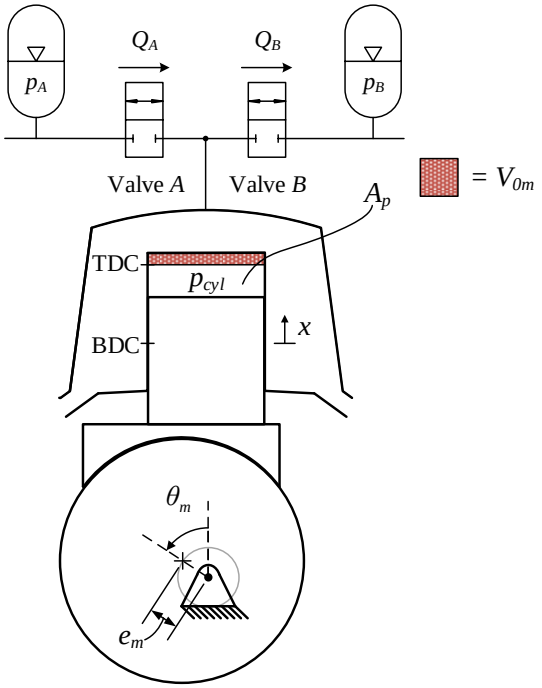

Figure A.5: Cylinder configuration of one cylinder with $\theta_m = \pi/4$

is the flow through valve A and B, and $\dot{V}_{cyl}$ is the rate of change in cylinder volume. $\dot{V}_{cyl}$ is positive if the volume is expanding. The cylinder volume is calculated as shown in Eq. A.14 and the rate of change in cylinder volume is calculated as shown in Eq. A.15.

$$V_{cyl} = V_{0m} + \frac{V_{dm}}{2} \cdot (1 - \cos(\theta_m)) \tag{A.14}$$

$$\dot{V}_{cyl} = \frac{V_{dm}}{2} \cdot \sin(\theta_m) \cdot \dot{\theta}_m \tag{A.15}$$

where V_{0m} is the dead volume in the cylinder and V_{dm} is the discharge volume of the cylinder. The volume flow through the on/off valves, Q_A and Q_B, are calculated by Eq. A.16 and Eq. A.17 respectively.

$$Q_A = \frac{u_A}{k_f} \cdot \sqrt{p_A - p_{cyl}} \cdot sign(p_A - p_{cyl}) \tag{A.16}$$

$$Q_B = \frac{u_B}{k_f} \sqrt{p_{cyl} - p_B} \cdot sign(p_{cyl} - p_B) \tag{A.17}$$

where k_f is the flow coefficient of the valves, and u_A and u_B are the opening ratios of the valves ranging from 0 to 1, where 0 is fully closed and 1 is fully open. Valve A and B have the same flow coefficient and the same dynamic response. The dynamic response is described by the second order system shown in Eq. A.18.

$$\ddot{u} = u_{con} \cdot \omega^2 - u \cdot \omega^2 - 2 \cdot \zeta \cdot \omega \cdot \dot{u} \tag{A.18}$$

where u_{con} is the control signal, ζ is the damping ratio and ω is the natural frequency. The control signal is either 0 or 1. The torque contribution from one cylinder is calculated

as shown in Eq. A.19

$$T_{cyl} = p_{cyl} \cdot A_p \cdot e_m \cdot \sin(\theta_m) \tag{A.19}$$

Finally, the total motor torque and the total flow in and out of the DHM is calculated as the sum of the contribution from all pistons, as shown below in Eq. A.20, A.21 and A.22 respectively.

$$T_{WDS} = \sum_{i=1}^{42} T_{cyl,i} \tag{A.20}$$

$$Q_{inm} = \sum_{i=1}^{42} Q_{A,i} \tag{A.21}$$

$$Q_{outm} = \sum_{i=1}^{42} Q_{B,i} \tag{A.22}$$

A.2.3.2 Valve Parameters

The fast switching on/off valve is by far the most critical element in digital hydraulic machines. Some important features are; high durability, low cost, low power consumption, zero or low leakage, and compact design [10]. Simulations and experimental results presented in [11] show that valve throttling losses are one of the major energy dissipative sources for hydraulic motors and that valve timing has a significant impact on valve throttling losses. The valves must, therefore, have high accuracy, high flow rate and low switching time. In [12], Daniel B. Roemer et al. developed an expression for the efficiency of a DHM as a function of a normalized valve switching time, $\bar{t}_s$, and a normalized valve flow coefficient, $\overline{k}_f$. The normalized valve parameters were defined as shown in Eq. A.23 and A.24.

$$\bar{t}_s = \frac{t_s}{T_{rev}} \quad \text{with} \quad T_{rev} = \frac{2 \cdot \pi}{\dot{\theta}_{max}} \tag{A.23}$$

$$\overline{k}_f = \frac{k_f}{\sqrt{\Delta p}/Q_{mean}} \quad \text{with} \quad Q_{mean} = \frac{V_d}{\pi/\dot{\theta}_{max}} \tag{A.24}$$

Figure A.6 shows the motor efficiency as a function of the normalized switching time and the normalized flow coefficient.

Using the results from Fig. A.6 and selecting the normalized flow coefficient and the normalized switching time to be 4 %, the target efficiency at 20 % displacement is 97 %. By rearranging Eq. A.23 and A.24 the valve switching time and the valve flow coefficient

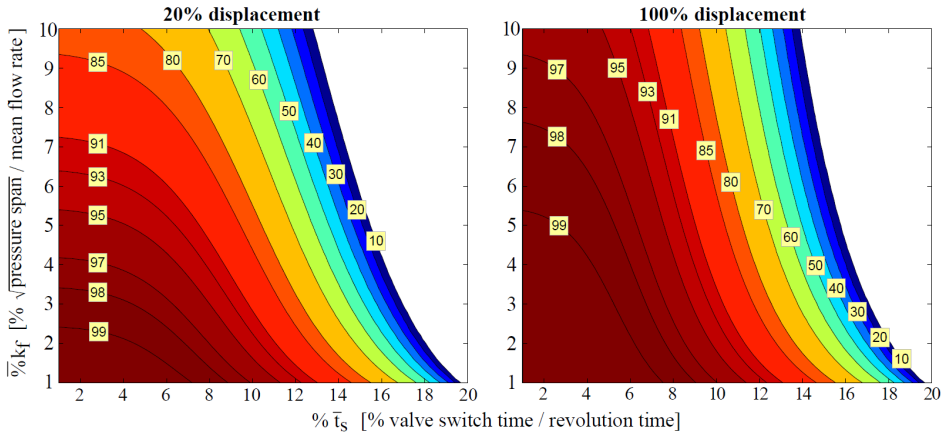

Figure A.6: Motor efficiency as a function of normalized valve switching time and normalized valve flow coefficient [13]

is calculated as shown below in Eq. A.25 and A.26 respectively.

$$\begin{aligned} \overline{t}_s &= \frac{t_s}{T_{rev}} \quad \text{with} \quad T_{rev} = \frac{2 \cdot \pi}{\dot{\theta}_{max}} \\ &\Downarrow \\ t_s &= \overline{t}_s \cdot T_{rev} \\ &= \overline{t}_s \cdot \frac{2 \cdot \pi}{\dot{\theta}_{max}} \end{aligned} \tag{A.25}$$

$$\begin{aligned} \overline{k}_f &= \frac{k_f}{\sqrt{\Delta p}/Q_{mean}} \quad \text{with} \quad Q_{mean} = \frac{V_d}{\pi/\dot{\theta}_{max}} \\ &\Downarrow \\ k_f &= \overline{k}_f \cdot \sqrt{\Delta p}/Q_{mean} \\ &= \overline{k}_f \cdot \frac{\sqrt{\Delta p} \cdot \pi}{V_d \cdot \dot{\theta}_{max}} \end{aligned} \tag{A.26}$$

The calculated flow coefficient and the switching time for the on/off valves for both the DHP and DHM are listed in Tab. A.2.

Table A.2: Valve parameters

	k_f	t_s
DHM	251560 $\frac{\sqrt{\Delta p}}{m^3/s}$	240 ms
DHP	53666 $\frac{\sqrt{\Delta p}}{m^3/s}$	1.3 ms

A.2.3.3 Pressure dynamics in line *A* and line *B*

For simplicity, only the calculation for the pressure gradient in line A is shown, but the pressure gradient in line B is calculated in the same manner. The pressure gradient in

line A is calculated as shown in Eq. A.27

$$\dot{p}_A = \frac{\beta}{V_A} \cdot (Q_{outp} - Q_{inm} - \dot{V}_{accA}) \tag{A.27}$$

where V_A is the volume in line A and accumulator A, Q_{outp} is the flow out of the pump, Q_{inm} is the flow into the motor and $\dot{V}_{accA}$ is the rate of change of accumulator volume. $\dot{V}_{accA}$ is positive if the volume is expanding and is calculated as shown below in Eq. A.28.

$$\dot{V}_{accA} = \dot{p}_A \cdot \frac{V_{accAg}}{n_{accA} \cdot p_A} \tag{A.28}$$

where V_{accAg} is the gas volume in accumulator A and n_{accA} is the polytropic exponent for accumulator A. Eq. A.28 is substituted into Eq. A.27 and rearranged as shown in Eq. A.29.

$$\dot{p}_A = \frac{\beta}{V_A} \cdot \frac{(Q_{outp} - Q_{inm})}{1 + \frac{\beta \cdot V_{accAg}}{V_A \cdot n_{accA} \cdot p_A}} \tag{A.29}$$

A.2.3.4 Control System

The control system for the DHWDS is divided into two, one for the pump and one for the motor. In general, the motor has an open loop torque controller which calculates motor displacement based on load measurements and a desired pressure drop across the motor. The pump has a displacement controller where the displacement is calculated based on the winch drum reference position and the known motor displacement. The pump also has a position feedback controller.

Motor Controller

To ensure a relatively smooth motor output torque, the 42 cylinder piston motor is divided into 14 banks, each with 3 pistons spaced equally around the shaft. The number of active banks, also called n_{step}, is calculated based on measurements of the payload, $\widetilde{M}_{Load}$, and a desired pressure drop across the motor, Δ_{pref}, as shown in Eq. A.30.

$$n_{step} \approx \frac{\widetilde{M}_{Load} \cdot g \cdot r_{winch}}{\Delta p_{ref} \cdot T_{step}}, \qquad \text{round of to nearest integer} \tag{A.30}$$

$n_{step} = 1$ corresponds to one active bank, $n_{step} = 2$ corresponds to two active banks and so on. Δp_{ref} is the desired pressure drop across the motor and T_{step} is the torque delivered by one active bank with a pressure drop across the motor equal to 1 Pa.

Pump Controller

The pump controller is based on the displacement controller first introduced in [14]. The DHM is directly connected to the drum, and the position reference of the drum is converted into a volume reference, V_{ref}, according to the motor displacement. Then the volume that already has been discharged from the pump, V_{est}, is calculated. The controller also has a position feedback controller, V_{err}, and compensates for the change of volume in accumulator A. Figure A.7 illustrates the DHP controller and the pump mode decision, D, is calculated as shown in Eq. A.31.

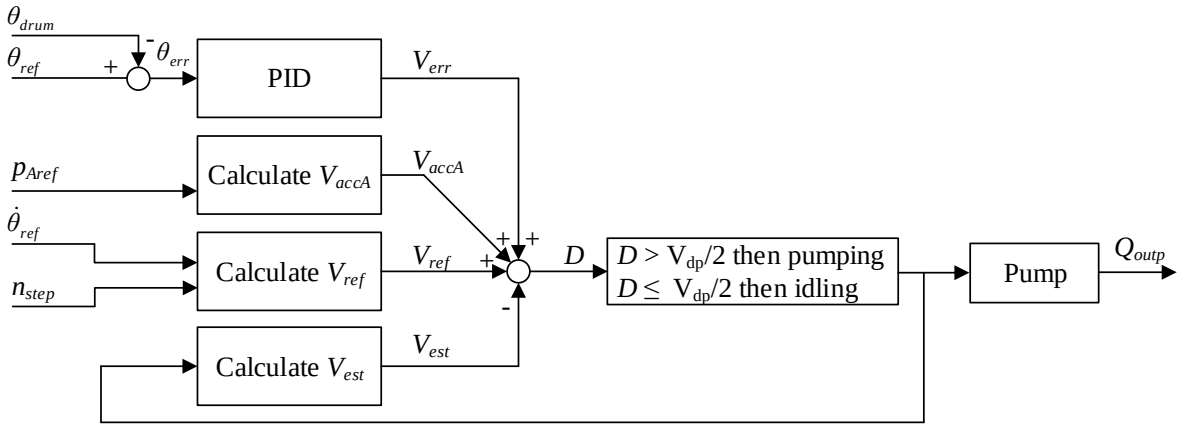

Figure A.7: Pump controller

$$D = V_{ref} + V_{accA} + V_{err} - V_{est}, \quad \rightarrow \quad \begin{cases} \text{pumping} & \text{if} \quad D > V_{dp}/2 \\ \text{idling} & \text{if} \quad D \leq V_{dp}/2 \end{cases} \tag{A.31}$$

where $D > V_{dp}/2$ means that the estimated volume discharged from the pump is a half piston discharge volume smaller than the desired volume and that the next cylinder will operate in pump mode. $D \leq V_{dp}/2$ means that the estimated volume discharged from the pump is greater then the needed volume and that the next cylinder will run in idle mode. V_{ref} is calculated by integrating Eq. A.32.

$$\dot{V}_{ref} = \frac{V_{dm} \cdot n_{step} \cdot 3 \cdot \dot{\theta}_{ref}}{2 \cdot \pi} \tag{A.32}$$

where $\dot{\theta}_{ref}$ is the speed reference of the winch drum. The estimated discharge volume, V_{est}, is calculated by the following equation.

$$V_{est} = n_{pump} \cdot V_{dp} \tag{A.33}$$

where n_{pump} is the total number of cylinders that already have been pumping and V_{dp} is the discharge volume of one of the pistons in the pump. The compression volume is not taken into account in Eq. A.33, but can be included. The small error introduced by excluding the compression volume will in this control system be compensated for in the

PID-controller. V_{accA} is calculated in Eq. A.34.

$$V_{accA} = \frac{(p_{Aref} - p_{A0}) \cdot V_{accAg0}}{n_{accA} \cdot p_{A0}} \tag{A.34}$$

where p_{A0} is the initial pressure in line A, V_{gA0} is the gas volume in accumulator A at the initial pressure p_{A0} and p_{Aref} is the reference pressure in line A. p_{Aref} is calculated as shown below in Eq. A.35.

$$p_{Aref} = \frac{\ddot{\theta}_{ref} \cdot J_{eff} + \widetilde{M}_{Load} \cdot g \cdot r_{winch}}{T_{step} \cdot n_{step}} + p_{B0} \tag{A.35}$$

where p_{B0} is the initial pressure in line B. V_{err} is the output signal from the PID-controller and is calculated as shown in Eq. A.36

$$V_{err} = \theta_{err} \cdot k_p + \dot{\theta}_{err} \cdot k_d + \int \theta_{err} \cdot k_i \ dt \tag{A.36}$$

where θ_{err} is the difference of the reference drum position and the actual drum position and k_p, k_d and k_i are the control parameters in the PID-controller.

A.3 SIMULATION RESULTS

In this section the simulation results are presented. The same control parameters are used in the conventional winch drive controller and the digital hydraulic winch drive controller for both load case 1 and load case 2. The control parameters for the CHWDS are as follows: $\Delta p_{ref} = 225\ bar$, $p_{B0} = 25\ bar$, $k_p = 7 \cdot 10^{-4}\ m^3$, $k_d = 2 \cdot 10^{-4}\ m^3 s$ and $k_i = 5 \cdot 10^{-3}\ m^3/s$. The control parameters for the DHWDS are as follows: $\Delta p_{ref} = 225\ bar$, $p_{B0} = 25\ bar$, $k_p = 0.1\ m^3$, $k_d = 0.025\ m^3 s$, and $k_i = 0.2\ m^3/s$.

A.3.1 Load Case 1

In load case 1 the payload is equal to 18000 kg and the speed is ramped up to 1 m/s with a ramp time of 2 s. Figure A.8 and A.9 show the simulation results of the CHWDS, left hand side, and the DHWDS, right hand side. The sub-plots from top to bottom in Fig. A.8 show the simulated payload position together with the reference position, the load speed together with the reference speed and finally the position error. The simulated payload position and speed follow their references well, both for the CWDS and the DHWDS. Maximum position error occurs when accelerating the load and is 9 mm for the CHWDS and 5.4 mm for the DHWDS. The position error for the CHWDS converges toward zero when the winch runs with constant speed and the error for the DHWDS oscillates around zero with a small amplitude.

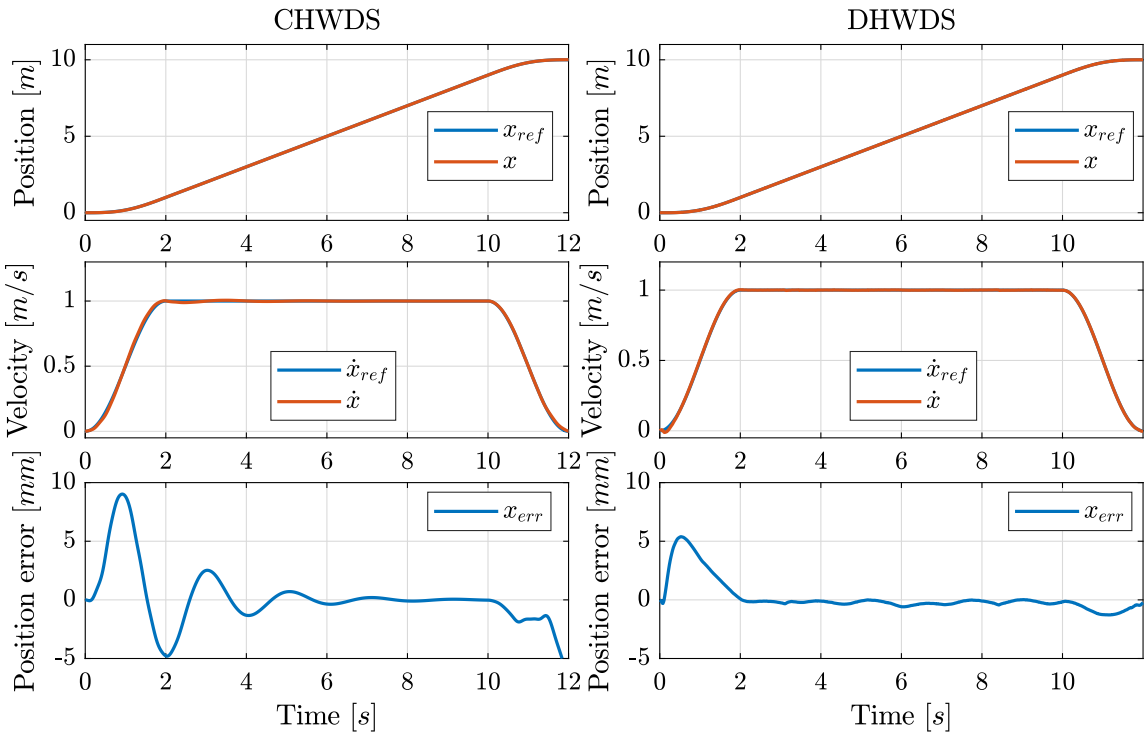

Figure A.8: Simulation results position and velocity tracking in load case 1

The top sub-plots in Fig. A.9 show the input power, output power and the power losses of the hydraulic system. On the right hand side, a moving average filter is also included. The moving average filter takes the average of the input power during a period of 0.2 s. The bottom sub-plots show the consumed energy together with the output energy and energy losses.

When driving with constant speed of 1 m/s and a payload equal to 18000 kg, the input power to the CHWDS is approximately 234 kW and the output power is approximately 176 kW, resulting in loss equal to 58 kW. The input power to the DHWDS is heavily oscillating because of the nature of the DHP. The DHP enables and disables pistons on a

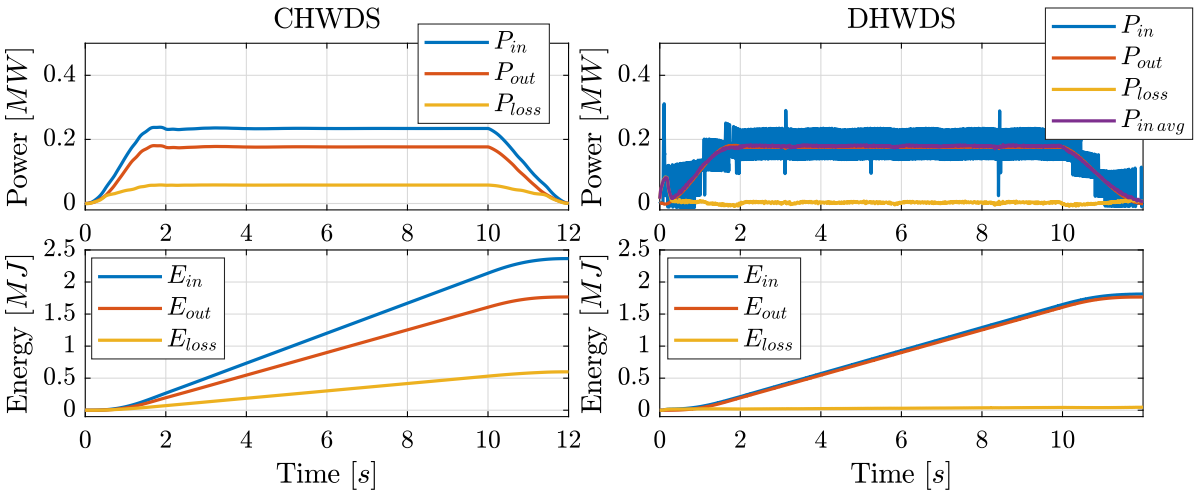

Figure A.9: Simulation results for power and energy consumption in load case 1

stroke by stroke basis which results in input power oscillations. The same peaks occur in the pump flow, but the accumulators connected to line A and B smooth out the peaks. The mean input power to the DHWDS when operating at constant speed is 181 kW and the mean loss is only 5 kW.

In the bottom sub-plots in Fig. A.9, it is easy to see that the energy losses are much greater for the CHWDS than for the DHWDS. The total energy consumed by the CHWDS is 2365 kJ and the loss is 599 kJ which results in a total system efficiency equal to 75 %. The total system efficiency for the DHWDS is 97 % where the total consumed energy is 1813 kJ and the total energy loss is only 47 kJ.

A.3.2 Load Case 2

In load case 2 the payload is equal to 4000 kg and the speed is ramped up to 1.5 m/s with a ramp time of 3 s. Figure A.10 and A.11 show the simulation results of the CHWDS, left hand side, and the DHWDS, right hand side.

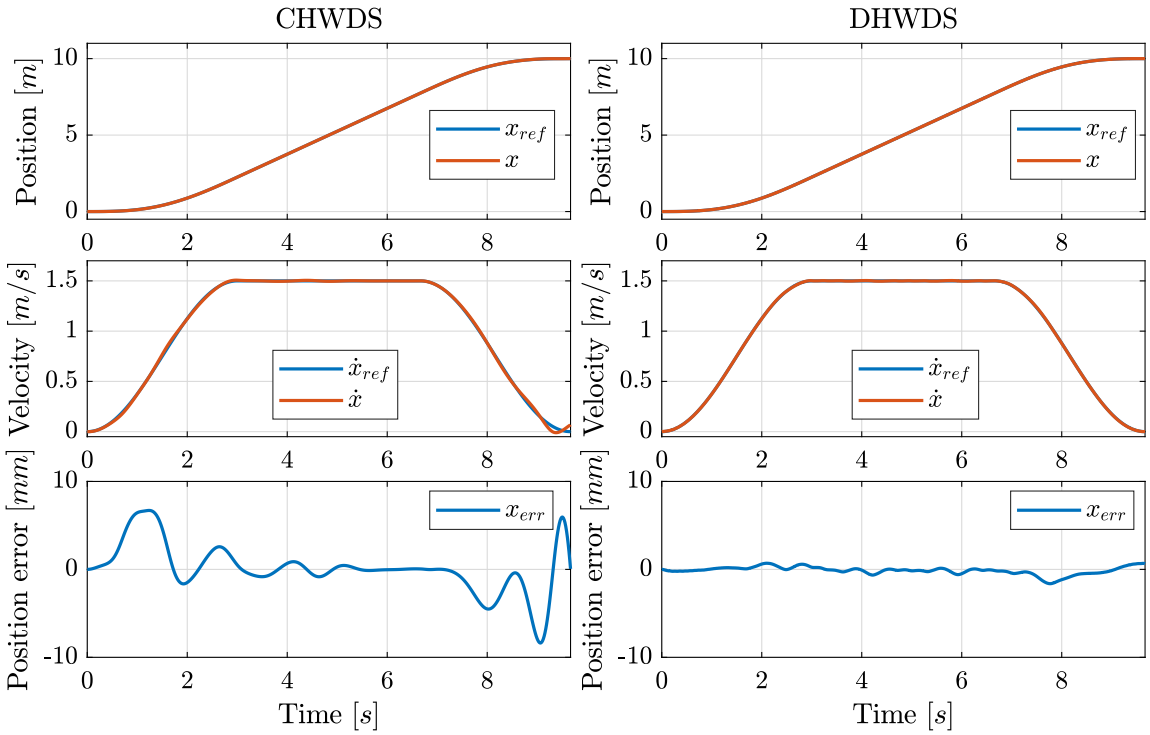

Figure A.10: Simulation results position and velocity tracking in load case 2

Figure A.10 shows that both drive systems follow their position and speed references well. The position error for the CHWDS tends to oscillate when accelerating or decelerating the load but stabilizes around zero when running at constant speed. The maximum position error for the CHWDS is -8.4 mm and only -1.6 mm for the DHWDS. The small oscillations shown in the position error for the DHWDS in load case 1 can also be seen in load case 2.

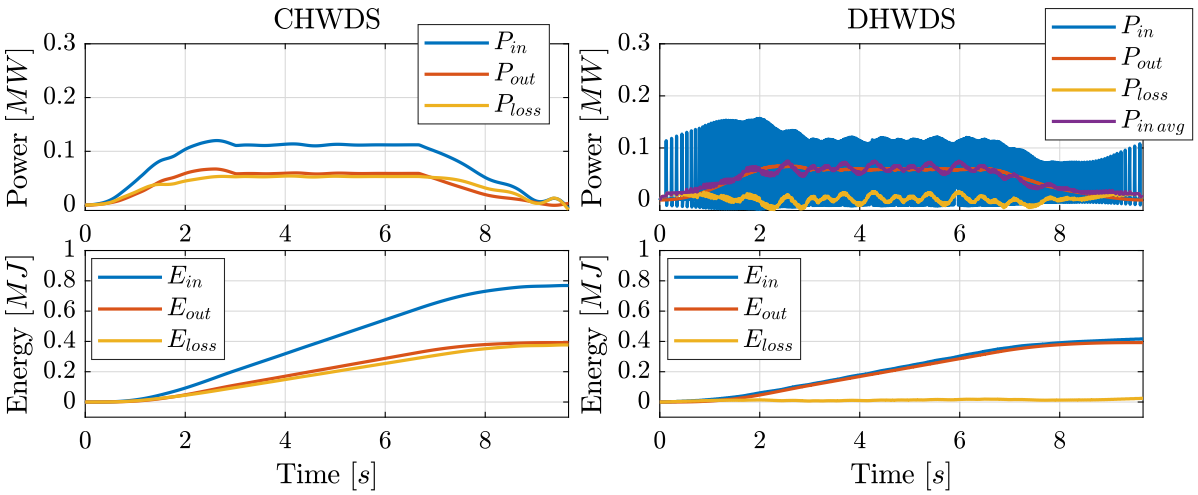

Figure A.11: Simulation results for power and energy consumption in load case 2

Figure A.11 shows that the input power to the CHWDS is approximately 112 kW and the output power is 59 kW when driving with a constant speed of 1.5 m/s. For the DHWDS the input power is heavily oscillating, but the mean value is approximately 61 kW. The total consumed energy for the simulated trajectory is 769 kJ for the CHWDS and only 417 kJ for the DHWDS. The losses are 377 kJ for the CHWDS and only 25 kJ for the DHWDS. This gives a total efficiency for the entire simulated trajectory equal to 51 % for the CHWDS and 94 % for the DHWDS.

A.3.3 Discussion

In this section, the presented results are summarized and further discussed. Some of the most important results are summarized in Tab. A.3 The total system efficiency for the

Table A.3: Summarized results

	Load case 1		**Load case 2**	
	CHWDS	DHWDS	CHWDS	DHWDS
Input power at constant speed	234 kW	181 kW	112 kW	61 kW
Power losses at constant speed	58 kW	5 kW	50 kW	1 kW
Total energy consumed	2365 kJ	1813 kJ	769 kJ	417 kJ
Total energy losses	599 kJ	47 kJ	377 kJ	25 kJ
Total efficiency	75 %	97 %	51 %	94 %
Max position error	9 mm	5.4 mm	-8.4 mm	-1.6 mm

CHWDS is 75 % in load case 1 and 51 % in load case 2 and the maximum position error is 9 mm and -8.4 mm respectively. The CHWDS has higher efficiency when operating with higher loads. The same tendency can be observed for the DHWDS, but the change in efficiency is not that big. When reducing the load from 18000 kg down to 4000 kg,

the efficiency of the CHWDS is reduced by 32 % and for the DHWDS, the efficiency is only reduced by 3 %. When operating with constant speed, the position error for the CHWDS tends to converge towards zero, while the position error for the DHWDS tends to oscillate with a small amplitude. These small oscillations are affected by control parameters, accumulator properties and the number of pistons in the DHP and the DHM.

The DHWDS consumes approximately 550 kJ less than the CHWDS when operating load case 1. If the same load were supposed to be hoisted 3000 m, the DHWDS would use 165 MJ less energy than the CHWDS. For one short lifting operation, the saved energy is not that much, but for a winch that is frequently used over time and with high lifting operations, the savings can be significant.

This study shows that there is a significant improvement in efficiency when using the DHWDS. Neither leakage and friction losses in the DHP and the DHM nor power consumption of the on/off valves are included in this study. The real efficiency will therefore most likely be lower than for the simulated system. Because the increase in efficiency is so high, especially when operating small loads, and knowing that previous studies show that digital hydraulic units have high efficiency for a wide range of operations [15], it is realistic to expect that the efficiency for the DHWDS will remain significantly higher than CHWDS even when all losses are included.

A.4 CONCLUSION

This simulation study compares the efficiency and controllability of a CHWDS and a DHWDS. Each winch drive system is simulated hoisting two different loads, one large load and one small load. The simulation results show that the system efficiency for the DHWDS was significantly higher than for the CHWDS, especially when operating small loads. This study shows that DHWDS has the potential of increasing efficiency in hydraulic winches while the controllability remains high.

Bibliography

[1] Mike L Christensen and David L Zimmerman. Optimization of offshore electrical power systems. *IEEE Transactions on Industry Applications*, (1):148–160, 1986.

[2] Witold Pawlus, Martin Choux, and Michael R Hansen. Hydraulic vs. electric: A review of actuation systems in offshore drilling equipment. *Modeling, Identification and Control*, 37(1):1–17, 2016.

[3] Karl-Erik Rydberg. Energy efficient hydraulic hybrid drives. In *11: th Scandinavian International Conference on Fluid Power, SICFP'09, June 2-4, Linköping, Sweden*, 2009.

[4] Jamie Taylor, Win Rampen, Daniel Abrahams, and Andrew Latham. Demonstration of a digital displacement hydraulic hybrid bus. In *2015 JSAE Annual Congress (Spring), Yokohama*, 2015.

[5] GS Payne, AE Kiprakis, M Ehsan, W H S Rampen, JP Chick, and AR Wallace. Efficiency and dynamic performance of digital displacement$^{\text{TM}}$ hydraulic transmission in tidal current energy converters. *Proceedings of the Institution of Mechanical Engineers, Part A: Journal of Power and Energy*, 221(2):207–218, 2007.

[6] M Karvonen, M Heikkilä, M Huova, M Linjama, and K Huhtala. Simulation study-improving efficiency in mobile boom by using digital hydraulic power management system. In *Proceedings of the Twelfth Scandinavian International Conference on Fluid Power*, pages 355–368, 2011.

[7] Mikko Heikkilä and Matti Linjama. Hydraulic energy recovery in displacement controlled digital hydraulic system. In *13th Scandinavian International Conference on Fluid Power; June 3-5; 2013; Linköping; Sweden*, number 092, pages 513–519. Linköping University Electronic Press, 2013.

[8] Mikko Heikkilä, Matti Karvonen, Matti Linjama, Seppo Tikkanen, and Kalevi Huhtala. Comparison of proportional control and displacement control using digital

hydraulic power management system. In *ASME/BATH 2014 Symposium on Fluid Power and Motion Control*, pages V001T01A026–V001T01A026. Citeseer, 2014.

[9] Masashi Sasaki, Atsushi Yuge, Toshikazu Hayashi, Hiroshi Nishino, Michiya Uchida, and Toshihide Noguchi. Large capacity hydrostatic transmission with variable displacement. In *The 9th International Fluid Power Conference*, volume 9, page 25, 2014.

[10] Bernd Winkler, Andreas Plöckinger, and Rudolf Scheidl. State of the art in digital valve technology. In *PROCEEDINGS–The Seventh Workshop on Digital Fluid Power*, pages 151–163, 2015.

[11] Hao Tian and James D Van de Ven. Experimental study of the influence of valve timing on hydraulic motor efficiency. In *ASME/BATH 2015 Symposium on Fluid Power and Motion Control*. American Society of Mechanical Engineers Digital Collection, 2016.

[12] Daniel Rømer, Per Johansen, Henrik C Pedersen, and Torben Ole Andersen. Analysis of valve requirements for high-efficiency digital displacement fluid power motors. In *8th International Conference on Fluid Power Transmission and Control, ICFP 2013*, pages 122–126. World Publishing Cooperation, 2013.

[13] Daniel Beck Rømer. *Design and optimization of fast switching valves for large scale digital hydraulic motors*. Ph.D. thesis, Department of Energy Technology, Aalborg University, 2014.

[14] M Heikkilä and M Linjama. Direct connection of digital hydraulic power management system and double acting cylinder-a simulation study. In *The Fourth Workshop on Digital Fluid Power, DFP*, volume 11, 2011.

[15] Win Rampen et al. Gearless transmissions of large wind turbines-the history and future of hydraulic drives. *Artemis IP Ltd., Midlothian, UK*, 2006.

Table A.4: Simulation parameters

Symbol	Value	Description
Winch		
r_{drum}	1.22 m	Drum radius
J_{winch}	22100 kgm^2	Inertia of winch drum and wire
L_w	3600 m	Drum capacity
SWL	20000 kg	Safe working load
General		
V_{A0}	1 l	Dead volume in line A
V_{B0}	1 l	Dead volume in line B
β	1.2 GPa	Bulk modulus
g	9.81 m/s^2	Acceleration of gravity

Table A.5: Simulation parameters conventional hydraulic winch drive system

Symbol	Value	Description
Motor		
V_{gm}	250 cc/rev	Max motor displacement
J_m	0.061 kg/m^2	Mass moment of inertia motor
τ_m	0.01 s	Time constant of the Swash plate response
Motor controller		
Δp_m	225 bar	Desired differential pressure across motor
Pump		
V_{gp}	500 cc/rev	Max pump displacement
τ_m	0.01 s	Time constant of the swash plate response
n	1800 rpm	Pump speed
Pump controller		
k_p	$7 \cdot 10^{-4}$	Controller gain
k_d	$2 \cdot 10^{-4}$	Controller gain
k_i	$5 \cdot 10^{-3}$	Controller gain
Gearbox		
i_{gear}	156	Gear ratio
n_{gear}	95 %	Efficiency gearbox

Table A.6: Simulation parameters digital hydraulic winch drive system

Symbol	Value	Description
Digital Hydraulic Motor		
N_{cyl}	42	Number of cylinders
V_{dm}	1600 cc/rev	Discharge volume per cylinder
V_0	1.6 l	Dead volume in cylinder
e_m	46.6 mm	Eccentricity of spherical motor shaft
J_m	10.2389 kg/m^2	Inertia of digital hydraulic motor
T_{step}	$75.9286 \cdot 10^{-5}$ Nm	Torque from one active bank with 1 Pa pressure drop
On/off Valve Motor		
k_{fm}	251560 $\frac{\sqrt{Pa}}{m^3/s}$	Flow coefficient
t_s	240 ms	Valve transition time
ζ	0.8	Damping ratio valve dynamic
ω	17 rad/s	Natural frequency valve dynamic
Motor Controller		
Δp_m	225 bar and 0 bar	Desired differential pressure across motor
Digital Hydraulic Pump		
N_{cyl}	9	Number of cylinders
V_{dp}	55.5 cc/rev	Discharge volume per cylinder
V_{0p}	0.0555 l	Dead volume in cylinder
e_p	46.6 mm	Eccentricity of spherical motor shaft
n	1800 rpm	Pump speed
On/off Valve Pump		
k_{fp}	53666 $\frac{\sqrt{Pa}}{m^3/s}$	Flow coefficient
t_s	1.3 ms	Valve transition time
ζ	0.8	Damping ratio valve dynamic
ω	3200 rad/s	Natural frequency valve dynamic
Pump Controller		
k_p	0.1	Controller gain
k_d	0.025	Controller gain
k_i	0.2	Controller gain
Accumulator *A*		
p_{maxA}	350 bar	Max pressure in accumulator A
p_{minA}	75 bar	Min pressure in accumulator A
p_{0A}	67.5 bar	Preload pressure in accumulator A
V_{accA}	4.4 l	Volume accumulator A
n_{accA}	1.4	Polytropic exponent
Accumulator *B*		
p_{maxB}	150 bar	Max pressure in accumulator B
p_{minB}	10 bar	Min pressure in accumulator B
p_{0B}	9 bar	Preload pressure in accumulator B
V_{accB}	3.9 l	Volume accumulator B
n_{accB}	1.4	Polytropic exponent

Paper B

Feasibility Study of a Digital Hydraulic Winch Drive System

Sondre Nordås, Morten Kjeld Ebbesen and Torben Ole Andersen

This paper has been published as:

S. Nordås, M. K. Ebbesen, and T. O. Andersen. Feasibility Study of a Digital Hydraulic Winch Drive System. In *The Proc. of The Ninth Workshop on Digital Fluid Power*, Aalborg, Denmark, 2017.

Feasibility Study of a Digital Hydraulic Winch Drive System

Sondre Nordås*, Morten Kjeld Ebbesen* and Torben Ole Andersen**

*University of Agder
Faculty of Engineering and Science
Jon Lilletunsvei 9, 4879 Grimstad, Norway

** Aalborg University
Faculty of Engineering and Science
Pontoppidanstræde 101, 9220 Aalborg East, Denmark

Abstract **– The offshore oil and gas industry has traditionally used hydraulically driven applications. Hydraulic systems are known to suffer from relatively low efficiency. Due to environmental issues, more efficient systems are now required. Today, the offshore oil and gas industry is experiencing a shift in driveline systems; high efficient electric motors tend to replace low efficient hydraulic systems. In addition to the electric motors, a new alternative to the conventional hydraulic system is digital hydraulic machines. This paper investigates the feasibility of using a digital hydraulic winch drive system and presents a new digital hydraulic winch drive control system. The simulated system is based on a 20000 kg hydraulic offshore auxiliary winch with a drum capacity of 3600 m of wire. The digital hydraulic winch drive system is a closed-circuit system with one high-speed digital pump and one low-speed high-torque digital motor. One of the biggest challenges in digital hydraulic pump/motor technology is the fast switching on/off valves. The valves must have high durability, low power consumption, zero leakage and low response time. The on/off valves in this study are modeled with an ideal behavior. The simulation results show that the payload follows the reference trajectory when using a digital hydraulic winch drive system for a wide range of loads and speeds.**

B.1 INTRODUCTION

Digital hydraulic pumps and motors differ from traditional variable displacement machines (typically piston type machines) in the way they achieve variable displacement. Traditionally variable displacement machines change displacement by changing the piston

stroke. Hence, every cylinder is pressurized and depressurized during one shaft revolution. Leakage losses, friction losses and compressibility losses are therefore almost constant independent of displacement which results in poor efficiency at partial displacement. In digital hydraulic machines, two fast switching on/off valves are connected to every single cylinder, one between the high-pressure manifold and the cylinder, and the other one between the cylinder and the low-pressure manifold. By controlling the on/off valves, every cylinder can be individually controlled. One cylinder can be active (operate in motor mode or pump mode) or be idling. In idle mode, the low-pressure valve is kept open during the entire shaft revolution. The displacement of the pump or motor is changed by changing the ratio of active cylinders and idling cylinders. During idling, the cylinder pressure is kept low resulting in a minimum of losses and high component efficiency even at partial displacement.

Digital hydraulic machines have earlier been proposed to be used in hydrostatic transmissions for large wind turbines. The company Artemis Intelligent Power (Artemis IP) is the leading pioneer in digital displacement technology and develops systems with digital displacement technology for a wide range of applications. In 2010 Mitsubishi Heavy Industries started developing a 7 MW wind turbine with a hydrostatic transmission using the digital displacement technology from Artemis IP. This digital hydraulic transmission consists of a 7 MW digital pump and two 3.5 MW digital motors driving two generators [1]. The total efficiency of the transmission is approximately 94%, 98% for the digital pump and 96% for the digital motors [2]. Artemis IP has with the hydrostatic transmission shown that digital hydraulic machines have the potential of converting slow rotational movement with high torque into high and steady rotational speed appropriate for generating electricity. However, is it possible to use digital hydraulic machines to transform high constant speed with low torque into variable high torque and low-speed movement?

The offshore oil and gas industry has several high torque low-speed applications, for example, mud pumps, top drives, drawworks, and winches. In the offshore oil and gas industry, winches are used in big cranes for heavy lifting operations but can also be used for smaller lifting operations on the drill floor and at the moon pool. One drilling unit can have several deck cranes for deck-to-deck lifting as well as loading and unloading of supply vessels and subsea lifting operations. Deck cranes come in different types and size, and at the moment the biggest cranes can have a safe working load up to 800 tons. Cranes on floating drilling units are often equipped with active heave compensation systems to compensate for the vertical motion caused by the waves when landing loads at the seabed. The hydraulic system on huge winches is often a closed circuit system with a variable displacement pump providing fluid to one or several variable displacement high-speed motors. A gearbox is connected between the motors and the winch drum. This

system suffers from poor efficiency, especially when handling low loads. The present work investigates the feasibility of using digital hydraulic machines in a closed circuit system where the digital motor is directly connected to the drum.

B.2 SIMULATION MODEL

The simulated system is based on a 20000 kg hydraulic offshore auxiliary winch with a capacity of 3600 m of wire. The digital hydraulic winch drive system consists of a digital hydraulic pump (DHP), a digital hydraulic motor (DHM), and two gas accumulators connected in a closed circuit system, as shown in Figure B.1. The DHP is driven by an electrical motor running at a constant speed of 1800 rpm. The DHM is directly connected to the winch drum without any gear box. The two gas accumulators are used to smooth out pressure and flow peaks in line A and B.

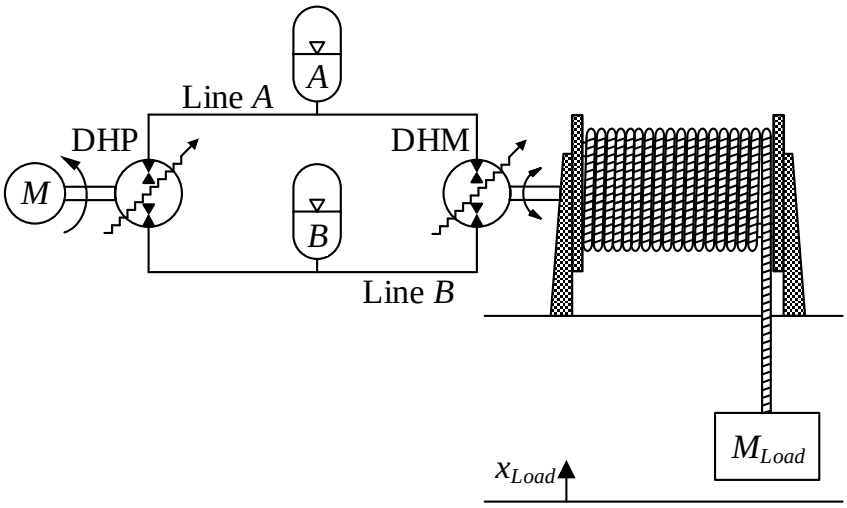

Figure B.1: Simulated winch system

B.2.1 Modeling of the Mechanical System

The mechanical system consists of the load, wire and the drum. All relevant winch parameters are shown in Figure B.2.

Assumptions made for the mechanical system:

- Winch has constant inertia. The winch inertia includes the inertia of the drum and the inertia of 3600 m of wire wound onto the drum.
- Radius of the winch, r_{winch}, is constant
- No friction

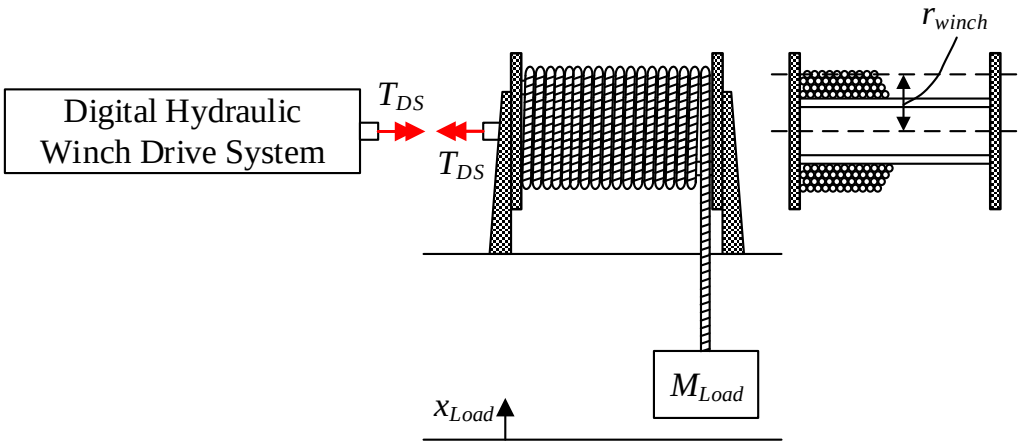

Figure B.2: Mechanical system

- No elasticity in wire

It is assumed that the winch has a constant inertia because no simulation hoists or lowers the payload more than 10 m, which is very small compared to the total wire length. The radius is also assumed to be constant because only the outer wire layer is used. The equation of motion for the winch drum is shown in Eq. B.1.

$$\ddot{\theta}_{drum} = \frac{T_{DS} - M_{Load} \cdot g \cdot r_{winch}}{J_{eff}} \tag{B.1}$$

where T_{DS} is the torque from the drive system acting on the drum, M_{Load} is the mass of the payload, g is the acceleration of gravity, r_{winch} is the radius of the outer winch layer, and J_{eff} is the effective mass moment of inertia. The effective mass moment of inertia includes the inertia of the payload, wire, drum and the DHM and is calculated as shown below in Eq. B.2.

$$J_{eff} = M_{Load} \cdot r_{winch}^2 + J_{winch} + J_{DS} \tag{B.2}$$

where J_{winch} includes the inertia of the drum and the wire wound on the drum and J_{DS} is the inertia of the DHM. The drive torque, T_{DS}, is given in the following section.

B.2.2 Modeling of the Digital Hydraulic Winch Drive System

The digital hydraulic winch drive system is a closed circuit system, see Figure B.3. The DHP and the DHM are two radial piston units with respectively 9 and 42 cylinders. Each one of the lines A and B are connected to an accumulator. The accumulator purpose is to smooth out flow and pressure peaks in the closed circuit system.

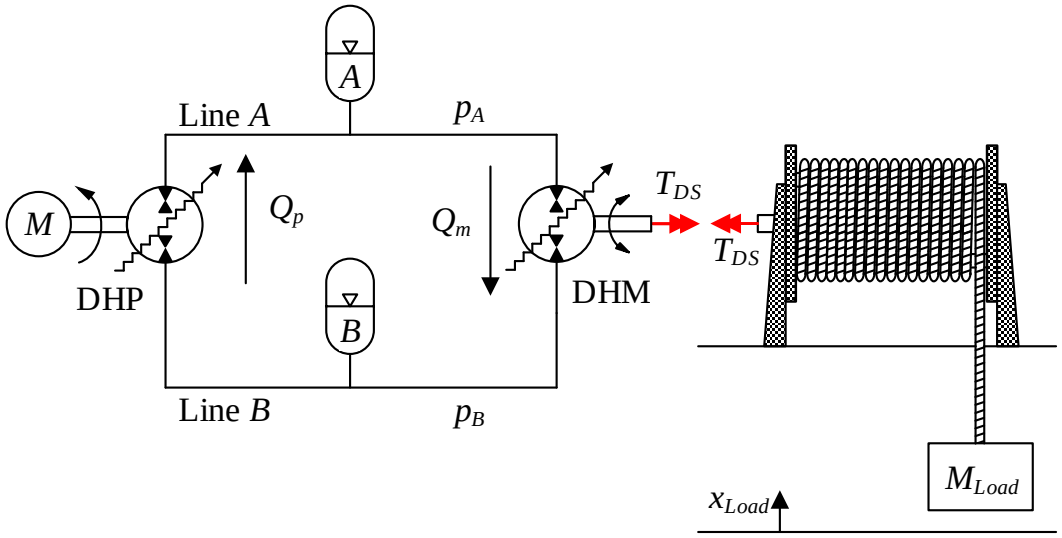

Figure B.3: Digital hydraulic winch drive system

B.2.2.1 Modeling of the Digital Hydraulic Pump and Motor

It is assumed that the cylinder configuration is the same for both the DHP and the DHM. For simplicity, only calculations for one of the pistons in the DHM are shown in this section, but the same method is used for all of the pistons, both for the DHM and the DHP. The on/off valves are assumed to be leak free and the DHP and DHM models do not include any friction or leakage.

Figure B.4 shows the cylinder configuration of one cylinder, note that a more complex cylinder configuration may also be used. The continuity equation is used to calculate the pressure gradient in the cylinder as shown in Eq. B.3.

$$\dot{p}_{cyl} = \frac{\beta}{V_{cyl}} \cdot \left(Q_A - Q_B - \dot{V}_{cyl} \right) \tag{B.3}$$

where β is the effective bulk modulus, V_{cyl} is the cylinder volume, Q_A and Q_B are the flows through valve A and B, and $\dot{V}_{cyl}$ is the rate of change in cylinder volume and is positive if the volume is expanding. The cylinder volume is calculated as shown in Eq. B.4 and the rate of change in cylinder volume is calculated as shown in Eq. B.5.

$$V_{cyl} = V_{0m} + \frac{V_{dm}}{2} \cdot (1 - \cos(\theta_m)) \tag{B.4}$$

$$\dot{V}_{cyl} = \frac{V_{dm}}{2} \cdot \sin(\theta_m) \cdot \dot{\theta}_m \tag{B.5}$$

where V_{0m} is the dead volume in the cylinder and V_{dm} is the piston discharge volume. The flow through the on/off valves, Q_A and Q_B, are calculate by Eq. B.6 and Eq. B.7

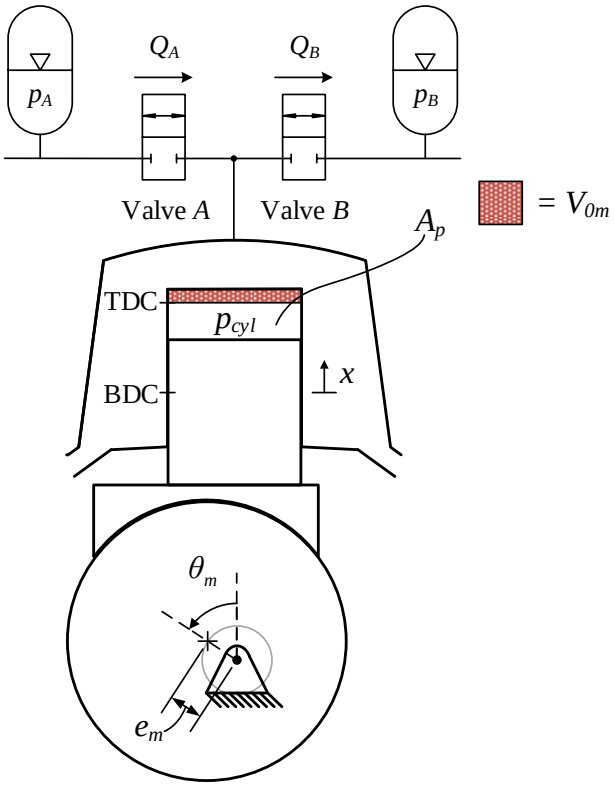

Figure B.4: Cylinder configuration of one cylinder with $\theta_m = \pi/4$

respectively.

$$Q_A = \frac{u_A}{k_f} \cdot \sqrt{p_A - p_{cyl}} \cdot sign(p_A - p_{cyl}) \tag{B.6}$$

$$Q_B = \frac{u_B}{k_f} \cdot \sqrt{p_{cyl} - p_B} \cdot sign(p_{cyl} - p_B) \tag{B.7}$$

where k_f is the flow coefficient of the valves, and u_A and u_B are the opening ratios of the valves ranging from 0 to 1, where 0 is fully closed and 1 is fully open. Valve A and B have the same flow coefficient and the same dynamic response. The dynamic response is described by the second order system shown in Eq. B.8.

$$\ddot{u} = u_{con} \cdot \omega^2 - u \cdot \omega^2 - 2 \cdot \zeta \cdot \omega \cdot \dot{u} \tag{B.8}$$

where u_{con} is the control signal, ζ is the damping ratio and ω is the natural frequency. The control signal is either 0 or 1. The torque contribution from one cylinder is calculated as shown in Equation B.9

$$T_{cyl} = p_{cyl} \cdot A_p \cdot e_m \cdot \sin(\theta_m) \tag{B.9}$$

Finally, the total motor torque and the flow in and out of the DHM are calculated as the sum of the contribution from all pistons, as shown below in Eq. B.10, B.11 and B.12

respectively.

$$T_{DS} = \sum_{i=1}^{42} T_{cyl,i} \tag{B.10}$$

$$Q_{in\,m} = \sum_{i=1}^{42} Q_{A,i} \tag{B.11}$$

$$Q_{out\,m} = \sum_{i=1}^{42} Q_{B,i} \tag{B.12}$$

B.2.2.2 Valve Control Strategy in Motor Mode

The timing of the valve actuation is important to achieve high efficiency and low pressure and flow peaks. The activation angles when operating in motor mode are shown in the simplified control sequence illustration in Fig. B.5. θ_{Ao} and θ_{Ac} are respectively the opening and closing angles for valve A, θ_{Bo} and θ_{Bc} are respectively the opening and closing angles for valve B and θ_{mcm} is the mode choice angel for the motor and is the angle where it is decided if the motor shall run in motor or idle mode.

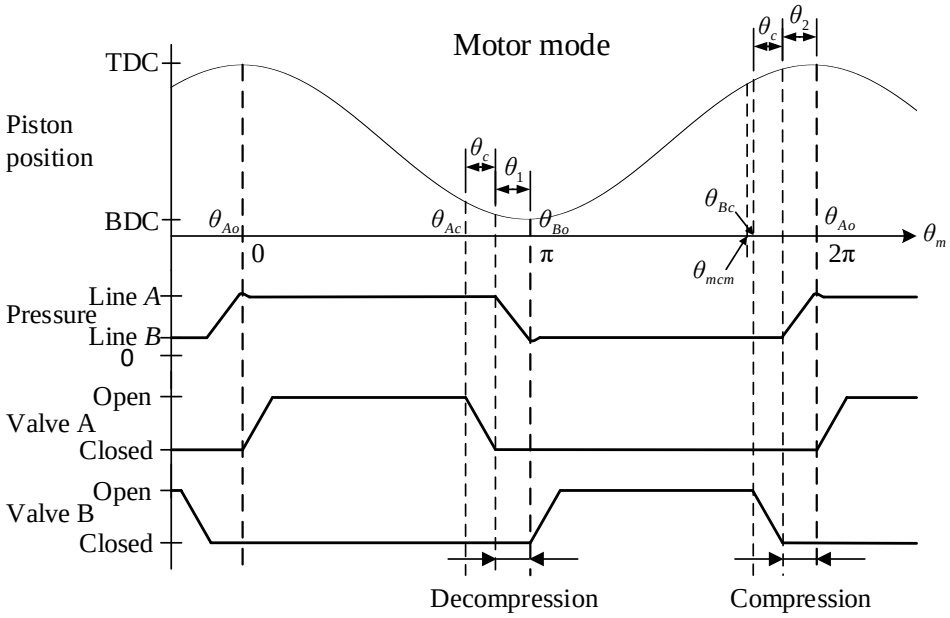

Figure B.5: Control sequence motor mode

The opening angle and closing angle for valve A and B are calculated as shown in Eq. B.13..B.16.

$$\theta_{Ao} = 0 \tag{B.13}$$

$$\theta_{Ac} = \pi - \theta_1 - \theta_c \tag{B.14}$$

$$\theta_{Bo} = \pi \tag{B.15}$$

$$\theta_{Bc} = 2 \cdot \pi - \theta_2 - \theta_c \tag{B.16}$$

where θ_1 is the angle the motor have to rotate to decompress the cylinder fluid from high-pressure level down to low-pressure level when the piston is close to and moving towards BDC. θ_2 is the angle the motor have to rotate to compress the cylinder fluid from low-pressure level up to high-pressure level when the piston is close to and moving towards TDC and θ_c is the angle the motor rotates while closing or opening the valve. The closing angle, θ_c, is given by Eq. B.17

$$\theta_c = \dot{\theta}_m \cdot t_s \tag{B.17}$$

where $\dot{\theta}_m$ is the motor speed and t_s is the valve traveling time.

The change in cylinder volume to compress or decompress the cylinder fluid is calculated based on the continuity equation shown in Eq. B.3.

$$\Delta p = \frac{\beta}{V_{cyl}} \cdot \Delta V$$

$$\Downarrow$$

$$\Delta V = \frac{V_{cyl} \cdot \Delta p}{\beta} \tag{B.18}$$

When calculating θ_1, the piston is close to BDC and the cylinder volume, V_{cyl} is assumed to be $V_{cyl1} = V_0 + V_{dm}$, and when calculating θ_2 the piston is close to TDC and the cylinder volume is assumed to be $V_{cyl2} = V_0$. The change in cylinder volume to compress and decompress the cylinder fluid is calculated as:

$$\Delta V_1 = \frac{V_{cyl1} \cdot (p_A - p_B)}{\beta} \tag{B.19}$$

$$\Delta V_2 = \frac{V_{cyl2} \cdot (p_A - p_B)}{\beta} \tag{B.20}$$

Knowing the needed change in volume, θ_1 and θ_2 are calculated as shown below.

$$\theta_1 = \cos^{-1}\left(1 - \frac{\Delta V_1 \cdot 2}{V_{dm}}\right) \tag{B.21}$$

$$\theta_2 = \cos^{-1}\left(1 - \frac{\Delta V_2 \cdot 2}{V_{dm}}\right) \tag{B.22}$$

B.2.2.3 Valve Control Strategy in Pump Mode

The opening and closing angles for valve A and B in pump mode and the mode choice angle for the pump, θ_{mcp}, are illustrated in Fig. B.6. The opening and closing angles for the valves are calculated as shown in Eq. B.23..B.26.

$$\theta_{Ao} = \pi + \theta_1 \tag{B.23}$$

$$\theta_{Ac} = 2 \cdot \pi - \theta_c \tag{B.24}$$

$$\theta_{Bo} = \theta_2 \tag{B.25}$$

$$\theta_{Bc} = \pi - \theta_c \tag{B.26}$$

where θ_c, θ_1 and θ_2 are calculated as shown in Eq. B.17, B.21 and B.22 respectively.

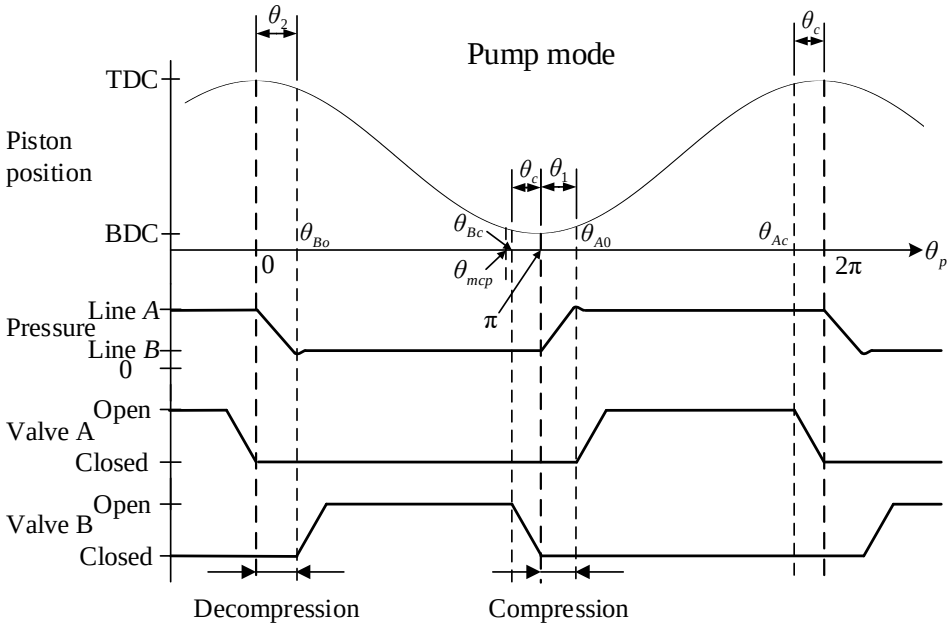

Figure B.6: Control sequence pump mode

B.2.2.4 Pressure dynamics in line *A* and line *B*

For simplicity, only the calculation for the pressure dynamics in line A is shown, but the pressure dynamics in line B is calculated in the same manner. The pressure gradient in line A is calculated as shown in Eq. B.27

$$\dot{p}_A = \frac{\beta}{V_A} \cdot (Q_{outp} - Q_{inm} - \dot{V}_{accA}) \tag{B.27}$$

where V_A is the volume in line A and accumulator A, Q_{outp} is the flow out of the pump, Q_{inm} is the flow into the motor and $\dot{V}_{accA}$ is the rate of changing of accumulator volume. $\dot{V}_{accA}$ is positive if the volume is expanding and is calculated as shown below in Eq. B.28

$$\dot{V}_{accA} = \dot{p}_A \cdot \frac{V_{accAg}}{n_{accA} \cdot p_A} \tag{B.28}$$

where V_{accAg} is the gas volume in accumulator A and n_{accA} is the polytropic exponent for accumulator A. Eq. B.28 is substituted into Eq. B.27 and rearranged as shown in Eq. B.29.

$$\dot{p}_A = \frac{\beta}{V_A} \cdot \frac{(Q_{outp} - Q_{inm})}{1 + \frac{\beta \cdot V_{accAg}}{V_A \cdot n_{accA} \cdot p_A}} \tag{B.29}$$

B.3 WINCH CONTROL SYSTEM

In conventional swash plate units, the displacement is controlled by changing the angle of the swash plate. In digital hydraulic units, each piston has to be controlled individually

resulting in an untraditional and complex control system. Section B.2.2.2 and B.2.2.3 describes the actuation sequence for the on/off valves when the piston runs in motor and pump mode respectively. This section describes how to decide which mode the pistons shall run in. Recall that θ_{mcm} shown in Fig. B.5 describes the angle where the decision for motor mode is taken, and that θ_{mcp} shown in Fig. B.6 describes the angle where the decision for pump mode is taken.

The control system for the winch is divided in two, one for the pump and one for the motor. In general, the motor has an open loop torque controller which calculates the displacement based on load measurements and a desired pressure drop across the motor. The pump has a displacement controller where the displacement is calculated based on the winch drum reference position and the known motor displacement. The pump also has a position feedback controller.

B.3.1 Motor Controller

The DHM is a radial piston motor with 42 cylinders. To ensure relatively smooth output torque, the motor is divided into 14 banks with three pistons in each bank that are evenly distributed around the shaft. Figure B.7 illustrates the motor controller. Based on a desired pressure drop across the motor, Δp_{ref}, and measurements of the load, $\widetilde{M}_{Load}$. The number of active banks, also called n_{step}, is calculated a shown in Eq. B.30.

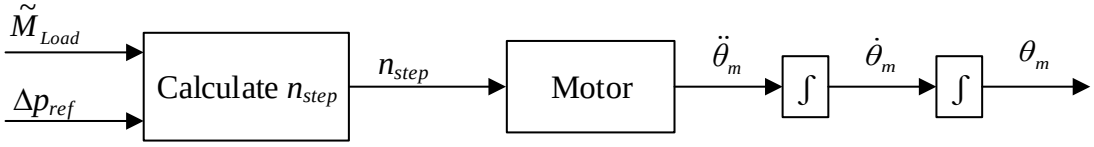

Figure B.7: Motor controller

$$n_{step} \approx \frac{\widetilde{M}_{Load} \cdot g \cdot r_{winch}}{\Delta p_{ref} \cdot T_{step}}, \qquad \text{round of to nearest integer} \tag{B.30}$$

where $n_{step} = 1$ corresponds to 1 active bank, $n_{step} = 2$ corresponds to 2 active banks and so on. T_{step} is the torque one bank can provide with a pressure drop across the motor equal to 1 Pa.

B.3.2 Pump Controller

The controller for the DHP is based on the displacement controller first introduced in [3]. This controller is mainly used in digital hydraulic power management systems, but can also be used in DHPs. The controller calculates a desired volume, V_{des}, which the DHP

shall deliver. If the desired volume is more than a half piston displacement higher than the volume the DHP already have delivered, V_{est}, the next piston will run in pump mode. If the difference is less than a half piston displacement, the next piston will run in idle mode. Figure B.8 shows an example of the control strategy.

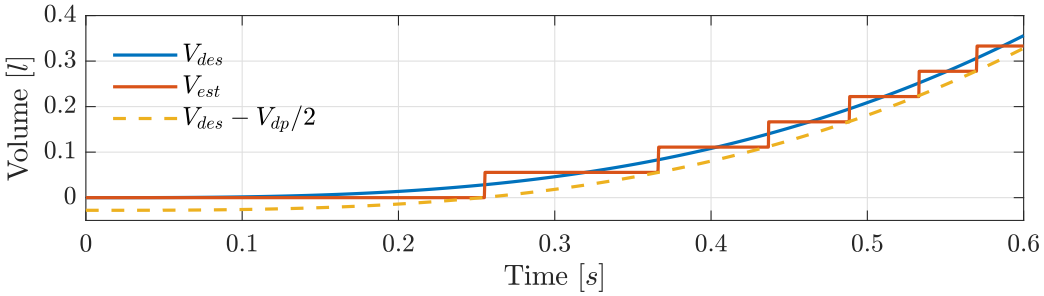

Figure B.8: Example control strategy

In the control system used in this study, the desired volume consists of three different parts, V_{ref}, V_{accA} and V_{err}. Figure B.9 illustrate the DHP controller where the mode choice, D, is calculated by Eq. B.31.

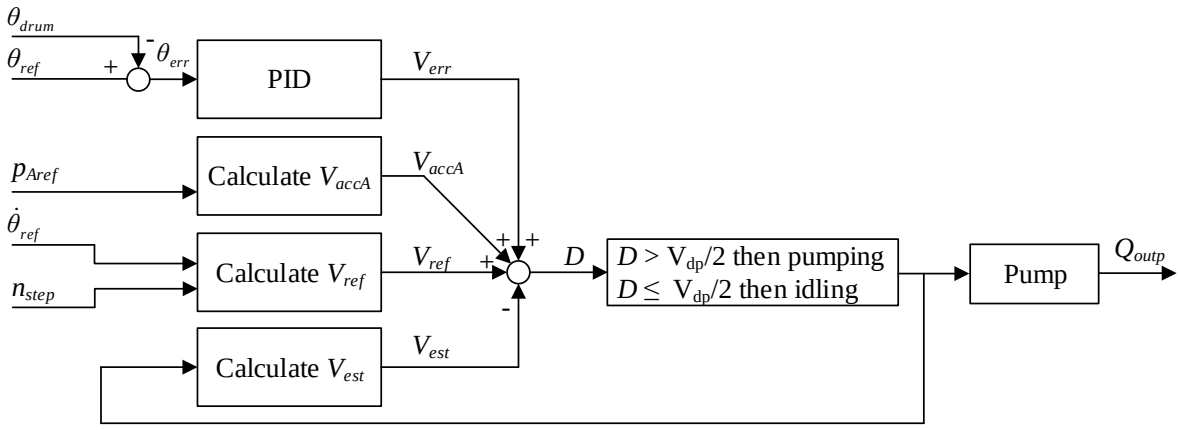

Figure B.9: Pump controller

$$D = V_{ref} + V_{accA} + V_{err} - V_{est}, \quad \rightarrow \quad \begin{cases} \text{pumping} & \text{if} \quad D > V_{dp}/2 \\ \text{idling} & \text{if} \quad D \leq V_{dp}/2 \end{cases} \tag{B.31}$$

where V_{ref} is the estimated volume that is needed to drive the DHM according to the winch drum reference position and is calculated by integrating Eq. B.32

$$\dot{V}_{ref} = \frac{V_{dm} \cdot n_{step} \cdot 3 \cdot \dot{\theta}_{ref}}{2 \cdot \pi} \tag{B.32}$$

where $\dot{\theta}_{ref}$ is the velocity reference of the winch drum.

The DHM is running with constant displacement. In order to accelerate or decelerate the payload, the pressure in line A has to be increased or decreased. When changing the

pressure in line A, the fluid volume of accumulator A will also change. The estimated change of fluid volume in accumulator A, V_{accA}, is also included in the controller. V_{accA} is calculated as shown in Eq. B.33.

$$V_{accA} = \frac{(p_{Aref} - p_{A0}) \cdot V_{accAg0}}{n_{accA} \cdot p_{A0}} \tag{B.33}$$

where p_{A0} is the initial pressure in line A, V_{accAg0} is the gas volume in accumulator A at the initial pressure p_{A0}, and p_{Aref} is the reference pressure in line A. p_{Aref} is calculated as shown in Eq. B.34

$$p_{Aref} = \frac{\ddot{\theta}_{ref} \cdot J_{eff} + \widetilde{M}_{Load} \cdot g \cdot r_{winch}}{T_{step} \cdot n_{step}} + p_{B0} \tag{B.34}$$

where $\ddot{\theta}_{ref}$ is the acceleration reference for the winch drum and p_{B0} is the initial pressure in line B. The output, V_{err}, is calculated as shown in Eq. B.35.

$$V_{err} = \theta_{err} \cdot k_p + \dot{\theta}_{err} \cdot k_d + \int \theta_{err} \cdot k_i \ dt \tag{B.35}$$

where θ_{err} is the difference between the reference winch drum position and the actual position and k_p, k_d and k_i are the PID-controller gains.

Finally, the estimated discharge volume, V_{est}, is calculated by the following equation.

$$V_{est} = n_{pump} \cdot V_{dp} \tag{B.36}$$

where n_{pump} is the total number of pistons that already have been pumping. The compression volume is not taken into account in Eq. B.36 but can be included. In this control system, the small error introduced by excluding the compression volume will be compensated for in the PID-controller.

B.4 Simulation results

This section presents the simulation results. In all, six different cases are simulated. For a winch, it is obviously important to be able to hoist and lower a payload. These properties are shown in the first two sections. Because of the nature of DHPs and DHMs, the output flow or output torque can be pulsating, especially when running with very low displacements. Therefore the third section presents results where a light payload is hoisted with a very low velocity. Experience from the industry shows that it is hard to control very light payloads. The fourth section presents, therefore, simulation results of hoisting an empty hook. In the fifth section, an error in measurements of the payload is introduced to investigate the robustness of the controller. Normally, the same motor displacement can be used during short lifting operations, but for longer lifting operations

it can be appropriate to change displacement due to changes in the load acting on the winch drum. The load acting on the winch drum can for example change when lifting a payload into or out of the water. In the last section, the simulation results show the effect of changing motor displacement while hoisting a constant load. In all cases, the feedback controller gains are the same and equal to $k_p = 0.1\ m^3$, $k_d = 0.025\ m^3 s$ and $k_i = 0.2\ m^3/s$.

B.4.1 Hoisting

This section presents the results of hoisting a payload equal to 18000 kg a distance of 10 m. The payload velocity is ramped up to 1 m/s with a ramp time of 2 s. Figure B.10 shows the simulation results. The initial pressure in line B is 25 bar, and the desired pressure drop across the motor is 225 bar. The calculated motor step is $n_{step} = 13$.

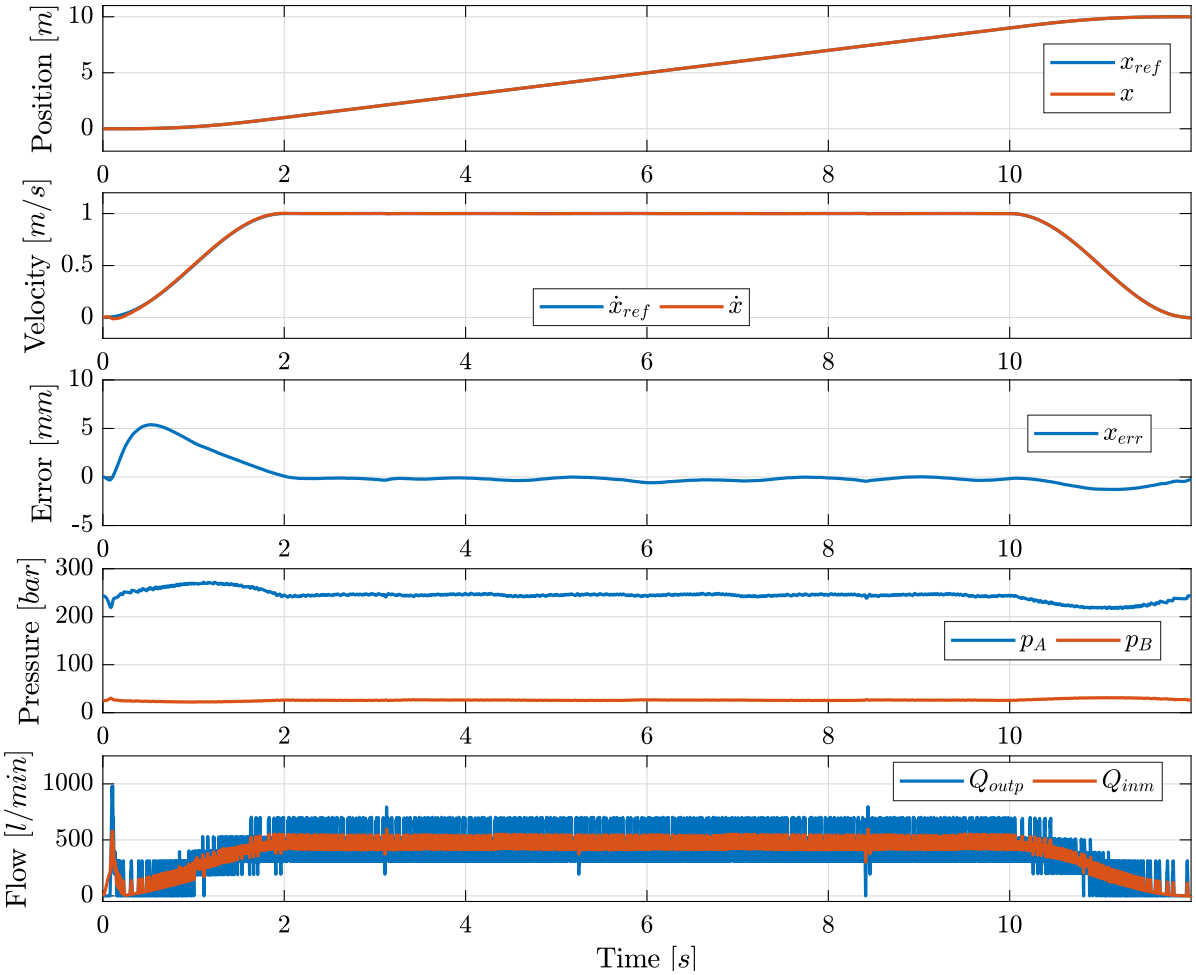

Figure B.10: Simulation results of hoisting with $M_{Load} = 18000\ kg$, $\Delta p_{ref} = 225\ bar$, $p_{B0} = 25\ bar$, $k_p = 0.1\ m^3$, $k_d = 0.025\ m^3 s$, and $k_i = 0.2\ m^3/s$

The first and second plot show that the payload follows the position reference and the velocity reference well. The third plot shows that maximum position error occurs when

accelerating the load and is approximately 5 mm. When the winch runs with constant speed, the position error is close to 0 mm. The fifth plot shows a flow peak in the beginning of the motion. This flow peak is needed to increase the pressure in line A and thereby increase the pressure drop across the motor and then accelerate the motor. The pump flow and motor flow are also heavily oscillating due to the concept of DHPs and DHMs. The pistons in DHPs and DHMs are enabled and disabled on a stroke by stroke basis resulting in flow and pressure ripples.

B.4.2 Lowering

This section presents the results of lowering a payload equal to 18000 kg a distance of 10 m. The velocity of the load is ramped down to -1 m/s with a ramp time of 2 s. Figure B.11 shows the simulation results. When lowering the load, the DHP acts like a motor and the DHM acts like a pump, meaning that cylinders in the DHP can only run in motor or idle mode and the pistons in the DHM can only run in pump or idle mode. The same control strategy as described in Section B.3 is used for both the DHP and the DHM. The initial pressure in line B is 25 bar and the desired pressure drop across the motor is 225 bar. The calculated motor step is $n_{step} = 13$.

The simulation results show that the payload follows the reference position and velocity well. Maximum position error is smaller than 1.5 mm.

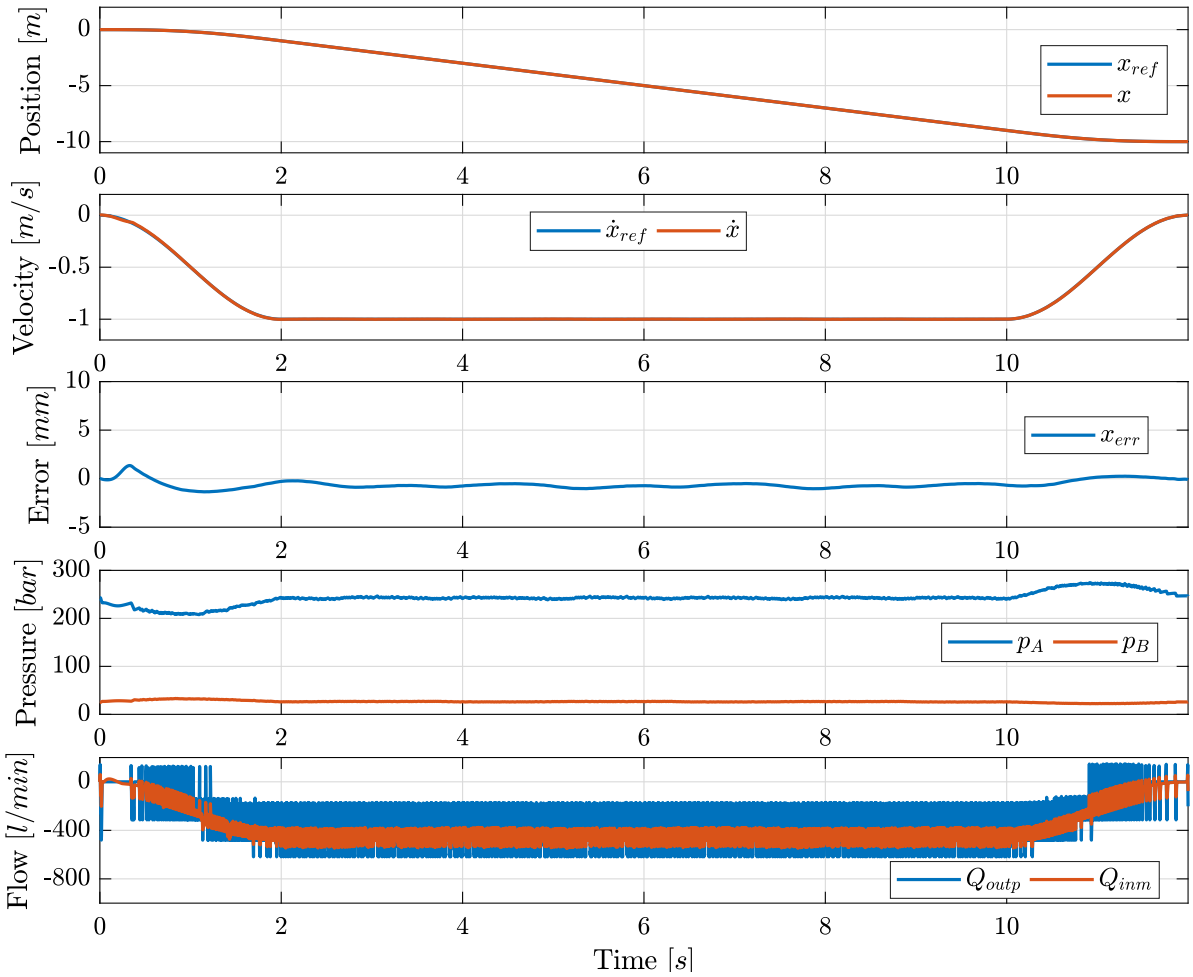

Figure B.11: Simulation results of lowering with $M_{Load} = 18000\ kg$, $\Delta p_{ref} = 225\ bar$, $p_{B0} = 25\ bar$, $k_p = 0.1\ m^3$, $k_d = 0.025\ m^3 s$, and $k_i = 0.2\ m^3/s$

B.4.3 Hoisting Small Load at Low Speed

Every single cylinder in the DHP is controlled individually on a stroke by stroke basis, which results in flow ripples when running in partial displacement. In the closed circuit system studied in this paper, two accumulators are connected to pressure line A and pressure line B to smooth out flow and pressure ripples. One critical scenario is when the required pump flow is low. This scenario occurs when the velocity reference and the load is low. Therefore, in this test, the payload is set to 4000 kg and maximum velocity is set to 0.2 m/s. The payload is hoisted 5 m and the ramp time for the velocity is 2 s. Figure B.12 shows the results with the initial pressure in line B equal to 25 bar and the desired pressure drop across the motor equal to 225 bar. The calculated motor step is $n_{step} = 3$.

The simulation results do not show any oscillations in velocity. The payload follows the position reference well with a maximum position error less than 2 mm when accelerating the load. The position error is close to 0 mm when the winch runs with constant speed. The simulated pump flow shows that the pump is only using one cylinder at a time. The

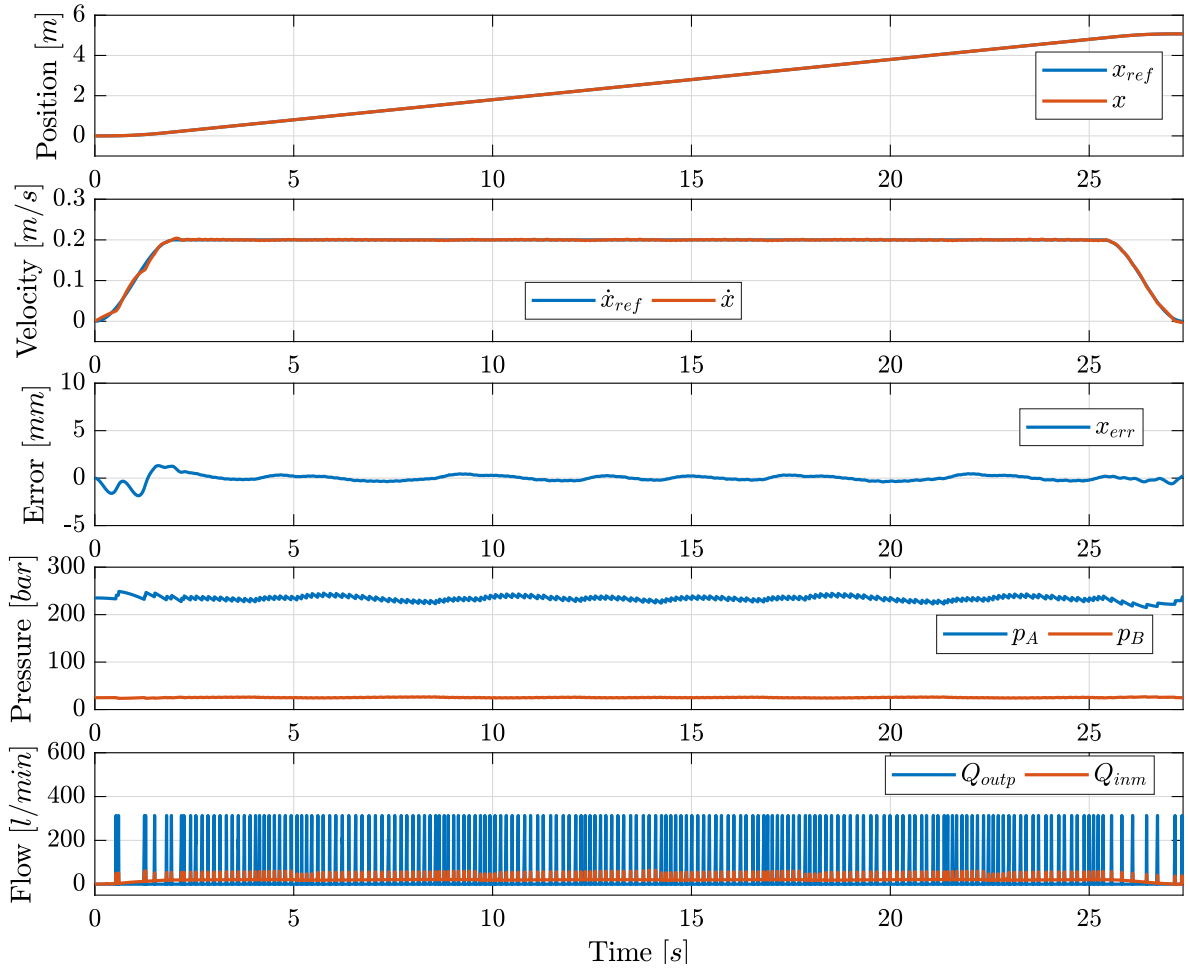

Figure B.12: Simulation results of hoisting with $V_{max} = 0.2\ m/s$, $M_{Load} = 4000\ kg$, $\Delta p_{ref} = 225\ bar$, $p_{B0} = 25\ bar$, $k_p = 0.1\ m^3$, $k_d = 0.025\ m^3 s$, and $k_i = 0.2\ m^3/s$

average frequency of pumping cylinders is only 7 hz.

B.4.4 Hoisting an Empty Hook

This case tests driving with a payload equal to 0 kg, which corresponds to operating with an empty hook. The desired pressure drop across the motor is 0 bar. The empty hook is hoisted 10 m and the velocity is ramped up to 1.5 m/s with a ramp time of 3 s. Because of the low pressure drop across the motor and the high inertia of the winch drum and the wire, the initial pressure in line B is set to 125 bar and the motor step is set to $n_{step} = 3$ to ensure that the pressure in line A remains above the minimum pressure for accumulator A while decelerating the load.

The simulation results show that the payload follows the reference position and velocity well. The maximum position error is approximately 3.5 mm and occurs right after the payload reaches maximum velocity. The position error converges towards 0 mm when the winch drum runs with constant velocity.

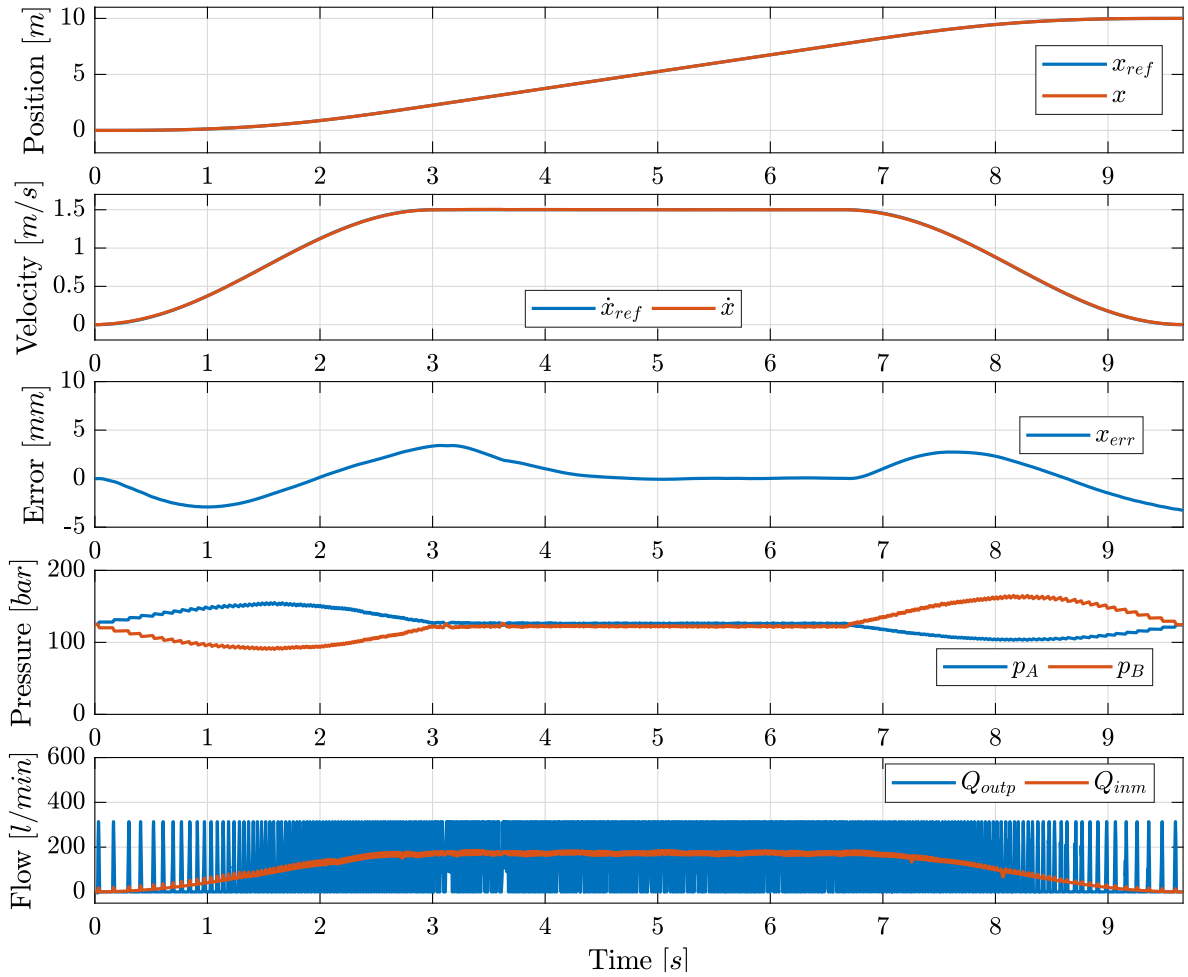

Figure B.13: Simulation results of hoisting with $M_{Load} = 0kg$, $\Delta p_{ref} = 0bar$, $p_{B0} = 125\ bar$, $k_p = 0.1\ m^3$, $k_d = 0.025\ m^3 s$, and $k_i = 0.2\ m^3/s$

B.4.5 Error in Load Measurement

Motor displacement is calculated based on a desired pressure drop across the motor and measurements of the payload. In this test, an error in the payload measurements is introduced to investigate the robustness of the control system. The actual payload is set to 18000 kg, but the measured value used in the controller is only 80 % af the actual load. The payload is hoisted 10 m and the velocity is ramped up to 1 m/s with a ramp time of 2 s. The simulation results are shown in Fig. B.14. The initial pressure in line B is set to 25 bar and the desired pressure drop across the motor is 225 bar. The calculated motor step is $n_{step} = 11$.

This case is similar to the case presented in Section B.4.1 except for the error in the load measurements. The simulation results show that an error in the payload measurements gives almost the same results as in Section B.4.1. The maximum position error is increased to 7.4 mm. Due to the measurement error, the calculated motor displacement is only $n_{step} = 11$ compared to $n_{step} = 13$ for the case without any measurements error. The

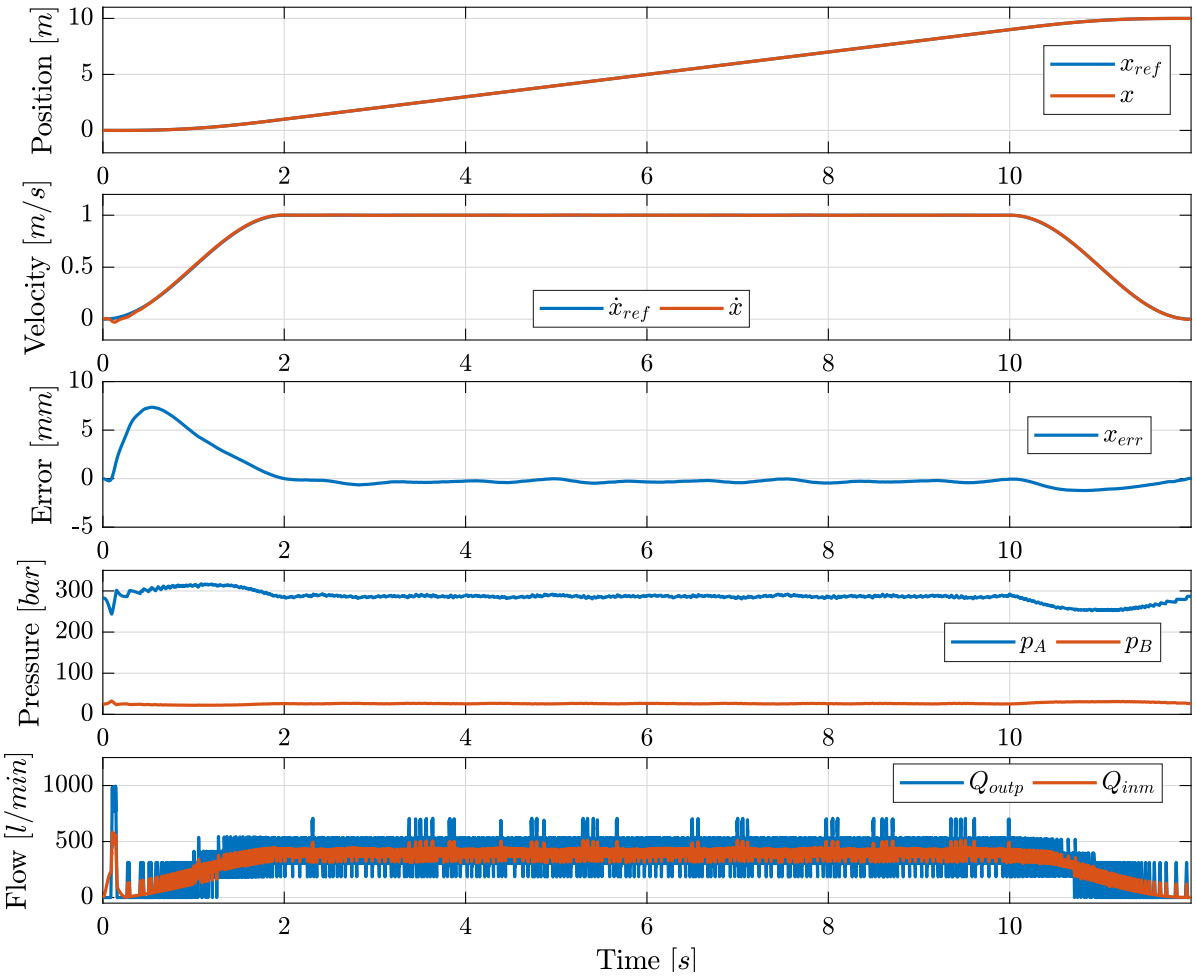

Figure B.14: Simulation results of hoisting a load with measured load equal 80 % of the real load and where $M_{Load} = 18000\ kg$, $\Delta p_{ref} = 225\ bar$, $p_{B0} = 25\ bar$, $k_p = 0.1\ m^3$, $k_d = 0.025\ m^3 s$, and $k_i = 0.2\ m^3/s$

difference in motor displacement results in a higher pressure in line A and a lower pump flow, but the position tracking performance remains almost unchanged.

B.4.6 Change of Motor Displacement

The winch studied in this paper has a capacity of 3600 m of wire. In cases where the load is lifted or lowered several hundreds of meters, the load acting on the winch drum will vary. The load can vary because the weight of the wire will act as an extra load when lowering or because the load is lowered into water. In cases like this, the motor must be able to change displacement during operation. Figure B.15 shows results from hoisting of a constant load equal to 15000 kg with a change in motor step from $n_{step} = 11$ to $n_{step} = 14$, full displacement, after 4 s. The initial pressure in line B is 25 bar and the desired pressure drop across the motor is 225 bar.

The motor starts to change displacement after 4 s. The time it takes to change motor

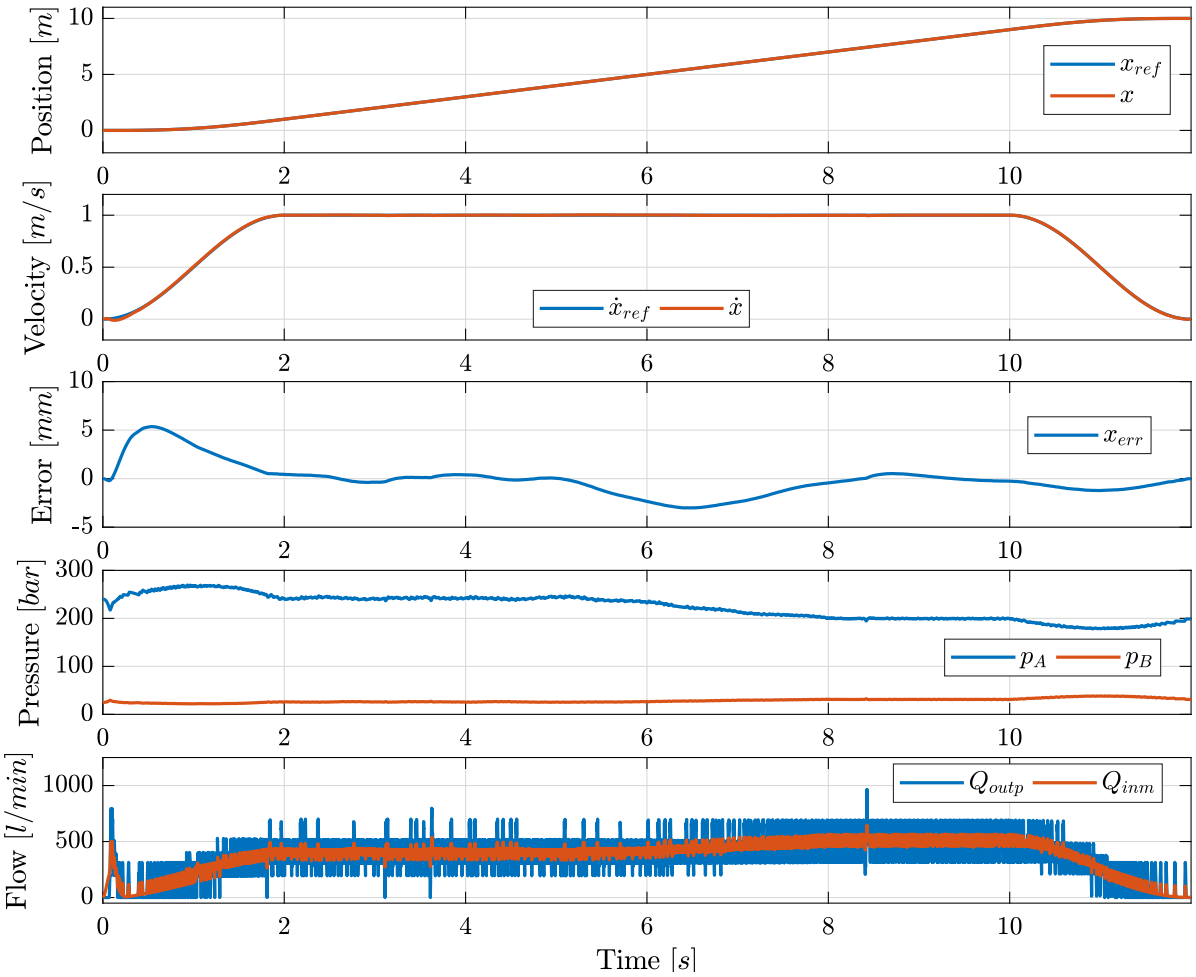

Figure B.15: Simulation results of hoisting a load when changing motor step from step 11 to step 14 with $M_{Load} = 15000\ kg$, $\Delta p_{ref} = 225\ bar$, $p_{B0} = 25\ bar$, $k_p = 0.1\ m^3$, $k_d = 0.025\ m^3 s$, and $k_i = 0.2\ m^3/s$

displacement is dependent of the motor speed. The motor have to rotate more than a half shaft revolution, $(2 \cdot \pi - \theta_{mcm} + \pi)$, to fully change displacement. When hoisting the payload with 1 m/s, the motor response time is approximately 4.4 s.

When changing motor displacement the position error increases to -3 mm, but approximates zero when the motor displacement has reached full displacement. In the pressure plot, it can be seen that the pressure in line A decreases when the motor displacement is changed. It can also been seen that the pump flow and motor flow increase.

Bibliography

[1] Masahide Umaya, Toshihide Noguchi, Michiya Uchida, Masaaki Shibata, Yasuhiro Kawai, and Ryosuke Notomi. Wind power generation-development status of offshore wind turbines. *Mitsubishi Heavy Industries Technical Review*, 50(3):29–35, 2013.

[2] Eize de Wries. Mitsubishi launches 7MW turbine. `https://www.windpowermonthly.com/article/1109873/mitsubishi-launches-7mw-turbine`. Accessed: 15-06-2017.

[3] M Heikkilä and M Linjama. Direct connection of digital hydraulic power management system and double acting cylinder-a simulation study. In *The Fourth Workshop on Digital Fluid Power, DFP*, volume 11, 2011.

Paper C

Analysis of Requirements for Valve Accuracy and Repeatability in High Efficient Digital Displacement Motors

Sondre Nordås, Morten Kjeld Ebbesen and Torben Ole Andersen

This paper has been published as:

S. Nordås, M. K. Ebbesen, and T. O. Andersen. Analysis of Requirements for Valve Accuracy and Repeatability in High Efficient Digital Displacement Motors. In *The Proc. of the BATH/ASME 2018 Symposium on Fluid Power and Motion Control*, Bath, United Kingdom, 2018.

Analysis of Requirements for Valve Accuracy and Repeatability in High Efficient Digital Displacement Motors

Sondre Nordås*, Morten Kjeld Ebbesen* and Torben Ole Andersen**

*University of Agder
Faculty of Engineering and Science
Jon Lilletunsvei 9, 4879 Grimstad, Norway

** Aalborg University
Faculty of Engineering and Science
Pontoppidanstræde 101, 9220 Aalborg East, Denmark

Abstract **– Traditional variable displacement piston machines achieve high efficiency when operating at high displacements, but struggle with poor efficiency at low displacements. The pistons are connected to high pressure and low pressure in conjunction with the output shaft position and the displacement is changed by changing the piston stroke, resulting in almost constant friction, leakage, and compressibility losses independent of displacement. In digital displacement machines, the rotary valve is replaced by two fast switching on/off valves connected to every cylinder. By controlling the fast switching on/off valves, the cylinders can be controlled individually and friction, leakage and compressibility losses can be minimized resulting in high efficiency even at low displacements. Previous studies have shown that high efficiency digital displacement machines require fast switching valves with high flow capacity and optimal valve timing strategy. When the digital displacement motor is to start, stop or be controlled at low speeds, the on/off valves must be able to open against high pressure difference. When opening the valves actively, the valve timing has to be conducted properly to minimize valve throttling losses and flow and pressure peaks. First, this paper shortly describes a previously developed method to estimate valve characteristics like transition time and flow capacity for a digital displacement machine. Then the paper presents a novel method of describing the required valve accuracy and repeatability to keep the valve throttling losses low and machine efficiency high.**

C.1 BACKGROUND

Digital displacement machines are typically radial piston machines with two fast switching on/off valves connected to each cylinder allowing for individual cylinder control. A simplified illustration of a digital displacement machine is shown in Fig. C.1. By controlling

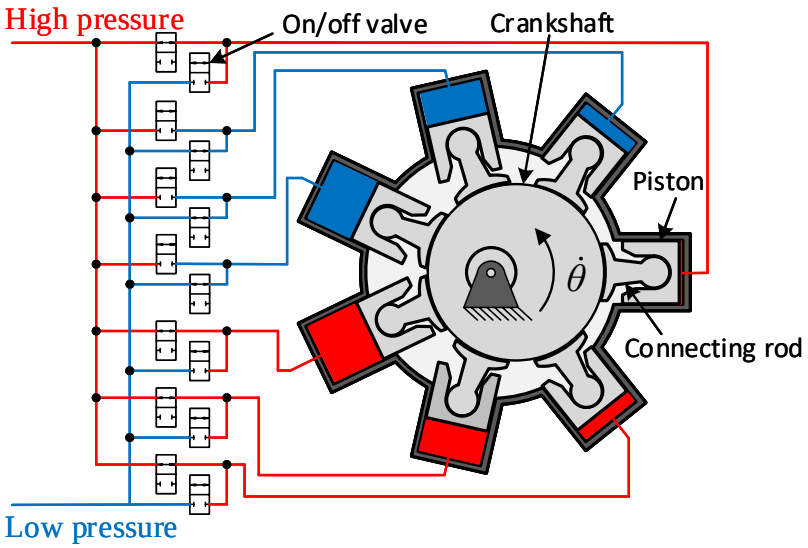

Figure C.1: Simplified illustration of a digital displacement machine running as a motor.

the on/off valves, each cylinder can be controlled to operate in motor mode, pump mode or idle mode. The individual piston control makes it possible to only pressurize cylinders when necessary, resulting in losses that scale with the displacement. Those losses are leakage losses, friction losses, and compressibility losses. In addition to increased efficiency at partial displacement, the individual cylinder control makes the digital displacement machine very flexible and suited for secondary control systems and regeneration of braking energy.

One of the most important components in digital displacement machines is the fast switching on/off valve. The on/off valve must have suitable characteristics for the digital displacement machine to achieve high efficiency for a wide range of operation conditions. The required valve characteristics are affected by displacement strategy, motor speed, and motor size. In addition to the valve characteristics, it is also highly important to design the valve timing to fully recover the potential energy in the compressed oil [1]. The term "valve timing" is used to describe the activation sequence of the valves when pressurizing and depressurizing the cylinder oil. An optimal valve timing strategy will in addition to low compressibility losses, result in low flow and pressure peaks in the hydraulic system. In [2] a method of estimating the required valve characteristics for full stroke displacement strategy and partial stroke displacement strategy is developed. Further down in this section, a short summary of the method presented in [2] is given, and

some aspects of optimal valve timing strategy are discussed. Note that the nomenclature can be found in Appendix A.

C.1.1 Valve Requirements in Full Stroke Displacement Strategy

In full stroke displacement strategy (FSDS), the cylinders are enabled and disabled on a stroke by stroke basis, and the fast switching on/off valves are only switched when the piston is close to top dead center (TDC) and bottom dead center (BDC). In those positions the piston speed and valve flow is low, and the valves can be timed to only switch when the pressure drop across them is small, resulting in very low valve switching losses. A more detailed description of FSDS can be found in [3].

Previous work shows that digital displacement motors running with FSDS can achieve high efficiency even at partial displacements [4, 5, 6]. In [7], the authors have developed a method of defining the required valve transition time and flow capacity. The presented method has been further improved in [2]. The improvements were carried out by modifying the valve movement and the valve timing strategy.

In [2] the author found that the motor efficiency can be generalized by introducing the normalized valve transition time, $\overline{T}_s$, and normalized allowable valve pressure drop, $\overline{\Delta}p$. The normalized valve transition time, $\overline{T}_s$, describes the valve transition time, T_s, as a percentage of the motor shaft revolution time, T_{rev}, as shown in Eqn. C.1. The normalized allowable valve pressure drop, $\overline{\Delta}p$, describes maximum valve pressure drop, $\Delta p_{valve,max}$, as a percentage of the pressure difference across the digital displacement machine, $\Delta p_{machine}$, as shown in Eqn. C.2. The efficiency map is shown in Fig. C.2.

$$\overline{T}_s = \frac{T_s}{T_{rev}} \quad \text{where} \quad T_{rev} = \frac{2 \cdot \pi}{\dot{\theta}} \tag{C.1}$$

$$\overline{\Delta}p = \frac{\Delta p_{valve,max}}{\Delta p_{machine}} \tag{C.2}$$

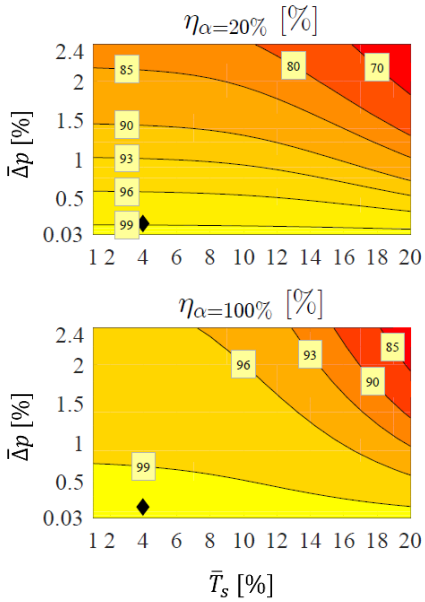

Figure C.2: Generalized efficiency map for a digital displacement motor running with FSDS where α indicates the relative displacement in FSDS [2].

The top plot maps the efficiency at 20% displacement and the bottom plot maps the efficiency at 100% displacement. It can be seen from the efficiency map in the top plot that maximum pressure drop across the valve should be less than approximately 0.5% of the pressure drop across the digital displacement machine to achieve efficiency above 96% at 20% displacement. The plotted span of valve transition time has a small influence on efficiency when the pressure drop across the valve is low. By choosing a target efficiency, the normalized valve parameters, $\overline{T}_s$ and $\overline{\Delta}p$, can be found from Fig. C.2. The required valve transition time, T_s, and flow capacity, Q_{ref}, for a motor with a given cylinder displacement, V_d, maximum speed, $\dot{\theta}_{max}$, and system pressure are given by:

$$T_s = \overline{T}_s \cdot T_{rev} \tag{C.3}$$

$$Q_{ref} = Q_{valve,max} \cdot \frac{\sqrt{\Delta p_{ref}}}{\sqrt{\Delta p_{valve,max}}} \tag{C.4}$$

where $Q_{valve,max}$ is the maximum flow through the valve, $\Delta p_{valve,max}$ is the maximum allowable pressure drop across the valve, and Δp_{ref} is a reference pressure set to 5 bar. The maximum flow, $Q_{valve,max}$, is calculated as shown in Eqn. C.5 and the maximum allowable pressure drop, $\Delta p_{valve,max}$, is calculated by rearranging Eqn. C.2 as shown in Eqn. C.6.

$$Q_{valve,max} = \frac{V_d}{2} \cdot \dot{\theta}_{max} \tag{C.5}$$

$$\Delta p_{valve,max} = \overline{\Delta}p \cdot \Delta p_{machine} \tag{C.6}$$

C.1.2 Valve Requirements in Partial Stroke Displacement Strategy

In partial stroke displacement strategy (PSDS), the cylinders are only active in a part of the cylinder stroke and idling in the remaining part of the stroke. The displacement is changed by increasing or decreasing the active part. In partial stroke displacement strategy, the valves can be switched mid-stroke where the piston speed and valve flow is high. This results in possible high flow throttling losses when switching the valves and makes it hard to time the valves to only switch when the pressure drop across them is small. A more detailed description of PSDS is given in [3].

Previous work shows that PSDS tends to achieve lower efficiency compared to FSDS, especially at low displacements [4, 5, 6]. In [2] the author, in addition to describing the valve requirements for FSDS, has used the same strategy to describe the valve requirements for PSDS. The result is shown in Fig. C.3, where the first plot shows the efficiency map at 75% displacement, the second plot at 50% displacement and the third plot at 25% displacement.

By comparing the efficiency map of FSDS shown in Fig. C.2 with the efficiency map of PSDS shown in Fig. C.3, it can be seen that the valve requirements for PSDS are more strict than for FSDS. The allowable maximum pressure drop across the valve has not changed remarkably compared to FSDS, but the transition time has more influence on the efficiency. To achieve efficiency above 96% at 20% displacement for FSDS, the normalized allowable pressure drop, $\overline{\Delta}p$, should be below 0.5% and the normalized switching time should be below 20% (maximum plotted value). In PSDS, the normalized allowable pressure drop, $\overline{\Delta}p$, should be below 0.5% and the normalized switching time should be below 1.67% in order to achieve approximately the same efficiency. In Tab. C.1, the actual valve transition time and valve flow capacity are calculated at various speeds for a digital displacement machine with $V_d = 50$ cc/rev and $\Delta p_{machine} = 200$ bar.

Table C.1: Valve flow capacity and valve transition time for chosen speeds. Recall that $\overline{\Delta}p = 0.5\%$ and $\overline{T}_s = 1.67\%$ results in $\eta_{\alpha_{PSDS}=25\%} > 96\%$ (see Fig. C.3) and $\overline{\Delta}p = 0.5\%$ and $\overline{T}_s = 20\%$ results in $\eta_{\alpha=20\%} > 96\%$ (see Fig. C.2).

Motor speed	**1000 rpm**	**100 rpm**	**10 rpm**
Q_{ref} when $\overline{\Delta}p = 0.5\%$	350 l/min	35 l/min	3.5 l/min
T_s when $\overline{T}_s = 1.67\%$	1 ms	10 ms	100 ms
T_s when $\overline{T}_s = 20\%$	12 ms	120 ms	1200 ms

Table C.1 shows that in order to achieve approximately same efficiency for both FSDS and PSDS, the machine operating with PSDS need much faster on/off valves than the

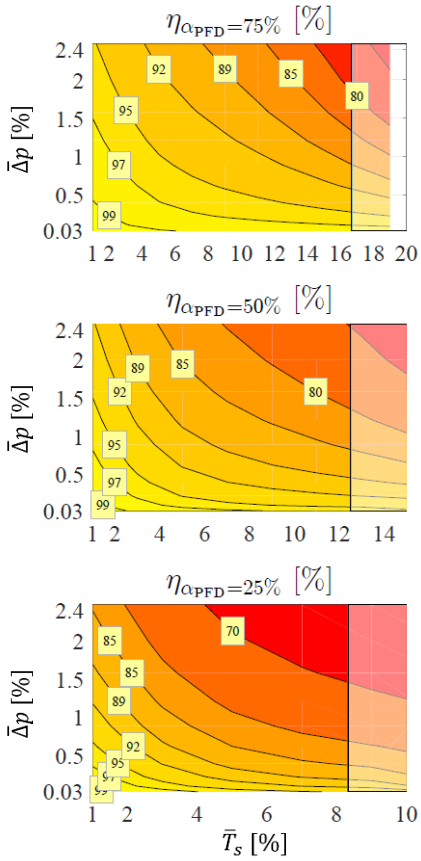

Figure C.3: Generalized efficiency map for a digital displacement motor running with PSDS where α_{PFD} indicates the relative displacement in PSDS [2]. The shaded areas in the right side of the diagrams indicate operating cycles where the high pressure valve is closing before it is fully opened [2].

machine operating with FSDS. It can also clearly be seen that when increasing the speed, the required flow capacity is increased and faster valves are needed.

C.1.3 Timing Strategy

Pressurized oil contains potential energy. Independent of displacement strategy, the valve timing strategy should be designed to recover the energy in the compressed oil fully. Artemis IP is the pioneer in digital displacement technology and is using poppet valves with electrical actuators [8, 9]. The poppet valve is passively opened, and the electrical actuator only needs to keep the valve open against flow forces. The term "passively open" indicates that the valve is mainly opened by pressure forces. One major advantage of this valve design is that the valve can only be actuated when the pressure on both sides of the valve is equalized resulting in full recovery of the energy in the compressed oil and low flow and pressure peaks. The disadvantages are that some additional means are required when the motor is to be started, stopped or controlled at low speeds [10]. This valve

configuration may therefore only be suited for high speed motors with infrequent starts and stops. In low speed motors with frequent starts, stops and changes of direction of rotation, the on/off valves should be able to switch independent of pressure difference [11]. Using valves that can be actively opened independent of the pressure difference across the valve can still fully recover the compression energy in the oil, but the valve timing does not get any help from the cylinder pressure, and optimal timing is more difficult to achieve.

An active valve is assumed to open at a certain time, but in fact, it may open a little bit earlier or later. In [4] the authors found that an opening error of only ±2 ms in a digital displacement machine running with partial stroke displacement strategy at 57% displacement and 3000 rpm resulted in large valve throttling losses. This result shows the importance of optimal valve timing and valves with high accuracy and repeatability. The work presented in this paper aims to map the sensitivity of efficiency in digital displacement motors running at various speeds to the repeatability and accuracy of the fast switching on/off valve.

C.2 SIMULATION MODEL OF A SINGLE CYLINDER DIGITAL DISPLACEMENT MOTOR

The simulation model is implemented in MATLAB R2018a and developed to analyze requirements for valve repeatability and accuracy. The requirements are evaluated by investigating the motor efficiency and valve throttling losses at different displacements and with different valve timing strategies. It is assumed that all cylinders in a digital displacement motor have the same characteristics. The motor efficiency and valve throttling losses are therefore only evaluated for one cylinder. The simulated system is illustrated in Fig. C.4. The cylinder configuration shown in Fig. C.4 is chosen because of its relation between motor shaft position, θ, and cylinder volume, V_{cyl}. The efficiency of the digital displacement motor is calculated as shown in Eqn. C.7.

$$\eta = \frac{E_{out}}{E_{in}} \tag{C.7}$$

where E_{in} is the input energy and E_{out} is the output energy. The input energy, E_{in}, and output energy, E_{out}, is calculated by integrating the input and output power for one shaft

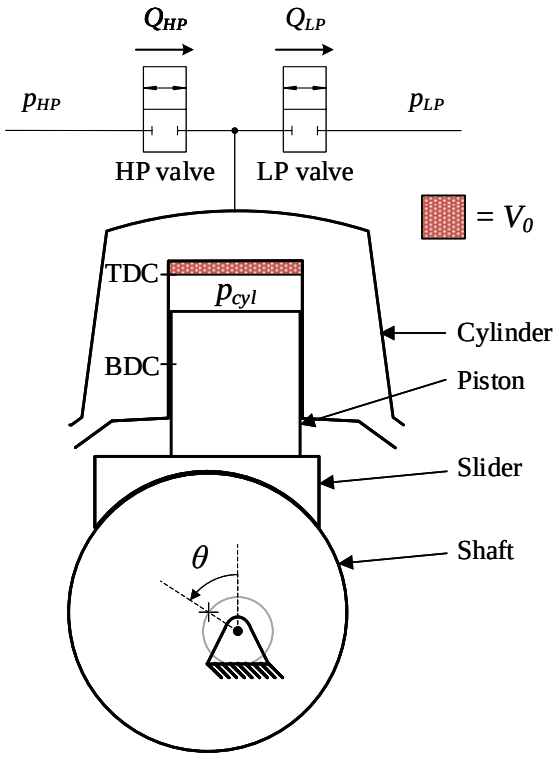

Figure C.4: Simulated system.

revolution,

$$E_{in} = \int P_{in}\ dt \quad \Downarrow$$

$$= \int Q_{HP} \cdot p_{HP} - Q_{LP} \cdot p_{LP} + \overbrace{\left(\dot{V}_{cyl} + Q_{LP} - Q_{HP}\right) \cdot p_{cyl}}^{P_{comp}}\ dt \tag{C.8}$$

$$E_{out} = \int P_{out}\ dt = \int \tau_{cyl} \cdot \dot{\theta}\ dt \tag{C.9}$$

where P_{in} is the input power, P_{out} is the output power, Q_{HP} is the flow through the high pressure valve, Q_{LP} is the flow through the low pressure valve, p_{HP} is the pressure in the high pressure source, p_{LP} is the pressure in the low pressure source, $\dot{V}_{cyl}$ is the rate of change in cylinder volume and positive if the volume is expanding, p_{cyl} is the chamber pressure, τ_{cyl} is the cylinder torque and $\dot{\theta}$ is the shaft speed. Pressurized oil contains potential energy. This energy is considered as an input energy and calculated as shown in the p_{comp}-part in Eqn. C.8. When increasing the cylinder volume without any flow entering or leaving the cylinder volume, $Q_{HP} = 0$ l/min and $Q_{LP} = 0$ l/min, the oil in the cylinder chamber is decompressed and the potential energy in the oil is used, hence p_{comp} is positive. If the cylinder is decompressed to much, cavitation will appear. Cavitation should be avoided with proper valve timing. When reducing the cylinder volume with both valves closed, the oil in the cylinder is compressed and potential energy is stored in the oil, hence p_{comp} is negative.

To calculate the needed parameters, several assumptions are made. The chosen cylinder configuration, shown in Fig. C.4, is not optimal considering losses. In this simulation, friction between the shaft and the slider is neglected as well as the friction between the slider and the piston and the friction between the piston and the cylinder. It is also assumed that the cylinder is leak free. Friction and leakage will affect the efficiency, but the main objective in this paper is to analyze how a deviation from optimal valve timing affects motor efficiency and valve throttling losses. Neglecting friction and leakage losses will not significantly affect the losses related to valve timing, but the calculated efficiency will be higher than for a real system with all losses represented.

In this study, the dynamic performance of the motor is not of interest. The motor inertia is therefore neglected and the motor speed, $\dot{\theta}$, is assumed to be constant. This means that the rotation of the motor is described with a kinematic driver while the dynamics of the oil is described with the ordinary pressure derivative and time integration. The pressure derivative in the cylinder is calculated by using the continuity equation,

$$\dot{p}_{cyl} = \frac{\beta_{eff}}{V_{cyl}} \cdot \left(Q_{HP} - Q_{LP} - \dot{V}_{cyl} \right) \tag{C.10}$$

where β_{eff} is the effective bulk modulus of the oil. The cylinder volume, V_{cyl}, is calculated as shown in Eqn. C.11 and $\dot{V}_{cyl}$ is calculated as shown in Eqn. C.12.

$$V_{cyl} = V_0 + \frac{V_d}{2} \cdot (1 - \cos\theta) \tag{C.11}$$

$$\dot{V}_{cyl} = \frac{V_d}{2} \cdot \sin(\theta) \cdot \dot{\theta} \tag{C.12}$$

where V_0 is the dead volume in the cylinder and V_d is the cylinder displacement. The volume flows through the valves, Q_{HP} and Q_{LP}, are calculated as shown in Eqn. C.13 and Eqn. C.14 respectively.

$$Q_{HP} = \frac{u_{HP}}{k_f} \cdot \sqrt{|p_{HP} - p_{cyl}|} \cdot sign(p_{HP} - p_{cyl}) \tag{C.13}$$

$$Q_{LP} = \frac{u_{LP}}{k_f} \cdot \sqrt{|p_{cyl} - p_{LP}|} \cdot sign(p_{cyl} - p_{LP}) \tag{C.14}$$

where u_{HP} and u_{LP} are the opening ratios of the high pressure and low pressure valves ranging from 0 to 1, where 0 is fully closed and 1 is fully open. Both valves have the same flow-pressure coefficient, k_f, and the same dynamic response. The flow-pressure coefficient, k_f, is calculated as shown in Eqn. C.15.

$$k_f = \frac{\sqrt{\Delta p_{ref}}}{Q_{ref}} \tag{C.15}$$

where Q_{ref} is the flow trough the valve when the valve is fully open and with a pressure drop equal to Δp_{ref}. Q_{ref} is called the valve flow capacity, and Δp_{ref} is in this work set

to 5 bar. The dynamic response of the valves are described by a second order system,

$$\ddot{u}_{HP} = u_{conHP} \cdot \omega^2 - u_{HP} \cdot \omega^2 - 2 \cdot \zeta \cdot \omega \cdot \dot{u}_{HP} \tag{C.16}$$

$$\ddot{u}_{LP} = u_{conLP} \cdot \omega^2 - u_{LP} \cdot \omega^2 - 2 \cdot \zeta \cdot \omega \cdot \dot{u}_{LP} \tag{C.17}$$

where u_{conHP} and u_{conLP} are the desired valve positions for the high pressure valve and low pressure valve respectively, ω is the natural frequency of the valves and ζ is the damping ratio. The desired valve positions, u_{conHP} and u_{conLP}, are either 0 or 1.

The output torque from one cylinder, τ_{cyl}, is calculated as shown in Eqn. C.18.

$$\tau_{cyl} = \frac{V_d}{2} \sin(\theta) \cdot p_{cyl} \tag{C.18}$$

The effective bulk modulus depends on a number of parameters like the fluid, the pressure, the entrained air, the container and the temperature. In this study, Hoffmann's model is used to estimate the effective bulk modulus, β_{eff} as shown in Eqn. C.19 [12].

$$\beta_{eff} = \beta_{max} \cdot \left[1 - exp\left(-0.4 - 2 \cdot 10^{-7} \cdot p_{cyl}\right)\right] \tag{C.19}$$

where β_{max} is the bulk modulus at maximum pressure.

C.2.1 Valve Control Strategy

This section gives a detailed description of the valve timing strategy used to achieve partial stroke displacement. An overview of the timing strategy is shown in Fig. C.5. The valve opening ratios, u_{HP} and u_{LP}, are illustrated together with the cylinder pressure, p_{cyl}, and piston position as a function of the motor shaft position, θ.

θ_{oHP} and θ_{cHP} are the opening and closing angle for the high pressure valve, θ_{oLP} and θ_{cLP} are the opening and closing angle for the low pressure valve, and ϕ is the control angle and describes the motor shaft position where the high pressure valve starts to close, $\theta_{cHP} = \phi$. In addition to describing the closing angle of the high pressure valve, ϕ is an expression of the displacement of the motor.

At $\theta = 0°$, the piston is at TDC, the cylinder pressure, p_{cyl}, is equal to the high pressure level, p_{HP}. The low pressure valve is closed and the high pressure valve starts to open. The high pressure valve stays open until the motor shaft position, θ, is equal to θ_{cHP}. When both the high pressure valve and the low pressure valve are closed, the cylinder pressure is decompressed due to increasing cylinder volume. Ideally, the low pressure valve will start to open at θ_{oLP} when the cylinder pressure is equal to the low pressure level. The low pressure valve is kept open until the motor shaft angle, θ, is equal to θ_{cLP}. The low pressure valve is fully closed right before the piston reaches TDC. The

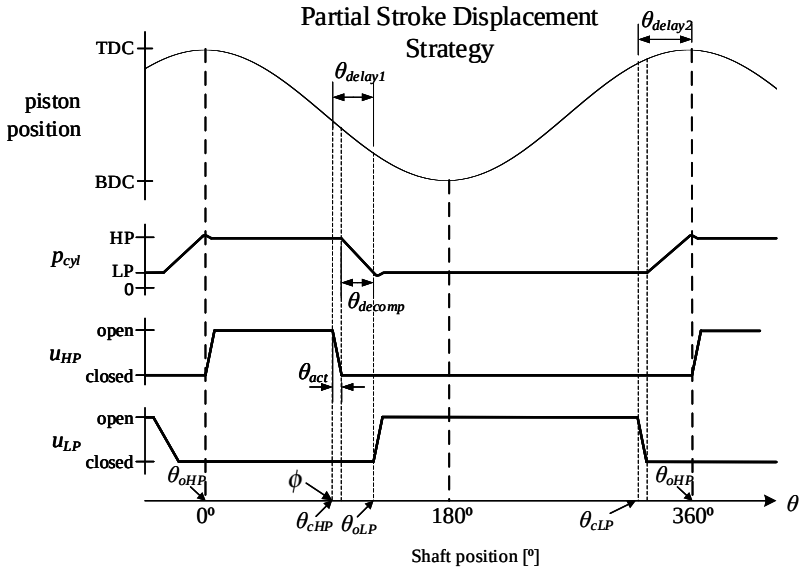

Figure C.5: Simplified illustration of valve timing strategy for partial stroke displacement strategy.

last piston movement is used to pressurize the cylinder oil up to high pressure level. From Fig. C.5, the opening and closing angles can be calculated as shown in Eqn. C.20 - C.23,

$$\theta_{oHP} = 0^{\circ} \tag{C.20}$$

$$\theta_{cHP} = \phi \tag{C.21}$$

$$\theta_{oLP} = \phi + \theta_{delay1} \tag{C.22}$$

$$\theta_{cLP} = 2 \cdot \pi - \theta_{delay2} \tag{C.23}$$

where θ_{delay1} is the angle the motor shaft rotates between closing the high pressure valve and opening the low pressure valve. θ_{delay2} is the angle the motor shaft rotates between closing the low pressure valve and opening the high pressure valve. The optimal delay angles, θ_{delay1} and θ_{delay2}, are hard to calculate precisely and are affected by the oil stiffness, dead volume in the cylinder, the pressure difference between the high pressure level and low pressure level, the motor speed, the valve transition time, the valve flow capacity and the opening profile of the valve [1, 13].

From Fig. C.5, it can be seen that θ_{delay1} can be calculated as shown in Eqn. C.24,

$$\theta_{delay1} = \theta_{act} + \theta_{decomp} \tag{C.24}$$

where θ_{act} is the angle the motor shaft rotates while closing the valves and θ_{decomp} is the angle the motor shaft has to rotate to decompress the cylinder pressure from high pressure level down to low pressure level. Knowing the valve transition time, T_s, and the motor shaft speed, $\dot{\theta}$, θ_{act} is calculated as,

$$\theta_{act} = T_s \cdot \dot{\theta} \tag{C.25}$$

The decompression angle, θ_{decomp} can be calculated based on Fig. C.6 and the continuity equation shown in Eqn. C.26. For simplicity, the bulk modulus of the oil is assumed to be constant and equal to β_{max}.

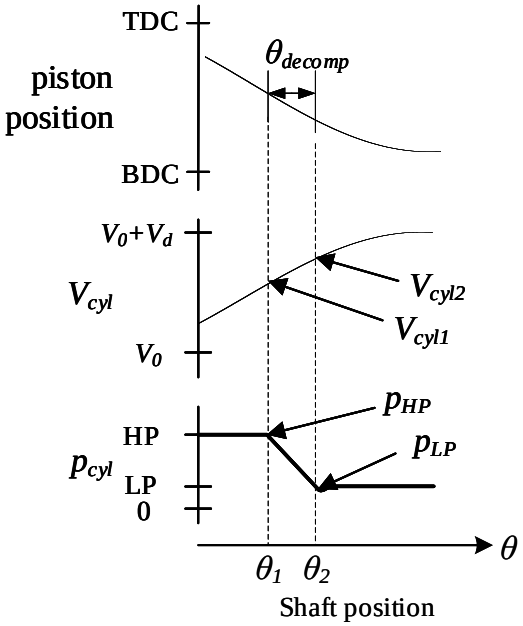

Figure C.6: Simplified illustration of the decompression phase used to calculate θ_{decomp}.

$$\Delta p = -\frac{\beta_{max}}{V_{cyl1}} \cdot \Delta V_{cyl} \tag{C.26}$$

where Δp is the desired change in pressure shown in Eqn. C.27, V_{cyl1} is the cylinder volume at $\theta = \theta_1$ and calculated using Eqn. C.11, and ΔV_{cyl} is the change in cylinder volume and shown in Eqn. C.28. ΔV_{cyl} is positive if the volume is expanding.

$$\Delta p = p_{LP} - p_{HP} \tag{C.27}$$

$$\Delta V_{cyl} = V_{cyl2} - V_{cyl1} \tag{C.28}$$

Substituting Eqn. C.11 into Eqn. C.28, the change in cylinder volume can be expressed as shown in Eqn. C.29.

$$\Delta V_{cyl} = \frac{V_d}{2} \cdot (\cos\theta_1 - \cos\theta_2) \tag{C.29}$$

Inserting Eqn. C.29 into Eqn. C.26 and solving for θ_2 results in Eqn. C.30.

$$\theta_2 = \cos^{-1}\left(\cos\theta_1 + \frac{2}{V_d} \cdot \frac{V_{cyl1}}{\beta_{max}} \cdot \Delta p\right) \tag{C.30}$$

Inserting Eqn. C.11 for V_{cyl1} using that $V_0 = V_d$, Eqn. C.30 can be simplified to

$$\theta_2 = \cos^{-1}\left(\cos\theta_1 + \frac{3 - \cos\theta_1}{\beta_{max}} \cdot \Delta p\right) \tag{C.31}$$

Finally, the decompression angle, θ_{decomp}, is calculated as shown in Eqn. C.32 and the result is plotted in Fig. C.7 for θ_1 ranging from 0° to 159°. The delay angle, θ_{delay2}, can be calculated by following the same procedure as for θ_{delay1}.

$$\theta_{decomp} = \theta_2 - \theta_1 \tag{C.32}$$

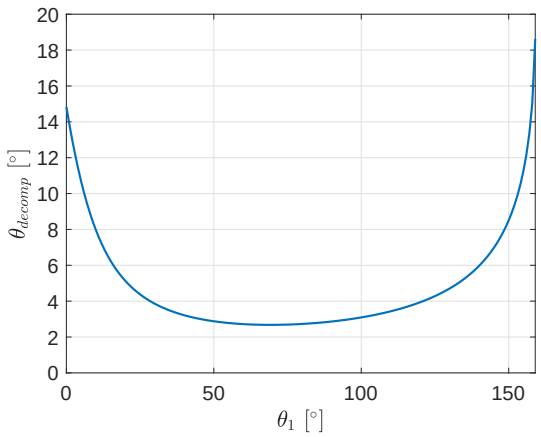

Figure C.7: Plot of the decompression angle, $\theta_{decomp}(\theta_1)$ with $\Delta p = 200\ bar$.

Assuming that no pressure build up occurs before the high pressure valve and low pressure valve are fully closed, the closing and opening angle for the low pressure valve can be calculated as shown in Eqn. C.23 and Eqn. C.22. In reality, when closing the high pressure valve, the cylinder pressure will start to decompress when the high pressure valve approaches closed position due to flow throttling. By using Eqn. C.22, the cylinder pressure will be below the low pressure level when opening the low pressure valve at θ_{oLP}. The same phenomena occurs when closing the low pressure valve. The pressure inside the cylinder starts to build up before the low pressure valve is fully closed and the cylinder pressure is therefore higher than the high pressure level when opening the high pressure valve at θ_{oHP}. The pressure overshoots can be seen in Fig. C.8.

Figure C.8 shows simulation results from the valve timing strategy presented in this section with $\phi = 140°$ and the parameters shown in Tab. C.2. The blue line is the cylinder pressure, the red line is the high pressure valve opening ratio, the yellow line is the low pressure valve opening ratio, the purple line is the volume flow through the high pressure valve, and the green line is the volume flow through the low pressure valve. The cylinder pressure is overshooting after decompressing the cylinder oil resulting in a small flow peak through the low pressure valve.

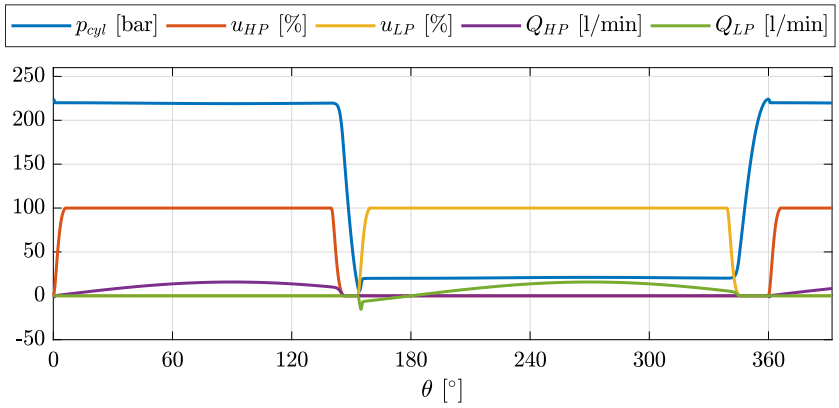

Figure C.8: Simulation results of described valve timing strategy.

C.3 RESULTS

The fixed simulation parameters are listed in Tab. C.2.

Table C.2: Fixed simulation parameters.

Parameter	Value	Description
V_d	50 cc/rev	Cylinder displacement
V_0	50 cc/rev	Dead volume in cylinder
p_{HP}	220 bar	Constant high pressure source
p_{LP}	20 bar	Constant low pressure source
$\overline{T}_s$	1.67%	Normalized valve transition time
$\overline{\Delta}p$	0.5%	Normalized pressure drop
β_{max}	1.2 MPa	Bulk modulus at maximum pressure
ζ	0.8	Damping ratio

Describing the valve characteristics by $\overline{T}_s$ and $\overline{\Delta}p$ as shown in Eqn. C.1 and Eqn. C.2 respectively, the simulated motor efficiency and valve losses will yield for all speeds. The real valve parameters, T_s and Q_{ref}, can be calculated as shown in Eqn. C.3 and Eqn. C.4.

The sensitivity of the digital displacement motor to the valve accuracy and repeatability is evaluated by performing a large number of simulations with different values of the control angle, ϕ, and the timing delay angle, θ_{delay1}. The efficiency is evaluated for every simulation and saved together with the valve throttling losses. The control angle, ϕ, is ranging from 40° to 154°, where 154° corresponds to full displacement. The timing delay angle, θ_{delay1}, is ranging from 0° to $\theta_{delay,max}$, where $\theta_{delay,max}$ is calculated as shown in Eqn. C.33. Note that the delay angle, θ_{delay2} is kept constant.

$$\theta_{delay,max} = \theta_{act} + \theta_{decomp} \tag{C.33}$$

Figure C.9 shows the efficiency map and the valve throttling losses. The first plot

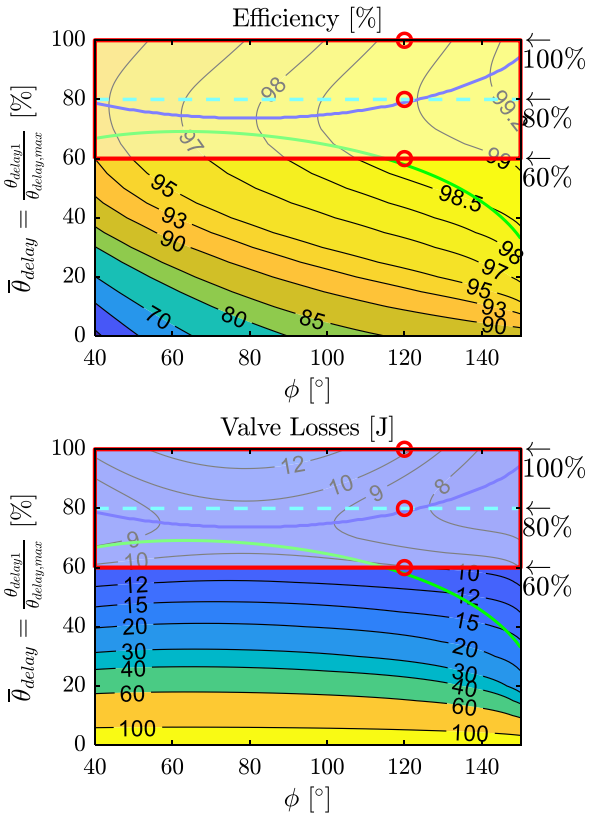

Figure C.9: Efficiency and valve losses as a function of displacement and the delay angle with valve characteristics described by; $\overline{T}_s = 1.67\%$ and $\overline{\Delta p} = 0.5\%$.

shows the efficiency and the second plot shows the valve losses. It can be seen that the efficiency is high and the valve throttling losses are low for high values of $\overline{\theta}_{delay}$. At low values of $\overline{\theta}_{delay}$, the efficiency drops and the valve throttling losses increases significantly. The blue line marks the highest efficiency and lowest valve losses as a function of the control angle, ϕ, and describes the optimal delay angle. It can be seen that the optimal delay angle, θ_{delay1}, varies with the control angle, ϕ. In this simulation, the best delay angle, θ_{delay1}, is between 75% and 95% of $\theta_{delay,max}$. Note that a change in dead volume, valve flow capacity, valve transition time, valve lift profile or oil stiffness will change the optimal delay angle.

In the area below the green line, the low pressure valve starts to open before the high pressure valve is fully closed, resulting in increased flow throttling losses due to flow running directly from the high pressure source into the low pressure source. By further reducing the normalized delay angle, $\overline{\theta}_{delay}$, below the green line, the time where both valves are open simultaneously will increase and result in a significant increase of flow throttling losses.

Figure C.10 shows simulated results of switching the valves with three different delay

angles and $\phi = 100°$. These three situations are also marked in Fig. C.9 with red rings.

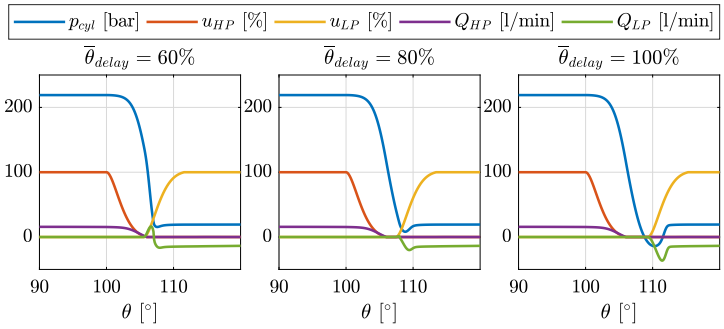

Figure C.10: Simulation results valve timing with $\phi = 100°$ and three different values of the delay angle: $\overline{\theta}_{delay} = 80\%$, $\overline{\theta}_{delay} = 70.75\%$ and $\overline{\theta}_{delay} = 20\%$.

In the first plot, the delay angle is 60% of $\theta_{delay,max}$. In this situation, the low pressure valve starts to open right after the high pressure valve has reached closed position. Hence the decompression phase is not fully completed before opening the low pressure valve, resulting in poor utilization of the potential energy in the pressurized oil and a flow peak in the low pressure valve. In the second plot, the timing delay angle is 80% of $\theta_{delay,max}$ and is close to optimal delay angle, blue line. It can be seen from the figure that the low pressure valve starts to open when the cylinder pressure is equal to the low pressure level, resulting in good recovery of the potential energy in the pressurized oil and only low flow and pressure peaks. In the last plot, the timing delay angle is 100% of $\theta_{delay,max}$ and above the optimal delay angle. This results in an overshoot in the cylinder pressure when decompressing the cylinder oil and a flow peak in the low pressure valve. The cylinder cavitates, but this can be avoided by including an anti-cavitation valve in the cylinder.

Even though the optimal low pressure valve opening angle is known, blue line in Fig. C.9, it is not possible to actuate the valve at the exact optimal position every time. Some times it may open a little too earl or too late. Simplifying the optimal normalized delay angle to be $\overline{\theta}_{delay} = 80\%$, marked with the cyan dotted line, the flow throttling losses will stay low, and the motor efficiency will stay high. Even though there is a delay in the timing of $\pm 20\%$, marked with the white transparent area inside a red box in Fig. C.9, the valve throttling losses will remain low and the motor efficiency will remain high. Switching the low pressure valve within $\pm 20\%$ of the simplified optimal normalized delay angle is more demanding in high speed motors than low speed motors. By knowing the motor speed, $\dot{\theta}$, the delay in time can be calculated as shown in Eqn. C.34 for various speeds.

$$T_{delay} = \frac{\pm 20\% \cdot \theta_{delay,max}}{\dot{\theta}} \tag{C.34}$$

In Fig. C.11, Eqn. C.34 is used to calculate the allowable delay in time at different displacements and speeds. Note that the y-axis is scaled logarithmically. It can be seen

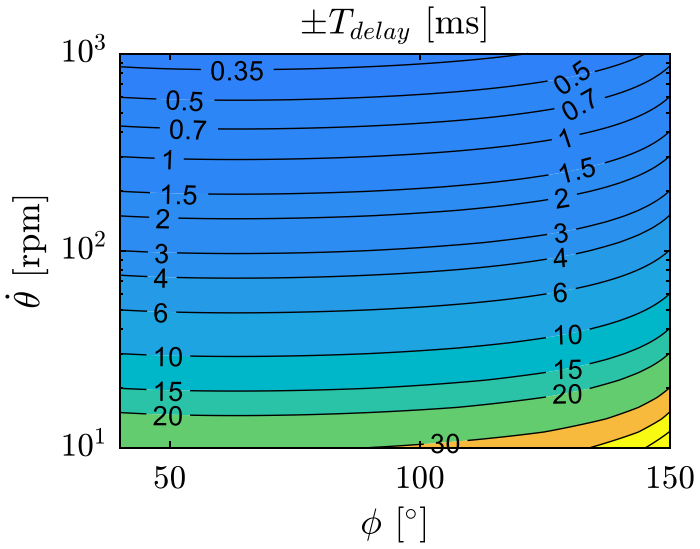

Figure C.11: Acceptable deviation from optimal valve timing.

that the required accuracy and repeatability is more strict in high speed motors than in low speed motors. The requirements are also more strict when switching mid stroke compared to close to BDC. When operating at 1000 rpm, the low pressure valve should be opened within approximately ±0.3 ms from optimal opening time. When operating at 10 rpm, the requirements is not that strict, and the low pressure valve should open within approximately ±30 ms from the optimal opening time.

C.3.1 Example Of Using Results

This section presents an example of how one can use the results presented in this paper to decide the parameters of the fast switching on/off valves used in a digital displacement motor. First, some motor parameters have to be decided. In this example, the cylinder displacement is chosen to be, $V_d = 50$ cc/rev, the dead volume is $V_0 = V_d$, maximum motor speed is 100 rpm and the target efficiency at 25% displacement is 96% when operating with partial stroke displacement strategy. Using Fig. C.3, it can be seen that by using $\overline{T}_s = 1.67\%$ and $\overline{\Delta}p = 0.5\%$ the target efficiency is approximately 96% at 25% displacement. By using Eqn. C.3 and Eqn. C.4, the valve transition time, T_s, and valve flow capacity, Q_{ref}, can be calculated to be 10 ms and 35 l/min respectively. Since $\overline{T}_s = 1.67\%$ and $\overline{\Delta}p = 0.5\%$ is the same values that are used in Fig. C.9, the plotted results can be used directly. The simplified normalized delay angle is chosen to be $\overline{\theta}_{delay} = 80\%$. Accepting that the low pressure valve can open within ±20% from the simplified normalized delay angle, Fig. C.11 can also be used directly. When running at 100 rpm, the low pressure valve should open within approximately ±3 ms from the optimal opening time.

In [14], a table presenting the ready to marked valves for digital hydraulic applications

is shown. One of the presented valves is the Bosch Rexroth WES type valve. This valve has the following characteristics; $T_s = 5$ ms and $Q_{ref} = 45$ l/min. Those characteristics are better than the requirements estimated earlier in this section ($T_s = 10$ ms and $Q_{ref} = 35$ l/min) menaing that the WES type valve can be used to achieve high efficiency for a digital displacement machine running at 100 rpm and with a cylinder displacement of 50 cc/rev. The WES type valve is a spool type valve and can open against high pressure differences, which makes it possible to start in motor mode without any additional systems. The valve must therefore be actively controlled. At 100 rpm, the valve should be opened within ±3 ms from optimal opening time to avoid unnecessary high valve throttling losses. One disadvantage is that a spool type valve may suffer from leakage when it is fully closed.

C.4 CONCLUSION

Efficiency in digital displacement motors is affected by displacement strategy, valve characteristics, and valve timing strategy. This paper presents a short summary of how the motor efficiency is affected by displacement strategy and valve characteristics based on previous work. Then a method of describing the required valve repeatability and accuracy is presented.

Generally, partial stroke displacement strategy has more strict valve requirements than full stroke displacement strategy, and high speed motors have also stricter valve requirements than low speed motors. When starting, stopping and controlling digital motors at low speeds, it is desirable to have valves that can open against high pressure difference. Those types of valves have to be actively opened, without any help from the cylinder chamber pressure. Optimal valve timing is, therefore, more difficult to achieve. The work presented in this paper shows that it is important with valves that have high repeatability and accuracy. Opening the low pressure valve too early or too late will result in pressure and flow peaks in the system in addition to increased flow throttling losses and reduced efficiency. The low pressure valve should start to open in less than ±0.3 ms from the optimal opening time when operating at high speeds above 1000 rpm. This results in high requirements for the controller and valve repeatability and accuracy. When operating at speeds below 10 rpm, the low pressure valve should open in less than ±30 ms from the optimal time, and the requirements of repeatability and accuracy are significantly reduced.

It has also been shown that the commercially available WES type valve from Bosch Rexroth can be used in small low speed motors running with PSDS.

Acknowledgment

The research presented in this paper has received funding from the Norwegian Research Council, SFI Offshore Mechatronics, project number 237896.

Bibliography

[1] Hao Tian. *STUDY OF ACTIVE VALVE TIMING ON EFFICIENT HYDRAULIC PISTON MOTOR OPERATIONS*. PhD Thesis, University of Minnesota, Minnesota, USA, August 2016.

[2] Christian Nørgård. *Design, Optimization and Testing of Valves for Digital Displacement Machines*. PhD Thesis, Aalborg University, Denmark, October 2017.

[3] Kyle Joseph Merrill. *MODELING AND ANALYSIS OF ACTIVE VALVE CONTROL OF A DIGITAL PUMP-MOTOR*. PhD Thesis, Purdue University, Indiana, USA, August 2012.

[4] Kyle J Merrill, Farid Y Breidi, and John Lumkes. Simulation based design and optimization of digital pump/motors. In *ASME/BATH 2013 Symposium on Fluid Power and Motion Control*, pages V001T01A045–V001T01A045. American Society of Mechanical Engineers, 2013.

[5] Kyle J. Merrill, Michael A. Holland, and John H. Lumkes. Analysis of digital pump/-motor operating strategies. *Proceedings of the 52nd national conference on fluid power*, March 2011.

[6] Farid Breidi, Tyler Helmus, and John Lumkes. High efficiency digital pump/motor. In *2015 Fluid Power Innovation & Research Conference (FPIRC15)*.

[7] Daniel Rømer, Per Johansen, Henrik C Pedersen, and Torben Ole Andersen. Analysis of valve requirements for high-efficiency digital displacement fluid power motors. In *8th International Conference on Fluid Power Transmission and Control, ICFP 2013*, pages 122–126. World Publishing Cooperation, 2013.

[8] Md Ehsan, WHS Rampen, and SH Salter. Modeling of digital-displacement pump-motors and their application as hydraulic drives for nonuniform loads. *Journal of dynamic systems, measurement, and control*, 122(1):210–215, 2000.

[9] GS Payne, AE Kiprakis, M Ehsan, W H S Rampen, JP Chick, and AR Wallace. Efficiency and dynamic performance of digital displacement$^{\text{TM}}$ hydraulic transmission in

tidal current energy converters. *Proceedings of the Institution of Mechanical Engineers, Part A: Journal of Power and Energy*, 221(2):207–218, 2007.

[10] Luke Wadsley. Optimal system solutions enabled by digital pumps. In *The 52nd National Conference on Fluid Power, NCFP*, 2011.

[11] Peter Chapple, Per N Lindholdt, and Henrik B Larsen. An approach to digital distributor valves in low speed pumps and motors. In *ASME/BATH 2014 Symposium on Fluid Power and Motion Control*, pages V001T01A041–V001T01A041. American Society of Mechanical Engineers, 2014.

[12] Mohieddine Jelali and Andreas Kroll. *Hydraulic servo-systems: modelling, identification and control*. Springer Science & Business Media, 2004.

[13] Miikka Jaurola and Kalevi Huhtala. A parameter study of a digital pump. *Fluid Power and Motion Control, FPMC*, pages 203–215, 2010.

[14] Bernd Winkler. Recent advances in digital hydraulic components and applications. *The Ninth Workshop on Digital Fluid Power*, 2017.

Appendix A: NOMENCLATURE

Table C.3: Nomenclature

Symbol	Description
E_{in}	Input energy
E_{out}	Output energy
k_f	Flow-pressure coefficient
P_{in}	Input power
P_{out}	Output power
p_{HP}	Pressure level in high pressure source
p_{LP}	Pressure level in low pressure source
p_{cyl}	Cylinder pressure
Q_{HP}	Flow through the high pressure valve
Q_{LP}	Flow through the low the pressure valve
Q_{ref}	Valve flow capacity
$Q_{valve,max}$	Max flow through valve
T_s	Valve transition time
T_{rev}	Time for one shaft revolution
V_0	Dead volume in the cylinder
V_{cyl}	Cylinder volume
V_{cyl1}	Cylinder volume at θ_1
V_{cyl2}	Cylinder volume at θ_2
V_d	Cylinder displacement
u_{HP}	Opening ratio high pressure valve
u_{LP}	Opening ratio low pressure valve
u_{conHP}	Desired valve position high pressure valve
u_{conLP}	Desired valve position low pressure valve
ω	Natural frequency
ζ	Damping ratio
τ_{cyl}	Cylinder torque
β_{eff}	Effective bulk modulus
β_{max}	Bulk modulus at maximum pressure
η	Total efficiency
ϕ	Control angle ($\theta_{cHP} = \phi$)
θ	Motor shaft position
θ_{oHP}	Opening angle high pressure valve
θ_{oLP}	Opening angle low pressure valve
θ_{cHP}	Closing angle high pressure valve ($\theta_{cHP} = \phi$)
θ_{cLP}	Closing angle low pressure valve
θ_{delay1}	Rotation angle between θ_{cHP} and θ_{oLP}
θ_{delay2}	Rotation angle between θ_{cLP} and θ_{oHP}
$\theta_{delay,max}$	Maximum value of θ_{delay1}
θ_{act}	Rotation angle while switching the valve
θ_{decomp}	Decompression angle
θ_1	Shaft position, start decompression phase
θ_2	Shaft position, end decompression phase
Δp_{ref}	Reference pressure drop across valve
Δp	Desired change in cylinder pressure

Symbol	**Description**
ΔV_{cyl}	Desired change in cylinder volume
$\Delta p_{machine}$	Pressure drop across the machine
$\Delta p_{valve,max}$	Pressure drop across valve at max flow
$\overline{T}_s$	Normalized valve transition time
$\overline{\Delta p}$	Normalized allowable valve pressure drop

Paper D

Dynamic Response of a Digital Displacement Motor Operating with Various Displacement Strategies

Sondre Nordås, Michael Møller Beck, Morten Kjeld Ebbesen and Torben Ole Andersen

This paper has been published as:

S. Nordås, M. M. Beck, M. K. Ebbesen, and T. O. Andersen. Dynamic Response of a Digital Displacement Motor Operating with Various Displacement Strategies. *Energies*, 2019, 12.9.

Dynamic Response of a Digital Displacement Motor Operating with Various Displacement Strategies

Sondre Nordås*, Michael Møller Beck**, Morten Kjeld Ebbesen* and Torben Ole Andersen**

*University of Agder
Faculty of Engineering and Science
Jon Lilletunsvei 9, 4879 Grimstad, Norway

** Aalborg University
Faculty of Engineering and Science
Pontoppidanstræde 101, 9220 Aalborg East, Denmark

Abstract **– Digital displacement technology has the potential of revolutionizing the performance of hydraulic piston pumps and motors. Instead of connecting each cylinder chamber to high and low pressure in conjunction with the shaft position, two electrically-controlled on/off valves are connected to each chamber. This allows for individual cylinder chamber control. Variable displacement can be achieved by using different displacement strategies, like for example the full stroke, partial stroke, or sequential partial stroke displacement strategy. Each displacement strategy has its transient and steady-state characteristics. This paper provides a detailed simulation analysis of the transient and steady-state response of a digital displacement motor running with various displacement strategies. The non-linear digital displacement motor model is verified by experimental work on a radial piston motor.**

D.1 Introduction

Digital displacement machines are experiencing increased interest due to their high energy efficiency. Traditional variable displacement piston machines suffer from low energy efficiency when operating at partial displacements. They change displacement by changing the piston stroke. During one shaft revolution, every single cylinder chamber is pressurized, resulting in almost constant friction, leakage, and compressibility losses independent of displacement. In digital displacement machines, each cylinder chamber is connected to two electrically-operated on/off valves. By controlling the on/off valves, each cylinder chamber can be controlled individually. The chambers are only pressurized when neces-

sary, resulting in losses that scale with the displacement, providing high energy efficiency even at partial displacements. A more detailed description of the digital displacement motor and pump technology can be found in [1, 2, 3, 4].

Control of digital displacement machines is complicated and non-conventional. Due to the individual cylinder chamber control, it is hard to develop models that can be used for model-based design of feedback controllers. Both continuous, discrete, and hybrid dynamical system approximations have been investigated. The continuous and discrete approximations are sufficient to describe the fundamental dynamics if the number of cylinders and displacement fraction is sufficiently high [5, 6, 7, 8, 9, 10, 11]. In the case of applying linear control theory on a variable speed unit, the shaft speed of the machine should not be lower than the speed used during linearization of the system. The hybrid dynamic approximation has high accuracy, but is quite complex and, therefore not suitable for use in stability analyses and control design [12, 13, 14]. This is due to a large number of states and multiple jump maps and sets.

Since it is hard to develop models that can be used for control design purposes, it is highly relevant to know the dynamic behavior of digital displacement machines. Different displacement strategies give different transient and steady-state behavior in addition to different energy efficiency characteristics. The chosen displacement strategy should be decided based on operation requirements related to the driven application. Furthermore, one application may use different displacement strategies in different parts of the operation. The energy efficiency of different displacement strategies has been investigated in several papers [15, 16, 17], but the transient and steady-state characteristics have only been investigated in a limited number of papers. In Reference [18], the authors showed that the full stroke displacement strategy can achieve smooth system output if a proper cylinder chamber actuation sequence is used. A proper cylinder chamber actuation sequence is for example when every second chamber is actuated. The number of smooth output rates increases rapidly when the total number of pistons increases. In Reference [19], the authors compared the output ripples from full stroke to the output ripples from the partial stroke displacement strategy. The result showed that the full stroke displacement strategy has the lowest output ripples when the displacement is greater than 50%. When operating down at 20% displacement, the partial stroke displacement strategy had the lowest output ripples. At this time, the work done in [20] may be the most comprehensive description of the transient and steady-state characteristics of digital displacement machines. The work included both the full stroke, partial stroke, and sequential partial stroke displacement strategy. The results showed that the full stroke displacement strategy is most suited for high speed machines where energy efficiency is important. The partial stroke displacement strategy is most suited for low speed machines where both tracking performance

and energy efficiency are important. The sequential partial stroke displacement strategy is most suited for very low-speed machines where control tracking performance is important and energy efficiency is of less importance. Still, a more detailed analysis of the dynamic behavior of digital displacement machines is missing.

This paper aims to compensate for the lack of knowledge regarding transient and steady-state characteristics for a digital displacement motor (DDM) operating with different displacement strategies. In all, three displacement strategies are analyzed: the full stroke displacement strategy (FSDS), the partial stroke displacement strategy (PSDS), and the sequential partial stroke displacement strategy (SPSDS). The analysis is conducted on a non-linear simulation model that is experimentally validated. The result shows that the transient response is highly affected by the shaft speed for some displacement strategies, but not for all. The steady-state response tends to oscillate due to switching between active and inactive cylinder chambers. The oscillations are affected by the chosen displacement strategy, the current displacement fraction, the number of pistons, and the shaft speed. The results of this analysis can be used to choose the most suitable displacement strategy when designing new controllers for DDMs.

The work presented in this paper is structured as follows: In Section D.2, the non-linear DDM model is described. In Section D.3, the analyzed displacement strategies are presented. The non-linear simulation model is validated in Section D.4. In Section D.5, the validated simulation model is used to analyze the transient and steady-state characteristics of the described displacement strategies. The results are then discussed in Section D.6, and a conclusion is given in Section D.7.

D.2 Simulation Model

This section describes the simulation model of the DDM. The simulated motor is a radial piston type with 15 pistons uniformly distributed around the shaft. The model was inspired by the model presented in [21]. A schematic representation of the DDM is shown to the right in Figure D.1.

For simplicity, the governing equations are only derived for a single cylinder chamber, but the same method is used for all chambers. The governing equations are derived based on the single cylinder chamber shown to the left in Figure D.1. It is assumed that each cylinder chamber is connected to a constant high and low pressure source and that friction and leakage are negligible. The main purpose of this study is to investigate the transient and steady-state response of the DDM. Neglecting the friction and leakage will not significantly influence the transient and steady-state response. Neglecting friction may result in a slightly higher magnitude of the output torque, but the main characteristics

can still be analyzed.

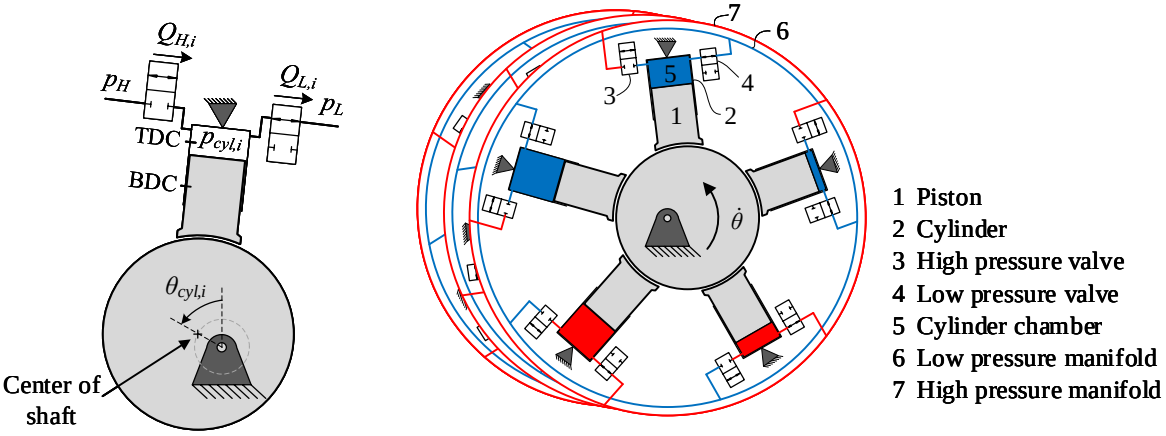

Figure D.1: Sketch of a single cylinder chamber (**left**) and a 15-piston DDM (**right**).

The pressure dynamics in cylinder chamber i is calculated by using the continuity equation,

$$\dot{p}_{cyl,i} = \frac{\beta_{eff,i}}{V_{cyl,i}} \cdot \left(Q_{H,i} - Q_{L,i} - \dot{V}_{cyl,i} \right) \tag{D.1}$$

where $\beta_{eff,i}$ is the effective bulk modulus of the hydraulic fluid, $V_{cyl,i}$ is the cylinder chamber volume, $Q_{H,i}$ is the flow through the high pressure valve, and $Q_{L,i}$ is the flow through the low pressure valve. The cylinder chamber volume, $V_{cyl,i}$, and its time derivative are given by:

$$V_{cyl,i} = V_0 + \frac{V_d}{2} \cdot (1 - \cos\theta_{cyl,i}) \tag{D.2}$$

$$\dot{V}_{cyl,i} = \frac{V_d}{2} \cdot \sin(\theta_{cyl,i}) \cdot \dot{\theta} \tag{D.3}$$

where V_0 is the dead volume in the cylinder chamber, V_d is the piston displacement, $\theta_{cyl,i}$ is the local shaft position relative to the piston position, and $\dot{\theta}$ is the shaft speed. The local shaft position is 0 rad when the piston is at top dead center (TDC). Due to the phase shift between the cylinders, the local shaft position, θ_i, is given by:

$$\theta_i = \theta + \frac{2 \cdot \pi}{N_c} \cdot (i - 1) \qquad\qquad i \in \{1, ..., N_c\} \tag{D.4}$$

where θ is the shaft position and N_c is the number of cylinders. The volume flow through the valves, $Q_{H,i}$ and $Q_{L,i}$, is described by the orifice equation given by:

$$Q_{H,i} = \frac{u_{H,i}}{k_f} \cdot \sqrt{|p_H - p_{cyl,i}|} \cdot \text{sign}(p_H - p_{cyl,i}) \tag{D.5}$$

$$Q_{L,i} = \frac{u_{L,i}}{k_f} \cdot \sqrt{|p_{cyl,i} - p_L|} \cdot \text{sign}(p_{cyl,i} - p_L) \tag{D.6}$$

where $u_{H,i}$ and $u_{L,i}$ are the opening ratios of the high pressure valve and low pressure valve ranging from 0–1, where zero is fully closed and one is fully open. Both valves have the same flow-pressure coefficient, k_f, and the same transient response. The transient response of the fast switching valves is described by a second-order system,

$$\ddot{u}_{H,i} = u_{conH,i} \cdot \omega^2 - u_{H,i} \cdot \omega^2 - 2 \cdot \zeta \cdot \omega \cdot \dot{u}_{H,i} \tag{D.7}$$

$$\ddot{u}_{L,i} = u_{conL,i} \cdot \omega^2 - u_{L,i} \cdot \omega^2 - 2 \cdot \zeta \cdot \omega \cdot \dot{u}_{L,i} \tag{D.8}$$

where $u_{conH,i}$ and $u_{conL,i}$ are the desired valve positions for the high pressure and low pressure valves, ω is the natural frequency of the valves, and ζ is the damping ratio. The desired valve positions, $u_{conH,i}$ and $u_{conL,i}$, are either zero or one and are given by the chosen valve actuation sequence. The valve actuation sequence is described in detail for each displacement strategy in Section D.3.

The effective bulk modulus is calculated according to [22] as shown below:

$$\beta_{eff,i} = \frac{1}{\frac{1}{\beta_L} + \frac{\epsilon_g}{p_{cyl,i}^{(abs)}}} \tag{D.9}$$

where β_L is the bulk modulus of the liquid and ϵ_g is the volume fraction of undissolved gas. The volume fraction of undissolved gas is calculated by:

$$\epsilon_g = \frac{1.0}{\left(\frac{1.0-\epsilon_{g0}}{\epsilon_{g0}}\right) \cdot \left(\frac{p_{atm}^{(abs)}}{p_{cyl,i}^{(abs)}}\right)^{-\frac{1}{\kappa}} + 1.0} \tag{D.10}$$

where ϵ_{g0} is the volume fraction of undissolved gas at atmospheric pressure, $p_{atm}^{(abs)}$ is the atmospheric pressure, and κ is the specific heat ratio.

The cylinder torque is given by:

$$T_{cyl,i} = \frac{V_d}{2} \cdot \sin(\theta_i) \cdot p_{cyl,i} \tag{D.11}$$

and the DDM output torque is the sum of the torque contribution from all pistons:

$$T_m = \sum_{i=1}^{N_{pis}} T_{cyl,i} \tag{D.12}$$

Unless stated otherwise, the simulation parameters shown in Table D.1 apply.

Table D.1: Simulation parameters.

Parameter	Symbol	Value	Unit
Piston chamber displacement	V_d	50	cc/rev
Cylinder chamber dead volume	V_0	50	cc
Number of pistons	N_{pis}	15	–
Motor speed	$\dot{\theta}$	100	rpm
Switching time on/off valves	T_s	5	ms
Flow-pressure coefficient	k_f	$1.2 \cdot 10^6$	$\sqrt{\text{Pa}} \cdot \text{s} \ /\text{m}^3$
High pressure	p_H	220	bar
Low pressure	p_L	20	bar
Bulk modulus liquid	β_L	1.2	GPa
Volume fraction of undissolved gas at $p_{atm}^{(abs)}$	ϵ_{g0}	0.01	–

D.3 Displacement Strategies

The motor displacement can be changed by using different displacement strategies. This section describes the valve activation sequence for the displacement strategies analyzed in this paper. Note that only motor operation is described, but the same strategy can also be used for pumping operation.

D.3.1 Full Stroke Displacement Strategy

Full stroke is considered to be the simplest displacement strategy. The cylinder chambers are activated and deactivated for entire piston strokes. The fast switching on/off valves are only switched when the pistons are close to top dead center (TDC) or bottom dead center (BDC). In those piston positions, the valve flow is low, minimizing the valve throttling losses when switching the valves. Furthermore, the valves are timed only to be actuated when the pressure drop across them is small. The displacement of the motor is changed by changing the number of active cylinder chambers.

Figure D.2 illustrates the valve timing strategy for a single cylinder chamber. Through the first shaft revolution, the chamber is deactivated, and through the second revolution, the chamber is activated. Plot 1 shows the piston position, Plot 2 the opening ratios of the valves, Plot 3 the chamber pressure, and Plot 4 the cylinder torque. For an inactive cylinder chamber, the high pressure valve is kept closed and the low pressure valve is kept open, resulting in only a very small torque contribution in the downstroke piston motion due to low chamber pressure. For an active cylinder chamber, the valves are switched close to TDC and BDC with the high pressure valve open during the downstroke piston

motion and the low pressure valve open during the upstroke piston motion. The torque contribution is high due to the high chamber pressure in the downstroke motion. It can be seen that for the active cycle, the high pressure valve and low pressure valve are in the closed position at the same time. This is to compress and decompress the chamber oil in order only to switch the valves when the pressure drop across them is small, resulting in a minimum of flow peaks, pressure peaks, and valve throttling losses.

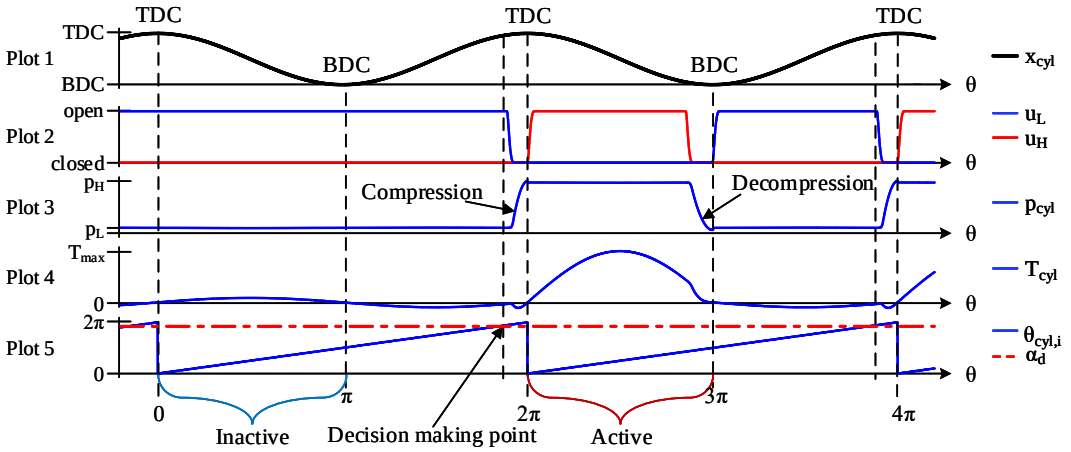

Figure D.2: Valve timing schematics for the full stroke displacement strategy.

For each cylinder, the decision of activating or deactivating the cylinder chamber is taken at a fixed angle once every shaft revolution. This position is illustrated in Figure D.2 with the decision angle α_d. The desired displacement fraction, D, is a continuous signal ranging from 0–1, which corresponds to zero and full displacement, respectively. The displacement fraction is converted into a cylinder actuation sequence by a first-order delta-sigma modulator, which determines whether the current cylinder shall be active or inactive. This method was first proposed by Johansen et al. [23] and later used in several control papers [5, 8, 9, 7]. A block diagram of the controller is shown in Figure D.3.

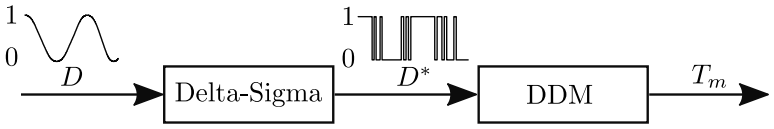

Figure D.3: Schematic of the open loop control system for FSDS.

Since the decision of activating or deactivating is made at a fixed shaft position ahead of TDC, the sampling time, T_{sample}, for the delta-sigma modulator is dependent on the number of cylinders and the rotational speed.

$$T_{sample} = \frac{2 \cdot \pi}{\dot{\theta} \cdot N_c} \tag{D.13}$$

where $\dot{\theta}$ is the shaft speed and N_c is the number of cylinders. If the shaft speed is varying, the sampling time is also varying.

D.3.2 Partial Stroke Displacement Strategy

In PSDS, all cylinder chambers are activated during every shaft revolution, but only in a portion of the downstroke piston motion. The displacement of the motor is changed by increasing or decreasing the active part. In this study, two versions of PSDS were investigated. In Version 1, the cylinder chamber can only have one active period during the downstroke piston motion. In Version 2, the cylinder chamber can be reactivated and have more than one active period.

D.3.2.1 Version 1 of the Partial Stroke Displacement Strategy

Figure D.4 shows the valve timing strategy for a single cylinder chamber operating with PSDS Version 1. The red dotted line in the bottom plot shows the state change angle α. The state change angle, α, describes at which local shaft position angle, $\theta_{cyl,i}$, the cylinder shall change state from active to inactive. If $\theta_{cyl,i} \leq \alpha$, the cylinder is active, else the cylinder is inactive.

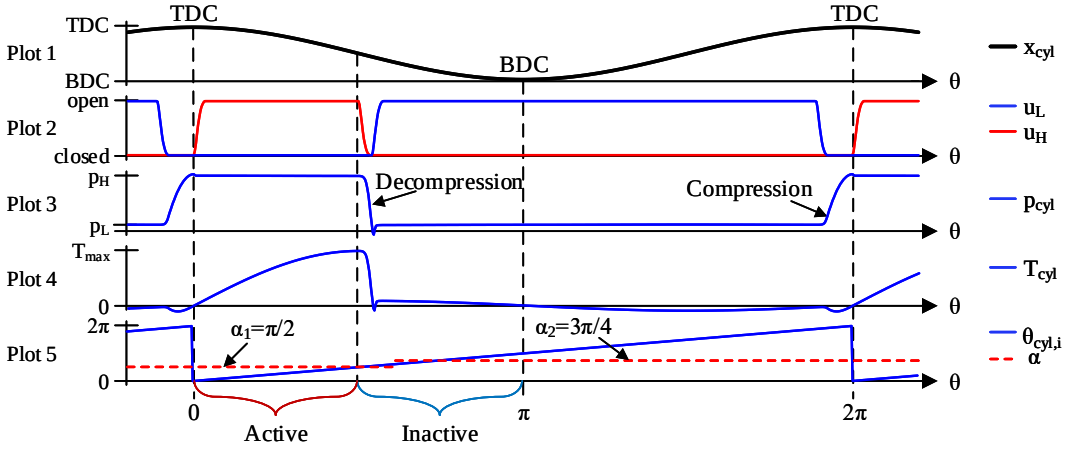

Figure D.4: Valve timing schematics for partial stroke displacement strategy Version 1.

For the illustrated situation shown in Figure D.4, the cylinder is active in the first half of the downstroke piston motion and deactivated in the remaining part, $\alpha_1 = \pi/2$. This situation corresponds to 50% displacement. Increasing the state change angle after the cylinder has been deactivated will not result in a reactivation of the cylinder due to the nature of the PSDS Version 1. Once the cylinder is deactivated, it cannot be re-actuated before the next shaft revolution.

As for the FSDS, PSDS Version 1 also has a decompression phase and a compression phase in order only to switch the valves when the pressure difference across them is small, resulting in a minimum of pressure and flow peaks. Switching the valves mid-stroke will result in higher flow throttling losses during switching compared to switching the valves closer to TDC or BDC due to higher piston velocity and, therefore, higher valve flow.

Hence, on/off valves used in PSDS should be faster compared to on/off valves used in FSDS to achieve the same energy efficiency at partial displacement [24].

The state change angle, α, is calculated based on the desired displacement ratio, D. The desired displacement ratio is defined as the ratio between the intake volume during the active motoring period and the maximum intake volume [20]. Based on the calculation of the cylinder volume shown in Equation D.2, the displacement ratio is calculated as shown below.

$$D = \frac{V_{cyl}(\alpha)}{V_{cyl}(\pi)} = \frac{\frac{V_d}{2} \cdot (1 - \cos\alpha)}{\frac{V_d}{2} \cdot (1 - \cos\pi)} = \frac{(1 - \cos\alpha)}{2} \tag{D.14}$$

where $V_{cyl}(\alpha)$ is the intake volume during the active motoring period and $V_{cyl}(\pi)$ is the maximum intake volume. The state changing angle, α, is then calculated by rearranging Equation (2.15) as:

$$\alpha = \cos^{-1}(1 - 2 \cdot D) \tag{D.15}$$

The state change angle, α, is updated continuously until the state change is carried out. Figure D.5 shows the block diagram of the open loop system. Note that due to the decompression phase shown in Figure D.4, the displacement fraction needs to be less than 0.95 to use the last piston movement to decompress the cylinder.

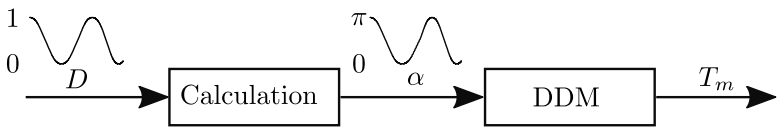

Figure D.5: Schematic of open loop control for PSDS (equal for Version 1 and Version 2).

D.3.2.2 Version 2 of the Partial Stroke Displacement Strategy

In PSDS Version 2, the cylinder is capable of being reactivated. Instead of only having one active period during the downstroke piston motion, the cylinder can be reactivated if the desired displacement ratio is changed; see Figure D.6. First, the desired displacement ratio was set to $D = 0.5$, giving a state change angle of $\alpha_1 = \pi/2$ rad. When $\theta_{cyl,i} = \alpha_1$, the cylinder chamber changed state from active to inactive. After a small period, the desired displacement ratio was stepped up to $D = 0.85$ which gave a state change angle of $\alpha_2 = 3\pi/4$ rad. Since $\theta_{cyl,i} < \alpha$, the cylinder was reactivated in the remaining rotation up to $\theta_{cyl,i} = \alpha_2$.

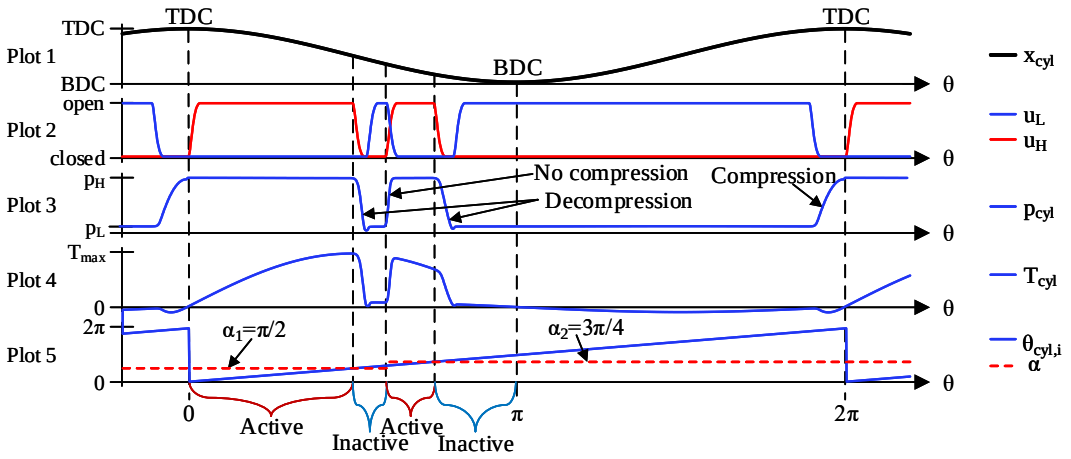

Figure D.6: Valve timing schematics for partial stroke displacement strategy Version 2.

It is not possible to compress the cylinder oil before reactivating the cylinder due to downwards piston motion. The high pressure valve must therefore open against a high pressure difference. To avoid cavitation in the cylinder chamber, both the high and low pressure valves were actuated at the same time, opening the high pressure and closing the low pressure valve. Reactivation of a cylinder chamber may result in high flow throttling losses due to flow running directly from the high pressure source to the low pressure source until the low pressure valve is fully closed. An anti-cavitation valve can be included to avoid the risk of cavitation in the case of poor timing of the valves.

D.3.3 Sequential Partial Stroke Displacement Strategy

In SPSDS, one combination of active and inactive cylinders was used in a limited amount of time before a new cylinder combination was activated. The best cylinder combination can, for example, be found by an optimization algorithm or a search routine. This displacement strategy is characterized by frequent switchings and therefore lower efficiency compared to, for example, FSDS. In this section, only a short description of the SPSDS is given. A more detailed description can be found in [25].

For simplicity, a five-cylinder motor will be used as an example when describing the concept of the SPSDS. For a five-cylinder motor, the cylinder states can be described by a 5-bit binary word, where "1" indicates that the cylinder is active and connected to the high pressure source and "0" indicates that the cylinder is inactive and connected to the low pressure source. The left plot in Figure D.7 shows the cylinder torque contribution from a five-cylinder motor when all cylinders are activated for an entire shaft revolution. When $\theta = 4\pi/7$ rad, three chambers provided a positive torque, and two chambers provided a negative torque. For a five-piston motor, there are in all $2^{N_c} = 32$ possible cylinder configurations. At $\theta = 4\pi/7$ rad, the 32 possible cylinder configurations gave only 31

distinct output torques because all cylinders connected to the high pressure source and all cylinders connected to the low pressure source gave the same output torque, $T_m = 0$ Nm. The 31 distinct output torques when $\theta = 4\pi/7$ are shown in the right plot in Figure D.7. The red point corresponds to activation of Cylinder Numbers 1 and 2 ($U_c = [1\ 1\ 0\ 0\ 0]$).

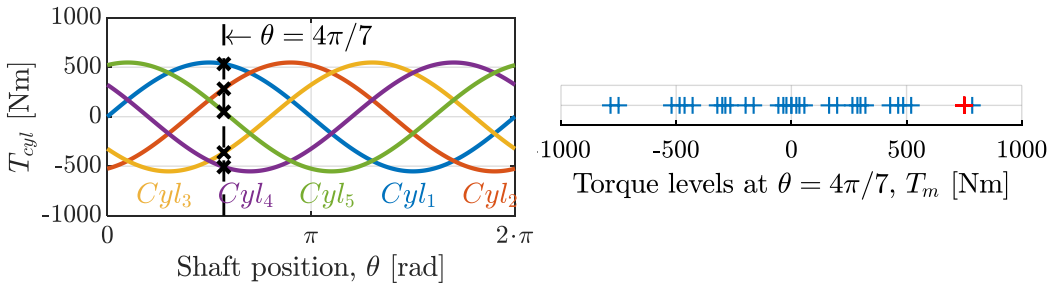

Figure D.7: Cylinder torque (**left plot**) and possible torque levels at $\theta = 4\pi/7$ (**right plot**).

Rotating the motor shaft one revolution with the same cylinder configuration will result in sinusoidal output torque. The cylinder configuration was therefore changed after a short period in order to meet the desired output torque. In this work, a search routine was used to find the best cylinder configuration. Figure D.8 shows the block diagram of the controller. The input to the system was the desired motor torque, and the output was the actual motor torque. A search routine was used to find the best cylinder configuration based on the desired motor torque T_{des}, the current motor shaft position θ, the motor shaft speed $\dot{\theta}$, and a look-up table. The look-up table was estimated offline and described the output torque $T_{11\ldots nm}$, for all possible cylinder configurations $U_{c1\ldots cm}$ at given shaft positions $\theta_{1\ldots n}$. In this work, the cylinder configuration, U_c, was updated every $T_{update} = 20$ ms and given by:

$$U_c(k) = \arg\left(\min_{U_c}\left(\left|\overline{T}_{LuT}(\theta, U_c) - T_{des}\right|\right)\right) \tag{D.16}$$

where k is the sample index and $\overline{T}_{LuT}$ is the average output torque estimated from the look-up table over the interval of rotation to which the valve configuration, $U_c(k)$, will be applied. The applied interval is defined as $[\theta, \theta + \Delta\theta]$ where $\Delta\theta = \dot{\theta} \cdot T_{update}$.

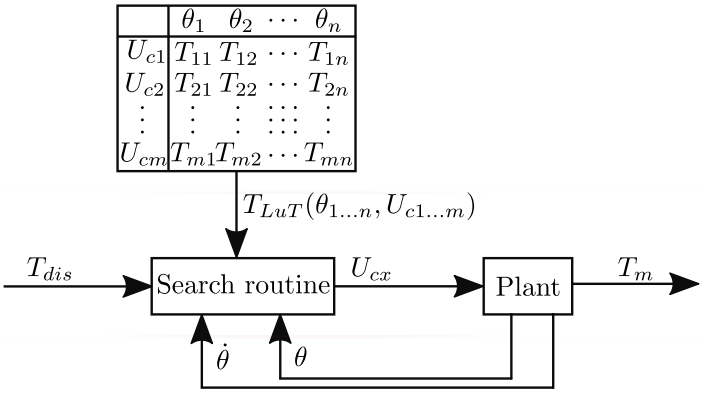

Figure D.8: Schematic of open loop control for SPSDS.

Figure D.9 shows the result of the described controller for a five-cylinder motor. The red line in the left plot shows the desired motor torque, T_{des}, and the blue line shows the actual motor torque, T_m. The right plot shows the torque contribution from every single cylinder. It can be seen that the cylinder configuration was frequently switched and that the best cylinder configuration included both motoring and pumping cylinders.

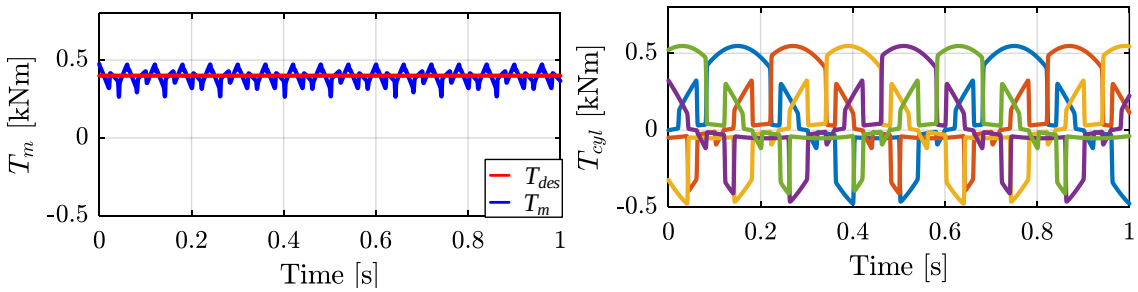

Figure D.9: Example of DDM operation with SPSDS.

D.4 Experimental Test Rig

In order to validate the simulation model of the DDM, a test rig has been developed. The test rig was designed to facilitate digital displacement operation on a single cylinder. It was assumed that all cylinders in the same motor had the same characteristics. Therefore, if the operation of one cylinder can be validated, the entire motor model is valid.

The test rig was based on a previously-developed test rig at Aalborg University, Denmark [24]. The previously-developed test rig was mainly developed to test the performance, durability, and power losses of novel prototype on/off valves used in digital displacement machine operation. The prototype valves were moving coil, moving magnet, and solenoid actuated poppet valves. Those poppet valves were designed to be passively opened. This limits the selection of displacement strategies. The test rig was therefore modified to operate with commercially-available valves that were able to open against high pressure difference in order to test the displacement strategies described in Section D.3.

The following sections present the test rig, hydraulic diagram, and validation of the simulation model.

D.4.1 Test Rig Description

A test rig for testing different displacement strategies has been designed and built. The test rig is shown in Figure D.10. The test rig was based on a five-cylinder Calzoni MR250 radial piston motor, which has been modified to operate with digital displacement technology on one cylinder. A permanent magnet synchronous electric machine was used to control the rotational speed. The control block was used to supply the modified radial piston motor with appropriate pressures and volume flows. The control block was supplied by a 250-kW variable displacement pump station, not shown in the picture. The power cabinet contained power supplies, valve drivers, a data acquisition system, and control systems.

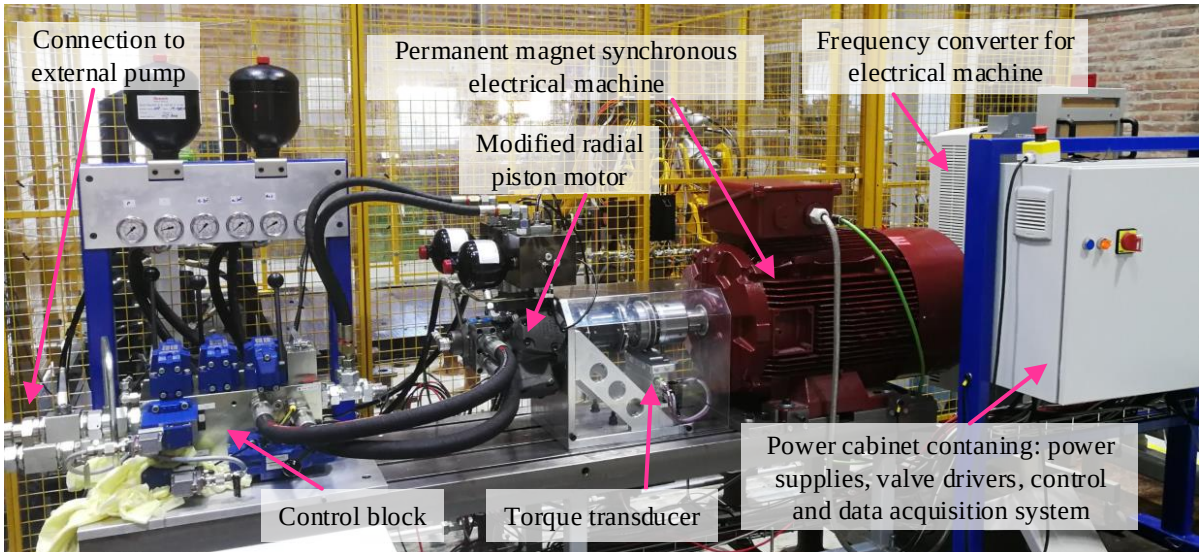

Figure D.10: Test rig.

D.4.1.1 Modification of the Hydraulic Motor

The hydraulic motor was modified to operate with digital displacement technology on a single cylinder. Figure D.11 shows the modified hydraulic motor with the custom-made valve block. The valve block consisted of two on/off valves, two accumulators, three pressure sensors, and a pressure relief valve with anti-cavitation function. The on/off valves (1) and (2) were normally open WES-type valves from Bosch Rexroth. The flow capacity was approximately 45 L/min with a pressure drop of 5 bar. The switching time was below 5 ms. The hydraulic accumulators were 0.7-L diaphragm types from Bosch Rexroth. The low pressure accumulator (3) was pre-pressurized with 5 bar, and the high pressure accumulator (4) was pre-pressurized with 80 bar. There were in all three pressure

transmitters mounted on the valve block. They measured the pressure in the low pressure source (5), high pressure source (6), and in the cylinder chamber (7). For safety reasons, a pressure relief valve with anti-cavitation function (8) was connected to the cylinder chamber to avoid very high cylinder chamber pressure and cavitation. A new top cover (10) for the modified cylinder has been designed and manufactured. This was done to block the original oil connection (12) between the port plate and the cylinder chamber and to create a new connection to the valve block. Also connected was an encoder on the motor shaft for shaft position measurements (not shown in Figure D.11). Table D.2 lists all parts used in the valve block.

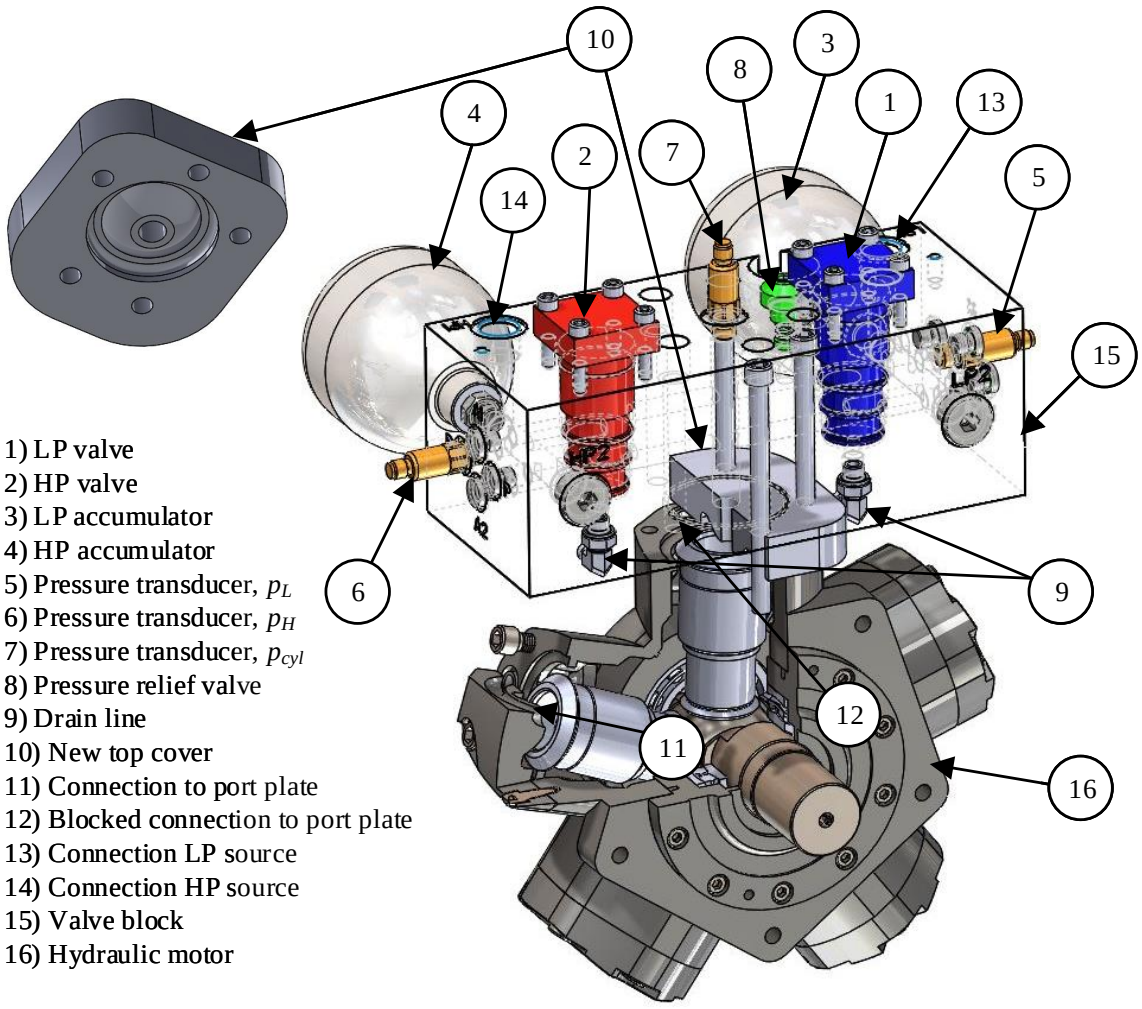

Figure D.11: Illustration of the modified radial piston motor.

Table D.2: Part list of the modified motor.

Description	Part Number	Ordering Code	Manufacturer
On/off valve	1 and 2	3WES 8 P1XK/AG24CK50/V	Bosch Rexroth
Accumulator	3 and 4	HAD-0.7-250-1x/50Z06A-1N111-BA	Bosch Rexroth
Pressure transducer	5	HM 20-2x-100-H-K35	Bosch Rexroth
Pressure transducer	6 and 7	HM 20-2x-400-H-K35	Bosch Rexroth
Pressure relief valve	8	PLC053 393000K179	Parker
Hydraulic motor	16	MR250D-P1Q1N1C1N07 00	Delivered by Parker
Position encoder	-	SCH32F-5000-D-08-26-65-00-S-C8-S3	Scancon

D.4.1.2 Hydraulic Diagram

The hydraulic diagram for the test rig is shown in Figure D.12. The hydraulic diagram was divided into three main parts; control block, valve block, and the non-modified cylinders. The control block delivered desired pressures and flows to the valve block and the non-modified cylinder chambers. The control block was designed to facilitate pumping, motoring, and idling (inactive) operation on the modified cylinder. In this study, only motor operation was used, and therefore, only motor operation will be described in this section. Pump operation was described in [26].

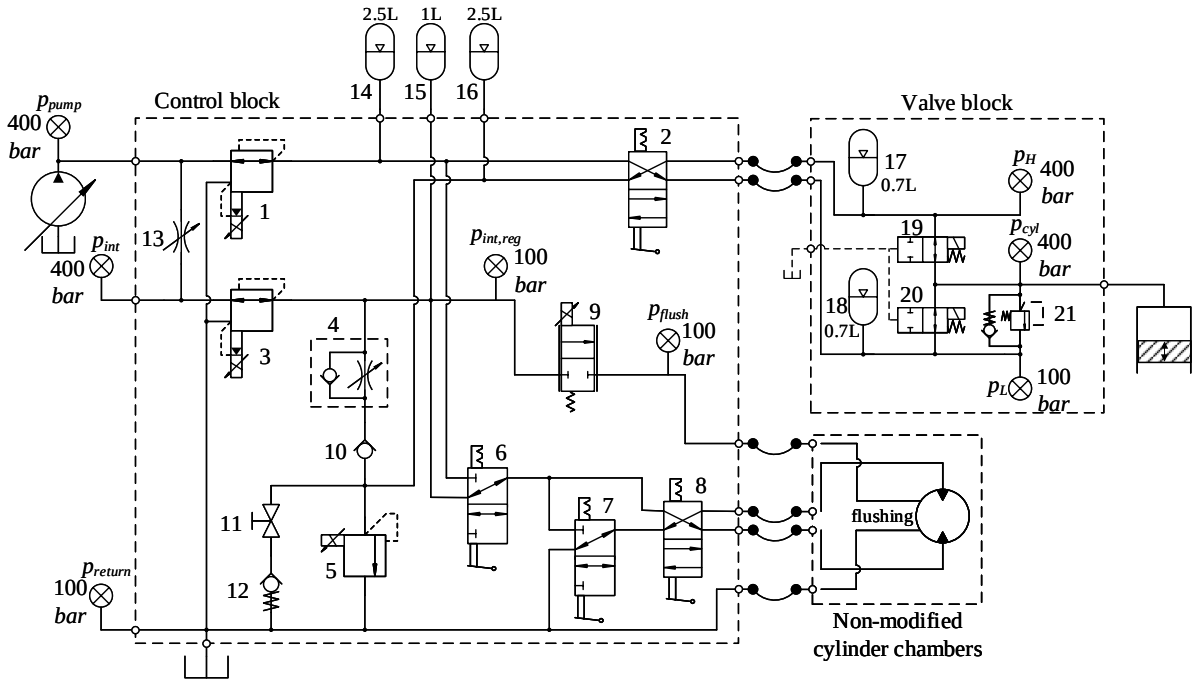

Figure D.12: Hydraulic diagram of the test rig [26].

The pressure reducing valves (1, 3) were used to control the pressure in the high pressure line, p_H, and in the intermediate pressure line, $p_{int,reg}$. The high pressure line was used to supply the modified cylinder chamber, and the intermediate pressure line was used

to supply the four remaining cylinder chambers and for flushing of the machine casing by using the flow control valve (9). During motor operation, the 4/2 directional control valve (2) was set opposite of drawn, the gate valve (11) was open, the pressure relief valve (5) was set to high pressure level, and the remaining cylinder chambers were short circuited by setting the 3/2 directional control valve (7) opposite of drawn. The accumulators were used to reduce the pressure oscillations introduced by the digital displacement operation.

D.4.1.3 Sensors

In addition to measuring pressures, as shown in the hydraulic diagram in Figure D.12, the shaft position and output torque were measured. An incremental Scancon encoder with 5000 ppr measured the shaft position, and an HBM T12 inductive torque transducer measured the output torque. The output torque was measured on the shaft connecting the radial piston motor to the permanent magnet synchronous electric machine.

D.4.2 Results from Experimental Work and Model Validation

The test rig has been used to validate the simulation model. The modified cylinder has been operated with FSDS, PSDS, and SPSDS. The experimental results have been compared to the simulation results. Table D.3 shows the opening and closing angles used in both the experimental work and in the simulation model. Table D.4 shows the operation conditions. The cylinder chamber dead volume V_d in the simulation model has been increased from $V_0 = 5.0 \cdot 10^{-5}$ m^3 (shown in Table D.1) to $V_0 = 1.308 \cdot 10^{-4}$ m^3 in order to use the same dead volume as in the experimental test setup.

Table D.3: Activation angles.

	FSDS	**PSDS**	**SPSDS**
Open HPV	0°	0°	60°
Close HPV	154°	90°	120°
Open LPV	180°	94°	125°
Close LPV	338°	338°	60°

Table D.4: Operation conditions.

Description	**Symbol**	**Value**
Operation speed	$\dot{\theta}$	100 rpm
High pressure level	p_H	110 bar
Low pressure level	p_L	10 bar

D.4.2.1 Full Stroke Operation

Figure D.13 shows measured and simulated results of the cylinder pressure p_{cyl} (red line) and cylinder torque T_{cyl} (blue line) during full stroke operation as a function of the shaft position. Note that the cylinder was at TDC when $\theta = 0$ rad and at BDC when $\theta = \pi$ rad. The left plot shows an inactive cylinder operation, and the right plot shows an active full stroke motor operation. The light colors show the experimental results, and the dark colors show the simulation results.

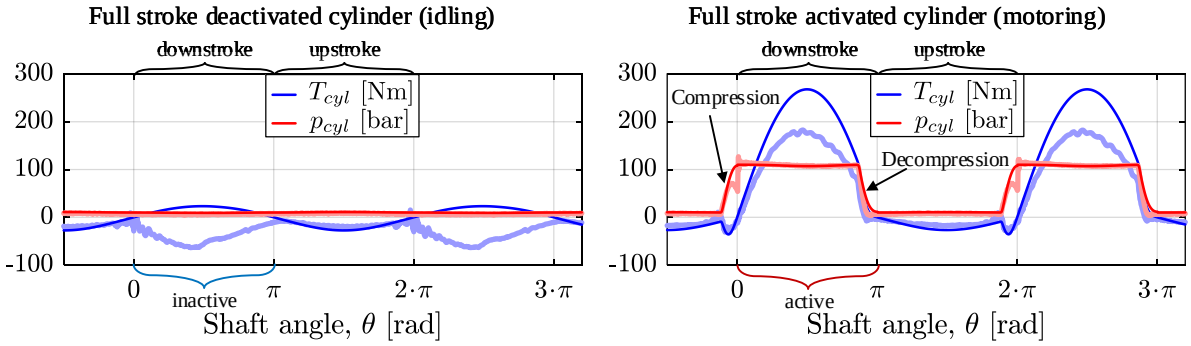

Figure D.13: Experimental and simulation results for idling and full stroke motor operation (light color is experimental results, and dark color is simulation results).

For the deactivated cylinder, the simulated chamber pressure matched the measured pressure. The simulated output torque matched the measured torque in the upstroke phase, but deviated in the downstroke phase. Some of the negative measured torque may be due to friction in the motor, but the non-modified cylinder chambers introduced most of it. As mentioned earlier, the four non-modified cylinder chambers were short circuited with a 1-L accumulator (15) connected to the short circuit line as shown in the hydraulic diagram in Figure D.12. If all five cylinders had been short-circuited, the fluid volume in the short-circuited line would be relatively constant when rotating the radial piston motor. Since one cylinder was disconnected, the pressure in the non-modified cylinders would be higher in the downstroke phase than the upstroke phase. The black line in the left plot in Figure D.14 shows the measured pressure in the short circuit line. The high pressure in the downstroke phase resulted in a negative torque contribution from the non-modified cylinders. This torque contribution was simulated by using the measured pressure. The green line, $T_{cyl,sim}$, shows the simulated torque from the non-modified cylinders added to the simulated cylinder torque, T_{cyl}. By including the negative torque, the simulated and experimental measured torques had a close fit, seen by the green- and light blue-colored lines. The pre-charge pressure of the accumulator (15) was 20 bar. A pre-charge pressure of 20 bar was unnecessarily high and should have been reduced to reduce the torque contribution from the non-modified cylinders.

In the active full stroke motor cycle, shown to the right in Figure D.13, the measured and simulated torque had the same trends. The simulated torque was a good match in the upstroke phase, but the measured torque had a lower magnitude in the downstroke phase due to the negative torque produced by the non-modified cylinders. The green line in the right plot in Figure D.14 shows the simulated cylinder torque when the torque contribution from the non-modified cylinders was included, $T_{cyl,sim}$. The results show that the simulated and measured torques were a good match, seen by comparing the green- and light blue-colored lines. The simulated cylinder pressure matched the measured pressure quite well, except for small deviations in the compression and decompression phase, seen in the right plot in Figure D.13. It can be seen that in the experimental work, the cylinder chamber fluid did not compress fully up to the high pressure level in the compression phase and decompressed slightly faster in the decompression phase. This may be due to leakage in the modified cylinder. In the simulation model, it was assumed that the cylinder was leak free. This assumption does not reflect reality. Some leakage was expected in order to reduce friction between moving parts in the cylinder. By including some leakage in the simulation model, the simulated pressure matched very well with the measured. The improvement can be seen in the compression and decompression phase in the right plot in Figure D.14.

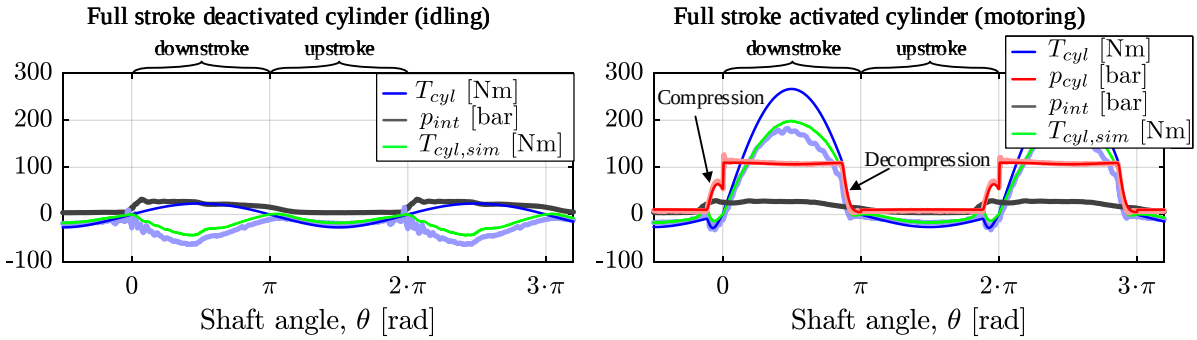

Figure D.14: Experimental and simulated results for full stroke motor operation when leakage was introduced in the simulation model (light color is experimental results, and dark color is simulation results).

The leakage was included as shown in Equation (3.1).

$$Q_L = \frac{w \cdot h^3}{12 \cdot \mu \cdot L} \cdot (p_{cyl} - p_d) \tag{D.17}$$

where w is the width of the leakage path, h is the height of the leakage path, L is the length of the leakage path, μ is the viscosity of the hydraulic fluid, and p_d is the drain pressure. The width of the leakage path was calculated as $w = \pi \cdot d_{cyl}$, where d_{cyl} is the diameter of the cylinder chamber. The height of the leakage path was adjusted until the

simulated pressure matched the measured pressure and kept within reasonable values. The drain pressure was set to $p_d = 5$ bar.

D.4.2.2 Partial Stroke and Sequential Partial Stroke Operation

Figure D.15 shows measured and simulated results of the chamber pressure p_{cyl} (red line) and the cylinder torque T_{cyl} (blue line) when motoring with PSDS Version 1 and SPSDS operation. In PSDS Version 1, shown to the left in Figure D.15, the cylinder chamber was deactivated at $\theta = \pi/2$ rad. This corresponds to the most critical switching position due to maximum piston velocity. It can be seen that the measured and simulated chamber pressure matched quite well, except in the compression phase due to some leakage in the cylinder and some small oscillations right after $\theta = 0$ rad and $\theta = 2\pi$ rad. In the downstroke phase, the measured and simulated cylinder torque had the same characteristics, but with a different magnitude due to the negative torque introduced by the non-modified cylinder chambers. In the upstroke phase, the measured and simulated output torque matched well.

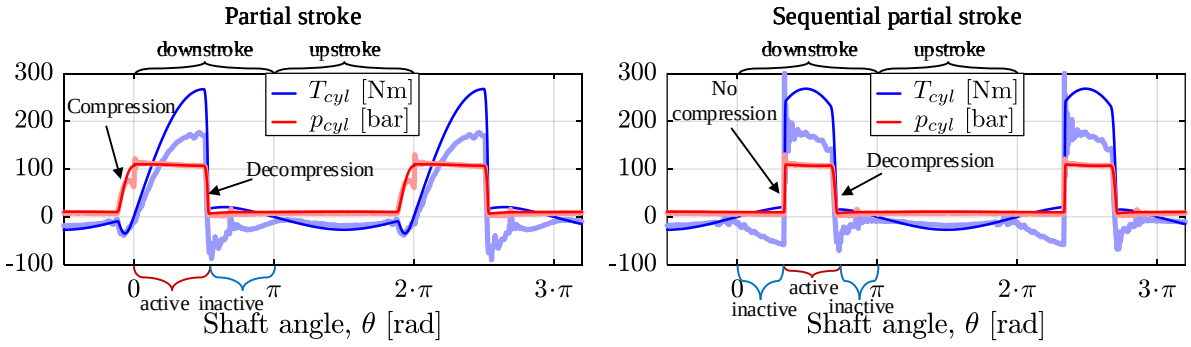

Figure D.15: Experimental and simulated results for partial stroke and sequential partial stroke motor operation (light color is experimental results, and dark color is simulation results).

In the sequential partial stroke operation sequence, shown to the right in Figure D.15, there was no compression phase, because the cylinder chamber was activated during the downstroke piston motion. Hence, the cylinder volume was increasing, and the cylinder fluid can therefore not be compressed. The high pressure valve was opened at the same angle as the low pressure valve was closed. The measured and simulated pressure matched very well. The measured and simulated output torques matched very well in the upstroke phase, but deviated in the downstroke phase due to the negative torque introduced by the four non-modified cylinder chambers. However, the torque characteristics were the same, except for some small oscillations in the measured torque.

PSDS Version 1 was quite similar to PSDS Version 2, except that in Version 2, the cylinder can be reactivated. Reactivation of a cylinder was shown in SPSDS operation. The PSDS Version 2 was therefore considered as a combination of PSDS Version

1 and SPSDS. If the simulation model was valid for PSDS Version 1 and SPSDS, it was also assumed that it was valid for PSDS Version 2.

D.4.3 Discussion

In the experimental measurements, there was some insecurity due to sensor accuracy and alignment of shaft position and piston position. The piston position was not measured, but estimated based on the shaft position measurements. The piston position was an essential parameter considering proper activation of the on/off valves. The piston position was aligned with the shaft position measurements by comparing measured and simulated results of the output torque and cylinder pressure. A deviation in the range of a few degrees was therefore assumed.

There was also insecurity in the valve switchings. The valve position was not measured, and we can therefore not know exactly when the valves are switched. However, since we are operating at a low speed, approximately 100 rpm corresponding to 600 ms per revolution, a valve that opens a few milliseconds too late or too early will not significantly affect the result.

By comparing the measured and simulated results, it has been shown that the results matched quite well except for some deviation in the pressure due to leakage in the cylinder and some deviation in the torque due to negative torque introduced by the four non-modified cylinder chambers. The main purpose of this work was to analyze the output torque. By modifying all cylinders, it was assumed that the measured output torque would be closer to the simulated output torque. The deviation between measured and simulated pressure was great in the compression phase, but small in the decompression phase. Since the compression phase occurred close to TDC, an error in the chamber pressure would have very small influence on the total motor torque, because the torque contribution at this point was low. The simulation model was therefore assumed to be a valid model of the digital displacement motor.

D.5 Dynamic Response Analysis

This analysis describes the transient and steady-state characteristics for a DDM operating with different displacement strategies. This section is divided into three subsections. Each subsection covers the transient and steady-state analysis of one displacement strategy.

D.5.1 Full Stroke Displacement Strategy

In FSDS, the cylinders were enabled and disabled on a stroke-by-stroke basis. This subsection describes the transient and steady-state characteristics of the DDM operating with FSDS.

D.5.1.1 Transient Response for the Full Stroke Displacement Strategy

The decision of either activating or deactivating the cylinder chamber was made ahead of TDC, marked by α_d in Figure D.2. This decision would affect the output torque until the piston reached BDC. Hence, the motor shaft had to rotate more than a half revolution to change displacement fully. As a result, the response time was affected by the shaft speed. Therefore, this analysis started by analyzing the transient behavior in the shaft position domain.

Figure D.16 shows the step response in the shaft position domain. The left plot shows the step-up response when the displacement fraction, D, was stepped from zero up to 0.25, 0.5, 0.75, and 1. The right plot shows the step-down response when the displacement fraction, D, was stepped from one down to 0.75, 0.5, 0.25, and 0. The step was applied at $\theta = 0$ rad. When stepping up, there was a small delay before the torque started to rise. This delay angle occurred since the decision of activating or deactivating the cylinder was made ahead of the compression phase. Right before the torque started to rise, there was a small drop in the torque due to the compression phase in the first activated cylinder. The response angle when stepping up was $\theta_{FSup} = \theta_d + \pi$. The delay angle, θ_d, was calculated as: $\theta_d = 2 \cdot \pi - \alpha_d$.

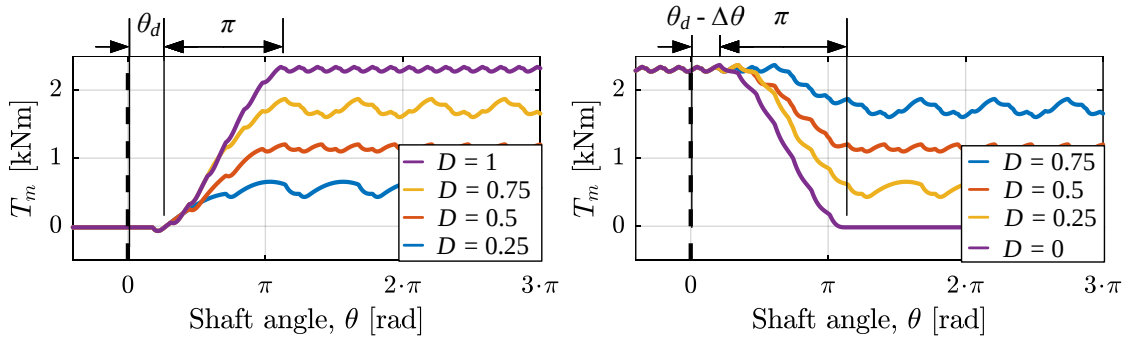

Figure D.16: Step-up response (**left plot**) and step-down response (**right plot**) using FSDS in the position domain.

When stepping down, there is also a delay before reducing the motor torque. When stepping down to zero displacement, the delay occurred because the decision of activating or deactivating the cylinder was made ahead of the decompression phase, similar to the step-up case. The extended delay that occurred when stepping down to $D > 0$ was due

to the nature of the delta-sigma modulator. The response angle when stepping down was $\theta_{FSdown} = \theta_d - \Delta\theta + \pi$, where $\Delta\theta$ is the phase shift between the cylinders and given by $\Delta\theta = 2 \cdot \pi / N_c$.

Due to the nature of the delta-sigma modulator and the actuation sequence of previous cylinders, the step-up and step-down response angles were in some cases less than the maximum response angles, θ_{FSup} and θ_{FSdown}. This phenomenon can be seen in Figure D.17. For the simulated case, it can be seen that the response angle when stepping up deviated from the normal for the green and purple line. When stepping down, the step response angle deviated from the normal for the blue and red line.

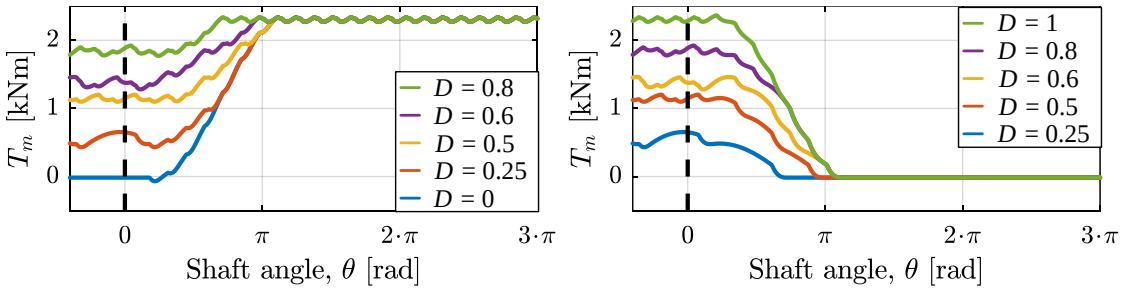

Figure D.17: Step-up response (**left plot**) and step-down response (**right plot**) using FSDS with variable response angles.

In Figure D.18, the step response is plotted in the time domain when stepping the displacement fraction from zero up to one at various speeds. It can clearly be seen that the response time was affected by the shaft speed. Assuming that the response angle was always at maximum, the response time was inversely proportional to the shaft speed.

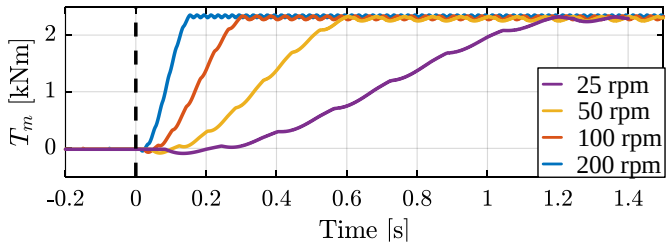

Figure D.18: Transient response FSDS in the time domain operating at various speeds.

D.5.1.2 Steady-State Response for the Full Stroke Displacement Strategy

The steady-state characteristics depend on the number of cylinders, the displacement fraction, and the shaft speed. Already in Figure D.16, it can be seen that the steady-state torque tended to oscillate. This section will discuss how the number of cylinders, the shaft speed, and the displacement fraction affected the steady-state torque.

The left plot in Figure D.19 shows the steady-state torque in the shaft position domain for motors with various numbers of cylinders and equal motor displacement. The right plot

shows the steady-state torque from a 15-cylinder motor operating at various displacement fractions. From the left plot, it can be seen that the amplitude of the torque oscillations can be reduced by increasing the number of cylinders. From the right plot, it can be seen that for some selected displacements, for example $D = 1$, $D = 0.5$, and $D = 0.2$, the output torque was relatively smooth. On the other hand, only a small change in the displacement may change the cylinder actuation sequence and result in a significant torque peak or drop; see $D = 0.1$, $D = 0.462$, and $D = 0.9$. A significant torque peak or drop may not be very critical in high speed motors due to a very short duration, but more critical in very low speed motors where the exposure time is much longer. Off course, the inertia of the load will also affect the impact of a torque peak or drop. The number of smooth outputs can be increased by increasing the number of cylinders.

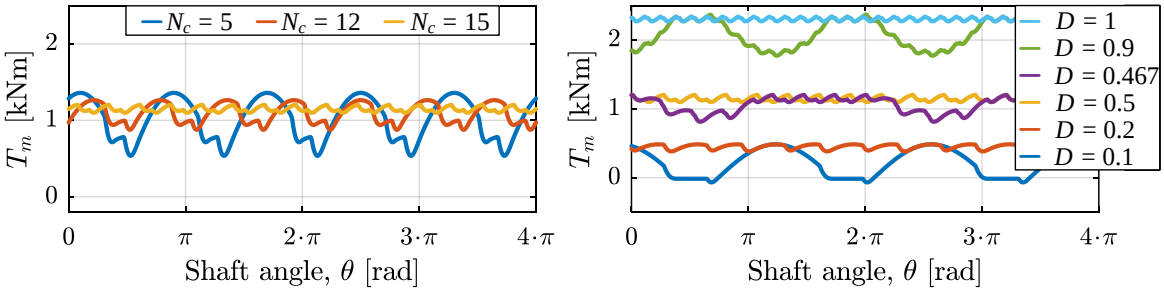

Figure D.19: Steady-state response FSDS with various numbers of cylinders (**left plot**) and at various displacements (**right plot**).

The frequency of the torque oscillations is affected by the rotational shaft speed. This can be seen in Figure D.18 where the frequency of the steady-state oscillations was clearly increased when increasing the speed.

D.5.2 Partial Stroke Displacement Strategy

In PSDS, the cylinders were activated in only a portion of the downstroke piston motion. This section describes the transient and steady-state characteristics for both PSDS Version 1 and PSDS Version 2. Note that the steady-state characteristics were the same in Version 1 and Version 2.

D.5.2.1 Transient Response Version 1 of the Partial Stroke Displacement Strategy

In PSDS Version 1, the cylinders can only have one active period during the downstroke motion. Hence, the motor needs to rotate in order to increase displacement, similar to the FSDS. Therefore, the step response is constant in the shaft position domain, but will vary with shaft speed in the time domain. Figure D.20 shows the step response in the

shaft position domain. In the left plot, the displacement fraction was stepped up from 0.1 to 0.25, 0.5. 0.75, and 0.95. In the right plot, the displacement was stepped down from 0.95 to 0.75, 0.5, 0.25, and 0.1. The step was applied at $\theta = 0$ rad.

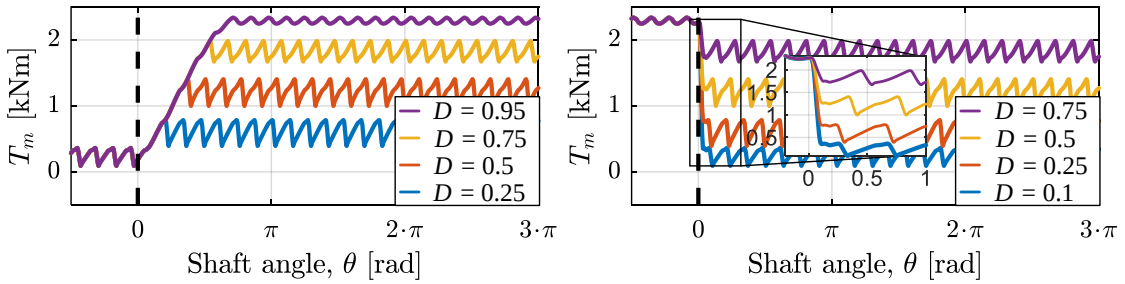

Figure D.20: Step-up response (**left plot**) and step-down response (**right plot**) using PSDS Version 1 in the position domain.

From the left plot, it can be seen that there was no delay before increasing the torque, but the step-up response angle was affected by the magnitude of the applied step. A small step gave a small response angle. In fact, the relation between the change in the state change angle ($\Delta\alpha$) and the response angle (θ_{PSup}) was 1:1, or $\Delta\alpha = \theta_{PSup}$.

It can be seen that the step-down response angle was much lower than the step-up response angle. The step-down response angle was affected both by the response time of the valves and the angle the shaft needed to rotate in order to decompress the cylinders. Assuming that the valve was fast compared to the time it took for the shaft to rotate the distance needed to decompress the oil, the response angle was approximately equal to $\theta_{PSdown} \approx \theta_{decomp}$, where θ_{decomp} is the decompression angle.

Figure D.21 shows the step response in the time domain at various speeds. The left plot shows the step-up response when the displacement ratio was stepped from 0.1–0.95. The right plot shows the step-down response when the displacement ratio was stepped down from 0.95–0.1. It can be seen that the step-down response time was much faster than the step-up response time. It can also bee seen that the response time was proportional to the speed. The step-up response time was equal to the time it took to rotate the step-up response angle (θ_{PSup}), and the step-down response time was equal to the time it took to rotate the step-down response angle (θ_{PSdown}).

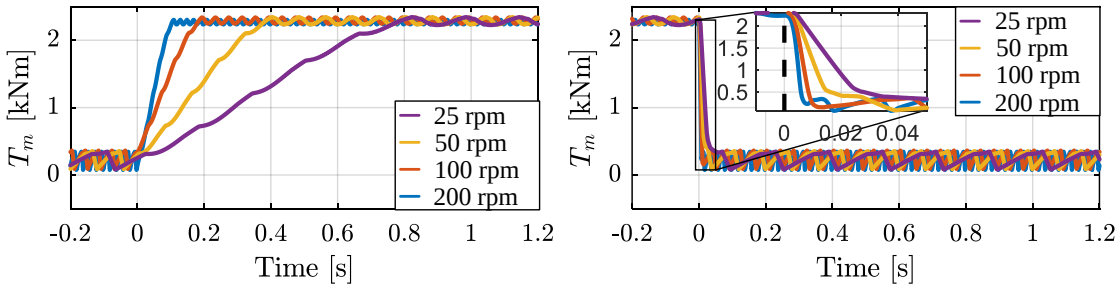

Figure D.21: Step-up response (**left plot**) and step-down response (**right plot**) using PSDS Version 1 in the time domain operating at various speeds.

D.5.2.2 Transient Response Version 2 of the Partial Stroke Displacement Strategy

In PSDS Version 1, the step-up response time was much larger than the step-down response time. The step-up response time can be improved by using valves that can reactivate an already deactivated cylinder chamber. In PSDS Version 2, the step-up response time was constant and no longer affected by the motor speed, nor the magnitude of the step. This is shown in Figure D.22. The left plot shows the step response in the time domain when stepping up at various speeds, and the right plot shows the step response in the time domain when stepping up to various displacement ratios with shaft speed kept constant. The left plot shows that the step-up response time was equal at various speeds. The step response was approximately equal to the response time of the on/off valves, which in this simulation was $T_s = 5$ ms. The right plot shows that the response time was equal regardless of the magnitude of the displacement step, unlike PSDS Version 1.

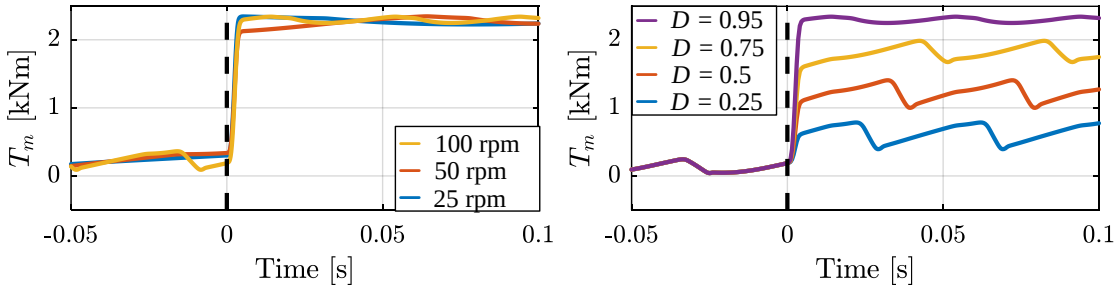

Figure D.22: Transient response PSDS Version 2 in the time domain at various speeds (**left plot**) and displacement step up to various displacements (**right plot**).

D.5.2.3 Steady-State Response Partial Stroke Displacement Strategy

The steady-state response was characterized by small ripples and was equal for PSDS Version 1 and Version 2. The shape was constant in the shaft position domain, but the frequency would vary with the speed in the time domain. Therefore, the steady-state torque shape was analyzed in the position domain.

The amplitude of the ripples was affected by the used displacement ratio and the displacement of the cylinders. The left plot in Figure D.23 shows the steady-state torque at different displacement ratios, and the right plot shows the steady-state torque for DDMs with various numbers of cylinders and equal motor displacement. The left plot shows that the maximum amplitude occurred when operating at 50% displacement. Fifty percent displacement corresponds to changing the cylinder state from active to inactive when $\theta_{cyl,i} = \pi/2$. From Equation (2.12), it can be seen that at this shaft position, the torque contribution is at its highest. The smoothest output torque occurred when operating with very high or very low displacement ratios, meaning that the valves were switched close to TDC or BDC where the torque contribution from each cylinder was low. From the right plot, it can be seen that the amplitude was reduced when the number of cylinders was increased; meaning that the cylinder displacement was reduced and therefore also the torque contribution from each cylinder was reduced. The frequency of the ripples was also increased when the number of cylinders was increased. The shaft speed would also affect the frequency of the output torque ripples.

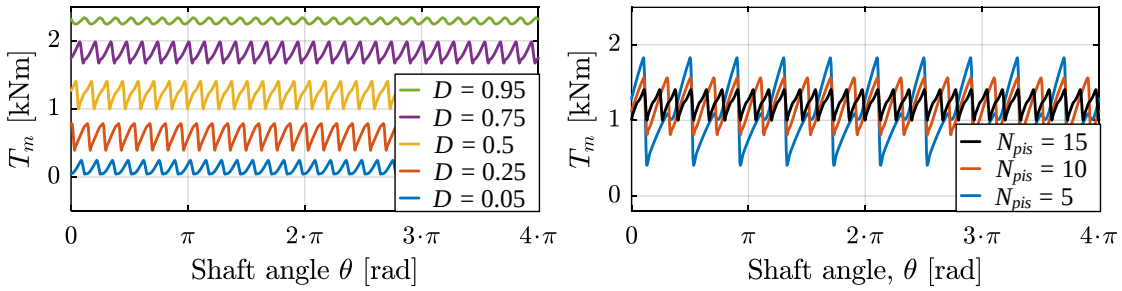

Figure D.23: Steady-state response PSDS at various displacements (**left plot**) and with various numbers of cylinders (**right plot**).

D.5.3 Sequential Partial Stroke Displacement Strategy

In SPSDS, the cylinders are activated for limited periods. The activation sequence was found by a search routine. In this section, the transient and steady-state characteristics of the SPSDS operation is analyzed.

D.5.3.1 Transient Response Sequential Partial Stroke Displacement Strategy

The step-up and step-down response in the time domain is shown in Figure D.24. The step-up and step-down responses had no delay and were equal and independent of the magnitude of the step and the shaft speed. The response time was mostly affected by the response time of the on/off valves.

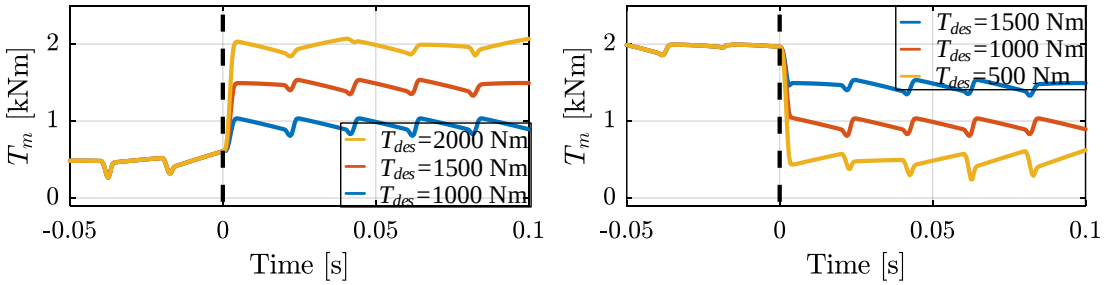

Figure D.24: Step-up response (**left plot**) and step-down response (**right plot**) using SPSDS in the time domain.

D.5.3.2 Steady-State Response Sequential Partial Stroke Displacement Strategy

The steady-state torque tends to oscillate. The torque ripples are affected by the motor speed, the number of cylinders, and also the update frequency of the controller. In Figure D.25, the desired torque was set to 2000 Nm. In the left plot, the motor was operated at various speeds, 100 rpm, 50 rpm, and 25 rpm, respectively. It can be seen that the torque ripples tended to decrease with shaft speed.

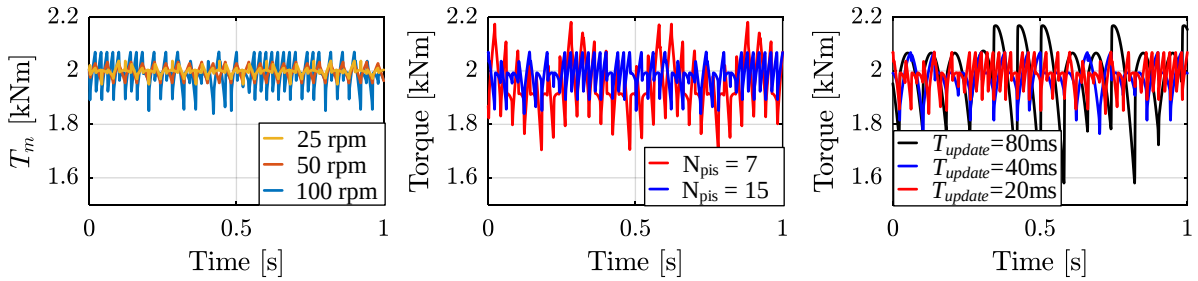

Figure D.25: Steady-state response SPSDS at various shaft speeds (**left plot**), with various numbers of cylinders (**mid plot**) and various controller update frequencies (**right plot**).

The middle plot shows the steady-state torque for two motors with equal motor displacement, but a different number of cylinders. The red line shows the output torque from a seven-piston motor, and the blue line shows the output torque from a 15-piston motor. It can be seen that the torque ripples were reduced when the number of cylinders was increased. This is because the number of possible cylinder configurations was affected by the number of cylinders (2^{N_c}). By increasing the number of cylinders, the number of distinctive output levels would also be increased. Hence, the probability of finding a valve configuration that meets the desired output torque was increased.

The right plot in Figure D.25 shows the motor output torque when the controller update frequency varied. The controller update time was set to 80 ms for the black line, 40 ms for the blue line, and 20 ms for the red line. A reduction in the torque ripples can be seen when the controller update time was changed from 80 ms and down to 40 ms.

A further reduction in the torque ripples can be seen when the update time was decreased down to 20 ms.

The search routine used in this work is shown in Equation (2.17). Another search routine may also affect the torque ripples. It is not in the scope of this work to further investigate other search routines.

D.6 Discussion

In this section, the transient and steady-state response of the presented displacement strategies will be discussed. In Figure D.26, both the input signal and the output torque are plotted when a sinusoidal input signal with increasing frequency is given. In order to be able to compare the output torque to the input signal, the values on the y-axis were normalized. The DDM was operating with FSDS in the first plot, PSDS Version 1 in the second plot, PSDS Version 2 in the third plot, and SPSDS in the last plot. The motor was operating at 50 rpm in all cases.

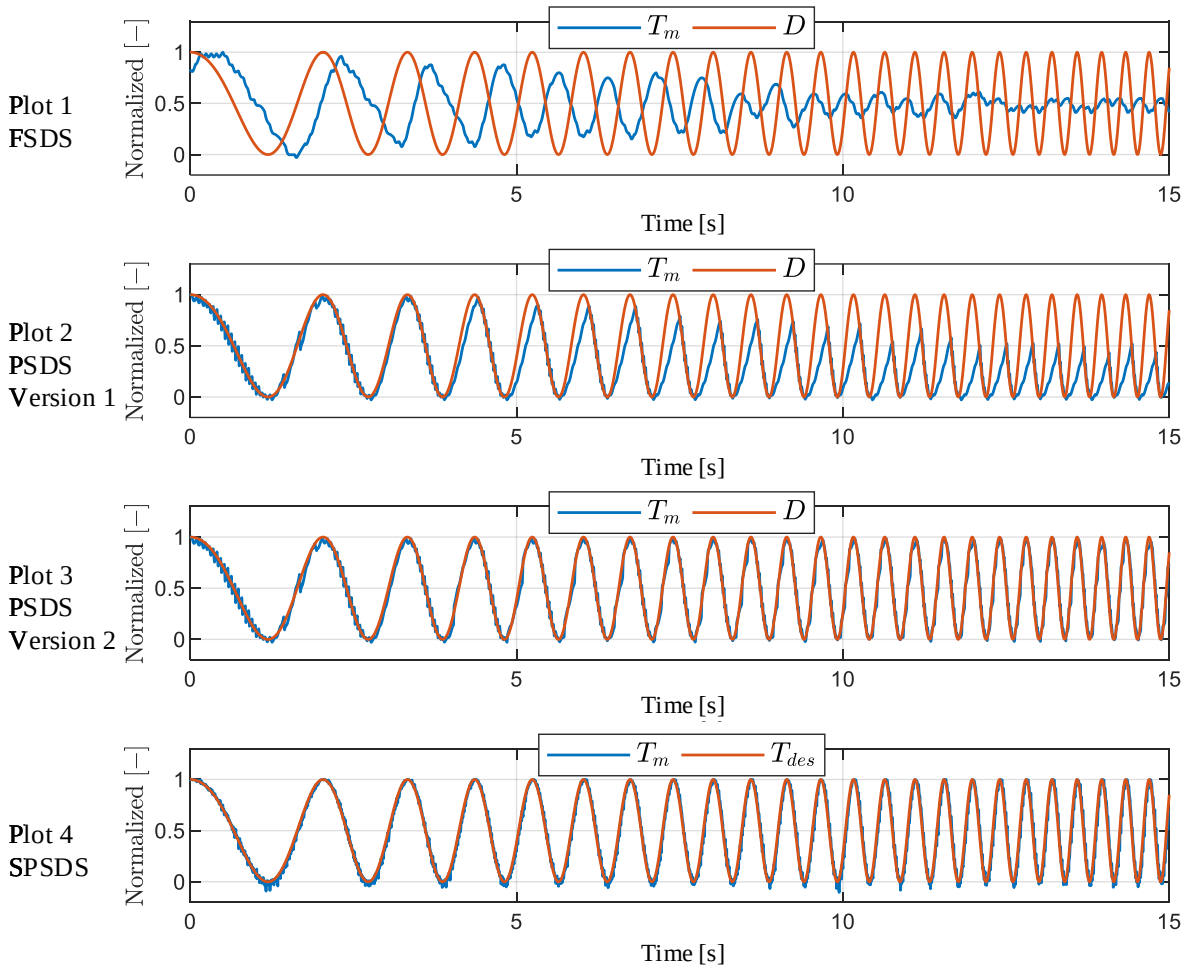

Figure D.26: DDM torque response with a sinusoidal input signal operating at 50 rpm.

As shown earlier, the transient response when operating with FSDS is known to have a delay and is highly affected by the operation speed. This can clearly bee seen in the top plot. At low frequencies, the output torque was phase shifted to the input signal due to the delay. When increasing the frequency, the amplitude of the output torque started to decrease because of the high response time at low operation speeds. By increasing the operation speed, the time delay would be reduced and the amplitude would reach one for a higher input frequency. The FSDS is most suited for use in high speed operations due to the delay in the transient response and the fact that the response time is highly affected by the speed. The FSDS is also considered to be the most energy efficient displacement strategy due to few valve switchings and only actuating the valves close to TDC and BDC where the volume flow is low.

Both in FSDS and PSDS 1, the response time was highly affected by the operation speed. However, the response of PSDS Version 1 shown in the second plot in Figure D.26 was much better than for FSDS, especially at low frequencies. This is because in PSDS Version 1, there was no delay, and the step up response time was affected by the magnitude of the step. A small step has a low response time. PSDS Version 1 is also known to have much faster response time when stepping down compared to stepping up. This is clearly seen when increasing the input frequency. The output torque followed the input signal in the torque reduction phase, but rose too slow in the torque increasing phase. The output torque tended to oscillate with small ripples. The magnitude of the ripples can be reduced by increasing the number of cylinders. The frequency was affected both by the number of cylinders and the operation speed. A small number of cylinders will result in a large magnitude of the ripples and should be avoided. Since the step-up response time is highly affected by the operation speed, this displacement strategy should only be used for medium and high speed operations. The controllability is considered to be higher than for FSDS, but the energy efficiency is considered to be lower due to activating all cylinder chambers and switching valves mid-stroke when the flow is high.

PSDS Version 2 can have more than one active period in one downstroke piston motion. This results in a response time that no longer is affected by the operation speed, but is closer to the response time of the on/off valves. The third plot in Figure D.26 shows that the PSDS Version 2 had high controllability and followed the input signal very well, also at higher frequencies. The small torque ripples seen for the PSDS Version 1 can also be seen for the PSDS Version 2 (best seen at low frequencies). Due to reactivation of cylinder chambers, the energy efficiency will be lower than for PSDS Version 1 and FSDS. Because of the high controllability, also at low speeds, the PSDS Version 2 is most suited for low speed operations.

The SPSDS is characterized by frequently switchings. From the fourth plot in Figure D.26,

it can bee seen that the output torque followed the input signal very well. The output torque had some small ripples. Those ripples were smaller than for the PSDS, but will be increased if the speed increases, the number of cylinders is reduced, or the controller update frequency decreases. Due to the frequent switchings, the energy efficiency was the lowest of the investigated displacement strategies. SPSDS should only be used in very low speed operations because the torque ripples are increased at higher speeds.

The main characteristics of the investigated displacement strategies are summarized in Table D.5.

Table D.5: Summary of transient and steady-state characteristics

		FSDS	**PSDS 1**	**PSDS 2**	**SPSDS**
Transient response	Delay-time	Some delay due to decision angle ahead of TDC	No delay	No delay	No delay
	Response time	Affected by shaft speed	Affected by shaft speed and displacement step	Affected by valve response time	Affected by valve response time
	Overshoot	No overshoot	No overshoot	No overshoot	No overshoot
Steady-state response	Magnitude of torque ripples	Affected by displacement ratio & number of cylinders	Affected by displacement ratio & number of cylinders	Affected by displacement ratio & number of cylinders	Affected by shaft speed, controller update rate & number of cylinders
	Frequency of torque ripples	Affected by shaft speed & number of cylinders	Affected by shaft speed & number of cylinders	Affected by shaft speed & number of cylinders	Affected by controller update rate

D.7 Conclusions

In this paper, the transient and steady-state characteristics of a DDM operating with FSDS, PSDS Version 1, PSDS Version 2, and SPSDS have been investigated by simulations. The simulation model has been verified by experimental work.

The FSDS is characterized by a response time that is proportional to the velocity of the motor. Generally, the motor has to rotate approximately a half shaft revolution to change displacement fully. Due to the nature of the delta-sigma modulator, the response angle may vary in some cases. The output torque is relatively smooth, but for some displacements, a significant peak or drop in the output torque may occur. By increasing the number of cylinders, the number of smooth output torques will be increased. The FSDS struggles to follow a sinusoidal input signal when the motor speed is low. Therefore, if controllability is important, this displacement strategy should only be used in high speed units.

In this paper, two different versions of the partial stroke displacement strategy have been investigated. In Version 1, the cylinders can only have one active period during

the downstroke piston motion. For this version, the motor had to rotate to increase the displacement. Therefore, the step-up response time was affected by the motor speed. The step-up response time was also affected by the magnitude of the step because the response angle was equal to the change of the state change angle, $\Delta\alpha$. The response time when stepping down was equal to the time it took to close the high pressure valve and decompress the deactivated cylinders, which was much faster than the response time when stepping up. The output torque tended to oscillate. The highest peaks occurred when operating at $D = 50\%$, which corresponds to the switching state when the torque contribution from each cylinder is at its highest. The magnitude of the torque ripples will be reduced when operating with displacements closer to full or zero displacements. The magnitude can also be reduced by increasing the number of cylinders.

In PSDS Version 2, the step-up response time has been reduced by allowing the cylinders to be reactivated. Reactivating a cylinder will result in higher valve throttling losses and flow and pressure peaks in the system, but will also improve the controllability at low speeds. The step-up response time is no longer affected by the speed or the magnitude of the step, but by the response time of the on/off valves. When giving a sinusoidal input signal, the PSDS Version 1 struggles to increase the output torque fast enough at higher frequencies and should therefore only be used in medium and high speed operations. The PSDS Version 2 follows the input signal well even at high input frequencies and low speed. The controllability for Version 2 is, therefore, better than for PSDS Version 1 and is suitable for operation at low and medium speeds.

The SPSDS is characterized by frequent switching. The response time was approximately equal to the response time of the on/off valves. The output torque was smoother when operating at low speeds compared to high speeds. Increasing the number of cylinders will increase the number of possible output torques and thereby reduce the torque ripples. The SPSDS has high controllability and follows a sinusoidal input signal smoothly when operating at low speeds. SPSDS is suited for use in very low speed operations, but should be avoided in high speed operations due to increased torque, flow, and pressure ripples at higher speeds.

Author Contribution: Conceptualization, S.N.; methodology, S.N.; software, M.M.B.; validation, S.N. and M.M.B.; investigation, S.N.; writing, original draft preparation, S.N.; writing, review and editing, S.N., M.K.E., and T.O.A.

Funding: This research was funded by the Norwegian Research Council, SFIOffshore Mechatronics, Project Number 237896.

Conflicts of Interest: The authors declare no conflict of interest.

Abbreviations

DDM	Digital displacement motor
FSDS	Full stroke displacement strategy
PSDS	Partial stroke displacement strategy
SPSDS	Sequential partial stroke displacement strategy
TDC	Top dead center
BDC	Bottom dead center

Bibliography

[1] W H S Rampen. The development of digital displacement technology. In *Proceedings of the ASME/Bath Symp. on Fluid Power & Motion Control*, pages 11–16, 2010. keynote address.

[2] Md Ehsan, WHS Rampen, and SH Salter. Modeling of digital-displacement pump-motors and their application as hydraulic drives for nonuniform loads. *Journal of dynamic systems, measurement, and control*, 122(1):210–215, 2000.

[3] Grégory S Payne, Uwe BP Stein, Mohammad Ehsan, Niall J Caldwell, and WHS Rampen. Potential of digital displacement hydraulics for wave energy conversion. In *Proceedings of the sixth European wave and tidal energy conference, Glasgow*, 2005.

[4] W. H. S. Rampen. Gearless transmissions for large wind turbines - the history and future of hydraulic drives. *Artemis Intelligent Power Ltd.*, 2006.

[5] Niels H Pedersen, Per Johansen, and Torben O Andersen. Feedback control of puls-density modulated digital displacement transmission using a continuous approximation. *IEEE/ASME Transactions on Mechatronics*, 2018. Under 3rd revision.

[6] Per Johansen, Daniel B Roemer, Torben O Andersen, and Henrik C Pedersen. Discrete linear time invariant analysis of digital fluid power pump flow control. *Journal of Dynamic Systems, Measurement, and Control*, 139(10):101007, 2017.

[7] Niels H Pedersen, Per Johansen, and Torben O Andersen. Event-driven control of a speed varying digital displacement machine. In *ASME/BATH 2017 Symposium on Fluid Power and Motion Control*, pages V001T01A029–V001T01A029. American Society of Mechanical Engineers, 2017.

[8] Niels H Pedersen, Per Johansen, and Torben O Andersen. Lqr feedback control development for wind turbines featuring a digital fluid power transmission system. In *9th FPNI Ph. D. Symposium on Fluid Power*, pages V001T01A024–V001T01A024. American Society of Mechanical Engineers, 2016.

[9] Niels H Pedersen, Per Johansen, and Torben O Andersen. Optimal control of a wind turbine with digital fluid power transmission. *Nonlinear Dynamics*, 91(1):591–607, 2018.

[10] Niels Henrik Pedersen, Per Johansen, and Torben Ole Andersen. Model predictive control and discrete analysis of partial stroke operated digital displacement unit. In *2018 Global Fluid Power Society PhD Symposium (GFPS)*, pages 1–9. IEEE, 2018.

[11] Niels Henrik Pedersen, Per Johansen, Anders Hedegaard Hansen, and Torben Ole Andersen. Model predictive control of low-speed partial stroke operated digital displacement pump unit. *Modeling, Identification and Control*, 39(3):167–177, 2018.

[12] Niels Henrik Pedersen, Per Johansen, Torben O Andersen, and Rudolf Scheidl. Nonlinear hybrid control oriented modelling of a digital displacement machine. In *Proceedings of the 9th Workshop on Digital Fluid Power, Aalborg, Denmark*, pages 7–8, 2017.

[13] Niels H Pedersen, Per Johansen, and Torben O Andersen. Four quadrant hybrid control oriented dynamical system model of digital displacement® units. In *BATH/ASME 2018 Symposium on Fluid Power and Motion Control*, pages V001T01A039–V001T01A039. American Society of Mechanical Engineers, 2018.

[14] Mateusz Sniegucki, Markus Gottfried, and Uwe Klingauf. Optimal control of digital hydraulic drives using mixed-integer quadratic programming. *IFAC Proceedings Volumes*, 46(23):827–832, 2013.

[15] GS Payne, AE Kiprakis, M Ehsan, W H S Rampen, JP Chick, and AR Wallace. Efficiency and dynamic performance of digital displacement™ hydraulic transmission in tidal current energy converters. *Proceedings of the Institution of Mechanical Engineers, Part A: Journal of Power and Energy*, 221(2):207–218, 2007.

[16] Kyle Joseph Merrill. *MODELING AND ANALYSIS OF ACTIVE VALVE CONTROL OF A DIGITAL PUMP-MOTOR*. Ph.D. thesis, Purdue University, Indiana, USA, August 2012.

[17] Mikko Heikkila, Jyrki Tammisto, Mikko Huova, M Huhtala, and Matti Linjama. Experimental evaluation of a piston-type digital pump-motor-transformer with two independent outlets. *Fluid Power and Motion Control, Bath, England*, pages 83–98, 2010.

[18] Linjama Matti and Kalevi Huhtala. Digital pump-motor with independent outlets. *The 11th Scandinavian Conference on Fluid Power, SICFP'09*, June 2009.

[19] K Merrill and J Lumkes. Operating strategies and valve requirements for digital pump/motors. In *Proceedings of the 6th FPNI-PhD Symposium, West Lafayette*, pages 249–258, 2010.

[20] Niels Henrik Pedersen, Per Johansen, and Torben Ole Andersen. Challenges with respect to control of digital displacement hydraulic units. *Modeling, Identification and Control*, 39(2):91–105, 2018.

[21] Daniel Beck Rømer. *Design and optimization of fast switching valves for large scale digital hydraulic motors*. Ph.D. thesis, Department of Energy Technology, Aalborg University, 2014.

[22] Michael Rygaard Hansen. In Compendium *Fluid Mechanics*. Department of Engineering, University of Agder, Norway, Lecture notes MAS126, 2015; pp. 28–30.

[23] Per Johansen, Daniel Beck Roemer, Torben Ole Andersen, and Henrik C Pedersen. Delta-sigma modulated displacement of a digital fluid power pump. In *7th Workshop on Digital Fluid Power*, pages 1–9. LCM GmbH, 2015.

[24] Christian Nørgård. *Design, optimization and testing of valves for digital displacement machines*. Ph.D. thesis, Aalborg University, 2017. doi: 10.5278/vbn. phd. eng. 00013, 2017.

[25] Brian SR Armstrong and Qinghui Yuan. Multi-level control of hydraulic gerotor motors and pumps. In *2006 American Control Conference*, pages 4619–4626. IEEE, 2006.

[26] Christian Nørgård, Jeppe H Christensen, and Michael M Beck. Test rig for valves of digital displacement machines. In *Proc. of The Ninth Workshop on Digital Fluid Power, Aalborg, Denmark*, 2017.

Paper E

Definition of Performance Requirements and Test Cases for Offshore/Subsea Winch Drive Systems with Digital Hydraulic Motors

Sondre Nordås, Morten Kjeld Ebbesen and Torben Ole Andersen

This paper has been published as:

S. Nordås, M. K. Ebbesen, and T. O. Andersen. Definition of Performance Requirements and Test Cases for Offshore/Subsea Winch Drive Systems with Digital Hydraulic Motors. In *The Proc. of the BATH/ASME 2019 Symposium on Fluid Power and Motion Control*, Sarasota, Florida, 2019.

Definition of Performance Requirements and Test Cases for Offshore/Subsea Winch Drive Systems with Digital Hydraulic Motors

Sondre Nordås*, Morten Kjeld Ebbesen* and Torben Ole Andersen**

*University of Agder
Faculty of Engineering and Science
Jon Lilletunsvei 9, 4879 Grimstad, Norway

** Aalborg University
Faculty of Engineering and Science
Pontoppidanstræde 101, 9220 Aalborg East, Denmark

Abstract **– A subsea crane is normally mounted on a floating vessel and equipped with a winch system. The crane can operate in water down to 3000 m. The vessel tends to move up and down due to waves. This heave motion makes offshore lifting operations challenging. In order to ease the winch operation in rough sea, the winch can be equipped with additional systems like active heave compensation and constant tension. In active heave compensation and constant tension system, both motion and force control of the winch are important. This paper presents a digital displacement winch drive system and gives a description of challenges related to subsea lifting operations. The operation challenges are used to design a set of test cases for evaluating the performance of the digital displacement winch drive system.**

E.1 INTRODUCTION

The digital displacement technology is experiencing increased interest due to its flexibility and promising results regarding energy efficiency. In a piston-type digital displacement machine, each cylinder chamber is connected to two fast switching on/off valves. By controlling the on/off valves, the cylinder chambers can be connected to either high or low pressure. This means that each cylinder can be controlled individually and only pressurized when necessary resulting in losses that scales with the motor displacement. A detailed description of the digital displacement technology can be found in [1, 2, 3, 4].

Digital displacement machines have earlier been proposed to be used in various applications like on- and off-road vehicles and in large power take-off systems in the renewable energy industry [5, 6, 7, 8, 9, 10, 11, 12]. Lately, the company Diinef AS proposed to use

the digital displacement technology in large offshore winches and presented a displacement strategy for use in very low speed operations [13].

Offshore winches intended for use in subsea cranes are normally single drum winches actuated by one or more high speed hydraulic motors and gearboxes. The driving torque is transferred to the winch drum through a pinion and gear ring mounted on the drum. Figure E.1 shows an example of a subsea crane with a winch actuated by 12 hydraulic motors.

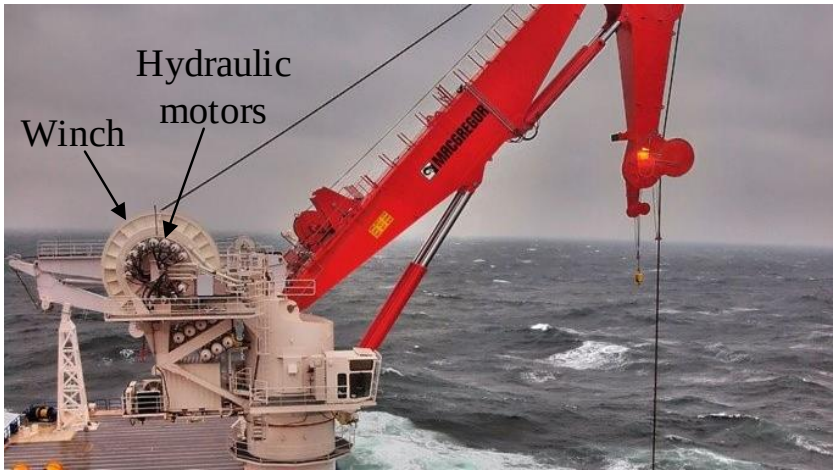

Figure E.1: Subsea crane equipped with a hydraulic winch system [14].

One of the main concerns during subsea lifting operations from a floating vessel is the disturbance from the sea waves. The lifting operation needs to be carried out within a specified weather window. A weather window is a period where the weather forecast indicates that a given set of activities can be performed within there required environmental conditions, for example within given wave heights and wave frequencies. The weather window is affected by the lifting operation, size of the vessel and type of payload. Waiting for suitable weather conditions is costly. Increasing this weather window will therefore result in cost reductions. One way of increasing the weather window is to include operation modes like active heave compensation (AHC) and constant wire tension (CT) systems. An AHC system is used to decouple the vertical vessel motion from the payload motion. This means that the winch operator can control the payload relative to a fixed surface, for example the sea bed. The AHC system, normally utilizes a motion reference unit (MRU) to measure the unwanted vessel motion and actively activate the winch to counteract this motion. The CT system is used to keep the wire tension at a given pre-set value regardless of motion. A load cell is normally used to measure the wire tension. If the measured value deviates from the pre-set value, the winch will pull in or pay out wire rope to maintain the pre-set value.

Several papers present control systems for both AHC and CT systems. In [15], the au-

thors proposed a position feedback with a velocity and acceleration feedforward controller for the motion controller and a closed feedback loop with a P controller for the force controller. In [16], the authors proposed a cascade controller to improve motion tracking performance. The cascade controller has an inner velocity loop with a velocity feedforward and an outer position loop. The outer position loop has a P controller and the inner velocity loop has a PI controller. The non-linearity of hydraulic winch systems decreases the motion tracking performance for linear controllers. The motion tracking performance can be improved by utilizing an adaptive feedforward controller [17], by using a backstepping sliding mode controller [18] or using predictive control where the winch parameters are estimated real-time [19]. An approach of damping the payload in active heave compensation has successfully been implemented in simulations by Yuan [20]. The novelty in [20] is to include the cable dynamics in the compensation system. Work presented in [21] proposes using measurements of wave amplitude as a feedforward compensator within an active heave compensation system to improve operation performance during the water entry phase.

Digital displacement motors are known to have pulsating output torque and to be complicated to control. Despite of these characteristics, we have in this paper chosen to show their control performance in an offshore winch drive system. The second section presents the simulation model of the mechanical winch system and the digital displacement motor. The third section describes the controller and gives a description of the displacement strategy used on the digital displacement motor. The fourth section presents challenges in subsea lifting operations and test the digital displacement winch drive system in three relevant test cases.

E.2 SIMULATION MODEL

In this study, a winch with max safe working load (SWL) equal to 20000 kg is used as a case study. The winch is a single drum winch type with a drum capacity of 3660 m of wire. The winch is driven by a digital displacement winch drive system consisting of several high torque low speed digital displacement motors (DDMs) with a total of 42 pistons. The motor torque is transfered to the winch drum through a pinion and gear ring. The pistons can be distributed on several motors placed around the gear ring on the winch drum. For simplicity, in the simulation model, it is assumed that all pistons are placed on one motor with the pistons uniformly distributed around the motor shaft.

The simulated system is shown in Figure E.2. r_d is the drum radius, r_{eff} is the effective radius of the outer wire layer, w_d is the drum width and m_{load} is the mass of the payload. The simulation model is divided into two main parts: the mechanical winch system and

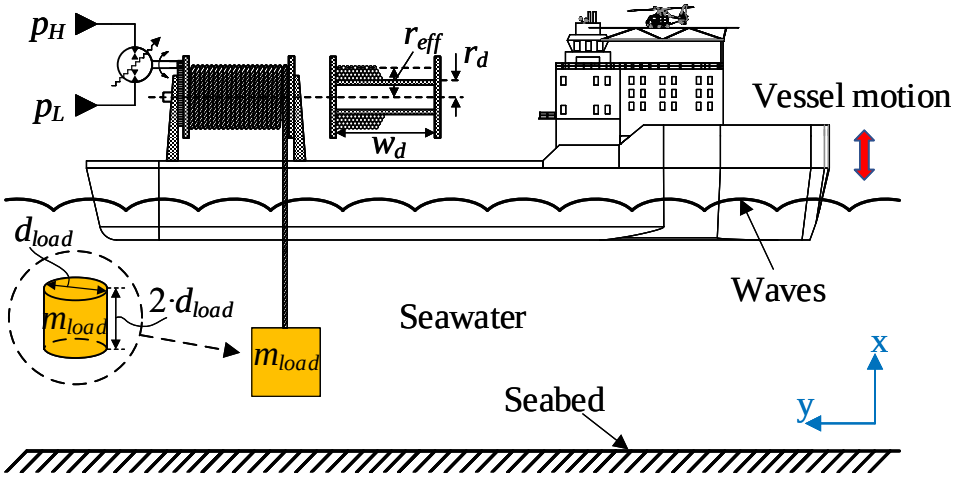

Figure E.2: Simulation system.

the digital displacement winch drive system.

E.2.1 Mechanical Winch System

The mechanical winch system consists of the winch drum, wire rope and the payload. The simulation model is based on the winch model described in [16]. It is assumed that the payload is either located in air or fully submerged in water. Hence, the transition phase between water and air is not included in this simulation model.

The simulation model is derived based on the dynamic model schematic, the free body diagram and the kinetic diagram shown in Figure E.3. The wire is modeled as a mass-spring-damper system and the seabed is modeled as a spring-damper system, shown in the dynamic model schematic. Based on the free body diagram and the kinetic diagram, Newton's second law of motion is used to describe the rotational motion of the drum and the vertical motion of the payload.

$$\sum \tau = J_{eff} \cdot \ddot{\theta}_d = T_{drive} - T_f - F_{w1} \cdot r_{eff} \tag{E.1}$$

$$\sum F_x = (m_c + m_a) \cdot \ddot{x}_{pl} = F_{w2} + F_b + F_N - F_d - m_c \cdot g \tag{E.2}$$

where T_{drive} is the driving torque acting on the drum, T_f is the friction torque in the drum bearings, F_{w1} is the wire force in the upper wire section, F_{w2} is the wire force in the lower wire section, r_{eff} is the effective radius of the outer wire layer, J_{eff} is the effective mass moment of inertia relative to the drum axis, m_c is the mass of the combined load, m_a is the added mass, F_b is the buoyancy force, F_d is the drag force, F_N is the seabed interaction force and g is the acceleration of gravity. The driving torque is given by the motor torque and calculated in Section E.2.2.

The friction torque in the drum bearings, T_f, is assumed to be a combination of

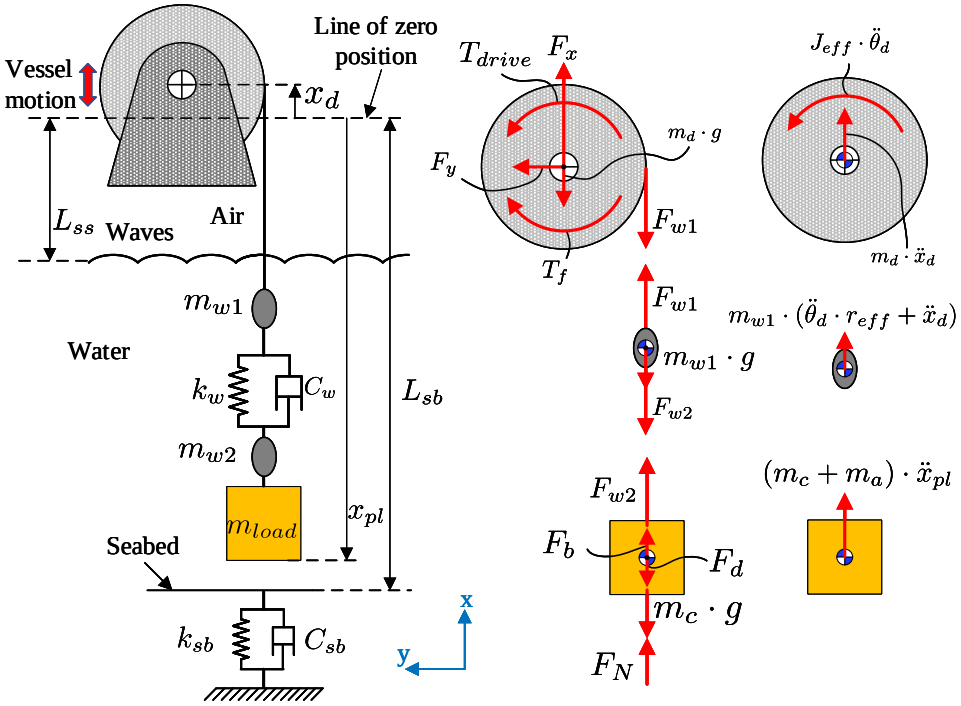

Figure E.3: System dynamics (left figure), free body diagram (middle figure) and kinetic diagram (right figure).

coulomb and viscous friction and it is calculated as shown in Equation E.3.

$$T_f = \underbrace{(m_d \cdot g + F_{w1}) \cdot r_b \cdot \mu_c \cdot \tanh(\dot{\theta}_d \cdot 1000)}_{T_{coulomb}} + \underbrace{\mu_v \cdot r_b \cdot \dot{\theta}_d}_{T_{viscous}} \tag{E.3}$$

where m_d is the mass of the drum and the mass of the wire rolled onto the drum, r_b is the radius of the drum bearings, μ_c is the coulomb friction coefficient and μ_v is the viscous friction coefficient. The coulomb friction coefficient is approximated as $\mu_c = 0.1$ and the viscous friction coefficient is approximated as $\mu_v = 1000\ Ns$. The term $\tanh(\dot{\theta}_d \cdot 1000)$ is used to avoid a step change of the coulomb friction torque when passing through $0\ rpm$, and to make the transition as steep as practical possible in the simulation model. However, this friction model is only an approximation and may not reflect the exact friction characteristics.

From the dynamic model schematic shown in Figure E.3, it can be seen that the wire is divided into two point masses, m_{w1} and m_{w2}, with a spring and damper in between. The connection between the upper wire section and the winch drum, and the connection between the lower wire section and the payload are assumed to be rigid. Hence, the motion of the upper wire section is a combination of the vertical motion of the vessel and the rotation of the drum, $\ddot{x}_{w1} = \ddot{\theta}_d \cdot r_{eff} + \ddot{x}_d$. The motion of the lower wire section is equal to the payload motion, $\ddot{x}_{w2} = \ddot{x}_{pl}$. The wire forces, F_{w1} and F_{w2}, can then be calculated

as shown in Equation E.4 and Equation E.5.

$$F_{w1} = m_{w1} \cdot (\ddot{\theta}_d \cdot r_{eff} + \ddot{x}_d) + m_{w1} \cdot g + F_{w2} \tag{E.4}$$

$$F_{w2} = \underbrace{(\theta_d \cdot r_{eff} + x_d - x_{pl}) \cdot k_w}_{F_{spring}} + \underbrace{(\dot{\theta}_d \cdot r_{eff} + \dot{x}_d - \dot{x}_{pl}) \cdot C_w}_{F_{damper}} \tag{E.5}$$

where $\ddot{x}_d$ is the vertical acceleration of the vessel, k_w is the spring stiffness of the wire and C_w is the damping coefficient. Note that Equation E.5 is only valid when the wire is stretched. If the wire is slack, then the wire force is $F_{w2} = 0\ N$. The spring stiffness is calculated based on the wire elasticity, E_w, wire cross-section area, A_w, and the length of the payed out wire, L_w, as shown in Equation E.6. The damping force is introduced to compensate for internal friction in the wire rope. The damping coefficient is defined as 10% of the spring stiffness [16] and calculated in Equation E.7. However, this wire model is only a rough estimation and may not reflect the exact characteristics of the wire.

$$k_w = \frac{E_w \cdot A_w}{L_w} \tag{E.6}$$

$$C_w = \frac{k_w}{10} \tag{E.7}$$

Note that Equation E.7 does not give the correct unit of the damping coefficient. The correct unit is Ns/m.

The payload is exposed to buoyancy when submerged in water and a viscous drag force during motion. The buoyancy force includes the buoyancy of the payload and the submerged wire. The buoyancy force, F_b, and drag force, F_d, is calculated as shown in Equation E.8 and Equation E.9 [22].

$$F_b = \rho_{sea} \cdot g \cdot (V_{pl} + V_w) \tag{E.8}$$

$$F_d = \frac{1}{2} \cdot \rho_{sea} \cdot C_d \cdot A_{pl} \cdot \dot{x}_{pl} \cdot |\dot{x}_{pl}| \tag{E.9}$$

where ρ_{sea} is the sea water density, V_{pl} is the volume of the payload, V_w is the volume of the submerged wire, C_d is the drag force coefficient and A_{pl} is the projected cross-section area of the payload normal to the motion. Note that the buoyancy and drag force are only applied when the payload is submerged in water. For the payload considered in this work, see Figure E.2, the drag coefficient is $C_d = 0.85$ [22].

The seabed is normally modeled as a spring-damper system [16]. The seabed interaction force, F_N, is calculated as shown in Equation E.10.

$$F_N = (-x_{pl} - L_{sb}) \cdot k_{sb} - \dot{x}_{pl} \cdot C_{sb} \tag{E.10}$$

where k_{sb} is the spring stiffness for the seabed, C_{sb} is the damping coefficient for the seabed and L_{sb} is the length down to the seabed. The spring stiffness is set to $k_{sb} = 4000000$

N/m and the damping coefficient is $C_{sb} = 1000000\ Ns/m$. F_N only acts if the payload is in contact with the seabed. In reality the damping and stiffness coefficient will depend on the contact area of the payload.

During winch operation, the wire rope is either payed in or out, causing variation in the mass moment of inertia and a stepwise variation of the effective drum radius due to switching between wire layers. In this study, it is assumed that each test case can be carried out on only one wire layer. The effective drum radius, r_{eff}, is therefore constant during the operation. The effective mass moment of inertia varies as a function of the mass of the wire on the drum. It is assumed that the wire is uniformly distributed around the drum. The effective mass moment of inertia is calculated as shown in Equation E.11.

$$J_{eff} = J_d + \underbrace{\frac{1}{2} \cdot m_{wd} \cdot (r_d^2 + r_{eff}^2)}_{J_{wire}} + J_m \cdot N_{gear}^2 \tag{E.11}$$

where J_d is the mass moement of inertia of the drum, m_{wd} is the mass of the wire rolled onto the drum, J_m is the mass moment of inertia of the DDM and N_{gear} is the gear ratio of the pinion and gear ring.

The combined mass, m_c, consists of the mass of the payload, m_{load}, hook, m_{hook}, and the lower wire section, m_{w2}. The combined mass is calculated as shown in Equation E.12.

$$m_c = m_{load} + m_{hook} + m_{w2} \tag{E.12}$$

The added mass, m_a, is inertia included when the load is submerged in water because the payload must move some volume of surrounding water as it moves through it. The added mass is in reality affected by the payload geometry, motion amplitude and the depth of submergence, but is normally calculated as shown in Equation E.13 [22].

$$m_a = \rho_{sea} \cdot C_A \cdot V_R \tag{E.13}$$

where C_A is the added mass coefficient and V_R is the reference volume. The added mass coefficient is set to $C_A = 0.72$ and the reference volume is $V_R = V_{pl}$ for the load considered in this work [22].

The vessel will heave due to wave motion. Ocean waves are irregular and random in shape, height, length and speed propagation. It is assumed that the vessel has a similar motion and that the heave motion can be described by the Pierson-Moskowitz wave spectrum [23]. The vessel motion is calculated using the method shown in [24]. An example of the heave motion of the vessel is shown in Figure E.4. In this figure, the significant wave height is set to $H_s = 1.3\ m$ and the typical wave period is $T_p = 9\ s$.

Equation E.4 and Equation E.5 show that the dynamics of the payload is affected by the vessel motion, but it is assumed that the motion of the payload will not affect the

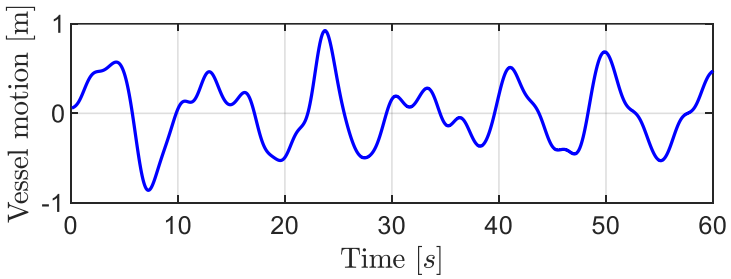

Figure E.4: Example of vessel motion described by Pierson-Moskowitz wave spectrum, $H_s = 1.3\ m$ and $T_p = 9\ s$.

motion of the vessel. This simplification is based on the following: the payload mass is much smaller then the mass of the vessel and the payload contribution to mass moment of inertia around the center of gravity is much smaller than the mass moment of inertia of the vessel.

E.2.2 Digital Displacement Winch Drive System

The digital displacement winch drive system consists of a high torque low speed DDM directly connected to a high pressure source and a low pressure source. The right side in Figure E.5 shows a schematic illustration of a 5 cylinder DDM and the left side shows the schematics of a single cylinder.

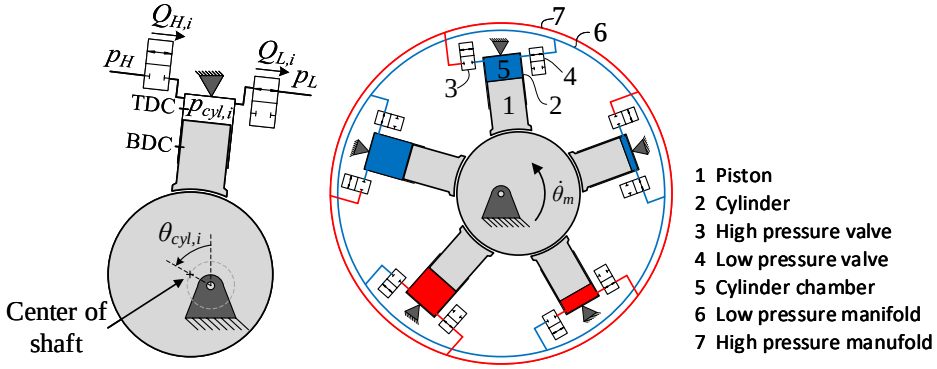

Figure E.5: Sketch of single cylinder (left side) and a 5 cylinder DDM (right side).

The output torque of the DDM is transfered to the winch drum through a pinion and gear ring. It is assumed that there are no friction losses between the pinion and the gear ring and that there is no slack. Hence, the following linear relations are applicable.

$$T_{drive} = T_m \cdot N_{gear} \tag{E.14}$$

$$\theta_m = \theta_d \cdot N_{gear} \tag{E.15}$$

where T_m is the DDM torque and θ_m is the rotational shaft position. The DDM output torque is the sum of the torque contribution from every single cylinder.

The simulation model of the DDM is based on the model described and experimental validated in [25]. For simplicity, the governing equations are derived for a single cylinder, cylinder number i, but the same procedure is used for all cylinders. The following assumptions are made for the DDM model:

- Constant pressure in the high and low pressure source.
- Valve dynamics can be described by a second order system.
- Leakage in valves and cylinders is negligible.
- Friction in the DDM is negligible.
- The combined inertia of the shaft and pistons is constant ($J_m = \text{constant}$)

The continuity equation is used to calculate the pressure dynamics in cylinder chamber i.

$$\dot{p}_{cyl,i} = \frac{\beta_{eff,i}}{V_{cyl,i}} \cdot \left(Q_{H,i} - Q_{L,i} - \dot{V}_{cyl,i} \right) \tag{E.16}$$

where $\beta_{eff,i}$ is the effective bulk modulus of the hydraulic fluid, $V_{cyl,i}$ is the cylinder volume, $Q_{H,i}$ is the volume flow through the high pressure valve and $Q_{L,i}$ is the volume flow through the low pressure valve.

The cylinder chamber volume and its rate of change are given by

$$V_{cyl,i} = V_0 + \frac{V_d}{2} \cdot (1 - \cos(\theta_{cyl,i})) \tag{E.17}$$

$$\dot{V}_{cyl,i} = \frac{V_d}{2} \cdot \sin(\theta_{cyl,i}) \cdot \dot{\theta}_m \tag{E.18}$$

where V_0 is the dead volume in the cylinder chamber, V_d is the piston displacement, $\theta_{cyl,i}$ is the local shaft position relative to the piston position, and $\dot{\theta}_m$ is the shaft speed. The dead volume is set to $V_0 = V_d$ and the piston displacement is $V_d = 260\ cc/rev$. The local shaft position is 0 rad when the piston is at top dead center. Due to phase shift between the cylinders, the local shaft position is given by

$$\theta_{cyl,i} = \theta_m + \frac{2 \cdot \pi}{N_c} \cdot (i - 1) \qquad i \in \{1..N_c\} \tag{E.19}$$

where $N_c = 42$ and is the number of cylinders.

The volume flows through the valves, $Q_{H,i}$ and $Q_{L,i}$, are described by the orifice equation as shown below.

$$Q_{H,i} = \frac{u_{H,i}}{k_f} \cdot \sqrt{|p_H - p_{cyl,i}|} \cdot sign(p_H - p_{cyl,i}) \tag{E.20}$$

$$Q_{L,i} = \frac{u_{L,i}}{k_f} \cdot \sqrt{|p_{cyl,i} - p_L|} \cdot sign(p_{cyl,i} - p_L) \tag{E.21}$$

where $u_{H,i}$ is the opening ratio of the high pressure valve, $u_{L,i}$ is the opening ratio of the low pressure valve and k_f is the flow pressure coefficient. The opening ratios of the valves

range from 0 to 1, where 0 corresponds to fully closed and 1 to fully open. The transition time of the valves is $T_s = 5\ ms$.

The opening ratios of the valves are described by second order systems,

$$\ddot{u}_{H,i} = u_{conH,i} \cdot \omega^2 - u_{H,i} \cdot \omega^2 - 2 \cdot \zeta \cdot \omega \cdot \dot{u}_{H,i} \tag{E.22}$$

$$\ddot{u}_{L,i} = u_{conL,i} \cdot \omega^2 - u_{L,i} \cdot \omega^2 - 2 \cdot \zeta \cdot \omega \cdot \dot{u}_{L,i} \tag{E.23}$$

where $u_{conH,i}$ is the desired position for the high pressure valve, $u_{conL,i}$ is the desired position for the low pressure valve, ω is the natural frequency of the valves and ζ is the damping ratio. The desired valve positions are either 0 or 1 and are given by the chosen displacement strategy. The displacement strategy is described in Section E.3.1.

The pressure dependent bulk modulus is calculated according to [26] as shown below.

$$\beta_{eff,i} = \frac{1}{\frac{1}{\beta_L} + \frac{\epsilon_g}{p_{cyl,i}^{(abs)}}} \tag{E.24}$$

where β_L is the bulk modulus of the hydraulic liquid and ϵ_g is the volume fraction of undissolved gas. The volume fraction of undissolved gas is calculated by

$$\epsilon_g = \frac{1.0}{\left(\frac{1.0-\epsilon_{g0}}{\epsilon_{g0}}\right) \cdot \left(\frac{p_{atm}^{(abs)}}{p_{cyl,i}^{(abs)}}\right)^{-\frac{1}{\kappa}} + 1.0} \tag{E.25}$$

where ϵ_{g0} is the volume fraction of undissolved gas at atmospheric pressure, $p_{atm}^{(abs)}$ is the atmospheric pressure and κ is the specific heat ratio. The volume fraction of undissolved gas at atmospheric pressure is set to $\epsilon_{g0} = 0.01$ and the specific heat ratio is $\kappa = 1.4$.

Finally, the torque contribution from cylinder i is calculated as shown in Equation E.26 and the total motor torque is the sum of the torque contribution from every single cylinder and calculated in Equation E.27.

$$T_{cyl,i} = \frac{V_d}{2} \cdot \sin(\theta_{cyl,i}) \cdot p_{cyl,i} \tag{E.26}$$

$$T_m = \sum_{i=1}^{N_c} T_{cyl,i} \tag{E.27}$$

E.3 CONTROL DESIGN

The controller is designed to facilitate operation by joystick, operation with AHC system and operation with CT system. The designed controller is shown in Figure E.6. The controller consists of a motion controller (D_{motion}) and a wire tension controller ($D_{tension}$). The motion controller is a PID controller with drum position feedback. When operating without AHC, the reference position is created by moving the joystick. When operating

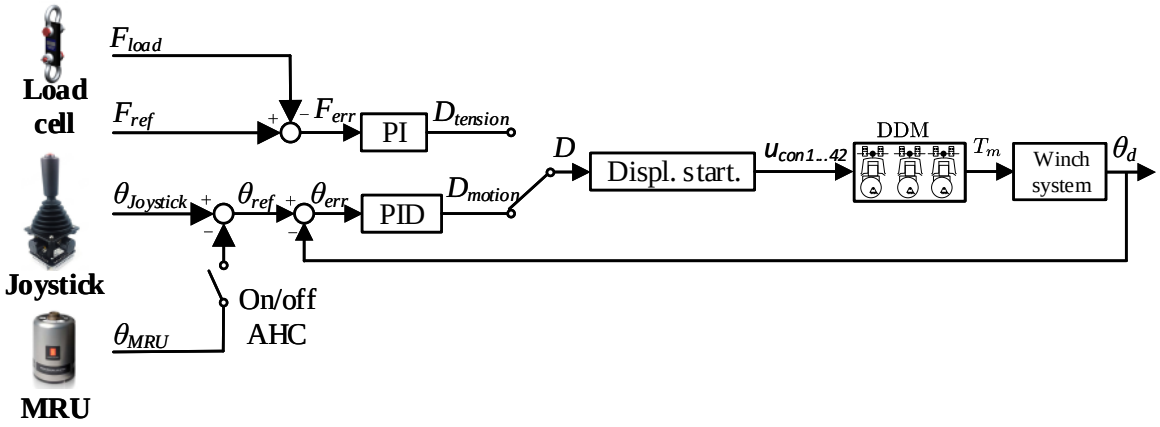

Figure E.6: Principal block diagram for winch controller.

with AHC, the vessel motion is subtracted from the joystick signal in order to decouple the vessel motion from the payload motion. The motion controller gains are $k_{p,m} = 50$, $k_{i,m} = 100$ and $k_{d,m} = 5$. The wire tension controller is a PI controller with wire tension feedback. The wire tension controller is enabled in CT mode. The controller gains are $k_{p,t} = 0.0001$ and $k_{i,t} = 0.001$.

The desired displacement, D, is transformed into valve control signals by a displacement strategy. Different displacement strategies have different characteristics, like energy efficiency characteristics, transient response characteristics and steady-state response characteristics [25, 27]. Therefore, the displacement strategy should be designed or chosen based on the desired features of the driven application. An offshore winch system is known to operate at low speeds, with frequent start and stop and frequently change direction of rotation. Based on the work presented in [25] it is found that partial stroke displacement strategy is a good choice for winch operations due to its high controllability at low speeds. The chosen displacement strategy is referred to as partial stroke displacement strategy version 2 in [25].

E.3.1 Partial stroke displacement strategy

This section describes the operation principle of partial stroke displacement strategy based on operation in the first quadrant, hence positive load and positive speed. In partial stroke displacement strategy, the cylinders are only activated in a portion of the down stroke piston motion. The term "active" means that the cylinder is connected to the high pressure source and contributes with a positive output torque. The displacement is changed by increasing or decreasing the active part. Figure E.7 shows the schematics of the valve actuation sequence for one cylinder. Note that the cylinder is able to be reactivated if the displacement reference is increased. Plot 1 shows the piston position, Plot 2 shows the opening ratios of the valves, Plot 3 shows the chamber pressure, Plot

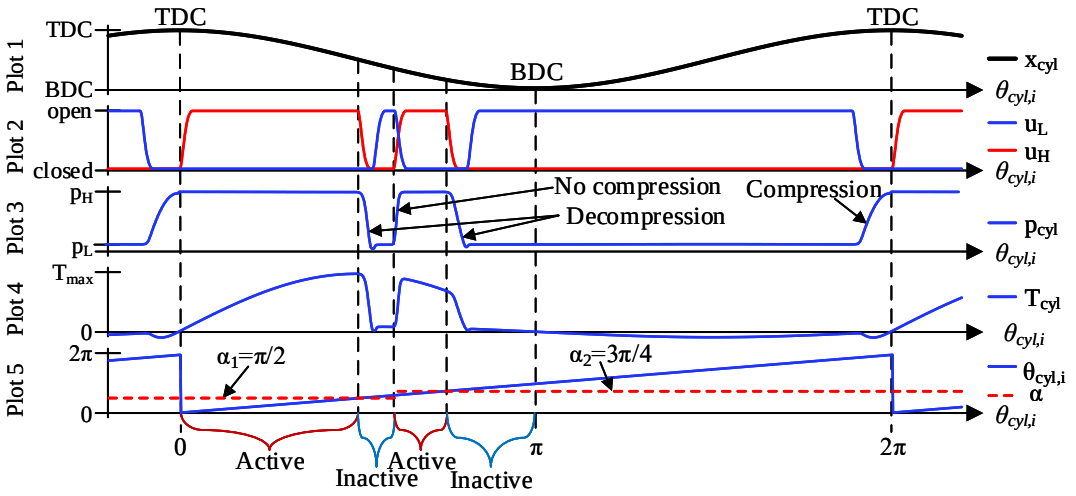

Figure E.7: Principal valve timing schematics for partial stroke displacement strategy.

4 shows the cylinder torque and Plot 5 shows the local shaft position ranging from 0 to 2π *rad*. The red dotted line in Plot 5 shows the state change angle or the control angle α. The control angle, α, describes at which local shaft position, $\theta_{cyl,i}$, the cylinder shall change state from active to inactive. If $\theta_{cyl,i} \leq \alpha$ the cylinder is active, else the cylinder is inactive.

For the illustrated situation shown in Figure E.7, the state change angle is first set to $\alpha_1 = \pi/2$. When $\theta_{cyl,i} = \alpha_1$, the cylinder is deactivated. After a short period of time, the state change angle is stepped up to $\alpha_2 = 3\pi/4$. Since the local cylinder angle is smaller then the new state change angle, $\theta_{cyl,i} < \alpha_2$, the cylinder is reactivated in the remaining shaft rotation up to $\theta_{cyl,i} = \alpha_2$.

The state change angle, α, is calculated based on the desired displacement ratio, D. Where D is defined as the displaced volume during the active period divided by the maximum piston displacement [27]. Based on the calculation of the cylinder chamber volume shown in Equation E.17, the displacement ratio is calculated by:

$$D = \frac{V_{cyl}(\alpha)}{V_{cyl}(\pi)} = \frac{1}{2} \cdot (1 - \cos(\alpha)) \tag{E.28}$$

where $V_{cyl}(\alpha)$ is the intake volume during the active period and $V_{cyl}(\pi)$ is the maximum intake volume. The state change angle is calculated by rearranging Equation E.28.

$$\alpha = \cos^{-1}(1 - 2 \cdot D) \tag{E.29}$$

E.3.2 Four Quadrant Operation

Winch operation requires an actuation system that is able to operate in all four quadrants, see Figure E.8. The green arrow shows the direction of the shaft speed and the red arrow shows the direction of the load.

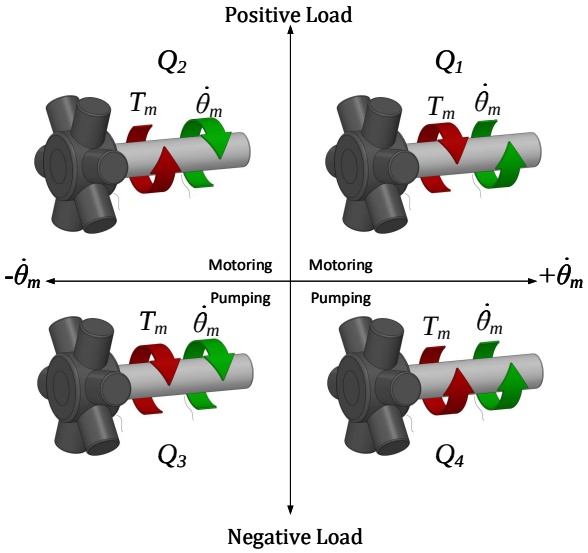

Figure E.8: Four quadrant operation

In partial stroke displacement strategy, the valve timing strategy shown in Figure E.7 is only valid for operation in quadrant 1. Each quadrant require a unique valve timing strategy. Figure E.9 shows a simplified schematic of the valve timing strategy for all four quadrants. The top graph shows the piston position and the next four graphs shows

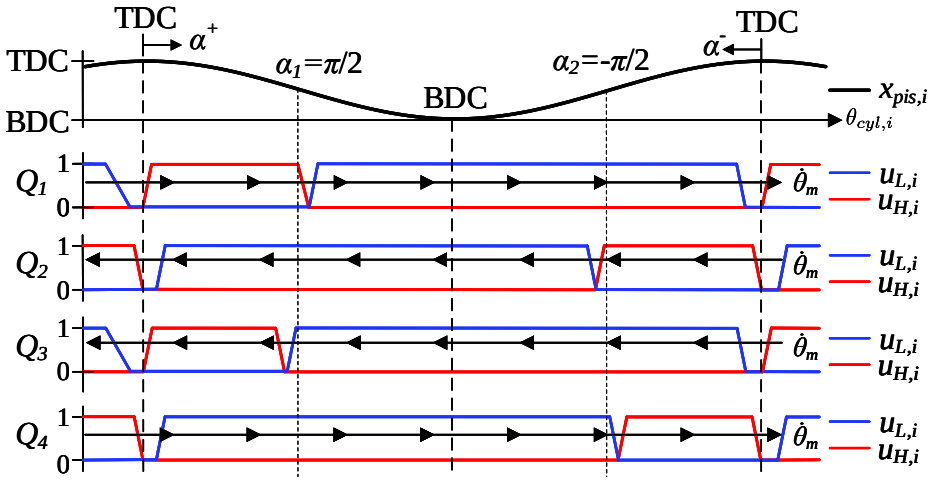

Figure E.9: Principal valve timing schematics for four quadrant operation.

the valve timing sequence for operation in quadrant 1 to 4 respectively. The red line is the opening ratio of the high pressure valve and the blue line is the opening ratio of the low pressure valve. The black line with arrows shows the direction of rotation. Arrows pointing to the right indicates positive direction and arrows pointing to the left indicates negative direction of rotation. Note that in quadrant 1 and quadrant 3, α_1 is used to switch cylinder state and in quadrant 2 and quadrant 4, α_2 is used to switch cylinder state.

The schematic of the motor controller is shown in Figure E.10. The input signal is the

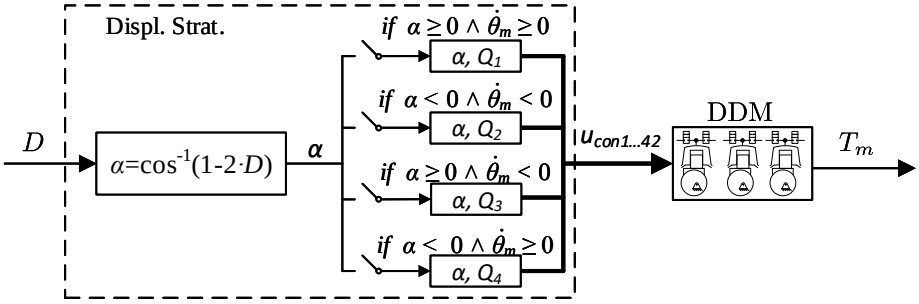

Figure E.10: Principal block diagram for motor controller.

desired displacement ratio, D, and the output is the motor torque, T_m. The state change angle, α, is calculated based on the desired displacement fraction by using Equation E.29. The valve timing strategy, Q_j, is selected by a switching controller. Based on given conditions, the proper valve timing strategy is selected. The given conditions are shown in Equation E.30.

$$Q = \begin{cases} Q_1 & if \quad \alpha \geq 0 \quad \wedge \quad \dot{\theta}_m \geq 0 \\ Q_2 & if \quad \alpha < 0 \quad \wedge \quad \dot{\theta}_m < 0 \\ Q_3 & if \quad \alpha \geq 0 \quad \wedge \quad \dot{\theta}_m < 0 \\ Q_4 & if \quad \alpha < 0 \quad \wedge \quad \dot{\theta}_m \geq 0 \end{cases} \tag{E.30}$$

where $\dot{\theta}_m$ is the motor shaft speed.

E.4 SIMULATION RESULTS

Subsea lifting operations can normally be divided into three main operations: deployment, recovery, and relocation of payloads on the seabed [28]. Each of these lifting operations can be further broken down to phases or steps. The most critical steps are:

- Landing or lift-off from deck.
- Entering or exiting the splash zone.
- Landing or lift-off from the seabed.

During landing and lift-off from the deck and crossing the splash zone, the winch is normally operated by a skilled operator without the use of any additional operation modes. During landing and lift-off from the seabed, the winch operator can use CT or AHC to ease the operation. Therefore, both motion control and wire tension control is important. In order to test the motion controller and tension controller, three test cases are designed.

For the first and second test case, it is assumed that the vessel heaves up and down due to the waves with a typical wave hight of $H_s = 1.3\ m$ and a typical wave period of $T_p = 9\ s$. The first test case simulates a landing sequence at the seabed when using AHC. The purpose is to test motion tracking performance at deep waters. A landing

situation is chosen in order to test the motion tracking performance with heavy and light payloads. Heavy payloads are tested before landing and light payloads are tested after landing. The weight of the payload is set to max SWL. The landing speed should be $< 0.15\ m/s$ and the maximum variation in payload position should be $< 5\ cm$ when AHC system is activated.

The second test case simulates a landing sequence on the seabed by using CT. The purpose is to test the wire tension control performance. A landing situation is chosen in order to test wire tension control at high tension and low tension. High tension is tested before landing and low tension is tested after landing. The weight of the payload is set to max SWL. The preset value of the tension is set slightly below the weight of the payload in water. The compensation error for the CT system should be < 5 % of maximum SWL and the impact force during landing must be low.

The third test case simulates a lifting operation where the payload is lifted in the air. During the lifting operation, external forces are applied to the payload in order to test the resistance to external force disturbance. In a real lifting operation, external forces can typically occur during water exit or water entry. This test case should be tested both with a payload mass equal to 75 % of max SWL and equal to 10 % of max SWL in order to test motion tracking performance of heavy and light payloads. The external force is set to 50 % of the force needed to hold the payload at rest and is applied as a step. The vessel motion is set to zero.

E.4.1 Test Case 1: Landing on the seabed with AHC

Figure E.11 shows the simulation results of landing a 20000 kg payload at the seabed by using AHC. The water depth is set to 1000 m. Plot 1 shows the drum position and the reference position, Plot 2 shows the tracking error, Plot 3 shows the payload position, Plot 4 shows the payload speed and Plot 5 shows the lower wire force, F_{w2}, and the seabed interaction force, F_N. Note that in Plot 2, the tracking error, $\theta_{err} = \theta_{ref} - \theta_d$, is multiplied with the effective radius, r_{eff}, to convert the error from rotation to translation. This conversion is done to get a better understanding of the magnitude of the error.

In the first 10 s the AHC is deactivated, the drum position is kept constant and the payload moves due to vessel motion. After 10 s, the AHC is activated, the winch drum starts to compensate for the vessel motion and the payload stabilizes at a constant depth with a variation of $\pm 1\ cm$. This results is better than the requirements of 5 cm, but may not be correct. In the simulation model, the slack between the pinion and the gear ring is not included. Including slack may increase the payload motion. In addition, it is assumed that the MRU can measure the exact motion of the vessel in real time. In reality, the measured vessel motion is not exactly equal the real vessel motion.

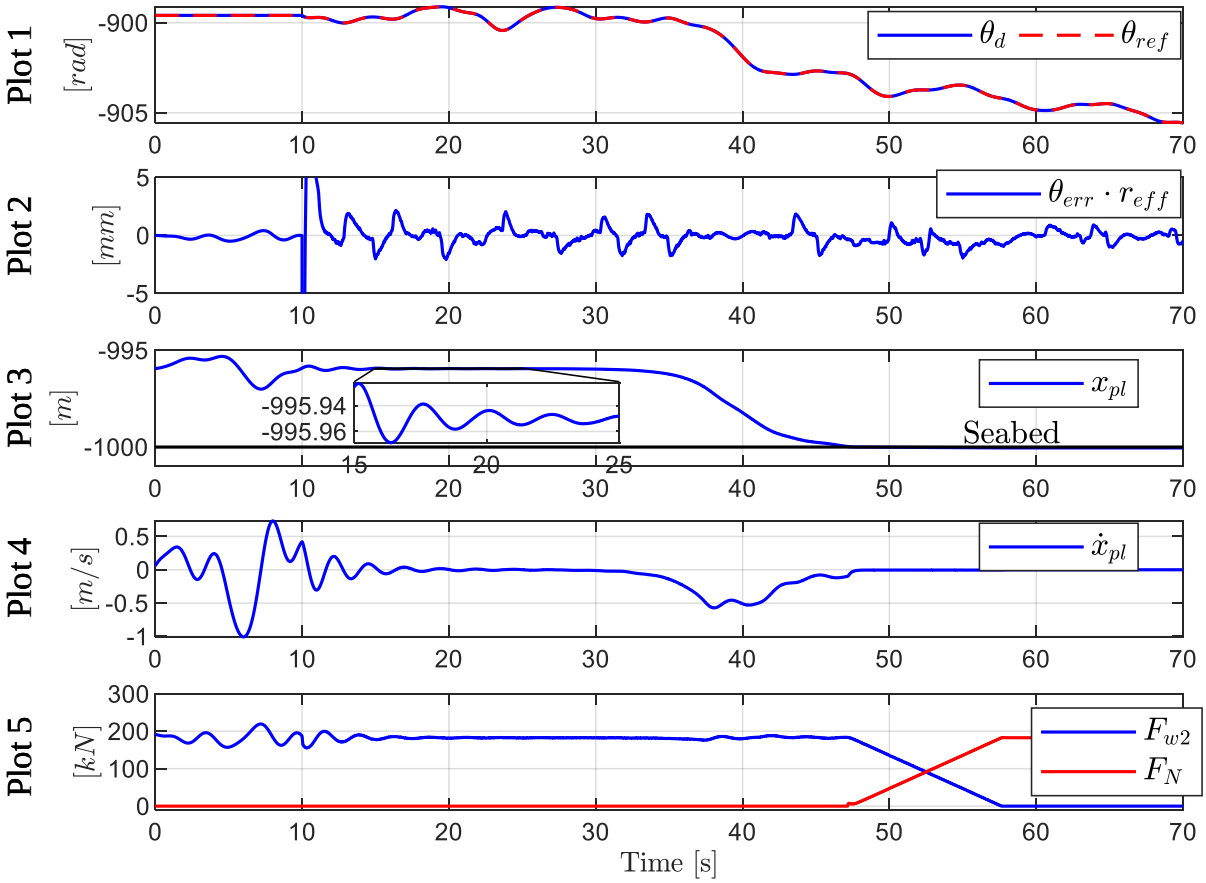

Figure E.11: Simulation result test case 1.

After 25 s, the lowering of the payload starts. The payload touches the seabed after approximately 47 s and at approximately 0.1 m/s, resulting in low impact forces and a slow reduction of the wire tension. The wire is fully un-tensioned after 58 s. The position error of the drum is kept within ± 3 mm except when turning on the AHC system. This peak occurs due to a step in the reference signal and can be avoided by including a more gentle start of the AHC mode. However, the simulation results show high tracking performance.

E.4.2 Test Case 2: Landing on the seabed with CT

Figure E.12 shows the simulation results of landing a 20000 kg payload at the seabed by using CT mode. The desired tension F_{ref} is set to 99.5 % of the payload's weight in water. Plot 1 shows the lower wire force, F_{w2}, the desired wire tension, F_{ref}, and the seabed interaction force, F_N, Plot 2 shows the tracking error, Plot 3 shows the drum position, Plot 4 shows the payload position and Plot 5 shows the payload velocity.

The result shows that the tracking error is kept below 1 kN. This force corresponds to an error of approximately 0.5 % of max SWL and is within the requirements of 5 %. The payload is landed after 17 s at a speed of approximately 0.5 m/s. This is a relatively

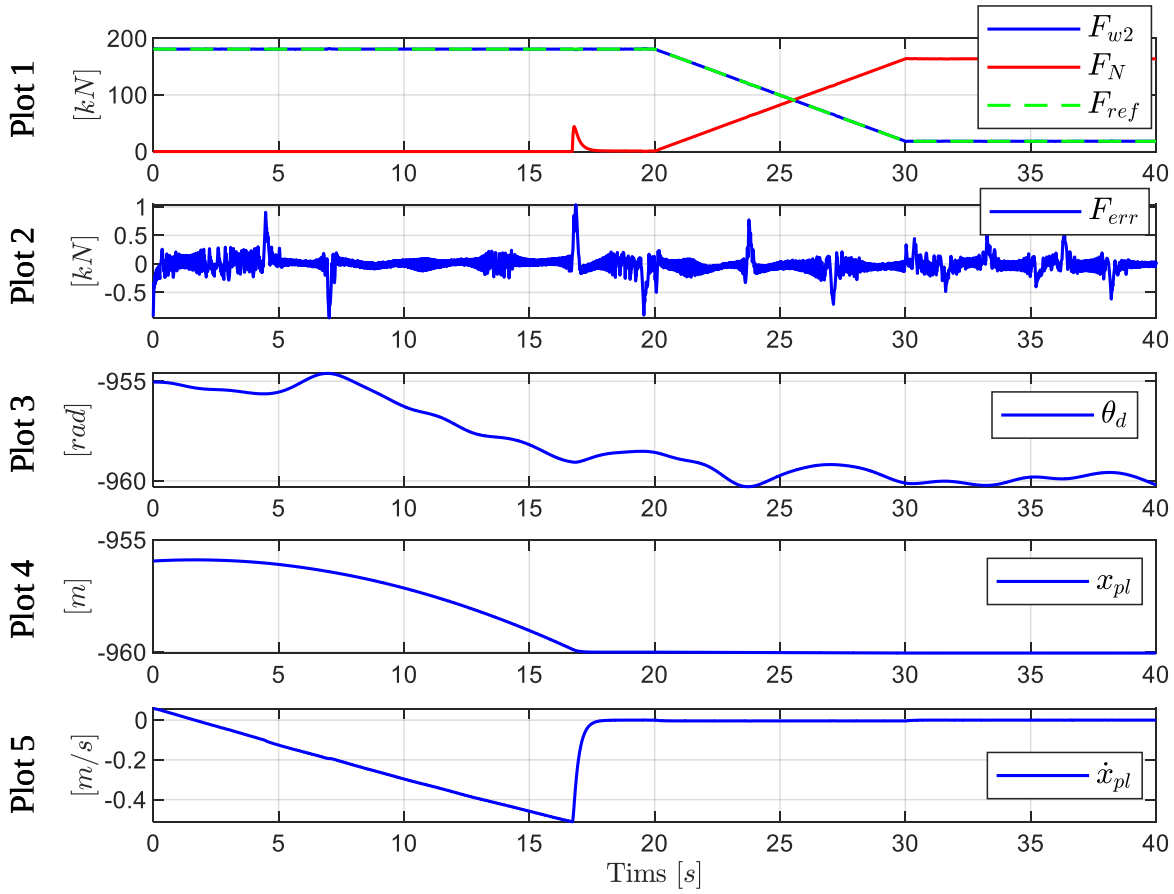

Figure E.12: Simulation result test case 2.

high speed, but the impact force is relatively low, see the peak in the red line in Plot 1, because most of the payload's weight is held by the winch. After 20 s, the wire tension is slowly reduced.

E.4.3 Test case 3: Motion control at deck with external force disturbance

In this test case, the vessel motion is set to zero and the payload is lifted in the air and exposed to external forces. The lifting operation is tested both with a heavy payload, $m_{load} = 15000\ kg$, and a light payload, $m_{load} = 1000\ kg$. The simulation results for the heavy payload is shown in Figure E.13 and for the light payload in Figure E.14.

The external force is set to $F_{ext} = 0.5 \cdot m_{load} \cdot g$. Plot 1 shows the drum position and the reference position, Plot 2 shows the tracking error, Plot 3 shows the payload position, Plot 4 shows the payload velocity and Plot 5 shows the lower wire force, F_{w2}, and the external force, F_{ext}.

The results show that the tracking error is close to 0 mm when operating with constant speed. When applying an external force, the tracking error gets a peak. However, after

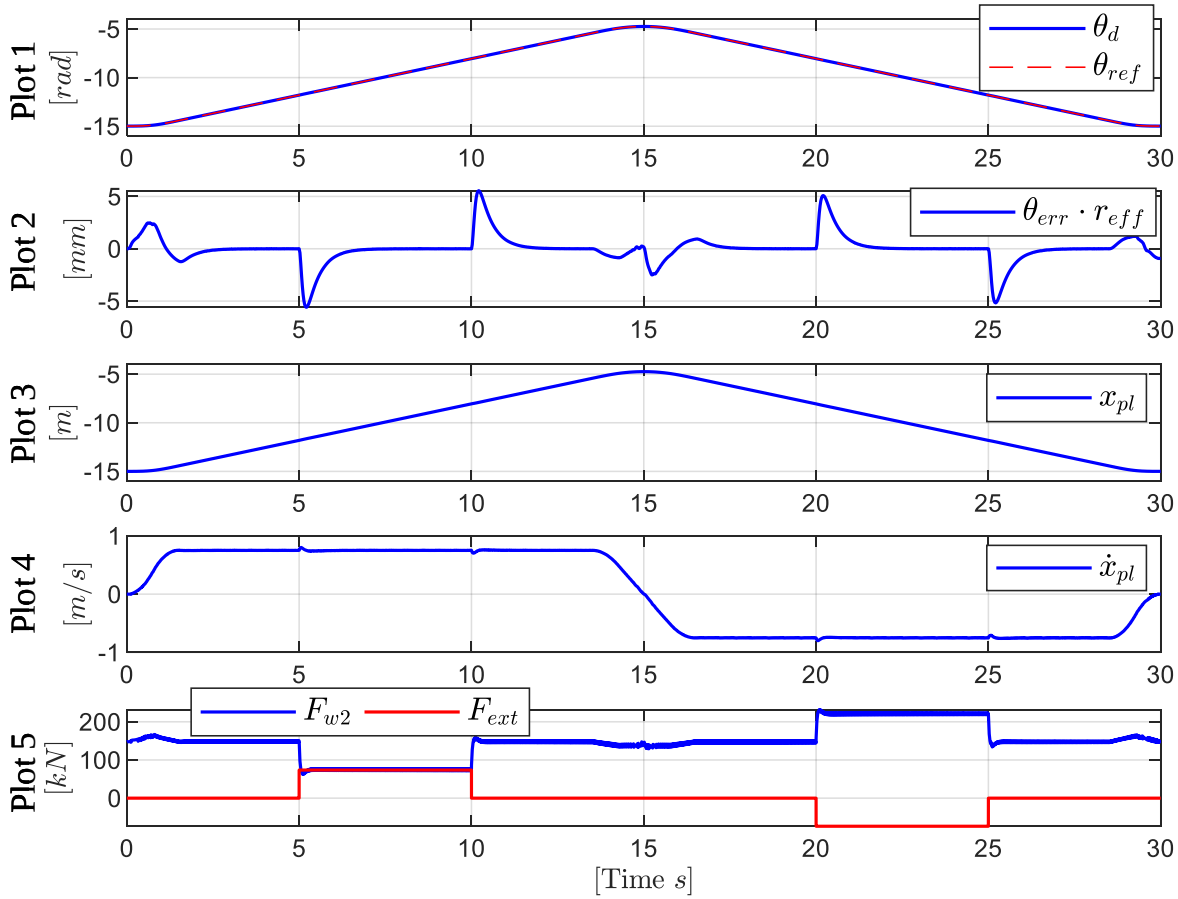

Figure E.13: Simulation result test case 3 with $m_{load} = 15000\ kg$.

a short time, the error approaches 0 mm again. The peak is bigger when handling high loads. This is because the external force depends on the weight of the payload and is bigger when handling heavier payloads. There are also oscillations in the position error when accelerating and when passing through 0 rpm. Overall, the motion tracking performance is good, also when applying external forces.

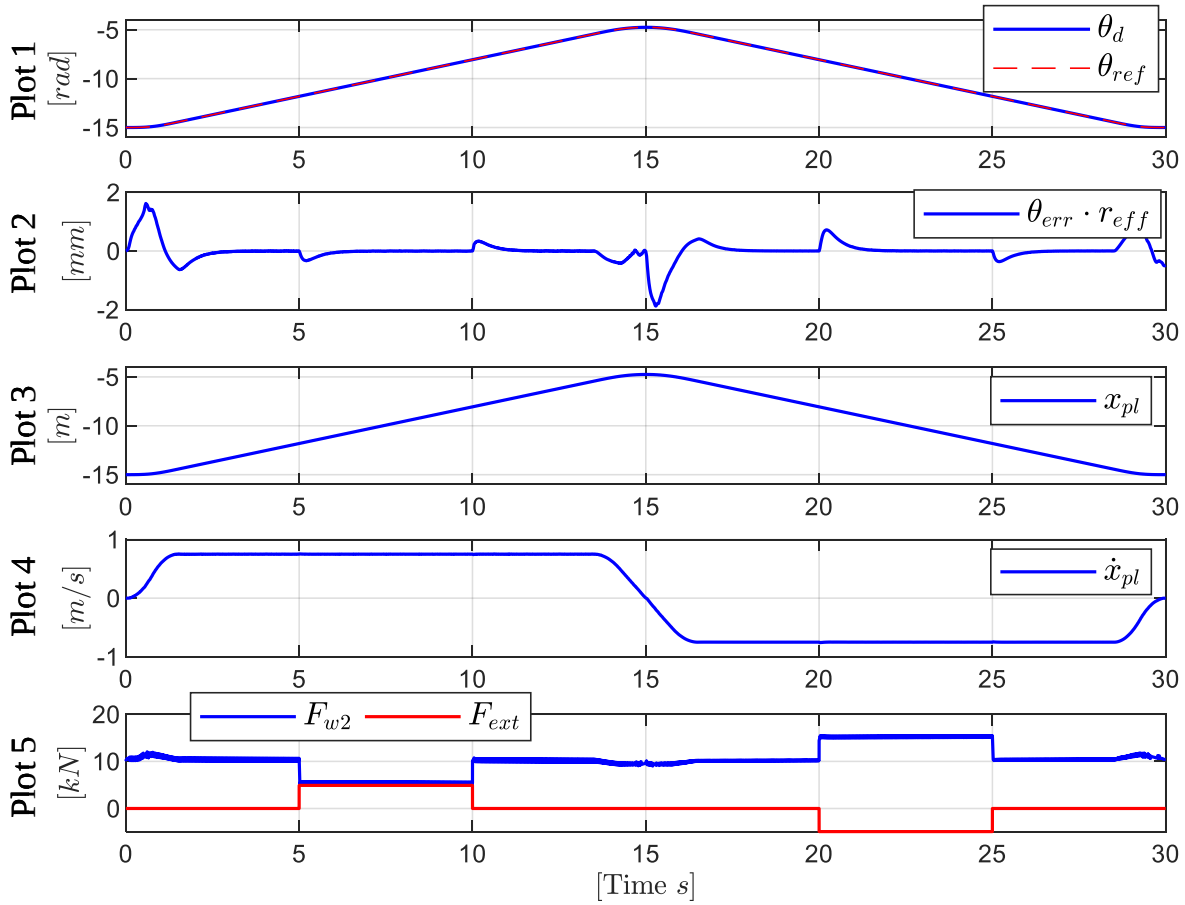

Figure E.14: Simulation result test case 3 with $m_{load} = 1000\ kg$.

E.5 CONCLUSION

This paper presents a digital displacement winch drive system. The digital displacement winch drive system consists of a high torque low speed digital displacement motor directly connected to the winch drum through a pinion and gear ring. Subsea lifting operations are challenging due to heave motion of the vessel and requires a highly skilled operator. Lift-off and landing at the deck, crossing the splash zone and lift-off and landing on the seabed are all challenging operations and require a winch with high motion tracking performance and wire tension tracking performance. When the AHC system is active, the variation in payload position should be below 5 *cm* and when the CT system is active the wire tension error should be below 5% of max SWL. The presented requirements are based on inputs from offshore winch manufacturers and the performance of systems used today.

Three different test cases have been used to evaluate the performance of the digital displacement winch drive system. The simulation results show that the proposed winch drive system can operate with high controllability. The presented simulation model and the test cases will in the future be used to test new controllers.

Acknowledgment

The research presented in this paper has received funding from the Norwegian Research Council, SFI Offshore Mechatronics, project number 237896.

Bibliography

[1] Win Rampen. The development of digital displacement technology. In *Proceedings of Bath/ASME FPMC Symposium*, 2010.

[2] Md Ehsan, WHS Rampen, and SH Salter. Modeling of digital-displacement pump-motors and their application as hydraulic drives for nonuniform loads. *Journal of dynamic systems, measurement, and control*, 122(1):210–215, 2000.

[3] Grégory S Payne, Uwe BP Stein, Mohammad Ehsan, Niall J Caldwell, and WHS Rampen. Potential of digital displacement hydraulics for wave energy conversion. In *Proceedings of the sixth European wave and tidal energy conference, Glasgow*, 2005.

[4] Win Rampen. Gearless transmissions of large wind turbines-the history and future of hydraulic drives. *Artemis IP Ltd., Midlothian, UK*, 2006.

[5] Excavator development program. url:http://artemis.armadillojam.co.uk/hybrid-hydraulic-excavator/. Accessed: 25-05-2018.

[6] M Karvonen, M Heikkilä, M Huova, M Linjama, and K Huhtala. Simulation study-improving efficiency in mobile boom by using digital hydraulic power management system. In *Proceedings of the Twelfth Scandinavian International Conference on Fluid Power*, pages 355–368, 2011.

[7] Karl-Erik Rydberg. Energy efficient hydraulic hybrid drives. In *11: th Scandinavian International Conference on Fluid Power, SICFP'09, June 2-4, Linköping, Sweden*, 2009.

[8] Jamie Taylor, Win Rampen, Daniel Abrahams, and Andrew Latham. Demonstration of a digital displacement hydraulic hybrid bus. In *Proc. 2015 JSAE Annual Congress*. Yokohama, 2015.

[9] Saving fuel in rail vehicles. url:http://www.artemisip.com/saving-fuel-in-rail-vehicles/. Accessed: 25-05-2018.

[10] GS Payne, AE Kiprakis, M Ehsan, W H S Rampen, JP Chick, and AR Wallace. Efficiency and dynamic performance of digital displacement^{TM} hydraulic transmission in tidal current energy converters. *Proceedings of the Institution of Mechanical Engineers, Part A: Journal of Power and Energy*, 221(2):207–218, 2007.

[11] Capturing the massive power generated by waves. url:http://www.artemisip.com/sectors/wave/. Accessed: 25-05-2018.

[12] Masahide Umaya, Toshihide Noguchi, Michiya Uchida, Masaaki Shibata, Yasuhiro Kawai, and Ryosuke Notomi. Wind power generation-development status of offshore wind turbines. *Mitsubishi Heavy Industries Technical Review*, 50(3):29, 2013.

[13] Henrik B Larsen, Magnus Kjelland, Anders Holland, and Per N Lindholdt. Digital hydraulic winch drives. In *ASME/BATH 2018 Symposium on Fluid Power and Motion Control*. American Society of Mechanical Engineers, 2018.

[14] Offshore cranes. url: https://www.macgregor.com/Products-solutions/products/offshore-and-subsea-load-handling/offshore-cranes/. Accessed: 2018-10-04.

[15] Magnus B Kjelland and Michael R Hansen. Offshore wind payload transfer using flexible mobile crane. 2015.

[16] Peter Gu, Ahmed Ahmed Walid, Yousef Iskandarani, and Hamid Reza Karimi. Modeling, simulation and design optimization of a hoisting rig active heave compensation system. *International Journal of Machine Learning and Cybernetics*, 4(2):85–98, 2013.

[17] Zhou Entao and Yang Wenlin. Research on the motion tracking feed forward control of hydraulic winch. In *Proceedings of the International Conference on Computer Engineering and Applications*, pages 440–443. IACSIT, 2009.

[18] Stian Skjong and Eilif Pedersen. Model-based control designs for offshore hydraulic winch systems. *Ocean Engineering*, 121:224–238, 2016.

[19] Zhou Entao, Yang Wenlin, and Lin Junzhe. Predictive control of hydraulic winch motion control. In *2009 2nd IEEE International Conference on Computer Science and Information Technology*, pages 1–4. IEEE, 2009.

[20] QingHui Yuan. Actively damped heave compensation (adhc) system. In *Proceedings of the 2010 American Control Conference*, pages 1544–1549. IEEE, 2010.

[21] Tor A Johansen, Thor I Fossen, Svein I Sagatun, and Finn G Nielsen. Wave synchronizing crane control during water entry in offshore moonpool operations-experimental results. *IEEE Journal of Oceanic Engineering*, 28(4):720–728, 2003.

[22] DNV GL. *DNVGL-RP-N103 Modelling and analysis of marine operation*, 7 2017.

[23] Willard J Pierson and Lionel Moskowitz. A proposed spectral form for fully developed wind seas based on the similarity theory of sa kitaigorodskii. *Journal of geophysical research*, 69(24):5181–5190, 1964.

[24] Sondre Sanden Tordal, Per-Ove Løvsland, and Geir Hovland. Testing of wireless sensor performance in vessel-to-vessel motion compensation. In *IECON 2016-42nd Annual Conference of the IEEE Industrial Electronics Society*, pages 654–659. IEEE, 2016.

[25] Sondre Nordås, Michael M Beck, Morten K Ebbesen, and Torben O Andersen. Dynamic response of a digital displacement motor operating with various displacement strategies. *Energies*, 12(9):1737, 2019.

[26] Michael Rygaard Hansen. In Compendium *Fluid Mechanics*. Department of Engineering, University of Agder, Norway, Lecture notes MAS126, 2015; pp. 28–30.

[27] Niels Henrik Pedersen, Per Johansen, and Torben Ole Andersen. Challenges with respect to control of digital displacement hydraulic units. 2018.

[28] DNV GL. *DNVGL-RP-N201 Lifting Appliances used in subsea operations*, 6 2017.

Paper F

Control of a Digital Displacement Winch Drive System

Sondre Nordås, Morten Kjeld Ebbesen and Torben Ole Andersen

This paper has been published as:

S. Nordås, M. K. Ebbesen, and T. O. Andersen. Control of a Digital Displacement Winch Drive System. Submitted to *Modeling, Identification and Control*, December 5, 2019

Control of a Digital Displacement Winch Drive System

Sondre Nordås*, Morten Kjeld Ebbesen* and Torben Ole Andersen**

*University of Agder
Faculty of Engineering and Science
Jon Lilletunsvei 9, 4879 Grimstad, Norway

** Aalborg University
Faculty of Engineering and Science
Pontoppidanstræde 101, 9220 Aalborg East, Denmark

Abstract **– Conventional hydraulic winch drive systems are known to suffer from low energy efficiency when operating at partial loads. In recent years, a new pump and motor technology have experienced increased interest due to their potential of achieving high energy efficiency in a wide range of operation conditions. This new technology is called digital displacement machine technology. Nowadays, there is a desire from the offshore oil and gas industry to use this digital displacement machine technology to design high efficient hydraulic winch drive systems. One part of the work needed to realize a digital displacement winch drive system is to design a controller and show that the digital winch drive system meets the required controllability. This paper aims to examine three different controllers. The first controller is called the base controller and is a PD controller with feedback linearization. The second controller is a sliding mode controller and the third controller is an adaptive controller. The first part of this paper presents the digital displacement winch drive system and the nonlinear simulation model. The digital displacement winch drive system consists of a secondary controlled digital displacement motor that is directly connected to the winch drum through a pinion and gear ring. The second part of the paper presents the controllers and the simulation results. In the end, the simulation results are discussed with respect to performance, robustness and implementation challenges.**

F.1 INTRODUCTION

In recent years, the interest for digital displacement machines has increased due to their promising results regarding energy efficiency and flexibility. In a piston type digital dis-

placement machine, each cylinder chamber is connected to two fast switching on/off valves. The on/off valves connect the cylinder chamber to either the high or low pressure source. A chamber connected to high pressure is referred to as an active chamber and a chamber connected to low pressure is referred to as an inactive or deactivated chamber. By controlling the on/off valves, each cylinder chamber can be controlled individually. The output of the digital displacement machine is controlled by controlling the activation sequence of the cylinder chambers. Different activation sequences, also called displacement strategies, can be used to achieve the same displacement. With proper valve timing, the efficiency remains high even at low displacements [1], and the individual cylinder control makes the machine flexible and suited for novel system design options, like the digital hydraulic power management system [2, 3]. Detailed information regarding the digital displacement machine technology can be found in several publications [4, 5, 6, 7, 8].

The digital displacement technology has been proposed to be used in various applications like on- and off-road vehicles and in large power take-off systems in the renewable energy industry [6, 9, 10, 11, 12, 13, 14]. Lately, the digital displacement technology has also been proposed by Diinef AS to be used to drive large winches in offshore and maritime applications [15].

A hydraulic winch is normally driven by one or multiple high speed motors connected to the winch drum through a gearbox, pinion and a gear ring mounted on the drum. Figure F.1 shows an example of a hydraulic winch with 12 hydraulic motors mounted on a subsea crane.

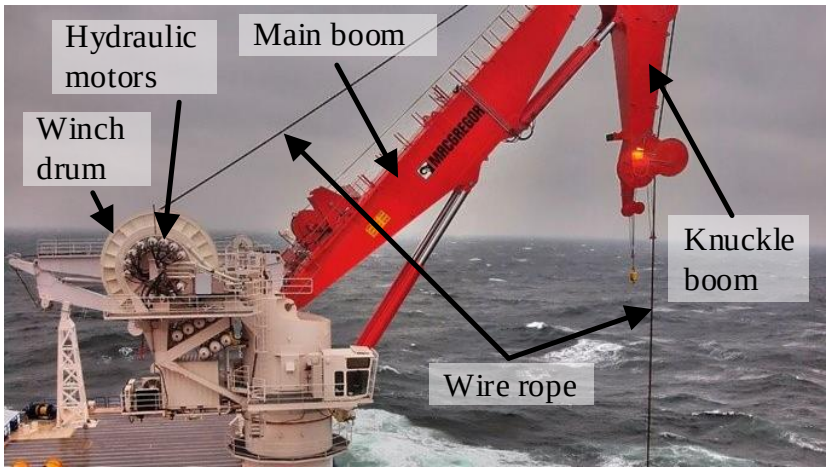

Figure F.1: Offshore crane with hydraulic winch [16].

The winch is normally controlled by a human operator that operates a joystick. In harsh weather, the vessel will heave up and down and make lifting operations, like for example deployment, recovery and relocation of payloads on the seabed, challenging. Additional systems like active heave compensation (AHC) is normally implemented in order to ease the lifting operation. The AHC system is used to decouple the payload's

motion from the vertical vessel motion. This means that the operator can use the joystick to control the payload's motion relative to a fixed surface, for example the seabed. The AHC system normally utilizes a motion reference unit to measure the vessel motion and actively operates the winch drum to counteract the measured movement.

Multiple controllers for hydraulic winch drive systems have been proposed in the literature. The proposed controllers are often limited to use in open circuit systems. In [17], the authors presented a combination of a position feedback and velocity feedforward AHC controller for an open circuit winch drive system. In [18], the authors proposed a cascade controller to improve motion tracking performance of an open circuit system. The cascade controller used a PI controller in the inner velocity loop and a P controller in the outer position loop. The nonlinearities in conventional open circuit winch drive systems reduce the tracking performance for linear controllers. Several nonlinear controllers have been proposed to improve the tracking performance. Examples are: model predictive controller [19], sliding mode controller [20, 21] and adaptive controller [22]. Other approaches to increase the heave compensation performance are to use measurements of the wave amplitude as a feed forward compensator within the AHC system [23] or to predict the heave motion and use this prediction as a part of the control strategy for the AHC system [24, 25].

The aim of this paper is to design and examine the performance of three controllers for a secondary controlled digital displacement winch drive system. The control of digital displacement machines is complicated and non-conventional. Each cylinder is activated and deactivated resulting in a non-continuous output signal. Also, multiple displacement strategies can be used to achieve the same displacement. Each displacement strategy has its dynamic response characteristics and energy efficiency characteristics. The dynamic response characteristics of the drive system are highly relevant when designing control systems. Therefore, in addition to the conventional classical controller, also a suitable displacement strategy must be designed. Designing controllers for digital displacement machines is therefore more complex than designing controllers for conventional hydraulic machines.

In [26], the authors examined the steady state and transient response characteristics of various displacement strategies and in [27], the authors revealed control challenges related to operations with various displacement strategies. In [28], the author developed models that can be used for model based design of digital displacement machines. These models include continuous [29], discrete [30, 31] and hybrid model approximation [32, 33]. The choice of model approximation depends on the used displacement strategy.

In this project, one version of the partial stroke displacement strategy is used to control the displacement of the digital displacement machine. The digital displacement

winch drive system and its nonlinear simulation model are described in Section F.2. The chosen displacement strategy is described in detail in Section F.3. Section F.4 presents a simplified model of the winch system that is used to design the controllers as shown in Section F.5. Section F.6 presents the simulation results when the designed controllers are tested on the non-linear simulation model presented in Section F.2. At the end of this paper, the results are discussed.

F.2 Digital Displacement Winch Drive System

The digital displacement winch drive system consists of a digital displacement pump (DDP) directly connected to a digital displacement motor (DDM) without any throttling valves, in a so called secondary control system. Figure F.2 shows a schematic illustration of the proposed winch drive system. The stepped arrows on the pump and motor symbol indicates that the pump and motor is a digital displacement unit.

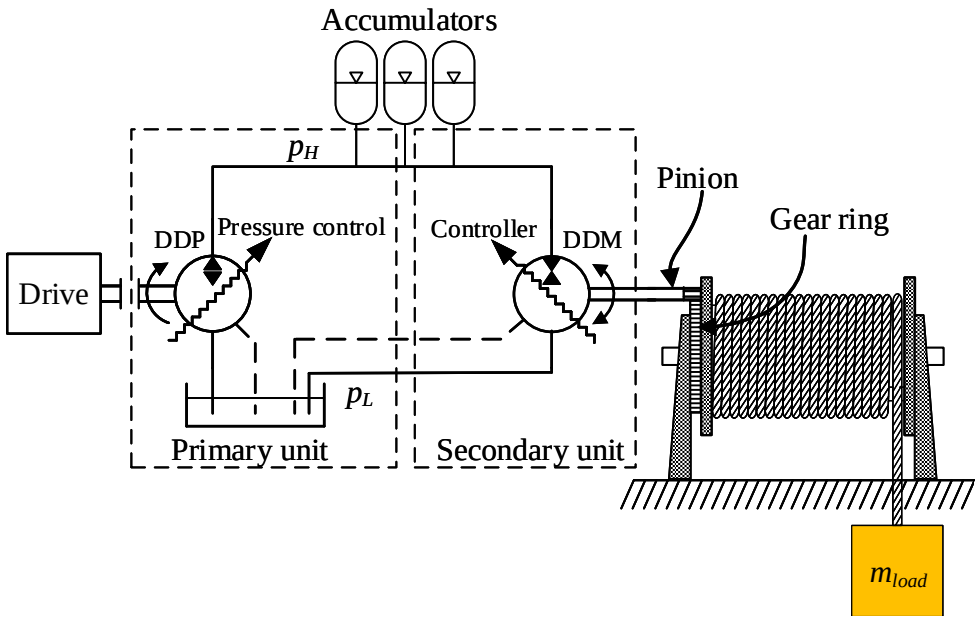

Figure F.2: Schematic illustration of the digital displacement winch drive system

The main task of the pressure controlled DDP is to maintain a minimum pressure in the high pressure line, p_H. The DDM is directly connected to the winch drum through a pinion and gear ring. The output torque is controlled by controlling the displacement of the DDM. The purpose of the accumulators is to store energy whenever the DDM operates in pump mode. The stored energy can later be used when the DDM operates in motor mode.

This paper is limited to examine control strategies for the DDM. It is therefore assumed that the DDP and the accumulator bank will provide a constant pressure in the high and

low pressure line. The secondary winch drive system can then be simplified to the system shown in Figure F.3. The simulated winch system is based on a 20000 kg winch system

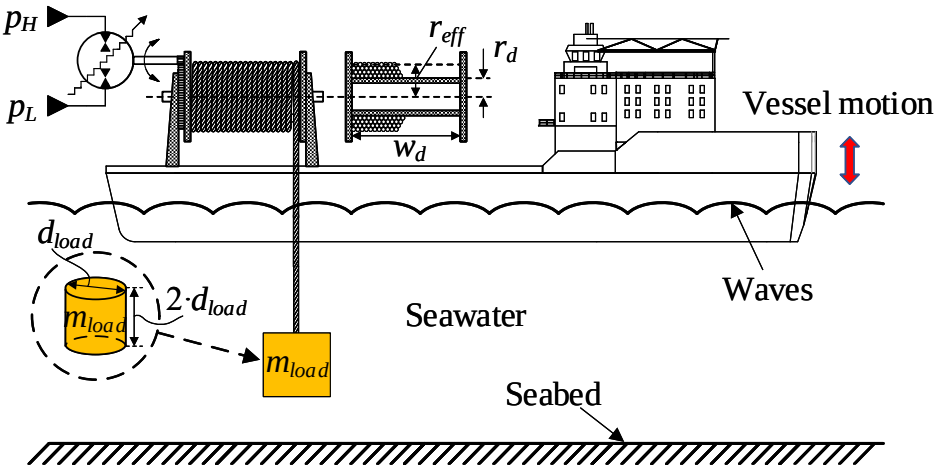

Figure F.3: Simulated winch system.

with a drum capacity of 3600 m. The winch is intended for use in subsea operations. r_d is the radius of the winch drum, r_{eff} is the effective radius of the outer wire layer, w_d is the width of the drum, and m_{load} is the mass of the payload. The payload is cylindrical shaped and its length is twice as long as the diameter. The simulation model is divided into two parts, the mechanical winch model and the digital displacement winch drive system.

F.2.1 Winch Model

The mechanical winch model consists of the winch drum, wire rope and payload. The simulation model is based on the winch model described in [18] and also used in [34]. It is assumed that the payload is either located in the air or fully submerged in water. The transition phase between air and water is not simulated. The following is included in the simulation model:

- Buoyancy force.
- Viscous drag force in water.
- Friction in drum bearings.
- Seabed dynamics.
- Wire elongation.
- Vertical heave motion of vessel.
- Inertia of winch drum, hydraulic drive system, wire rope and payload.

The winch model is set up based on the dynamic model schematic, free body diagram and the kinetic diagram shown in Figure F.4.

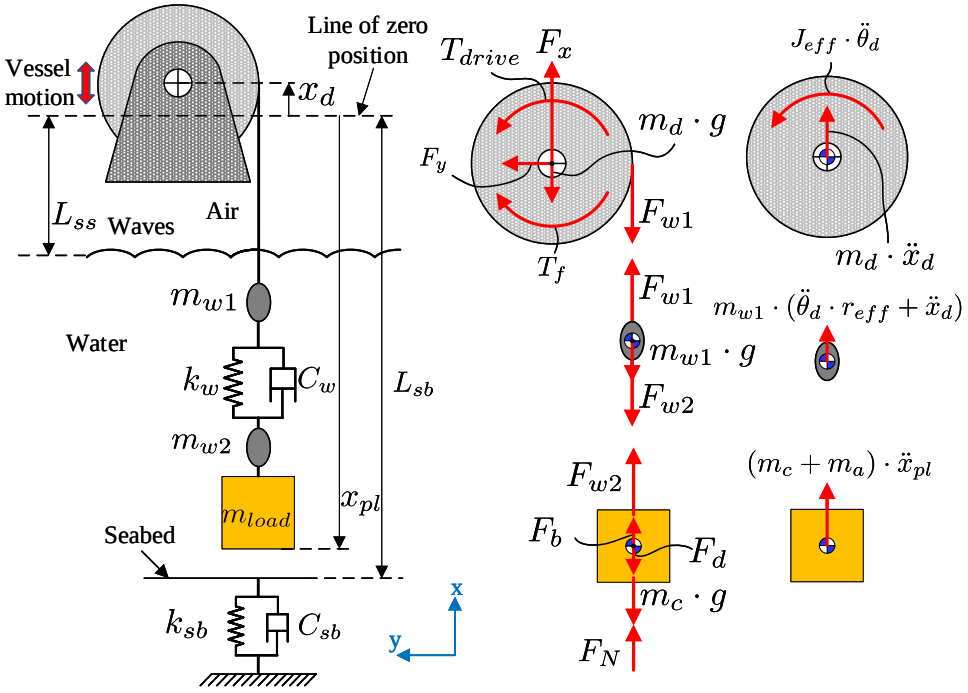

Figure F.4: System dynamics, free body diagram and kinetic diagram.

Note that the payload position is calculated from the center of the drum when the vessel is at rest with no vertical motion, marked by the *line of zero position* in Figure F.4. The payload position is negative when the payload is below the line of zero position. The length from the line of zero position and down to the sea surface is $L_{ss} = 20$ m and the length down to the seabed is $L_{sb} = 1000$ m.

The winch drum's rotational motion and the payload's vertical motion is described by using Newton's second low of motion as shown below.

$$\sum \tau = J_{eff} \cdot \ddot{\theta}_d = T_{drive} - T_f - F_{w1} \cdot r_{eff} \tag{F.1}$$

$$\sum F_x = (m_c + m_a) \cdot \ddot{x}_{pl} = F_{w2} + F_b + F_N - F_d - m_c \cdot g \tag{F.2}$$

where T_{drive} is the driving torque acting on the drum, T_f is the friction torque in the drum bearings, F_{w1} is the wire force between the winch drum and the upper wire section, F_{w2} is the wire force between the upper and lower wire section, r_{eff} is the effective radius of the outer wire layer, J_{eff} is the effective mass moment of inertia relative to the drum shaft, m_c is the combined mass of the payload, winch hook and the lower wire section, m_a is the added mass, F_b is the buoyancy force, F_d is the viscous drag force, F_N is the seabed interaction force and g is the acceleration of gravity. The driving torque is given by the DDM and calculated in section F.2.2.

The friction torque in the drum bearings, T_f, is assumed to be a combination of

coulomb and viscous friction and calculated as shown in Equation (F.3).

$$T_f = \underbrace{(m_d \cdot g + F_{w1}) \cdot r_b \cdot \mu_c \cdot \tanh(\dot{\theta}_d \cdot 1000)}_{T_{coulomb}} + \underbrace{\mu_v \cdot r_b \cdot \dot{\theta}_d}_{T_{viscous}} \tag{F.3}$$

where m_d is the mass of the winch drum and the wire rolled onto it, r_b is the radius of the bearings, μ_c is the coulomb friction coefficient and μ_v is the viscous friction coefficient. The coulomb friction coefficient is approximated as $\mu_c = 0.1$ and the viscous friction coefficient is approximated as $\mu_v = 1000$ Ns/rad. The term $\tanh(\dot{\theta}_d \cdot 1000)$ is used to avoid a step in the coulomb friction torque when passing through 0 rpm. However, this friction model is only a rough approximation and may not reflect the exact friction characteristics.

The wire is divided into two point masses, m_{w1} and m_{w2}, with a spring and damper in between, as illustrated in Figure F.4. The connection between the upper wire section and the winch drum, and the connection between the lower wire section and the payload are assumed to be rigid. Hence, the motion of the upper wire section is a combination of the vertical motion of the vessel and the rotation of the drum, $\ddot{x}_{w1} = \ddot{\theta}_d \cdot r_{eff} + \ddot{x}_d$. The motion of the lower wire section is equal to the motion of the payload, $\ddot{x}_{w2} = \ddot{x}_{pl}$. Based on those relations, the wire forces, F_{w1} and F_{w2}, can be calculated as shown below.

$$F_{w1} = m_{w1} \cdot (\ddot{\theta}_d \cdot r_{eff} + \ddot{x}_d) + m_{w1} \cdot g + F_{w2} \tag{F.4}$$

$$F_{w2} = \underbrace{(\theta_d \cdot r_{eff} + x_d - x_{pl}) \cdot k_w}_{F_{spring}} + \underbrace{(\dot{\theta}_d \cdot r_{eff} + \dot{x}_d - \dot{x}_{pl}) \cdot C_w}_{F_{damper}} \tag{F.5}$$

where $\ddot{x}_d$ is the vertical acceleration of the vessel, k_w is the spring stiffness of the wire and C_w is the damping coefficient. Note that Equation (F.5) is only valid when the wire is stretched. For slack wires, the wire force is set to $F_{w2} = 0$ N. The spring stiffness is calculated based on the wire E-modulus, E_w, wire cross-section area, A_w, and the length of the payed out wire, L_w, as shown in Equation (F.6). The damping force is introduced to compensate for internal friction in the wire rope. The damping coefficient is defined as 10 % of the spring stiffness and calculated as shown in Equation (F.7). Note that Equation (F.7) does not give the correct unit of the damping coefficient. The correct unit is Ns/m.

$$k_w = \frac{E_w \cdot A_w}{L_w} \tag{F.6}$$

$$C_w = \frac{k_w}{10} \tag{F.7}$$

The spring stiffness and the damping coefficient is only a rough estimation and may not reflect the exact values.

The payload and wire rope are exposed to buoyancy when submerged in water and a viscous drag force during motion. The buoyancy force, F_b, and drag force, F_d is calculated

according to [35] as shown below.

$$F_b = \rho_{sea} \cdot g \cdot (V_{pl} + V_w) \tag{F.8}$$

$$F_d = \frac{1}{2} \cdot \rho_{sea} \cdot C_d \cdot A_{pl} \cdot \dot{x}_{pl}^2 \cdot \text{sign}(\dot{x}_{pl}) \tag{F.9}$$

where ρ_{sea} is the sea water density, V_{pl} is the volume of the payload, V_w is the volume of the wire, C_d is the drag force coefficient and A_{pl} is the projected cross-section area of the payload normal to the motion. For a circular cylinder shaped payload with a length twice as long as the diameter, the drag coefficient is $C_d = 0.85$ [35].

The seabed is modeled as a spring-damper system [18]. The seabed interaction force is modeled as shown in Equation (F.10).

$$F_N = \begin{cases} 0 & x_{pl} \geq -L_{sb} \\ (-x_{pl} - L_{sb}) \cdot k_{sb} - \dot{x}_{pl} \cdot C_{sb} & x_{pl} < -L_{sb} \end{cases} \tag{F.10}$$

where k_{sb} is the spring stiffness and C_{sb} is the damping coefficient for the seabed. The seabed spring stiffness and damping coefficient is set to $k_{sb} = 4000000$ N/m and $C_{sb} = 1000000$ Ns/m respectively.

During operation, the wire rope is either payed in or out causing variations in the effective mass moment of inertia. Also, the effective radius will change when changing from one wire layer to another. For the simulated winch system, one wire layer can accommodate more than 180 m of wire on the inner wire layer. This length is significantly larger than the distance the payload is moved in the test cases used in this work. It is therefore assumed that the simulations are carried out without changing wire layer and that the effective radius, r_{eff}, is constant. However, the effective mass moment of inertia will vary with the amount of payed out wire. It is assumed that the wire is uniformly distributed around the drum. The effective mass moment of inertia is calculated as shown in Equation (F.11)

$$J_{eff} = J_d + \underbrace{\frac{1}{2} \cdot m_{wd} \cdot (r_d^2 + r_{eff}^2)}_{J_{wire}} + J_m \cdot N_{gear}^2 \tag{F.11}$$

where J_d is the mass moment of inertia of the drum, m_{wd} is the mass of the wire rolled onto the drum, J_m is the mass moment of inertia of the digital displacement motor and N_{gear} is the gear ratio of the pinion and gear ring.

The combined mass, m_c, consists of the mass of the payload, m_{load}, hook, m_{hook}, and the lower wire section m_{w2}. The combined mass is calculated as shown in Equation (F.12)

$$m_c = m_{load} + m_{hook} + m_{w2} \tag{F.12}$$

The added mass, m_a, is an inertia that is included to the payload when the payload is submerged in water. The extra inertia occurs because the payload must move some

volume of surrounding water as it moves through it. The added mass is affected by the payload geometry, motion amplitude and the depth of submergence [35]. A reasonable approximation of the added mass can be calculated as shown in Equation (F.13) [35].

$$m_a = \rho_{sea} \cdot C_A \cdot V_R \tag{F.13}$$

where C_A is the added mass coefficient and V_R is the reference volume. For a circular cylinder shaped payload with the length twice as long as the diameter, the added mass coefficient is $C_A = 0.72$ and the reference volume is $V_R = V_{pl}$ [35].

The winch model parameters are listed in Table F.1 which can be found in Appendix A.

F.2.2 Digital Displacement Winch Drive Model

The digital displacement winch drive system consists of a high torque low speed DDM directly connected to the winch drum through a pinion and a gear ring. It is assumed that there are no friction losses and no slack between the pinion and the gear ring. Hence, the following linear relations are applicable.

$$T_{drive} = T_m \cdot N_{gear} \tag{F.14}$$

$$\theta_m = \theta_d \cdot N_{gear} \tag{F.15}$$

where T_m is the output torque of the DDM and θ_m is the DDM's shaft position.

The simulation model of the DDM is based on the model derived in [36] and has earlier been used and experimentally validated in [26]. For simplicity, the simulation model is derived based on single cylinder, but the same method is used for all cylinders. Figure F.5 illustrates a 15 cylinder radial piston DDM, left side, and a single cylinder, right side. The illustration of the single cylinder is used to derive the equations for the simulation model. The following assumptions are made for the DDM model:

- Constant pressure in the high and low pressure line.
- Valve dynamics can be described by a second order system.
- Leakage in valves and cylinders are negligible.
- Friction in motor is negligible.
- The effective mass moment of inertia of the DDM is assumed to be constant ($J_m =$ constant).

The continuity equation is used to calculate the pressure dynamics in cylinder number i.

$$\dot{p}_{cyl,i} = \frac{\beta_{eff,i}}{V_{cyl,i}} \cdot \left(Q_{H,i} - Q_{L,i} - \dot{V}_{cyl,i} \right) \tag{F.16}$$

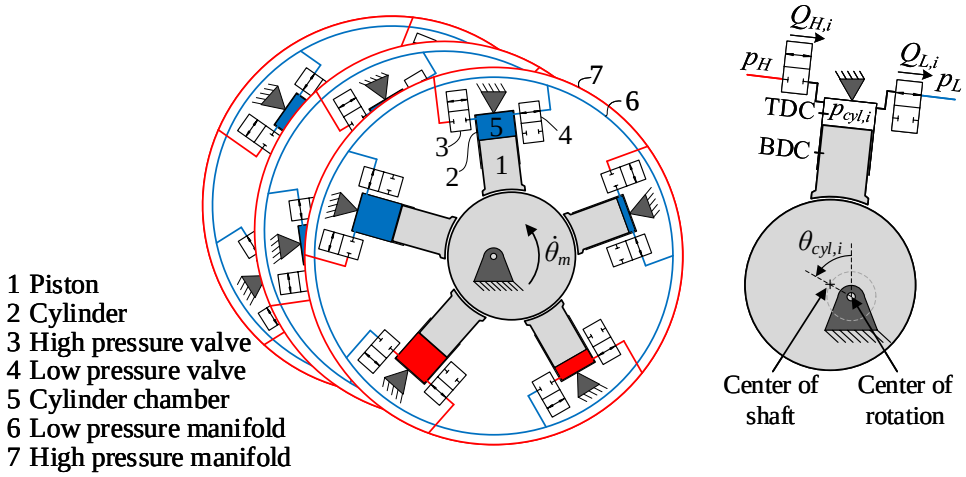

Figure F.5: Schematics illustration of a radial DDM, left side, and a single cylinder, right side

where $\beta_{eff,i}$ is the effective bulk modulus of the hydraulic fluid, $V_{cyl,i}$ is the cylinder volume, $Q_{H,i}$ is the volume flow through the high pressure valve and $Q_{L,i}$ is the volume flow through the low pressure valve.

The cylinder volume and its time derivative are calculated as shown in Equation (F.17) and Equation (F.18) respectively.

$$V_{cyl,i} = V_0 + \frac{V_d}{2} \cdot (1 - \cos(\theta_{cyl,i})) \tag{F.17}$$

$$\dot{V}_{cyl,i} = \frac{V_d}{2} \cdot \sin(\theta_{cyl,i}) \cdot \dot{\theta}_m \tag{F.18}$$

where V_0 is the dead volume in the cylinder, V_d is the piston displacement, $\theta_{cyl,i}$ is the local shaft position relative to the piston position and $\dot{\theta}_m$ is the rotational shaft speed. Note that $\dot{\theta}_m = \dot{\theta}_{cyl,i}$. The local shaft position is defined to be $\theta_{cyl,i} = 0$ rad when the piston is at top dead center (TDC), as shown on the single cylinder in Figure F.5. Due to the phase shift between the cylinders, the local shaft position can be calculated as

$$\theta_{cyl,i} = \theta_m + \frac{2 \cdot \pi}{N_c} \cdot (i - 1) \qquad i \in \{1, ..., N_c\} \tag{F.19}$$

where N_c is the number of pistons in the DDM.

The valve flows, $Q_{H,i}$ and $Q_{L,i}$, are calculated by the orifices equation as shown in Equation (F.20) and Equation (F.21) respectively.

$$Q_{H,i} = \frac{u_{H,i}}{k_f} \cdot \sqrt{|p_H - p_{cyl,i}|} \cdot \text{sign}(p_H - p_{cyl,i}) \tag{F.20}$$

$$Q_{L,i} = \frac{u_{L,i}}{k_f} \cdot \sqrt{|p_{cyl,i} - p_L|} \cdot \text{sign}(p_{cyl,i} - p_L) \tag{F.21}$$

where $u_{H,i}$ is the opening ratio of the high pressure valve, $u_{L,i}$ is the opening ratio of the low pressure valve, k_f is the valve flow coefficient, p_H and p_L are the pressures in the high and low pressure line respectively and $p_{cyl,i}$ is the pressure in the cylinder chamber. The

opening ratio of the valves is ranging from 0 to 1, where 0 corresponds to fully closed and 1 to fully open.

The valve dynamics are described by a second order system as shown in Equation (F.22) and Equation (F.23)

$$\ddot{u}_{H,i} = u_{conH,i} \cdot \omega^2 - u_{H,i} \cdot \omega^2 - 2 \cdot \zeta \cdot \omega \cdot \dot{u}_{H,i} \tag{F.22}$$

$$\ddot{u}_{L,i} = u_{conL,i} \cdot \omega^2 - u_{L,i} \cdot \omega^2 - 2 \cdot \zeta \cdot \omega \cdot \dot{u}_{L,i} \tag{F.23}$$

where $u_{conH,i}$ is the control signal for the high pressure valve, $u_{conL,i}$ is the control signal for the low pressure valve, ω is the natural frequency of the valves and ζ is the damping ratio. Due to the nature of the on/off valves, the control signals are either 0 or 1, corresponding to fully closed and fully open respectively. The valve control signals are given by the motor controller and the chosen displacement strategy. A detailed description of the chosen displacement strategy is given in Section F.3.

The pressure dependent bulk modulus is calculated according to [37] as shown below.

$$\beta_{eff,i} = \frac{1}{\frac{1}{\beta_L} + \frac{\epsilon_g}{p_{cyl,i}^{(abs)}}} \tag{F.24}$$

where β_L is the bulk modulus of the hydraulic liquid and ϵ_g is the volume fraction of undissolved gas. The volume fraction of undissolved gas is calculated by

$$\epsilon_g = \frac{1}{\left(\frac{1-\epsilon_{g0}}{\epsilon_{g0}}\right) \cdot \left(\frac{p_{atm}^{(abs)}}{p_{cyl,i}^{(abs)}}\right)^{-\frac{1}{\kappa}} + 1} \tag{F.25}$$

where ϵ_{g0} is the volume fraction of undissolved gas at atmospheric pressure, $p_{atm}^{(abs)}$ is the atmospheric pressure and κ is the specific heat ratio. The specific heat ratio is assumed to be 1.4.

Finally, the torque contribution from cylinder number i is calculated by

$$T_{cyl,i} = \frac{V_d}{2} \cdot \sin(\theta_{cyl,i}) \cdot p_{cyl,i} \tag{F.26}$$

and the total motor torque is the sum of the torque contribution from every single cylinder.

$$T_m = \sum_{i=1}^{N_c} T_{cyl,i} \tag{F.27}$$

The digital displacement motor model parameters are listed in Table F.2 which can be found in Appendix A.

F.3 Displacement Strategy

The design of the displacement strategy is important and is one of the things that makes the design of controllers for DDMs more challenging than for conventional hydraulic motors. The displacement strategy can be of a new design or be chosen from already designed displacement strategies. All displacement strategies have their own characteristics. The winch drive system must be able to operate at low speeds with frequent starts and stops and frequent changes in direction of rotation. Based on the work presented in [26], both the partial stroke displacement strategy and the sequential partial stroke displacement strategy are found to be suitable for use in a winch drive system due to high controllability at low operation speeds. The sequential partial stroke displacement strategy is known to switch the valves and reactivate cylinders more often than the partial stroke displacement strategy. It is therefore assumed that the partial stroke displacement strategy has higher energy efficiency and is, therefore, the selected displacement strategy. Note that the selected displacement strategy is referred to as *partial stroke displacement strategy version 2* in [26] but is in this paper referred to as the *partial stroke displacement strategy*.

F.3.1 Partial Stroke Displacement Strategy

This section describes the displacement strategy based on operation in motor mode with positive speed.

In partial stroke displacement strategy, the cylinders are only activated in a portion of the down stroke piston motion. The term "active" means that the cylinder is connected to the high pressure line and contributes with a positive or negative output torque. The displacement is changed by increasing or decreasing the active period. Figure F.6 shows the schematics of the valve actuation sequence for a single cylinder chamber. Plot 1 shows the cylinder position, Plot 2 shows the opening ratio for the high and low pressure valve, Plot 3 shows the cylinder pressure, Plot 4 shows the cylinder torque contribution and Plot 5 shows the local shaft position. The red dashed line in Plot 5 shows the state change angle, also called the control angle, α. The control angle describes at which local shaft position, $\theta_{cyl,i}$, the cylinder shall change state from active to inactive. If $\theta_{cyl,i} \leq \alpha$ then the cylinder shall be active, else the cylinder is inactive.

First in Figure F.6, the state change angle is set to $\alpha = \alpha_1 = \pi/2$ rad, which corresponds to 50 % displacement. When $\theta_{cyl,i} = \alpha_1$, the cylinder is deactivated. After a short period of time, the state change angle is stepped up to $\alpha = \alpha_2 = 3\pi/4$ rad. Since the local cylinder angle is smaller than the new state change angle, $\theta_{cyl,i} < \alpha_2$, then the cylinder is reactivated in the remaining shaft rotation up to $\theta_{cyl,i} = \alpha_2$.

The state change angle, α, is calculated based on the desired displacement ratio D_m.

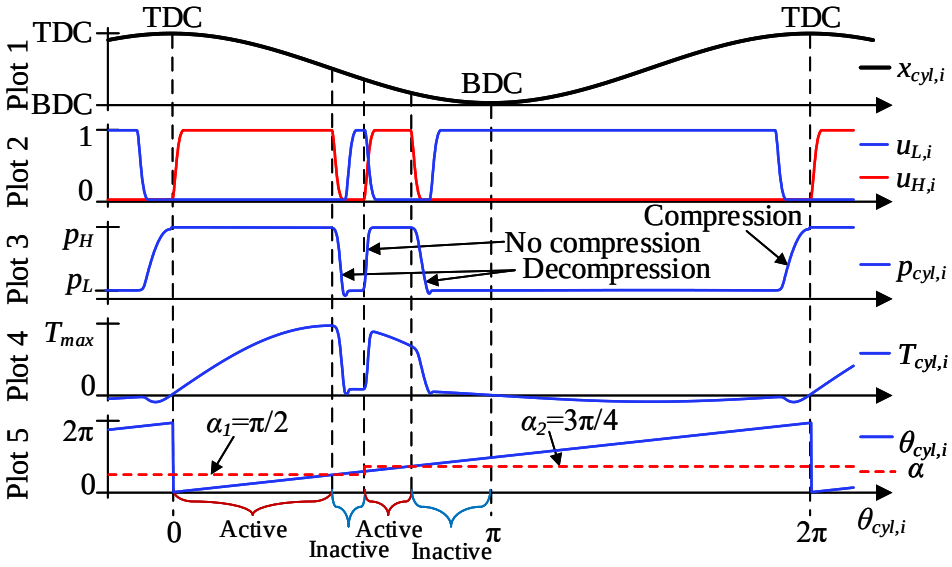

Figure F.6: Schematic illustration of the valve timing strategy in partial stroke displacement strategy.

D_m is defined as the displaced volume during the active period divided by the maximum piston displacement. Based on the calculation of the cylinder chamber volume shown in Equation (F.17), the displacement ratio can be calculated by:

$$\begin{aligned} D_m &= \frac{V_{cyl}(\alpha)}{V_{cyl}(\pi)} \\ &= \frac{1}{2} \cdot (1 - \cos(\alpha)) \end{aligned} \tag{F.28}$$

where $V_{cyl}(\alpha)$ is the intake volume during the active period and $V_{cyl}(\pi)$ is the maximum intake volume. The state change angle is then calculated by rearranging Equation (F.28).

$$\alpha = \cos^{-1}(1 - 2 \cdot D_m) \tag{F.29}$$

One of the benefits of the DDM, is that the decompression and compression phase can be optimized for every operation condition. Optimizing the compression and decompression phase is not in the scope of this work and a routine for calculating the optimal compression and decompression phase are therefore not implemented. In this study, when changing state from active to inactive, the low pressure valve is opened when the high pressure valve is fully closed. When reactivating a cylinder, the high pressure valve and the low pressure valve are actuated at the same time. This strategy will result in unnecessary high flow peaks and flow throttling losses. One technique of optimizing the decompression and compression phase have been investigated in [38].

F.3.2 Four Quadrant Operation

Winch operation requires a drive system that is able to operate in all four quadrants. Four quadrant operation is illustrated in Figure F.7. The green arrow shows the direction

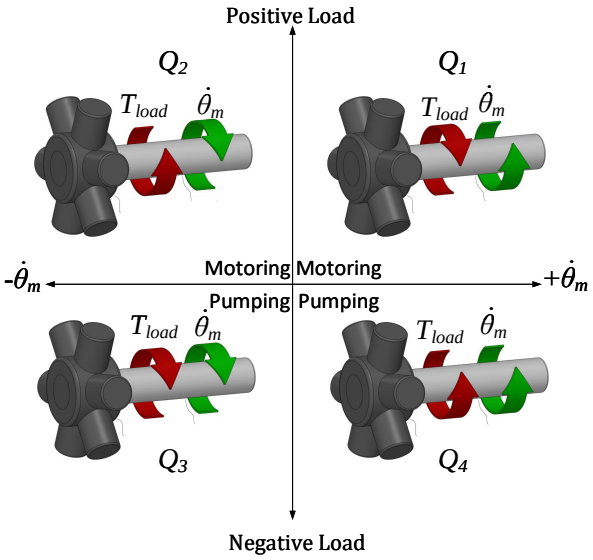

Figure F.7: Four quadrant operation.

of rotation of the motor shaft and the red arrow shows the direction of the load torque. Normally, the drive system operates in quadrant 1 during hoisting and quadrant 3 during lowering. However, in special cases, as for example in AHC mode or operation with an empty hook, all four quadrants may be used.

In partial stroke displacement strategy, the valve timing strategy shown in Figure F.6 is only valid for operation in quadrant 1. Each quadrant requires a unique valve timing strategy. Figure F.8 shows a simplified schematic illustration of the valve timing strategy for all four quadrants. The top graph shows the piston position and the next four graphs show the valve timing sequence for operation in quadrant 1 to 4 respectively. The red line shows the opening ratio of the high pressure valve and the blue line shows the opening ratio of the low pressure valve. The black line with arrows shows the direction of rotation. Arrows pointing to the right indicates positive direction and arrows pointing to the left indicates negative direction of rotation. Note that in quadrant 1 (Q_1) and quadrant 3 (Q_3), the control angle, α_1, is used to switch cylinder state and in quadrant 2 (Q_2) and quadrant 4 (Q_4) the control angle, α_2, is used to switch cylinder state.

The schematic of the motor controller is shown in Figure F.9. The input signal is the desired displacement ratio, D_m, and the output is the motor torque, T_m. The state change angle, α, is calculated based on the desired displacement fraction by using Equation (F.29). The valve timing strategy, Q_j where $j = 1...4$, is selected by a switching controller. Based on given conditions, the proper valve activation strategy is selected. The given conditions

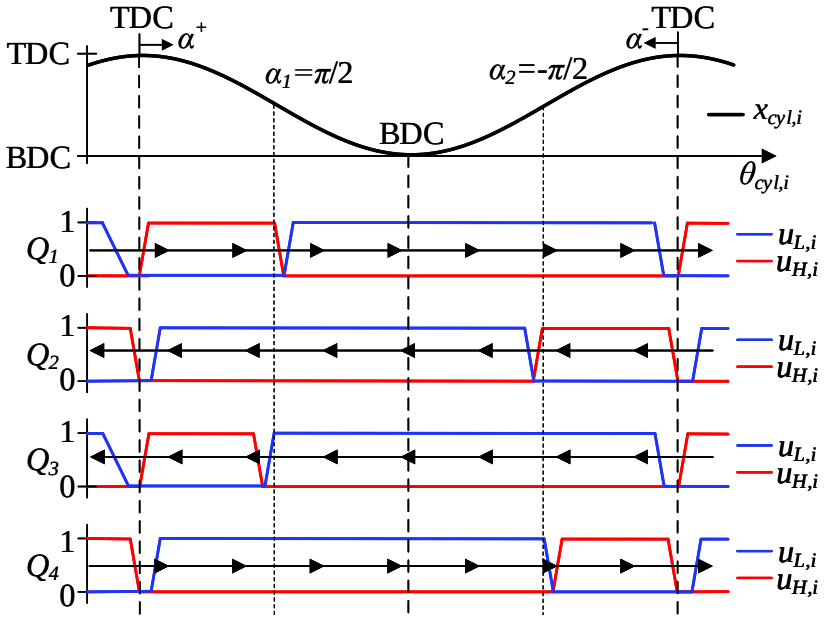

Figure F.8: Schematic illustration of the valve timing strategy for four quadrant operation

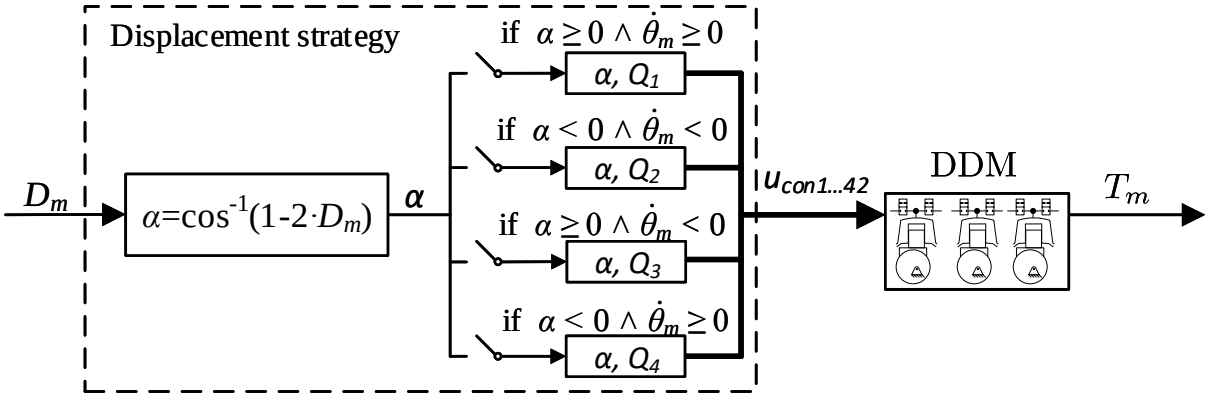

Figure F.9: Motor controller

are shown in Equation (F.30).

$$Q = \begin{cases} Q_1 & \text{if} \quad \alpha \geq 0 \quad \wedge \quad \dot{\theta}_m \geq 0 \\ Q_2 & \text{if} \quad \alpha < 0 \quad \wedge \quad \dot{\theta}_m < 0 \\ Q_3 & \text{if} \quad \alpha \geq 0 \quad \wedge \quad \dot{\theta}_m < 0 \\ Q_4 & \text{if} \quad \alpha < 0 \quad \wedge \quad \dot{\theta}_m \geq 0 \end{cases} \tag{F.30}$$

The state change angle and the valve timing strategy is then sent to the on/off valves on the DDM which activates and deactivates cylinder chambers resulting in an output torque.

F.4 Model Simplification

In order to design model based feedback controllers, the nonlinear simulation model presented in Section F.2 is simplified. In the simplified model it is assumed that the wire

elasticity can be neglected and the motor torque is linear to the desired displacement. The new simplified dynamic model schematic, free body diagram and the kinetic diagram are shown in Figure F.10.

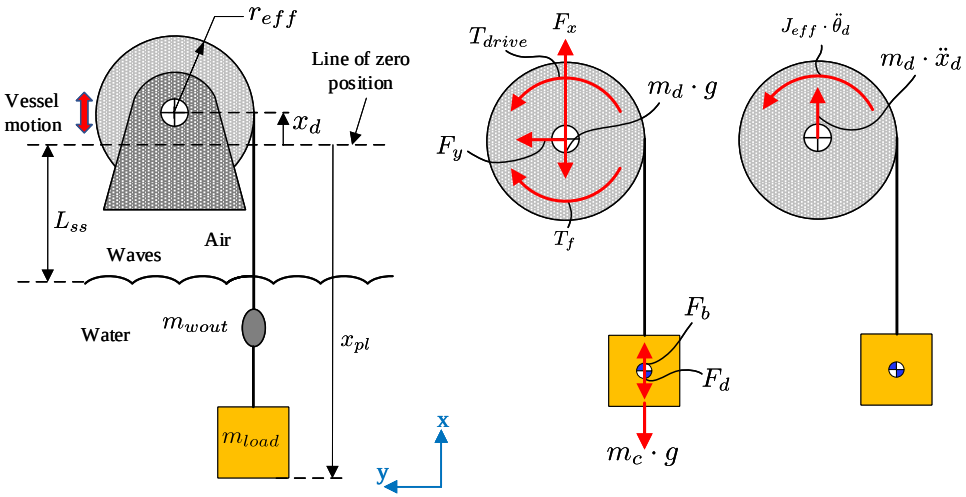

Figure F.10: Simplified system dynamics, free body diagram and kinetic diagram.

The equation of motion for the winch drum is derived based on the free body diagram and the kinetic diagram and shown in Equation (F.31).

$$\overline{J}_{eff} \cdot \ddot{\theta}_d = \overline{T}_{drive} - r_{eff} \cdot (m_c \cdot g + F_d - F_b) - \overline{T}_f \tag{F.31}$$

where overline indicates that the parameter is a simplified version of the real parameter. The driving torque is given by the hydraulic motor. In this simplified model, the driving torque is assumed to be linear to the input signal, D_m, and expressed by:

$$\overline{T}_{drive} = \frac{\Delta p_{motor} \cdot V_m}{2 \cdot \pi} \cdot N_{gear} \cdot D_m \tag{F.32}$$

where $\Delta p_{motor} = p_H - p_L$ is the pressure difference across the motor, V_m is the maximum motor displacement, N_{gear} is the gear ratio between the pinion and the gear ring and D_m is the displacement ratio ranging from -1 to 1. In order to validate the simplified driving torque, the driving torque from the simplified model, $\overline{T}_{drive}$, is compared to the driving torque from the nonlinear model, T_{drive}, when a sinusoidal input signal with increasing frequency is given. The motor is running at 50 rpm and the results are shown in Figure F.11. The blue line shows the driving torque from the nonlinear model, and the red line shows the driving torque from the simplified model. The simulation results show that the simplified model is a sufficient representation of the nonlinear model, even at high input frequencies. However, the output torque from the nonlinear model tends to oscillate, while the output torque from the simplified model is smooth. This is best seen in the first 5 s of Figure F.11 where the blue line looks thick due to the oscillating output torque caused by fast switchings between active and inactive cylinder chambers.

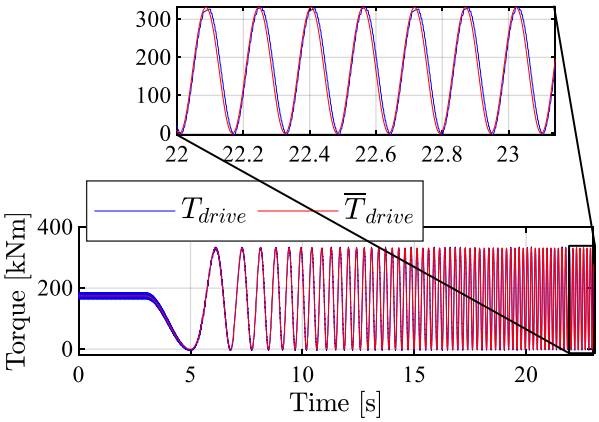

Figure F.11: Comparison between simple model and non-linear model of the driving torque.

The friction torque is calculated by

$$\begin{aligned}\overline{T}_f = &(m_{tot} \cdot g + F_d - F_b) \cdot r_b \cdot \mu_c \cdot \text{sign}\left(\dot{\theta}_d\right) \\ &+ \mu_v \cdot r_b \cdot \dot{\theta}_d \end{aligned} \tag{F.33}$$

where m_{tot} is the mass of the winch drum, payload and the wire.

The effective mass moment of inertia, J_{eff}, is calculated as shown in Equation (F.34).

$$\begin{aligned}\overline{J}_{eff} = &J_d + \frac{1}{2} \cdot m_{wd} \cdot \left(r_d^2 + r_{eff}^2\right) + J_m \cdot N_{gear}^2 \\ &+ (m_{load} + m_{wout}) \cdot r_{eff}^2 \end{aligned} \tag{F.34}$$

where m_{wout} is the mass of the wire that is payed out.

F.5 Control Design

A schematic illustration of the control structure is shown in Figure F.12. The reference

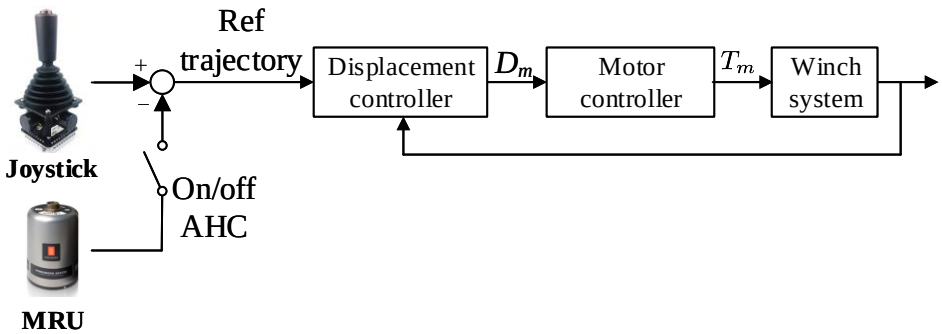

Figure F.12: Schematic illustration of the control system

trajectory is created by a joystick. In case of activating the AHC system, the vessel motion is subtracted from the reference signal created by the joystick. The displacement controller transforms the reference trajectory into a desired motor displacement ratio.

The displacement controller is a classic controller and can be of any type, with or without feedback signals. The motor controller transforms the desired motor displacement ratio into an output torque that drives the winch. The motor controller is shown in Figure F.9.

In this section, three different displacement controllers are designed. The designed controllers are referred to as the base controller, the sliding mode disturbance controller and the adaptive controller.

F.5.1 Base Controller

The base controller is designed based on the simplified model presented in Section F.4. The equation of motion, shown in Equation (F.31), is first rewritten to a more general form.

$$\begin{aligned}
\overline{J}_{eff} \cdot \ddot{\theta}_d &= \overline{T}_{drive} - r_{eff} \cdot (m_c \cdot g + F_d - F_b) - \overline{T}_f \Rightarrow \\
\ddot{\theta}_d &= \frac{\frac{\Delta p_{motor} \cdot V_m}{2 \cdot \pi} \cdot N_{gear}}{\overline{J}_{eff}} \cdot D_m \\
&\quad - \frac{r_{eff} \cdot (m_c \cdot g + F_d - F_b)}{\overline{J}_{eff}} - \frac{\overline{T}_f}{\overline{J}_{eff}} \\
&= b \cdot D_m - f
\end{aligned} \tag{F.35}$$

where

$$b = \frac{\frac{\Delta p_{motor} \cdot V_m}{2 \cdot \pi} \cdot N_{gear}}{\hat{J}_{eff}} \tag{F.36}$$

$$f = \frac{r_{eff} \cdot (m_c \cdot g + F_d - F_b)}{\overline{J}_{eff}} + \frac{\overline{T}_f}{\overline{J}_{eff}} \tag{F.37}$$

If the parameters b and f are exactly known, the following control law will give optimal tracking performance.

$$D_{m,opt} = \frac{u_n + f}{b} \tag{F.38}$$

with the nominal controller

$$u_n = \ddot{\theta}_{ref} - c_2 \cdot \dot{e} - c_1 \cdot e \tag{F.39}$$

where $e = \theta_d - \theta_{ref}$ and θ_{ref} is the reference position for the drum. c_1 and c_2 are controller gains and must be positive. Inserting the optimal control law, given in Equation (F.38),

into Equation (F.35) results in the following closed loop response.

$$\begin{aligned}\ddot{\theta}_d &= b \cdot D_{m,opt} - f \\ &= b \cdot \frac{u_n + f}{b} - f \\ &= u_n \Downarrow \end{aligned} \tag{F.40}$$

$$\begin{aligned}\ddot{\theta}_d &= \ddot{\theta}_{ref} - c_2 \cdot \dot{e} - c_1 \cdot e \\ \ddot{\theta}_d - \ddot{\theta}_{ref} + c_2 \cdot \dot{e} + c_1 \cdot e &= 0 \\ \ddot{e} + c_2 \cdot \dot{e} + c_1 \cdot e &= 0 \end{aligned} \tag{F.41}$$

where the position error, e, will converge to zero exponentially.

In reality, the parameters b and f are not known exactly because of unmodeled dynamics, uncertainties in the simulation parameters and other disturbances. Therefore, only an approximation of the control law can be implemented:

$$D_m = \frac{u_n + \hat{f}}{\hat{b}} \tag{F.42}$$

where $\hat{}$ indicates that the parameter is estimated based on system knowledge and state measurements. Inserting the best approximation of the control law, shown in Equation (F.42), into Equation (F.35) gives the following closed loop response:

$$\begin{aligned}\ddot{\theta}_d &= b \cdot D_m - f \\ &= b \cdot \frac{u_n + \hat{f}}{\hat{b}} - f \\ &= \frac{b}{\hat{b}} \cdot u_n + \frac{b}{\hat{b}} \cdot \hat{f} - f \\ &= u_n - \left(f - \frac{b}{\hat{b}} \cdot \hat{f} + u_n \cdot \left(1 - \frac{b}{\hat{b}} \right) \right) \\ &= u_n - \Delta_{b,f} \end{aligned} \tag{F.43}$$

where

$$\Delta_{b,f} = f - \frac{b}{\hat{b}} \cdot \hat{f} + u_n \cdot \left(1 - \frac{b}{\hat{b}} \right) \tag{F.44}$$

$\Delta_{b,f}$ is called the model error and represents the error dynamics between the estimated model and the real system.

The control law presented in Equation (F.42) is referred to as the base controller (BC). Assuming that the model error is low and negligible, the control performance will be good. In the second controller, it is assumed that the model error may be of significant impact on the system. In order to handle the model error, a compensator is designed to compensate for the model error. The compensator, u_c, is designed by using a sliding mode

disturbance controller. In the third controller, it is also assumed that the model error may affect the system. Instead of designing a compensator, the simulation parameters are adapted to their real values by an adaptive controller.

F.5.2 Sliding Mode Disturbance Controller

The BC presented in the previous section is not optimal due to the model error. This section presents therefore a compensator, u_c, that shall cancel out the model error. The designed compensator is a sliding mode disturbance compensator (SMDC). First, the control law in Equation (F.42) is modified to include the compensator, u_c.

$$D_{m,SMC} = \frac{u_n + u_c + \hat{f}}{\hat{b}} \tag{F.45}$$

Inserting the new control law into Equation (F.35) gives the following closed loop dynamics.

$$\begin{aligned}
\ddot{\theta}_d &= b \cdot D_{m,SMC} - f \\
&= b \cdot \frac{u_n + u_c + \hat{f}}{\hat{b}} - f \\
&= \frac{b}{\hat{b}} \cdot u_n + \frac{b}{\hat{b}} \cdot u_c + \frac{b}{\hat{b}} \cdot \hat{f} - f \\
&= u_n + u_c + \left(\frac{b}{\hat{b}} \cdot \hat{f} - f + (u_n + u_c) \cdot \left(\frac{b}{\hat{b}} - 1 \right) \right) \\
&= u_n + u_c + \Delta_{b,f,SMC}
\end{aligned} \tag{F.46}$$

where

$$\Delta_{b,f,SMC} = \left(\frac{b}{\hat{b}} \cdot \hat{f} - f + (u_n + u_c) \cdot \left(\frac{b}{\hat{b}} - 1 \right) \right) \tag{F.47}$$

$\Delta_{b,f,SMC}$ is the model error. The aim of the compensator is to compensate for the model error such that

$$\ddot{\theta}_d = u_n, \quad \text{for } u_c \to -\Delta_{b,f,SMC} \tag{F.48}$$

The compensator is designed by following the structure in [39]. The model parameters, b and f, are unknown but are assumed to be bounded. The bounds are given by the following equations.

$$|\hat{f} - f| \leq F \tag{F.49}$$

and

$$0 < b_{min} \leq b \leq b_{max} \tag{F.50}$$

$$\Downarrow$$

$$\beta^{-1} \leq \frac{b}{\hat{b}} \leq \beta \tag{F.51}$$

where

$$\beta = \frac{b_{max}}{b_{min}} \tag{F.52}$$

A time-varying sliding surface is defined by Equation (F.53) and its derivative by Equation (F.54).

$$s = \dot{\theta}_d - z \tag{F.53}$$

$$\dot{s} = \ddot{\theta}_d - \dot{z} \tag{F.54}$$

where $\dot{z}$ is chosen to $\dot{z} = u_n + u_c + \nu_{SMC}$ and $\nu_{SMC} = L \cdot \text{sign}(s)$. Inserting for $\ddot{\theta}_d$, given in Equation (F.46), and $\dot{z}$ into Equation (F.54) gives:

$$\begin{aligned} \dot{s} &= u_n + u_c + \Delta_{b,f,SMC} - u_n - u_c - \nu_{SMC} \\ &= \Delta_{b,f,SMC} - L \cdot \text{sign}(s) \end{aligned} \tag{F.55}$$

The condition for sliding mode is $s = 0$. A Lyapunov function is used to investigate if sliding occurs. The Lyapunov function is chosen as shown in Equation (F.56) and its derivative is shown in Equation (F.57).

$$V(s) = \frac{1}{2} \cdot s^2 \tag{F.56}$$

$$\dot{V}(s) = s \cdot \dot{s} \tag{F.57}$$

Inserting Equation (F.55) for $\dot{s}$ results in

$$\dot{V}(s) = s \cdot (\Delta_{b,f,SMC} - L \cdot \text{sign}(s)) \tag{F.58}$$

If the constraint $\dot{V}(s) \leq -\eta \cdot |s|$ with $\eta > 0$ can be fulfilled, it may be concluded that $s \to 0$ as $t \to T < \infty$, whereafter sliding occurs i.e. $s = 0$ for $t \geq T$. The gain L in Equation (F.58) must be chosen such that $\dot{V}(s) \leq -\eta \cdot |s|$ will always apply. Based on Equation (F.58) and knowing that $s \cdot \text{sign}(s) = |s|$, the gain L must be chosen to satisfy Equation (F.59).

$$\begin{aligned} \dot{V}(s) = s \cdot (\Delta_{b,f,SMC} - L \cdot \text{sign}(s) &\leq -\eta \cdot |s| \Downarrow \\ L \cdot |s| \geq \eta \cdot |s| + |s| \cdot |\Delta_{b,f,SMC}|_{max} &\Downarrow \\ L \geq \eta + |\Delta_{b,f,SMC}|_{max} &\Downarrow \\ L \geq \eta + \left| \frac{b}{\hat{b}} \cdot \hat{f} - f + (u_n + u_c) \cdot \left(\frac{b}{\hat{b}} - 1 \right) \right|_{max} & \\ \geq \eta + \left| \left(\hat{f} - f \right) + \left(u_n + u_c + \hat{f} \right) \cdot \left(\frac{b}{\hat{b}} - 1 \right) \right|_{max} & \end{aligned} \tag{F.59}$$

From Equation (F.49) and Equation (F.51) it is known that $|\hat{f} - f| \leq F$ and $\left|\frac{b}{\hat{b}}\right|_{max} = \beta$. Based on those relations, Equation (F.59) can be rewritten as shown in Equation (F.60).

$$L \geq \eta + F + \left|u_n + u_c + \hat{f}\right| \cdot (\beta - 1) \tag{F.60}$$

Choosing L large enough will ensure sliding mode within a finite time.

For sliding to occur, $s = 0$ for $t > T$, will also require that $\dot{s} = 0$ [39]. By using that $\dot{s} = 0$ for $t \geq T$ and Equation (F.55), an equivalent controller, u_{eq} is designed as shown below.

$$\begin{aligned} 0 =& \Delta_{b,f,SMC} - L \cdot \text{sign}(s) \Downarrow \\ u_{eq} =& L \cdot \text{sign}(s) = \Delta_{b,f,SMC} \end{aligned} \tag{F.61}$$

In the ideal case, the compensator controller, u_c, should be chosen such that $u_c = -u_{eq}$. Inserting this controller will introduce a chattering problem due to the term sign(s). Therefore, a continuous approximation, u_{av}, of the equivalent controller is implemented. The equivalent controller can be continuously approximated by use of, for example, a low pass filter as shown in [21] or a tanh-function as shown in [40]. However, in this project, the equivalent controller is approximated as shown in Equation (F.62).

$$u_{av} = -L \cdot \text{sat}(s, \epsilon) \tag{F.62}$$

where

$$\text{sat}(s, \epsilon) = \frac{s}{|s| + \epsilon}, \text{ where } \epsilon > 0 \tag{F.63}$$

The designed controller will give the following system response:

$$\ddot{\theta}_d = u_n + u_c + \Delta_{b,f,SMC} \approx u_n \tag{F.64}$$

with

$$u_c = -u_{av} \approx -\Delta_{b,f,SMC} \tag{F.65}$$

The control parameter L and ϵ shall be chosen based on a compromise between tracking performance and control effort in addition to satisfying Equation (F.60).

F.5.3 Adaptive Controller

The purpose of the sliding mode controller was to compensate for the model error by designing a compensator controller. In stead of compensating for the model error, the main idea of the adaptive controller (AC) is to adjust the model parameters to cancel out the

model error. The AC utilizes the same control law as used for the BC, shown in Equation (F.42). Instead of estimating $\hat{b}$ and $\hat{f}$ based on system knowledge and measurements, the model parameters are adjusted to its real value by a gradient based adaption law. The adaption law is designed by following the structure for a self-tuning controller described in [41].

First, the equation of motion shown in Equation (F.35) is rewritten in vector form.

$$\begin{aligned}\ddot{\theta}_d &= b \cdot D_m - f \\ &= \underbrace{\begin{bmatrix} D_m & -1 \end{bmatrix}}_{\mathbf{W}} \cdot \underbrace{\begin{bmatrix} b \\ f \end{bmatrix}}_{\mathbf{a}} \\ &= \mathbf{W} \cdot \mathbf{a}\end{aligned} \tag{F.66}$$

The estimated system dynamics is calculated by Equation (F.67).

$$\ddot{\hat{\theta}}_d = \mathbf{W} \cdot \hat{\mathbf{a}} \tag{F.67}$$

where $\hat{\mathbf{a}}$ consists of the estimated parameters $\hat{b}$ and $\hat{f}$. The prediction error is defined as

$$\begin{aligned}e_{pre} &= \ddot{\hat{\theta}}_d - \ddot{\theta}_d \\ &= \mathbf{W} \cdot \hat{\mathbf{a}} - \mathbf{W} \cdot \mathbf{a} \\ &= \mathbf{W} \cdot \tilde{\mathbf{a}}, \text{ where } \tilde{\mathbf{a}} = \hat{\mathbf{a}} - \mathbf{a}\end{aligned} \tag{F.68}$$

A gradient based adaption law is used to estimate the model parameters. The implemented adaption law is shown in Equation (F.69).

$$\dot{\hat{\mathbf{a}}} = -p_0 \cdot \mathbf{W}^T \cdot e \tag{F.69}$$

where p_0 is a positive controller gain. The convergence of the model parameters is examined by using a Lyapunov function. The Lyapunov function is chosen as shown in Equation (F.70) and its derivative is shown in Equation (F.71).

$$V = \tilde{\mathbf{a}}^T \cdot \tilde{\mathbf{a}} \tag{F.70}$$

$$\dot{V} = 2 \cdot \tilde{\mathbf{a}}^T \cdot \dot{\tilde{\mathbf{a}}} \tag{F.71}$$

It is assumed that the real system parameters are constant, or at least varying very slowly compared to the estimated parameters, hence $\dot{\tilde{\mathbf{a}}} \approx \dot{\hat{\mathbf{a}}}$. Using this relation and Equation (F.68), Equation (F.69) can be written as

$$\dot{\tilde{\mathbf{a}}} = -p_0 \cdot \mathbf{W}^T \cdot \mathbf{W} \cdot \tilde{\mathbf{a}} \tag{F.72}$$

Inserting this into Equation (F.71) results in

$$\dot{V} = -2 \cdot p_0 \cdot \tilde{\mathbf{a}}^T \cdot \mathbf{W}^T \cdot \mathbf{W} \cdot \tilde{\mathbf{a}} \tag{F.73}$$

Equation (F.73) shows that $\dot{V}$ is at least negative semi-definite and implies that the gradient based parameter estimator is always stable. V is the squared parameter error and is never increasing, $\dot{V} \leq 0$. The convergence of the estimated parameters to the true parameters depends on the signals in $\mathbf{W}$. Since the reference signal is a part of the signals in $\mathbf{W}$, the reference trajectory will affect the convergence of the model parameters. As long as the signals in $\mathbf{W}$ are non-zero, the prediction error, e_{pre}, will converge to zero. This does not necessarily mean that the estimated parameters, $\hat{\mathbf{a}}$, will converge to the real parameters, $\mathbf{a}$. This only means that for the given input signal, D_m, both the model and the real system gives the same output, $\ddot{\hat{\theta}}_d = \ddot{\theta}_d$. For example, for a constant input signal, D_m = constant, there may be several solutions for $\hat{b}$ and $\hat{f}$ that gives the same output, $\ddot{\hat{\theta}}_d$. If a variable input signal is given, then there will be fewer solutions for $\hat{b}$ and $\hat{f}$ that gives the same output as the real system. This means that the probability for the model parameters to converge to its real values is higher when a variable input signal is given.

F.6 Simulation Results

High controllability of the winch is especially important during lift-off and lift-down at the deck, crossing the splash zone and lift-off and lift-down at the seabed. During lift-off and lift-down at deck and crossing the splash zone, the amount of payed out wire is small, resulting in a stiff lifting appliance. When landing the payload at the seabed, maybe, several thousand meters below the sea surface, the amount of payed out wire is large resulting in completely different dynamic characteristics of the lifting appliance. Therefore, two different test cases are used to test the designed controllers. The first test case imitates a lifting operation in the air with a small amount of the wire payed out. The second test case imitates a landing situation at the seabed. In test case 1, the vessel has no vertical heave motion but in test case 2, the vessel heaves up and down due to waves. In test case 2 the AHC system is used to stabilize the payload during landing.

F.6.1 Test Case 1: Motion Control in Air with External Force Disturbance

The first test case simulates a lift operation in air. The payload starts in a hanging position and is hoisted 10 m and then lowered back to the initial position with a trapezoidal velocity profile. During the lifting operation, an external force is applied to the payload

in order to test the controller's robustness to unmodeled external forces. In a real lifting operation, such external force may occur during water exit or entry, or in case of collision with other objects. The external force is set to 50 % of the force needed to hold the payload at rest. This test case is tested both with a payload equal to 15000 kg and 1000 kg in order to test the controllability with both heavy and light payloads.

Load case 1

In load case 1, the payload is set to 15000 kg. The simulation results are shown in Figure F.13. Plot 1 shows the drum position and the reference position, Plot 2 shows the tracking error, Plot 3 shows the payload position, Plot 4 shows the payload speed and Plot 5 shows the external force, F_{ext}, together with the wire force in the lower wire section, F_{w2}. Note that the tracking error in Plot 2 is transformed from the rotation domain and into the translation domain by multiplying the error in radians by the effective radius, $\theta_{err} \cdot r_{eff}$. This transformation is done to get a better understanding of the magnitude of the error.

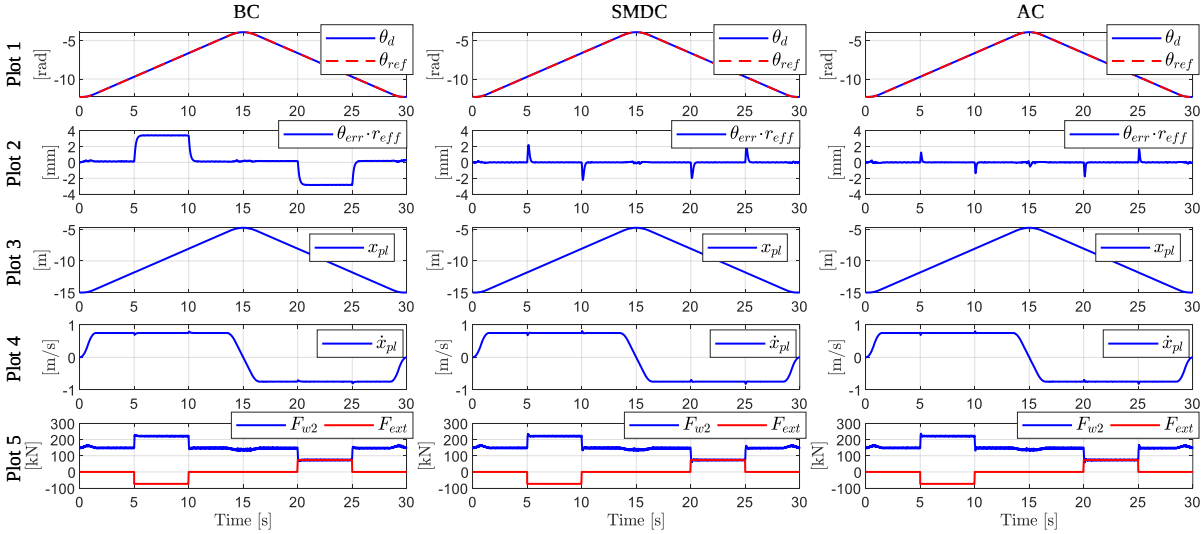

Figure F.13: Simulation results of test case 1 and load case 1 using the base controller (BC), the sliding mode disturbance controller (SMDC) and the adaptive controller (AC).

The external force is applied as a negative force, acting in downward direction, in the hoisting phase and as a positive force, acting in upward direction, in the lowering phase. The external force is applied as a step and lasts for 5 s. The left plots show the simulation results for the BC, the middle plots show the results for the SMDC and the right plots show the results for the AC.

The simulation results are relatively equal for all controllers in Plot 1, Plot 3, Plot 4 and Plot 5. Generally, the winch drum follows the reference trajectory well with small peaks in the payload speed when applying and removing the external force, after 5 s, 10 s, 15 s and 20 s respectively. In Plot 2, it can be seen that the tracking performance of the BC is characterized by a small steady state error when driving with constant speed and

some small oscillations when accelerating and decelerating the payload. The steady state error is very small when no external load is applied but gets a step when the external force is applied.

The SMDC and the AC has no steady state error. The tracking error have some small oscillations when accelerating and decelerating the payload. When the external force is applied, only a small peak in the tracking error can be seen.

Load case 2

In load case 2, the payload is set to 1000 kg. The simulation results are shown in Figure F.14. Compared to load case 1, the tracking performance is even better for light payloads. A step in the tracking error can be seen after 18 s in Plot 2 for the BC. This step occurs because the DDM changes operation quadrant.

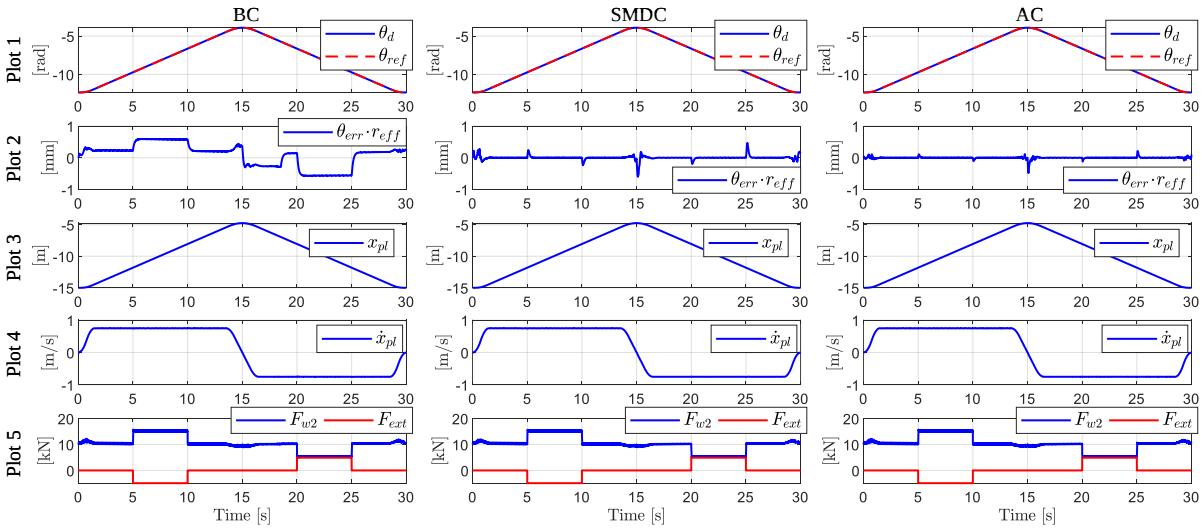

Figure F.14: Simulation results of test case 1 and load case 2 using the base controller (BC), the sliding mode disturbance controller (SMDC) and the adaptive controller (AC).

F.6.2 Test Case 2: Deep Water Landing

Test case 2 imitates a landing operation at the seabed. It is assumed that the vessel heaves up and down due to waves. Waves are irregular and random in shape, height, length and speed. It is assumed that the vessel has a similar motion and that the motion can be described by a Pierson-Moskowitz wave spectrum [42]. The heave motion is calculated by using the method described in [43] with a significant wave height of $H_s = 1.3$ m and a typical wave period of $T_p = 9$ s. An example of the vessel position when using this method is shown in Figure F.15. In order to compare the controllers, the same vessel motion is used for all three controllers.

A landing situation is chosen in order to test the tracking performance in AHC with a

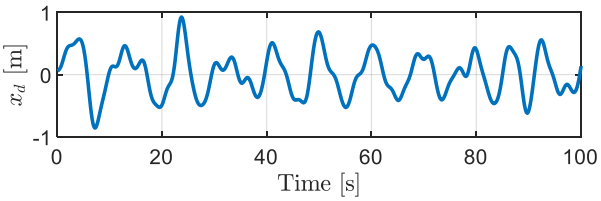

Figure F.15: Example of the vessel position described by the Pierson-Moskowitz wave spectrum with $H_s = 1.3$ m and $T_p = 9$ s.

heavy and light load and when a high amount of wire is payed out. Tracking performance with a heavy load is tested before landing and with a light load after landing. The mass of the payload is set to 20000 kg and the water depth is set to $L_{sb} = 1000$ m.

In general, the landing speed should be low in order to avoid high impact forces. A high impact force may damage the payload. Also, payloads placed at the seabed tend to sink into the soil. The lifting force needed to free the structure is dependent on the content of the soil and the impact force. Higher impact force results in higher suction force.

The AHC system should optimally cancel all of the vertical motion of the payload. In the literature there are simulation studies of AHC systems that shows compensation efficiencies of 84 % [44], 90-95 % [45], 95 % [46], 97.5 % [47] and 99 % [18]. The compensation efficiency is among other affected by the vessel motion, the surrounding medium and the payload. It is therefore hard to compare compensation performance and set a required compensation efficiency. However, based on input from offshore winch manufactures, the AHC system should at least reduce the payload motion below ±5 cm.

The simulation results for test case 2 are shown in Figure F.16. Plot 1 shows the

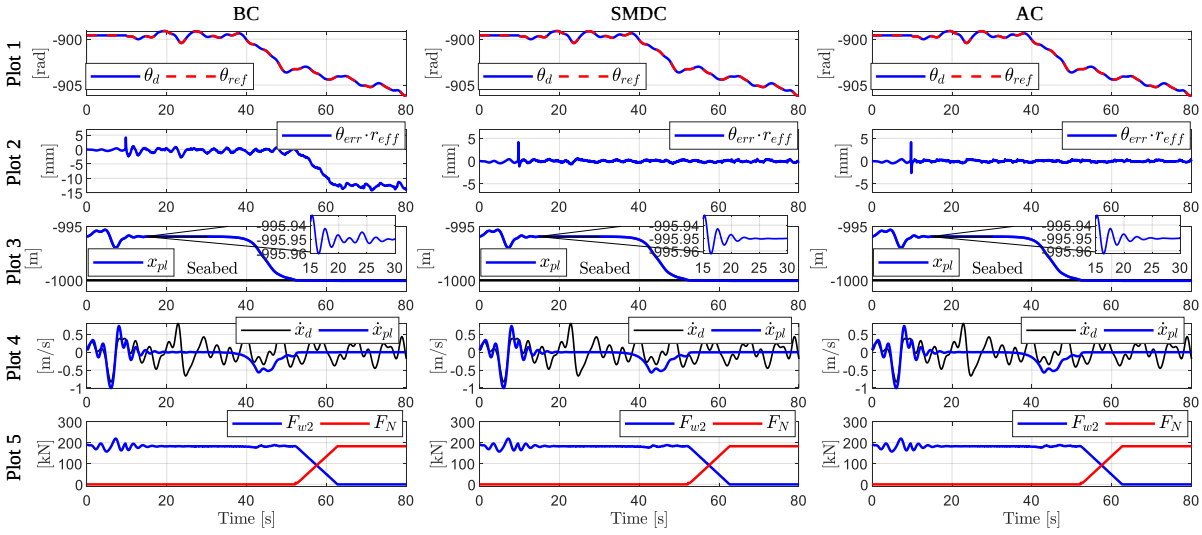

Figure F.16: Simulation results of test case 2 using the base controller (BC), the sliding mode disturbance controller (SMDC) and the adaptive controller (AC).

drum position and the reference position, Plot 2 shows the tracking error, Plot 3 shows the payload position, Plot 4 shows the vertical vessel velocity together with the payload velocity and and Plot 5 shows the lower wire force, F_{w2}, together with the seabed interaction force, F_N. The payload starts at approximately -995 m and is lowered down to the seabed at -1000 m. In the first 10 s, the winch drum is stopped and the payload moves up and down with the vessel motion. This can be seen in Plot 4 where the payload velocity matches the vessel velocity. After 10 s, the AHC system is activated and the payload is stabilized at a constant depth. Hence, the payload velocity approaches 0 m/s and the payload position is almost constant. This can be seen in the zoomed window in Plot 3. After 30 s, the lowering phase starts. The payload touches the seabed after approximately 52 s and the winch drum keeps paying out wire in order to slowly remove the tension in the wire rope. The wire tension is fully removed after approximately 62 s.

The simulation results shows that all controllers provides high controllability. The AHC system is capable of reducing the payload motion below ± 1 cm with the BC and even lower with the AC and the SMDC. This payload motion is within the requirements of ± 5 cm.

All controllers have a step in the tracking error when starting the AHC mode, see Plot 2 at 10 s. This occurs because the vessel motion is subtracted instantaneously from the reference trajectory when the AHC system is turned on. This results in a step in the desired drum position and therefore also a step in the tracking error. A smoother start-up of the AHC mode will reduce the tracking error when starting the AHC mode. After the AHC mode is activated, the tracking performance is best for the SMDC and the AC. The tracking error for the BC increases when the payload touches the ground. This is because the estimated parameters $\hat{b}$ and $\hat{f}$ used in the BC do not include the interaction force between the payload and the seabed. The model and the real system is therefore not the same after the payload touches the ground which results in increased tracking error.

All controllers provide a low landing speed, below 0.1 m/s, resulting in a low impact forces.

F.7 Discussion

This section compares all controllers regarding tracking performance, robustness and implementation issues.

F.7.1 Performance

All controllers showed high controllability and high tracking performance, however there are some differences. Figure F.17 shows the tracking error for all test cases and all

controllers. The upper plot shows the tracking error for test case 1 with load case 1, the middle plot shows the tracking error for test case 1 with load case 2 and the bottom plot shows the tracking error for test case 2. The results show that the tracking performance for

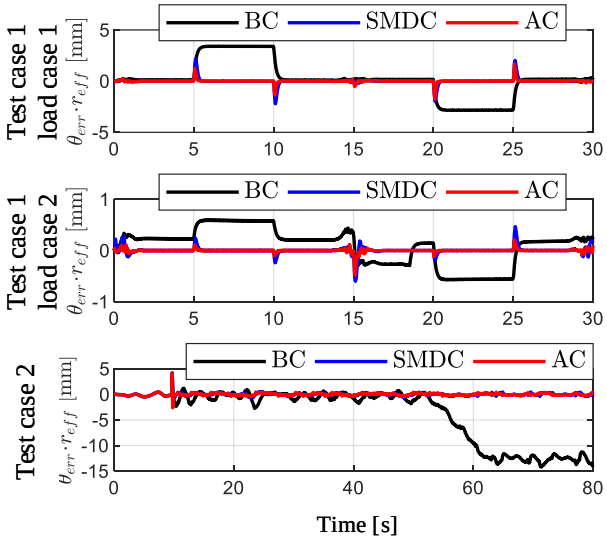

Figure F.17: Tracking error in test case 1 load case 1 (top plot), test case 1 load case 2 (middle plot) and test case 2 (bottom plot).

the SMDC and the AC is better than for the BC. The tracking performance for the SMDC and the AC is characterized by zero tracking error when driving with constant speed and only small peaks or oscillations in the tracking error when accelerating and decelerating the load, driving through 0 rpm and when an external load is applied or removed. The BC is characterized by a steady state error when driving with constant speed. Also, the steady state error is changed if an external force is applied to the system. This change in steady state error can be seen in test case 1 when the external load is applied and removed, after 5 s, 10 s, 20 s and 25 s respectively, and in test case 2 when the payload is in contact with the seabed, after 52 s.

The good tracking performance results in good compensation performance of the AHC system. For all controllers, the payload motion is reduced below $\pm$ 1 cm, which is below the requirement of $\pm$ 5 cm. However, a perfect tracking of the reference signal does not necessarily result in perfect heave compensation. For successful implementation of the AHC system, it is important to measure or estimate the vessel motion precisely and in real time. The applied reference trajectory must reflect the real vessel motion. An error in the reference signal will result in a compensation error.

The good tracking performance for the SMDC and the AC has some disadvantages. In order to achieve the high controllability, the cylinders in the DDM are reactivated more often when using the SMDC and AC compared to the BC. Figure F.18 shows the torque contribution from every single cylinder in test case 2 for a selected time period, 48 s to

50 s respectively.

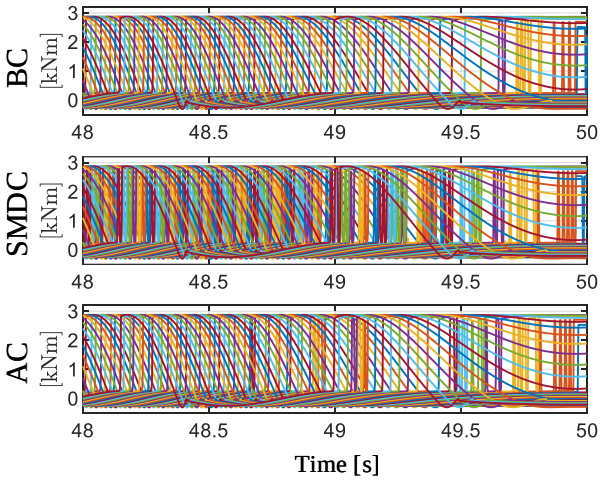

Figure F.18: Torque contribution from all cylinders in a limited period, 48 s to 50 s, in test case 2.

The upper plot shows the results for the BC, the middle plot shows the results for the SMDC and the bottom plot shows the results for the AC. Multiple vertical lines with the same color consecutively indicates that one cylinder is reactivated multiple times. It can be seen that the cylinders in the middle plot are reactivated more often then in the top and bottom plot. This means that the SMDC reactivates the cylinder chambers more often than the AC and the BC. The BC reactivates the cylinders fewest times. Reactivation of cylinders are undesirable because it introduces losses in the system.

F.7.2 Robustness

The robustness of the controllers is tested by applying an external force in test case 1. The results show that the SMDC and AC are very robust. The SMDC and the AC have a maximum tracking error below ± 2.5 mm when applying the external load in load case 1. The BC has a steady state error with maximum value below ± 3.5 mm in test case 1. Comparing the tracking error from load case 1 to the tracking error in load case 2 shows that the tracking performance when using the SMDC and the AC are almost the same and therefore not affected by the mass of the payload. For the BC, the steady state tracking error when operating with constant speed and without any external force is also almost equal in load case 1 and load case 2. However, the tracking error that occurs when the external load is applied is greater for load case 1 compared to load case 2 because the external force is higher.

F.7.3 Implementation

All controllers require a reference trajectory of the drum position, velocity and acceleration in addition to measurements of the drum position and velocity. The BC and the SMDC also require measurements of the payload mass while the AC requires measurement of the drum acceleration.

The BC has only two control parameters while the AC has three control parameters and the SMDC has four. The control parameter p_0 in the AC is relatively easy to tune by trial and error. However, p_0 should not be chosen too small or too large. A low value may result in a slow convergence of the model parameters and a too high value may result in an oscillatory behavior and slow convergence. Tuning of the control parameters L and ϵ in the SMDC is also relatively simple. Several combinations give satisfactory results. But one should remember that L must be chosen to satisfy Equation (F.60). A large value of L and a small value of ϵ result in good tracking performance but also high control effort with frequent reactivation of cylinder chambers. L and ϵ should therefore be chosen based on a compromise between tracking performance and control effort.

The convergence of the estimated parameters in the AC and also the stability of the system is depending on the desired displacement ratio, D_m. For example when lowering the load several thousand meters, the desired displacement ratio will be relatively constant and the estimated parameters, $\hat{b}$ and $\hat{f}$, may not converge to its real values. This may result in an unstable system. If the AC controller is implemented in a real system, one should include a safety function that resets the model parameters estimated by the gradient based adaption law to the parameters estimated for the BC if the deviation becomes too large.

F.8 Conclusion

This paper presents a digital displacement winch drive system and three controllers for the secondary controlled digital displacement motor. The main motivation for using digital displacement machines in a winch drive systems is to increase the energy efficiency compared to conventional hydraulic winch drive systems, especially when operating at low loads. One step to realize the digital displacement winch drive system is to design controllers that provide acceptable control performance of the winch system. The designed controllers are in this study evaluated regarding control performance, robustness and implementation issues. The simulation study shows that all controllers have good control performance. The SMDC and the AC have better controllability than the BC. However the good controllability for the SMDC and the AC requires more reactivations of the cylinder champers, which will result in increased energy losses. The BC has fewest control

parameters while the SMDC has the most. All controllers needs the reference trajectory of the drum position, velocity and acceleration in addition to measurements of the drum position and velocity. Only the AC needs measurements of the acceleration. All examined controllers have advantages and disadvantages. It is therefore important to consider all performance requirements and operation conditions before selecting a control strategy.

Acknowledgments

The research presented in this paper has received funding from the Norwegian Research Council, SFI Offshore Mechatronics, project number 237896.

Appendix A

Table F.1: Winch model parameters

Symbol	Value	Description
A_w	9.1e-4 m^2	wire rope cross-section area
C_A	0.72	added mass coefficient
C_d	0.85	drag force coefficient
C_{sb}	1000000 N/m	damping coefficient seabed
d_{load}	0.18/0.69/0.8 m	diameter payload
E_w	200 GPa	E-modulus wire rope
g	9.81 m/s^2	acceleration of gravity
J_d	1111 kgm^2	mass moment of inertia drum
J_m	0.378 kgm^2	mass moment of inertia DDM
k_{sb}	4000000 N/m	spring stiffness of the seabed
L_{sb}	1000 m	length to seabed
L_{ss}	20 m	length to sea surface
m_{load}	1/15/20 tonne	mass of the payload
N_{gear}	10	gear ratio pinion and gear ring
r_b	0.5 m	radius bearing
r_d	0.8 m	radius of drum
w_d	1.26 m	width of the drum
μ_c	0.1	coulomb friction coefficient
μ_v	1000 Ns/rad	viscous friction coefficient
ρ_{sea}	1024 kg/m^3	density sea water
ρ_w	5.66 kg/m	density of the wire rope

Table F.2: Digital displacement winch drive system parameters

Sym.	Value	Description
k_f	$2.3{\cdot}10^5$ s$\sqrt{\text{Pa}}/\text{m}^3$	valve flow coefficient
N_c	42	number of cylinders
$p_{atm}^{(abs)}$	101325 Pa	atmospheric pressure
p_H	220 bar	pressure in high pressure line
p_L	20 bar	pressure in low pressure line
V_0	$2.6{\cdot}10^{-4}$ m^3	dead volume in cylinder chamber
V_d	$2.6{\cdot}10^{-4}$ m^3/rev	cylinder displacement
β_L	1.2 GPa	bulk modulus of the hydraulic fluid
ϵ_{g0}	0.01	volume fraction of undissolved gas at $p_{atm}^{(abs)}$
ζ	0.8	is the damping ratio
κ	1.4	specific heat ratio
ω	833 Hz	is the natural frequency of the valves

Table F.3: Controller gains

Symbol	Value	Description
c_1	385 s^{-2}	controller gain BC, SMDC and AC
c_2	38.5 s^{-1}	controller gain BC, SMDC and AC
L	80 s^{-2}	controller gain SMDC
ϵ	5 s^{-1}	controller gain SMDC
p_0	50 s^{-1}	controller gain AC

Bibliography

[1] W. H. S. Rampen. Gearless transmissions for large wind turbines - the history and future of hydraulic drives. *Artemis Intelligent Power Ltd.*, 2006.

[2] Mikko Heikkila, Jyrki Tammisto, Mikko Huova, M Huhtala, and Matti Linjama. Experimental evaluation of a piston-type digital pump-motor-transformer with two independent outlets. *Fluid Power and Motion Control, Bath, England*, pages 83–98, 2010.

[3] Mikko Heikkilä, Linjama Matti, and Kalevi Huhtala. Digital hydraulic power management system with five independent outlets - simulation study of displacement controlled excavator crane. *The 9th International Fluid Power Conference, Aachen, Germany*, March 2014.

[4] Md Ehsan, WHS Rampen, and SH Salter. Modeling of digital-displacement pump-motors and their application as hydraulic drives for nonuniform loads. *Journal of dynamic systems, measurement, and control*, 122(1):210–215, 2000.

[5] Grégory S Payne, Uwe BP Stein, Mohammad Ehsan, Niall J Caldwell, and WHS Rampen. Potential of digital displacement hydraulics for wave energy conversion. In *Proceedings of the Sixth European Wave and Tidal Energy Conference, Glasgow*, 2005.

[6] GS Payne, AE Kiprakis, M Ehsan, W H S Rampen, JP Chick, and AR Wallace. Efficiency and dynamic performance of digital displacement$^{\text{TM}}$ hydraulic transmission in tidal current energy converters. *Proceedings of the Institution of Mechanical Engineers, Part A: Journal of Power and Energy*, 221(2):207–218, 2007.

[7] W H S Rampen. The development of digital displacement technology. In *Proceedings of the ASME/Bath Symp. on Fluid Power & Motion Control*, pages 11–16, 2010. keynote address.

[8] Christian Nørgård. *Design, optimization and testing of valves for digital displacement machines*. PhD thesis, Aalborg University, 2017. doi: 10.5278/vbn. phd. eng. 00013, 2017.

[9] Artemis Intellegent Power. Excavator development program. `http://artemis.armadillojam.co.uk/hybrid-hydraulic-excavator/`, July 2016. Accessed: 25-05-2019.

[10] M Karvonen, M Heikkilä, M Huova, M Linjama, and K Huhtala. Simulation study-improving efficiency in mobile boom by using digital hydraulic power management system. In *Proceedings of the The Twelfth Scandinavian International Conference on Fluid Power*, pages 355–368, 2011.

[11] Karl-Eirik Rydberg. Energy efficient hydraulic hybrid drives. *The 11th Scandinavian Conference on Fluid Power, SICFP'09, Lindköping, Sweden*, June 2009.

[12] Jamie Taylor, Win Rampen, Daniel Abrahams, and Andrew Latham. Demonstration of a digital displacement hydraulic hybrid bus. In *Proc. 2015 JSAE Annual Congress, Yokohama, Japan*, 2015.

[13] Artemis Intellegent Power. Saving fuel in rail vehicles. `http://www.artemisip.com/saving-fuel-in-rail-vehicles/`, June 2015. Accessed: 25-05-2018.

[14] Masahide Umaya, Toshihide Noguchi, Michiya Uchida, Masaaki Shibata, Yasuhiro Kawai, and Ryosuke Notomi. Wind power generation-development status of offshore wind turbines. *Mitsubishi Heavy Industries Technical Review*, 50(3):29, 2013.

[15] Henrik B Larsen, Magnus Kjelland, Anders Holland, and Per N Lindholdt. Digital hydraulic winch drives. In *BATH/ASME 2018 Symposium on Fluid Power and Motion Control*, pages V001T01A028–V001T01A028. American Society of Mechanical Engineers, 2018.

[16] MacGregor. Offshore cranes. url: https://www.macgregor.com/Products-solutions/products/offshore-and-subsea-load-handling/offshore-cranes/, 2019. Accessed: 04-10-2018.

[17] Magnus B Kjelland and Michael R Hansen. Offshore wind payload transfer using flexible mobile crane. *Modeling, Identification and Control*, 36(1):1–9, 2015.

[18] Peter Gu, Ahmed Ahmed Walid, Yousef Iskandarani, and Hamid Reza Karimi. Modeling, simulation and design optimization of a hoisting rig active heave compensation system. *International Journal of Machine Learning and Cybernetics*, 4(2):85–98, 2013.

[19] Zhou Entao, Yang Wenlin, and Lin Junzhe. Predictive control of hydraulic winch motion control. In *2009 2nd IEEE International Conference on Computer Science and Information Technology*, pages 1–4. IEEE, 2009.

[20] Stian Skjong and Eilif Pedersen. Model-based control designs for offshore hydraulic winch systems. *Ocean Engineering*, 121:224–238, 2016.

[21] Lasse Schmidt, Torben O Andersen, Per Johansen, and Henrik C Pedersen. A robust control concept for hydraulic drives based on second order sliding mode disturbance compensation. In *ASME/BATH 2017 Symposium on Fluid Power and Motion Control*, pages V001T01A033–V001T01A033. American Society of Mechanical Engineers, 2017.

[22] Lasse Schmidt, Torben O Andersen, Henrik C Pedersen, and Michael M Bech. An arbitrary order adaptive control structure with application to a hydraulic winch drive. In *ASME/BATH 2017 Symposium on Fluid Power and Motion Control*, pages V001T01A035–V001T01A035. American Society of Mechanical Engineers, 2017.

[23] Tor A Johansen, Thor I Fossen, Svein I Sagatun, and Finn G Nielsen. Wave synchronizing crane control during water entry in offshore moonpool operations-experimental results. *IEEE Journal of Oceanic Engineering*, 28(4):720–728, 2003.

[24] Jorg Neupert, Tobias Mahl, Bertrand Haessig, Oliver Sawodny, and Klaus Schneider. A heave compensation approach for offshore cranes. In *2008 American Control Conference*, pages 538–543. IEEE, 2008.

[25] Markus Richter, Eckhard Arnold, Klaus Schneider, Johannes K Eberharter, and Oliver Sawodny. Model predictive trajectory planning with fallback-strategy for an active heave compensation system. In *2014 American Control Conference, Portland, OR, USA*, pages 1919–1924. IEEE, 2014.

[26] Sondre Nordås, Michael M Beck, Morten K Ebbesen, and Torben O Andersen. Dynamic response of a digital displacement motor operating with various displacement strategies. *Energies*, 12(9):1737, 2019.

[27] Niels Henrik Pedersen, Per Johansen, and Torben Ole Andersen. Challenges with respect to control of digital displacement hydraulic units. *Modeling, Identification and Control*, 39(2):91–105, 2018.

[28] Niels Henrik Pedersen. *Development of Control Strategies For Digital Displacement Units*. PhD thesis, Aalborg University, Denmark, 2018.

[29] Niels H Pedersen, Per Johansen, and Torben O Andersen. Feedback control of puls-density modulated digital displacement transmission using a continuous approximation. *IEEE/ASME Transactions on Mechatronics*, 2018. Under 3rd revision.

[30] Per Johansen, Daniel B Roemer, Torben O Andersen, and Henrik C Pedersen. Discrete linear time invariant analysis of digital fluid power pump flow control. *Journal of Dynamic Systems, Measurement, and Control*, 139(10):101007, 2017.

[31] Niels H Pedersen, Per Johansen, and Torben O Andersen. Event-driven control of a speed varying digital displacement machine. In *ASME/BATH 2017 Symposium on Fluid Power and Motion Control, Sarasota, Florida, USA*, pages V001T01A029–V001T01A029. American Society of Mechanical Engineers, 2017.

[32] Niels Henrik Pedersen, Per Johansen, Torben O Andersen, and Rudolf Scheidl. Nonlinear hybrid control oriented modelling of a digital displacement machine. In *Proceedings of the 9th Workshop on Digital Fluid Power, Aalborg, Denmark*, pages 7–8, 2017.

[33] Niels H Pedersen, Per Johansen, and Torben O Andersen. Four quadrant hybrid control oriented dynamical system model of digital displacement® units. In *BATH/ASME 2018 Symposium on Fluid Power and Motion Control, Bath, UK*, pages V001T01A039–V001T01A039. American Society of Mechanical Engineers, 2018.

[34] Sondre Nordås, Morten Kjeld Ebbesen, and Torben Ole Andersen. Definition of performance requirements and test cases for offshore/subsea winch drive systems with digital hydraulic motors. In *ASME/BATH 2019 Symposium on Fluid Power and Motion Control, Sarasota, Florida, USA*. American Society of Mechanical Engineers, 2019. FPMC2019-1670.

[35] DNV GL. *DNVGL-RP-N103 Modelling and analysis of marine operation*, 7 2017.

[36] Daniel Beck Rømer. *Design and optimization of fast switching valves for large scale digital hydraulic motors*. PhD thesis, Department of Energy Technology, Aalborg University, 2014.

[37] Michael Rygaard Hansen. In Compendium *Fluid Mechanics*, 2015. Department of Engineering, University of Agder, Norway, Lecture notes MAS126, 2015; pp. 28–30.

[38] Farid El Breidi. *Investigation of digital pump/motor control strategies*. Ph.D. thesis, Purdue University, Indiana, USA, August 2016.

[39] J. Komsta, J. Adamy, and P. Antoszkiewicz. Input-output linearization and integral sliding mode disturbance compensation for electro-hydraulic drives. In *2010 11th International Workshop on Variable Structure Systems (VSS)*, pages 446–451, June 2010.

[40] Michael Rygaard Hansen, Torben Ole Andersen, and Henrik Clemmensen Pedersen. Robust control of a hydraulically actuated manipulator using sliding mode control. In *Fluid Power Transmission and Control ICFP'2005*, pages 864–868, 2005.

[41] Jean-Jacques E Slotine, Weiping Li, et al. *Applied nonlinear control*, volume 199. Prentice hall Englewood Cliffs, NJ, 1991.

[42] Willard J Pierson and Lionel Moskowitz. A proposed spectral form for fully developed wind seas based on the similarity theory of sa kitaigorodskii. *Journal of geophysical research*, 69(24):5181–5190, 1964.

[43] Sondre Sanden Tordal, Per-Ove Løvsland, and Geir Hovland. Testing of wireless sensor performance in vessel-to-vessel motion compensation. In *IECON 2016-42nd Annual Conference of the IEEE Industrial Electronics Society*, pages 654–659. IEEE, 2016.

[44] Liujun Li and Shaojun Liu. Modeling and simulation of active-controlled heave compensation system of deep-sea mining based on dynamic vibration absorber. In *2009 International Conference on Mechatronics and Automation*, pages 1337–1341. IEEE, 2009.

[45] JT Hatleskog and MW Dunnigan. Active heave crown compensation sub-system. In *OCEANS 2007-Europe*, pages 1–6. IEEE, 2007.

[46] Philip Bennett et al. Active heave: The benefits to operations as seen in the north sea. In *SPE/IADC drilling conference*. Society of Petroleum Engineers, 1997.

[47] Umesh A Korde. Active heave compensation on drill-ships in irregular waves. *Ocean engineering*, 25(7):541–561, 1998.